Nanocomposites et mousses à base de nanofibrilles de cellulose : rhéologie au cours de leur mise en forme et propriétés mécaniques

Florian Martoïa

UNIVERSITÉ GRENOBLE ALPES

THÈSE

Pour obtenir le grade de

DOCTEUR DE L'UNIVERSITÉ GRENOBLE ALPES

Spécialité : **Matériaux, Mécanique, Génie Civil, Electrochimie**

Arrêté ministériel : 7 août 2006

Présentée par

Florian MARTOÏA

Thèse dirigée par **Naceur BELGACEM** et
codirigée par **Pierre DUMONT et Laurent ORGÉAS**

préparée au sein **des Laboratoires LGP2 et 3SR**
dans **l'École Doctorale Ingénierie – Matériaux, Mécanique, Environnement, Energétique, Procédés, Production**

Nanocomposites et mousses à base de nanofibrilles de cellulose : rhéologie au cours de leur mise en forme et propriétés mécaniques

Thèse soutenue publiquement le **« 30 novembre 2015 »**,
devant le jury composé de :

Tatiana BUDTOVA
Directeur de recherche, Mines ParisTech (Rapporteur)
Guillaume OVARLEZ
Directeur de recherche, CNRS (Rapporteur)
Jean-Yves CAVAILLÉ
Professeur, INSA de Lyon (Président)
Véronique MICHAUD
Professeur, Ecole Polytechnique Fédérale de Lausanne (Examinateur)
Jean-Luc PUTAUX
Directeur de Recherche, CNRS (Membre invité)
Naceur BELGACEM
Professeur, Université de Grenoble Alpes (Directeur de thèse)
Pierre DUMONT
Professeur, INSA de Lyon (co-Directeur de thèse)
Laurent ORGÉAS
Directeur de recherche, CNRS (co-Directeur de thèse)

Résumé

Ce travail porte sur l'incorporation de nanorenforts biosourcés de type nanofibrilles de cellulose (NFC) dans les matériaux composites à matrice polymère et sur l'utilisation de ces nanoparticules pour l'élaboration de mousses. Ces nouveaux matériaux biosourcés peuvent être utilisés par exemple pour la conception de structures sandwich. L'étude à caractère expérimental, théorique et numérique s'articule autour de trois axes visant à optimiser tant les procédés d'élaboration que les propriétés en service de ces matériaux.

Dans un premier temps, la rhéologie des suspensions concentrées de NFC, fluides à seuil thixotropes, a été étudiée aux échelles macro et mésoscopiques en utilisant un dispositif original de rhéométrie couplé à des mesures de champs cinématiques par vélocimétrie ultrasonore. Nous montrons ainsi que l'écoulement des suspensions de NFC est fortement hétérogène et présente des phénomènes de glissement aux parois et de multiples bandes de cisaillement couplés avec des écoulements de type « bouchon ». Sur la base de cette étude, un modèle rhéologique multi-échelles est proposé. Ce modèle tient compte d'une part de l'architecture anisotrope des réseaux connectés de NFC dans ces suspensions, et d'autre part des interactions mécaniques et physico-chimiques aux échelles nanométriques. Il permet de montrer que les interactions colloïdales et hydrodynamiques, ainsi que la tortuosité et l'orientation des NFC jouent un rôle majeur sur la contrainte seuil et sur le comportement rhéofluidifiant de ces suspensions.

Dans un deuxième temps, des nanocomposites à matrice polymère ont été élaborés sous forme de films en faisant varier sur une très grande plage la fraction volumique de NFC. En utilisant d'une part des techniques de microscopie (AFM, MEB) et de diffraction aux rayons X, et d'autre part des essais mécaniques (traction, DMA) nous montrons que les NFC ont une orientation plane et s'organisent en réseaux connectés par des liaisons hydrogènes, que ces réseaux jouent un rôle majeur sur le comportement mécanique des nanocomposites et que le comportement élastique des nanocomposites est bien en deçà des prévisions données par les modèles micromécaniques de la littérature. À partir de ces constatations, nous proposons un modèle multi-échelles original où les nano-mécanismes de déformation prépondérants sont ceux se produisant dans les parties amorphes des NFC et au niveau des très nombreuses interfaces entre NFC.

Enfin, nous avons étudié l'influence des conditions d'élaboration, de la nature et de la concentration des NFC sur les microstructures (notamment au moyen d'images tridimensionelles obtenues par microtomographie synchrotron à rayons X), les propriétés mécaniques (essais de compression) et les micro-mécanismes de déformation (essai in situ de compression en microtomographie) de mousses préparées par cryodessiccation de suspensions aqueuses de NFC.

Abstract

This study focuses on the use of cellulose nanofibrils (NFCs) as bio-based nano-reinforcement in polymer composites and foams. These renewable materials can be used in place of traditional materials to fabricate for instance sandwich panels. This experimental, theoretical and numerical study aims at optimizing the fabrication of NFC-based materials and their use properties.

In the first part of this study, the rheology of concentrated NFC suspensions that behave as thixotropic yield stress fluids is investigated at macro- and mesoscales using an original rheo-ultrasonic velocimetry (rheo-USV) setup, enabling the local flow kinematic to be measured. We show that the flow of NFC suspensions is highly heterogeneous and exhibits complex situations with the coexistence of wall slippage, multiple shear bands and plug-like flow bands. Using this experimental database, we develop an original multiscale rheological model for the prediction of the rheology of NFC suspensions. The model takes into account the anisotropic fibrous nature of NFC networks as well as colloidal and mechanical interaction forces that occur at the nanoscale. The model predictions show that colloidal and hydrodynamic interaction forces as well as the orientation and the wavy nature of NFCs play a major role on the yield stress and shear thinning behaviour of the suspensions.

In the second part of this work, NFC-reinforced polymer nanocomposite films are fabricated for a wide range of NFC contents. Using advanced microscopy techniques (AFM, SEM), X-ray diffraction and mechanical tests (tensile and DMA tests), we show (i) that NFCs form highly connected nanofibrous structures with in-plane random orientation, (ii) that these connected NFC networks play a leading role on the mechanical behaviour of the nanocomposites and (iii) that the elastic properties of nanocomposite films are much lower than the predictions of the micromechanical models of the literature. In light of these observations, we propose an alternative multiscale model in which the main involved deformation nano-mechanisms are those occurring both in the amorphous segments of the nanofibers and in the numerous nanofiber-nanofiber contact zones.

Finally, in a third part we focus on the effect of the processing conditions, the suspension type and the NFC concentration on the microstructure (using X-ray synchrotron microtomography), the mechanical properties (using compression tests) and the deformation micromechanisms (using in situ compression test with X-ray microtomography) of various foams prepared from NFC suspensions by freeze-drying.

Table des matières

Introduction

Contexte général de l'étude

Les matériaux composites à matrices polymériques et les structures sandwich qui en sont issues sont de plus en plus utilisés dans de nombreux domaines comme le génie civil, l'industrie des transports ou bien encore celle des sports et loisirs. Ces matériaux et structures sont principalement employés pour toutes les applications qui requièrent à la fois rigidité et légèreté. Les structures sandwich résultent généralement de l'assemblage par collage ou soudure de deux peaux minces et rigides sur une âme plus légère qui maintient leur écartement. Les peaux rigides sont généralement constituées de stratifiés à matrice thermodurcissable ou thermoplastique et d'un renfort fibreux (sous forme de mat, tricot ou tissu) de verre, de carbone ou bien encore d'aramide selon les propriétés d'usage recherchées. Les âmes les plus utilisées sont les structures en nids d'abeilles (à base de papier et carton, polymère thermoplastique ou métal) et les mousses (métalliques, minérales, céramiques et polymères). Ainsi, une part importante des pièces conçues actuellement est constituée de matériaux d'origine non renouvelable qui présentent souvent une faible recyclabilité et un impact environnemental important.

Les nouvelles réglementations et l'évolution sociétale, économique, environnementale et sanitaire nous incitent à concevoir et développer des produits plus légers, plus performants, plus respectueux de l'environnement mais également plus compétitifs. Dans ce contexte, le remplacement progressif des matériaux traditionnels (fibres, matrices et mousses synthétiques) par des matériaux d'origine renouvelable à plus faible impact environnemental est un enjeu primordial. Dans cette optique, la biomasse végétale est une source de matière renouvelable importante qui offre une alternative intéressante. En effet, l'exploitation de la biomasse végétale, dont la production annuelle est estimée à 172 milliards de tonnes de matière sèche, permet d'obtenir une très grande diversité de matériaux et de briques élémentaires parmi lesquelles :

- les fibres lignocellulosiques issues du bois ou des plantes annuelles ;
- les nanofibrilles de cellulose (NFC), particules élementaires de taille nanométrique qui renforcent la paroi des fibres ligno-cellulosiques ;
- les biopolymères et les biomolécules.

Les fibres lignocellulosiques constituent une matière première biosourcée très abondante. Elles peuvent notamment être utilisées (en vrac ou sous forme de nappes) pour renforcer des matrices polymères. Les matériaux composites biosourcés à renfort naturel présentent généralement de bonnes propriétés mécaniques spécifiques. Celles-ci restent néanmoins assez dispersées, difficiles à contrôler et sont généralement encore inférieures à celles obtenues avec des composites « classiques » à fibres de verre. Ceci constitue un frein important à leur utilisation, par exemple en tant que peaux dans la conception de structures sandwich. En effet, pour que ces matériaux puissent être utilisés comme matériaux de substitution dans des applications industrielles, leurs propriétés doivent être au moins équivalentes à celles des composites classiques et leur coût de production doit rester compétitif.

Malheureusement, plusieurs aspects relatifs aux propriétés intrinsèques des renforts naturels (variabilité des propriétés géométriques et mécaniques des fibres, sensibilité à l'humidité), aux interfaces fibres-matrices (mouillabilité, adhésion) et aux conditions d'élaboration (contrôle difficile de la microstructure au cours de la mise en forme) sont susceptibles d'altérer fortement les propriétés en service des biocomposites. Plusieurs voies d'amélioration sont aujourd'hui étudiées afin d'accroître leurs performances mécaniques. Par exemple, de nombreux travaux de la littérature sont dédiés à l'optimisation des propriétés d'interface entre les fibres et les matrices (*cf.* chapitre 1).
Une stratégie émergente qui suscite un interêt croissant auprès de la communauté scientifique consiste à ajouter aux renforts naturels des composites des particules de taille nanométrique quasiment exemptes de défauts dont les propriétés mécaniques intrinsèques sont très élevées. L'idée générale consiste à renforcer à toutes les échelles macro, méso, micro et nanométriques les composites de sorte à accroître leur rigidité, leur ténacité et leur résistance à la fissuration. Actuellement, la plupart des études se sont essentiellement concentrées sur l'utilisation de nanotubes de carbone (NTC). Bien que possédant d'impressionnantes propriétés mécaniques et morphologiques, ces particules ont un coût de production élevé. En outre, les NTC ont un fort impact environnemental (production, toxicité, recyclabilité), peu favorable à une démarche de développement durable. Dans ce contexte, les nanofibrilles de cellulose extraites des fibres végétales présentent une alternative intéressante aux NTC. En effet, les nanofibrilles de cellulose constituent potentiellement, au regard de leurs propriétés morphologiques (élancement $l/d \approx 100 - 500$) et mécaniques (module d'élasticité $E \approx 80 - 100$ GPa) remarquables, d'excellents nanorenforts biosourcés de matrices polymères intéressants. Ainsi, des composites biosourcés à plusieurs échelles de renforts pourraient être produits en imprégnant des renforts naturels par des matrices polymériques chargées en NFC (Fig. 1). Cette stratégie permettrait d'obtenir des matériaux biosourcés aux propriétés mécaniques au moins équivalentes à celles des peaux utilisées actuellement (composites à fibres de verre). Ces nouveaux matériaux pourraient alors servir de peaux pour des structures sandwich.

Par ailleurs, plusieurs travaux de recherche ont récemment montré que les suspensions aqueuses de nanofibres de cellulose pouvaient aussi être utilisées pour élaborer des matériaux poreux biosourcés de faible voire très faible densité tels que des mousses (*cf.* chapitre 1). Le

développement de nouvelles mousses solides à base de NFC est actuellement en plein essor et montre l'énorme potentiel de ces matériaux en tant que matériaux de structures (p. ex. pour les structures sandwich). Ces nouveaux matériaux pourraient à terme remplacer les mousses synthétiques classiquement utilisées dans les structures sandwich (Fig. 1). Pour cela, leurs performances mécaniques spécifiques doivent être au moins équivalentes à celles des matériaux existants.

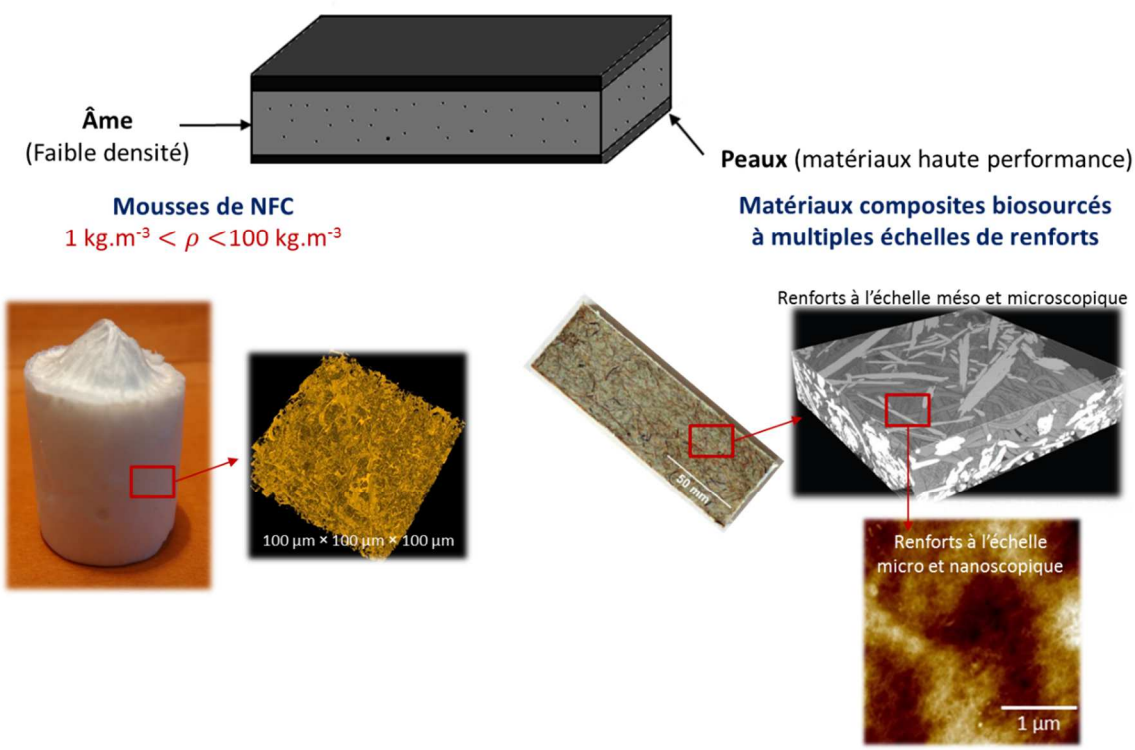

Figure 1. Exemple de structure composite biosourcée. Les peaux se présentent sous la forme de biocomposites à double échelle de renforts (renforts à base de fibres de plantes annuelles et de nanofibres de cellulose) et l'âme se présente sous la forme d'une mousse de NFC.

Les problématiques liées à la conception et au développement d'une structure sandwich biosourcée telle que celle montrée sur la Figure 1 sont multiples. D'une manière générale, la fabrication de ce type de structure requiert, entre autres, de bien maîtriser les procédés d'élaboration des peaux composites et de l'âme ainsi que l'assemblage (collage, soudage) des différents matériaux.

L'élaboration de composites à microstructure controlée et optimisée constitue encore aujourd'hui le sujet d'une intense activité de recherche. Atteindre cet objectif passe généralement par une bonne compréhension et maîtrise de la mécanique des renforts fibreux aux différentes échelles (assemblage de fibres, mèches de fibres, fibres unitaires), ainsi que de l'écoulement de la matrice de polymère en leur sein. Les problématiques propres à la mise en forme de composites traditionels (*cf.* chapitre 1) vont de surcroît être rendues plus complexes dans le cas des matériaux composites à double échelle de renforts :

- La première difficulté réside dans le mélangeage et la dispersion des NFC extraites en suspension dans l'eau avec les résines de polymères, qui sont souvent hydrophobes. Cette étape de mise en œuvre importante constitue encore aujourd'hui l'un des principaux verrous entravant fortement le développement de l'utilisation des NFC dans les composites. La plupart des procédés actuels de mélangeage et de mise en forme conduisent à des matériaux composites hétérogènes où les nanofibres sont présentes dans un état d'aggrégation important. Ce point sera décrit de manière plus détaillée dans le chapitre 1 de ce manuscrit.
- La deuxième difficulté réside dans le contrôle de la microstructure des composites aux différentes échelles lors de leur mise en oeuvre. L'élaboration de composites à plusieurs échelles de renforts implique de maîtriser (i) le comportement du renfort fibreux, comme pour les composites classiques, (ii) l'écoulement de la matrice de polymère en son sein et, (iii) le placement des NFC, c'est-à-dire d'assurer une distribution optimisée en taux et orientation des nanofibres. Les suspensions de fibres présentent généralement un comportement rhéologique complexe et encore mal appréhendé, ceci est d'autant plus vrai lorsque les renforts sont biosourcés et de taille nanométrique. À cet égard, nous verrons en effet dans le chapitre 1 que les suspensions de NFC sont sujettes à des méso et micromécanismes d'écoulement et de structuration-déstructuration extrêmement complexes.
- Pour tirer parti des propriétés remarquables des NFC et ainsi concevoir des matériaux aux propriétés optimisées, il est également nécessaire de comprendre comment les NFC s'agencent lorsqu'elles sont ajoutées à des polymères et quels sont les mécanismes de déformation et de transfert de charge qui prédominent à leur échelle, à l'échelle nanométrique. Ces données conditionnent la stratégie de placement des nanofibres dans les composites lors de leur mise en forme à l'état mou.

De même, l'élaboration de mousses de NFC aux propriétés microstructurales et mécaniques controlées n'est pas triviale. Elle implique de comprendre comment ces particules fibreuses de taille nanométrique s'agencent lors du processus de fabrication et quels sont les paramètres du procédé qui contrôlent l'architecture finale des matériaux. Tous ces aspects sont encore peu compris et maîtrisés.

D'autres aspects relatifs au comportement thermo-hygromécanique des composites et des mousses biosourcées ou bien encore les propriétés d'isolation phonique et thermique nécessitent d'être également intégrés au processus global de conception et de dimensionnement des structures sandwich. En effet, les matériaux biosourcés sont des matériaux issus du vivant dont le comportement présente généralement une sensibilité à la température et à l'humidité bien plus prononcée que les matériaux synthétiques.

Objectifs de la thèse

C'est dans ce contexte général que s'inscrit cette étude. Cependant, comme il s'agit d'un projet de recherche dont les thématiques sont relativement récentes et encore peu développées, nous avons fait le choix de concentrer notre étude sur plusieurs problématiques qui se situent en amont de la conception des structures composites sandwich biosourcées. L'objectif sous-jacent aux différentes études présentées dans ce manuscrit est de contribuer, par l'expérience et la modélisation, à l'optimisation des procédés d'élaboration de composites multi-échelles et de mousses à partir de nanorenforts fibreux biosourcés, ici, des nanofibrilles de cellulose.

Afin de mieux comprendre ces nouveaux systèmes, nous avons fait le choix, dans ce projet de thèse, de se placer dans un cadre simplifié qui s'articule autour de **3 axes principaux** :

- **La rhéologie des NFC**

L'élaboration des matériaux composites à matrice polymérique et renforts fibreux, ou bien des mousses passe généralement par des étapes de mise en forme ou d'élaboration où les renforts fibreux sont présents dans des suspensions aux comportements rhéologiques complexes et encore peu étudiés. En vue d'optimiser l'élaboration de ces matériaux, nous nous sommes intéressés à la rhéologie de suspensions aqueuses de NFC. Dans cette approche simplifiée du problème, où l'eau joue le rôle de matrice modèle, nous avons proposé dans le **chapitre 2** de ce manuscrit, une nouvelle méthodologie expérimentale pour comprendre et caractériser les écoulements complexes de ces suspensions de particules biosourcées de taille nanométrique. Plus particulièrement, dans cette partie nous avons étudié l'influence des propriétés microstructurales et physico-chimiques des NFC sur la rhéologie des suspensions aqueuses qu'elles forment aux échelles macroscopique (échelle du rhéomètre) et mésoscopique (échelle de l'écoulement). Pour les deux types de suspension de NFC étudiées, nous avons cherché à relier leur comportement rhéologique complexe éudié à l'échelle macroscopique à leur cinématique locale d'écoulement.
Àpartir de cette analyse, nous proposons dans le **chapitre 3** un modèle rhéologique multi-échelles construit à partir des mécanismes de déformation et d'écoulement aux échelles fines.

- **Les nanocomposites**

Les propriétés mécaniques des matériaux composites à base de NFC sont encore relativement mal connues et la modélisation de ces propriétés reste encore un problème largement ouvert. La plupart des modèles micromécaniques de la littérature ne parviennent pas à reproduire le comportement mécanique de nanocomposites. Cette déficience peut constituer un frein majeur à la conception et au dimensionnement théorique des structures constituées de ces matériaux. Dans l'objectif d'apporter des éléments de réponse à cette problématique importante, nous avons cherché à élaborer des composites modèles en utilisant une matrice hydrosoluble qui se mélange facilement aux suspensions de NFC et qui, de surcroît, possède une très bonne affinité chimique avec les nanofibres de cellulose. Nous avons ensuite caractérisé la microstructure et

les propriétés mécaniques des matériaux ainsi obtenus. À partir de ces données, nous avons proposé dans le **chapitre 4** un modèle micromécanique original pour décrire l'élasticité des nanocomposites renforcés par des NFC.

- **Les mousses de NFC**

Le développement de nouvelles mousses solides à base de NFC est actuellement en plein essor et montre l'énorme potentiel de ces matériaux en tant que matériaux de structures. Cependant, les liens entre les microstructures de ces mousses et leur procédé d'élaboration sont encore mal appréhendées ce qui a pour conséquence une mauvaise maîtrise des propriétés mécaniques des mousses ainsi élaborées. Ainsi, dans le **chapitre 5**, nous avons étudié différents procédés d'élaboration de mousses à partir de suspensions aqueuses de NFC. L'analyse des microstructures de ces mousses, de leur comportement mécanique et des micromécanismes de déformation sous-jacents nous ont permis de proposer de nouvelles voies pour élaborer des mousses à l'architecture et au comportement optimisés.

Chapitre 1

Aperçu général sur les matériaux biosourcés et leurs produits dérivés

Dans ce premier chapitre, nous allons présenter quelques éléments bibliographiques sur les matériaux d'origine renouvelable, en se focalisant plus particulièrement sur les biocomposites (partie 1.2), les nanocomposites (partie 1.3) et les nouveaux matériaux poreux cellulosiques (partie 1.4).

1.1 Matériaux biosourcés

1.1.1 Définition

Les matériaux dits biosourcés sont des matériaux issus de ressources renouvelables, c'est-à-dire des matériaux directement ou indirectement issus de la biomasse (végétale, animale, bactérienne, fongique)[1,2,3]. Cette famille de matériaux est assez vaste et peut être grossièrement déclinée en plusieurs sous-catégories :

- les matériaux issus directement ou indirectement de fibres végétales (fibres de bois et de plantes annuelles), qui font l'objet du présent travail ;
- les matériaux issus directement ou indirectement des organes de réserve des végétaux (graines, racines, tubercules, rhyzomes, fruits), par exemple les matériaux élaborés à partir d'amidon ou de saccharose ;
- les matériaux biosourcés issus des algues et des micro-organismes ;
- les matériaux issus directement ou indirectement de la biomasse animale tels que la chitine et le chitosan, polymères extraits des cuticules externes des insectes et des carapaces des crustacés.

Dans le système de classification proposé, la première sous-catégorie est la plus importante en termes de disponibilité et de diversité des matériaux produits. En effet, la cellulose, les hémicelluloses et la lignine, constituants majoritaires de la paroi des fibres végétales, sont les polymères les plus abondants sur la terre. Environ 10^{11} t de cellulose sont biosynthétisées chaque année par photosynthèse[4].

Pour prendre conscience de la richesse et du potentiel des fibres végétales en tant que matière première renouvelable, il faut comprendre un peu mieux la structure et les constituants de ces objets. Dans la suite de cette étude, la structure des fibres végétales est tout d'abord détaillée (partie 1.1.2.1). Nous décrivons ensuite les principaux procédés d'extraction des fibres et de leurs constituants élémentaires aux différentes échelles (partie 1.1.2.2), ainsi que leurs caractéristiques morphologiques et mécaniques (partie 1.1.2.3). Enfin, dans la partie 1.1.2.4, nous présentons quelques exemples de matériaux à base de fibres végétales ou élaborés à partir de briques élémentaires (nanoparticules, biopolymères) issues de ces fibres.

1.1.2 La fibre végétale : une matière première biosourcée abondante

Les fibres végétales présentent des avantages certains et bien connus comme par exemple un faible coût de production (1.5 à 2 €/kg pour des fibres de lin, moins de 1 €/kg pour les fibres de bois blanchies), une faible masse volumique ($\rho \approx 1200$ à 1400 kg m^{-3}), un module élastique ($E \approx 10 - 60$ GPa) et une contrainte à rupture élevées ($\sigma \approx 400 - 700$ MPa), une grande disponibilité à travers le monde, une surface réactive et la possibilité de générer de l'énergie sans résidu après combustion à la fin de leur cycle de vie[1-5]. Par ailleurs, leur structure hiérarchisée et semi-cristalline ainsi que leur composition biochimique riche et variée impliquent que les

fibres végétales sont une matière première renouvelable intéressante pour de multiples matériaux biosourcés.

1.1.2.1 Structure et composition des fibres végétales

Les fibres végétales, souvent appelées abusivement « fibres de cellulose », constituent les squelettes organiques des cellules des végétaux (Fig. 1-1.a,b). Dans le bois ou les plantes, ces fibres se présentent sous forme de faisceaux qui assurent la rigidité et la résistance mécanique[6,7]. En première approche, la paroi des fibres peut être assimilée à des assemblages de plis composites (couches P, S1, S2, S3, Fig. 1-1.c) constitués d'une matrice amorphe d'hémicellulose ($\approx 30\%$) de lignine ($\approx 30\%$), voire de pectine ($\approx 1-2\%$) renforcée par des macro ou mésofibrilles de cellulose semi-cristallines ($\approx 40\%$). Dans la paroi primaire (P), les macrofibrilles sont relativement désordonnées tandis que dans la paroi secondaire (S2) elles s'enroulent en hélice suivant un angle (nommé angle microfibrillaire θ sur la Fig. 1-1.c) par rapport à l'axe longitudinal de la fibre[7]. Entre les différentes couches ou strates (S1, S2, S3), l'agencement des macrofibrilles peut changer brusquement (Fig. 1-1.c). À une échelle plus fine, ces macrofibrilles de cellulose (0.5 µm de diamètre, Fig. 1-1.d) sont constituées d'un ensemble de faisceaux (10 à 100 nm de diamètre, Fig. 1-1.e) formés de fibrilles élémentaires (3.5 à 5 nm de diamètre, Fig. 1-1.e et Fig. 1-1.f) disposées sous forme de mèches. Les nanofibrilles de cellulose (NFC) (ou « *cellulose nanofiber* » (CNF) en anglais) qui font l'objet de ce travail désigne à la fois les faisceaux de fibrilles (Fig. 1-1.e) et les fibrilles élémentaires (Fig. 1-1.f).

À une échelle supramoléculaire (< 1 nm), chaque fibrille élémentaire (Fig. 1f) est constituée d'environ une trentaine de brins ou chaînes de cellulose ayant un degré de polymérisation (DP) compris entre 5000 et 10000 en fonction des végétaux[7]. De même, la composition chimique et l'agencement des microfibrilles dans les fibres végétales (Fig. 1c) varient en fonction de l'origine botanique.

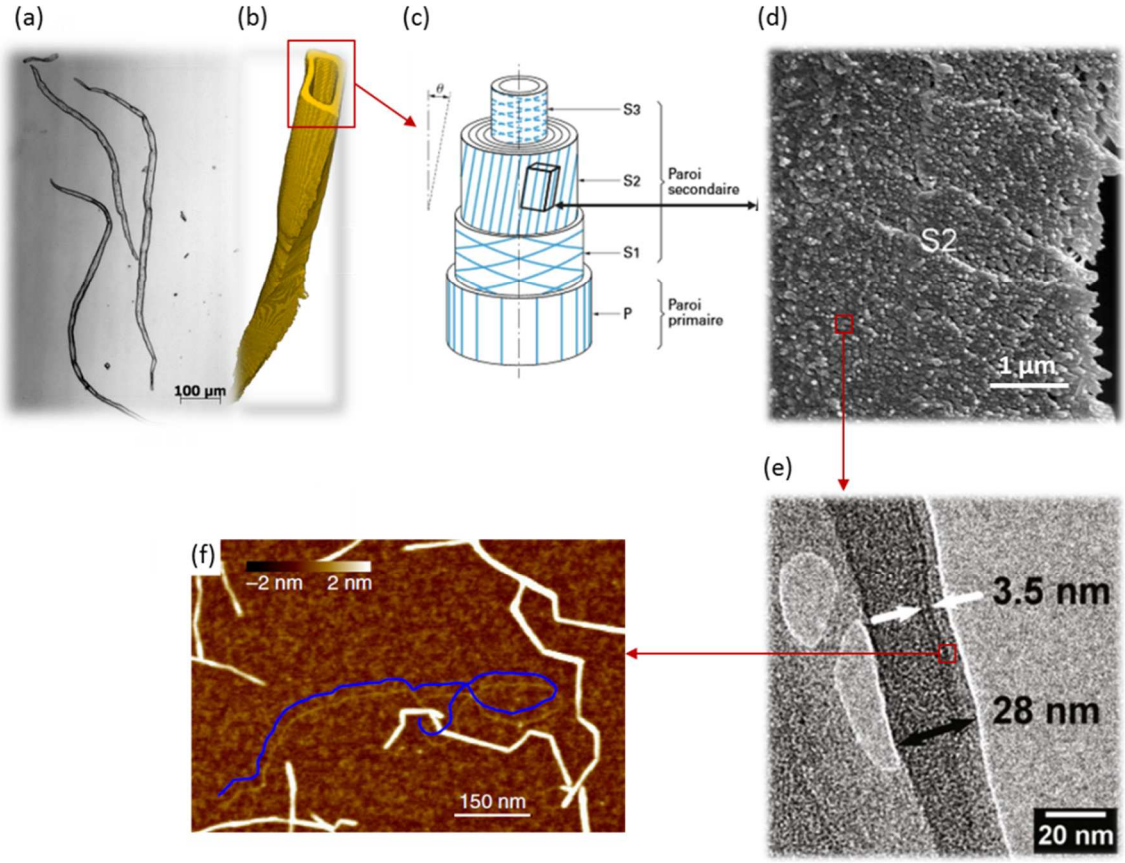

Figure 1-1. (a) Micrographie d'une suspension de fibres d'eucalyptus obtenue au microscope optique montrant 3 fibres élémentaires. (b) Image 3D d'une fibre de résineux obtenue par microtomographie à rayons X sur la ligne ID19 de l'ESRF (taille de voxel : 0.32^3 µm^3)[8]. (c) Schéma simplifié de la microstructure d'une fibre végétale montrant l'agencement des macrofibrilles de cellulose[9]. (d) Micrographie MEB de la paroi d'une fibre de cellulose (couche S2)[10]. (e) Micrographie MET d'un faisceau (28 nm de diamètre) constitué de fibrilles élémentaires (3.5 nm de diamètre) disposées sous forme de mèches[11]. (f) Micrographie AFM d'un film de nanofibrilles de cellulose (extraites à partir de fibres de bois). Le contour bleu indique une unique chaîne de cellulose (hauteur mesurée à l'AFM d'environ 0.5 nm)[12].

1.1.2.2 Les procédés d'extraction

1.1.2.2.1 Extraction des fibres végétales

D'une manière générale, les fibres végétales sont extraites par des traitements chimiques et mécaniques[7,13]. On distingue les procédés d'extraction propres à l'industrie papetière et les procédés issus de l'industrie du textile. Dans la suite de cette étude, les principaux traitements d'extraction des fibres végétales sont brièvement présentés. Le lecteur intéressé pourra se reporter à plusieurs ouvrages[13,7,14] pour des approfondissements sur le sujet.

- **Procédés issus de l'industrie papetière**

La fabrication d'une pâte à papier de fibres vierges (fibres en suspension dans l'eau) se fait généralement à partir de fibres de bois de résineux et de feuillus. On distingue deux grandes familles de pâtes vierges qui diffèrent selon leur technique d'obtention : les pâtes mécaniques (Fig. 1-2.c) et les pâtes chimiques (Fig. 1-2.a,b). L'objectif commun à ces deux procédés reste

néanmoins le même : séparer de manière individuelle les fibres liées les unes aux autres au sein des végétaux par un ciment ligneux[13].

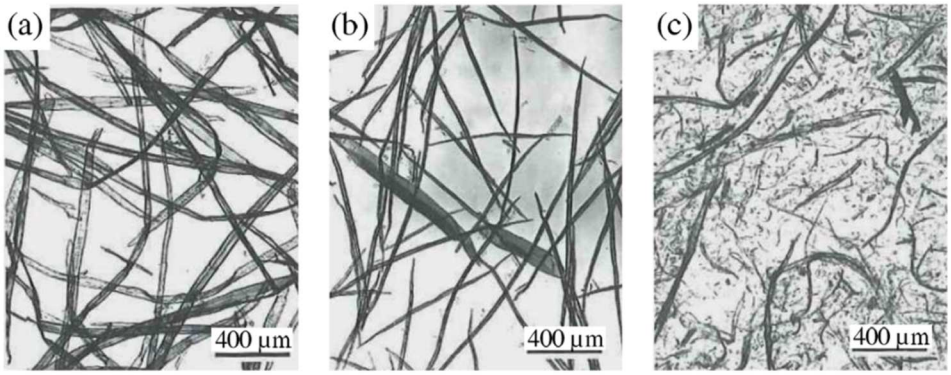

Figure 1-2. Fibres non raffinées de pâte chimique issues (a) d'épicéa et (b) de bouleau. (c) Fibres de pâte thermomécanique issues d'épicéa[14].

- Les pâtes mécaniques sont traditionnellement obtenues à partir de rondins ou de copeaux de bois broyés ou râpés en présence d'eau (défibrage mécanique). Les rondins de bois sont pressés contre d'énormes meules abrasives tandis que les copeaux de bois sont désintégrés par des appareils munis de disques équipés de lames tranchantes. Le défibrage peut être aussi réalisé à haute température ($T > 100$°C) et sous pression afin de ramollir les fibres et ainsi faciliter leur extraction et individualisation. En général, ces traitements mécaniques permettent d'obtenir un rendement de matière première important (environ 90 à 95% en masse), car toute la matière première végétale est transformée en pâte, y compris les lignines[13]. Les pâtes obtenues sont néanmoins de mauvaise qualité et contiennent généralement des fibres grossières, plutôt courtes et partiellement déstructurées, des agrégats ainsi que de nombreux contaminants et impuretés (Fig. 1-2.c). En outre, la surface des fibres est recouverte d'une quantité importante de lignine, ce qui engendre d'importants problèmes d'interfaces dans les papiers et composites[14].

- Les procédés chimiques de défibrage du bois ont pour propriétés de séparer les fibres de bois tout en éliminant quasiment totalement leur contenu en lignine. Deux procédés sont utilisés pour obtenir ces pâtes : le procédé bisulfite et le procédé kraft. Dans les deux cas, la séparation des fibres (à partir de copeaux de bois) est obtenue par cuisson en milieux aqueux, à haute température ($T \approx 130 - 180$°C), sous pression et pendant plusieurs heures dans un réacteur chimique. À l'issue de la cuisson, les éléments indésirables sont dissous dans le milieu aqueux qui devient une liqueur à évacuer. Les fibres extraites sont ensuite lavées et éventuellement soumises à des opérations chimiques de blanchiment. La cuisson donne un rendement de matière bien inférieur aux procédés mécaniques (environ 45 à 55% en masse), mais les pâtes sont d'excellente qualité. Elles sont constituées de fibres individualisées longues (Fig. 1-2.a) présentant généralement de très bonnes propriétés mécaniques.

- **Procédés issus de l'industrie textile**

Les fibres végétales utilisées dans le textile sont généralement extraites à partir de plantes annuelles (lin, chanvre, ramie, etc.), par voie sèche en utilisant des traitements principalement mécaniques. Plusieurs étapes sont nécessaires pour séparer les fibres de la tige des plantes[9]. La première étape consiste à faire rouir la plante. Le rouissage a lieu généralement dans le champ. Dans le cas du lin par exemple, les plantes coupées ou arrachées sont laissées au sol ce qui permet aux micro-organismes de libérer des enzymes dégradant les pectines qui lient les fibres entre elles au sein de la tige. Cette étape est suivie d'une étape de broyage mécanique dont l'objectif est de fragmenter les parties ligneuses. Le teillage permet ensuite de séparer les nombreux fragments ligneux (« bûchettes ») du reste des fibres ou faisceaux de fibres. Les faisceaux de fibres sont alors peignés et cardés. Cette étape permet de séparer les fibres longues des fibres courtes, de les démêler et de les aérer. Les fibres longues constituent « la filasse » qui part vers les filatures pour la filière textile tandis que les fibres courtes ou « étoupes de teillage » sont transformées en « non-tissés » (Fig. 1-9.b) ou mélangées à d'autres fibres[9].

Notons également que des traitements mécaniques, physiques et chimiques complémentaires peuvent être requis afin d'obtenir par exemple une meilleure séparation des faisceaux de fibres en fibres unitaires ainsi qu'un « nettoyage » de leur surface accru (élimination des nombreuses cires et pectines résiduelles[9]).

1.1.2.2.2 Extraction des nanofibrilles (NFC) et nanocristaux (NCC) de cellulose

L'édifice complexe et très hiérarchisé qui forme la paroi des fibres végétales peut être « déstructuré » par des processus chimiques ou mécaniques pour en extraire des fibrilles ou mèches de fibrilles semi-cristallines pratiquement exemptes de défauts (Fig. 1-1.e, Fig. 1-1.c,d)[4]. Les matériaux obtenus à l'issue de ces traitements sont appelés « nanocelluloses ». On distingue dans cette famille, les nanofibrilles de cellulose (NFC) et les nanocristaux de cellulose (NCC) qui diffèrent les unes des autres par leurs propriétés morphologiques et cristallographiques[4].

- **Extraction des NFC**

La plupart des nanofibrilles de cellulose sont aujourd'hui obtenues par voie mécanique[4,15,16]. L'objectif de cette opération mécanique est de soumettre les parois cellulaires végétales à un cisaillement mécanique intense afin de « relâcher » la structure d'origine des fibres présentée dans la partie 1.1.2.1 (Fig. 1-1.c)[4,15,16]. À l'issue de ce traitement, des mèches ou faisceaux de nanofibrilles ayant des diamètres de l'ordre de 10 à 100 nm et des longueurs pouvant atteindre la dizaine de microns sont obtenues[4,17,18]. Trois technologies dérivées de l'industrie agroalimentaire et pharmaceutique sont classiquement utilisées[4].

- Le traitement mécanique peut être réalisé à l'aide d'un homogénéisateur haute pression de type Gaulin (Fig. 1-3.a). Avec cette technique, les suspensions aqueuses de fibres (1 à 2% en masse) sont pompées à haute pression vers une soupape (fente mince) mue par un ressort permettant une succession rapide d'ouvertures et de fermetures générant par ailleurs une forte chute de pression. Les fibres traversant cette fente mince sont alors soumises à de fortes sollicitations de cisaillement et d'impact[19].

- Une alternative à l'homogénéisateur est le microfluidiseur (Fig. 1-3.b). Dans ce cas, la suspension de fibres (1 à 2% en masse) est pompée à haute pression au travers de plusieurs chambres « d'interaction » en forme de z[16].

- La déstructuration mécanique des fibres peut être également réalisée par un procédé de broyage par friction (utilisé au cours de ce travail) (Fig. 1-3.c). Le broyeur se compose de deux disques en céramique dont les surfaces sont munies de barres et de rainures (Fig. 1-3.c). Le disque supérieur est fixe tandis que le disque inférieur est en rotation rapide (typiquement $1500 - 3000$ tr/min). L'entrefer entre les deux disques est réglable. La suspension de fibres est introduite dans une trémie et dispersée sous l'effet de la force centrifuge au travers de l'entrefer. Les fibres sont alors soumises à des forces de compression, cisaillement et friction[20,18].

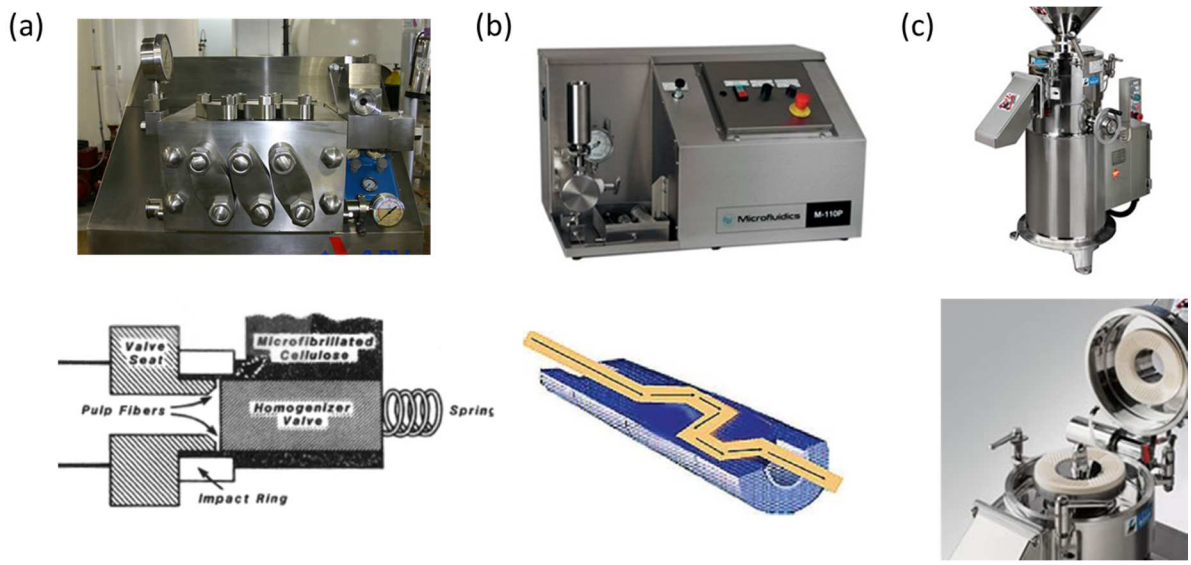

Figure 1-3. (a) Photographie et schéma de principe d'un homogénéisateur haute pression (GEA process Engineering Inc., Italie). (b) Photographie et schéma montrant la chambre d'interaction en forme de z du microfluidiseur (Microfluidics Inc., USA). (c) Photographies d'un dispositif de broyage par friction (Masuko Sangyo, Japon).

Les suspensions de NFC obtenues à l'issue de ces traitements mécaniques sont des suspensions aqueuses ayant un aspect de gel même à de très faibles concentrations (1 à 2% en masse). Bien que l'eau soit le milieu liquide le plus utilisé, tout autre liquide polaire pourrait l'être également. Cependant, le degré de fibrillation obtenu à l'issue du traitement mécanique va dépendre du pouvoir de gonflement que ce liquide possède sur les fibres de cellulose[4].

- **Prétraitements des fibres**

Les procédures d'extraction mécaniques décrites précédemment sont associées à une consommation d'énergie élevée. En effet, de 10 à 60 cycles d'homogénéisation sont souvent nécessaires afin d'augmenter le degré de fibrillation[17,18]. Spence *et coll.*[21] ont notamment montré que la consommation électrique associée à un processus d'extraction réalisé au moyen d'un homogénéisateur était de l'ordre de 70 000 kW/t. Cette énergie est plus de 70 fois supérieure à celle requise pour produire de la pâte à papier (1000 kW/t)[15]. En outre, les NFC produites uniquement par traitement mécanique restent grossières malgré l'apport énergétique important.

Par conséquent, plusieurs prétraitements des fibres ont été proposés pour faciliter le processus de désintégration mécanique[16,15]. D'une manière générale, les stratégies développées visent à fragiliser les liaisons hydrogènes entre les mèches de nanofibrilles dans les fibres. Parmi les nombreux prétraitements développés[4], les plus couramment utilisés (et mis en œuvre dans ce travail) sont :

- Le prétraitement enzymatique visant à altérer la cohésion de la paroi des fibres végétales (dégradation du degré de polymérisation des chaînes de cellulose) par le biais d'enzymes de type endoglucanase[22,23] (Fig. 1-4).

- L'oxydation induite par le réactif 2,2,6,6-tétraméthyl-1-pipéridinyloxy (TEMPO) visant à introduire dans la structure de la cellulose native des groupes fonctionnels carboxylates (-COO^-) et aldéhydes (-COH), c'est-à-dire des charges répulsives en surface pour faciliter la séparation des mèches de nanofibrilles de cellulose dans les fibres (Fig. 1-5.b). Cette méthode consiste plus précisément en une réaction d'oxydation des fibres de cellulose par l'addition d'hypochlorite de sodium (NaClO) en présence des catalyseurs TEMPO et NaBr à un pH de $10-11$ à température ambiante[24,25] (Fig. 1-5.a). D'autres prétraitements tels que la carboxyméthylation[26] ou la quaternisation[27] peuvent être également utilisés afin d'introduire des charges à la surface des mèches de fibrilles de cellulose.

Ces prétraitements permettent de diminuer considérablement la consommation énergétique à environ 1000 kW/t, rendant ainsi les procédures d'extraction des NFC industriellement viables[4].

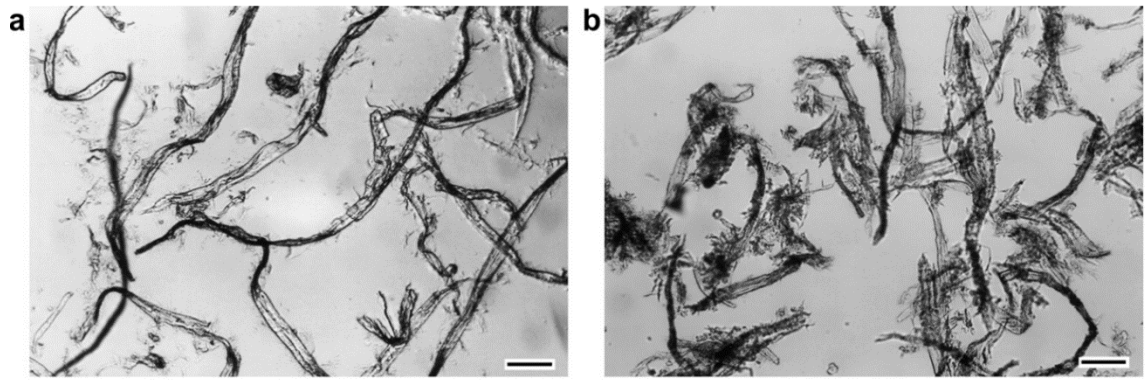

Figure 1-4. Suspensions de fibres ayant subi une opération de raffinage (pâte chimique de résineux) : (a) sans et (b) avec traitement enzymatique. La barre d'échelle correspond à 100 µm. Figure adaptée de Henriksson et *coll.*[22].

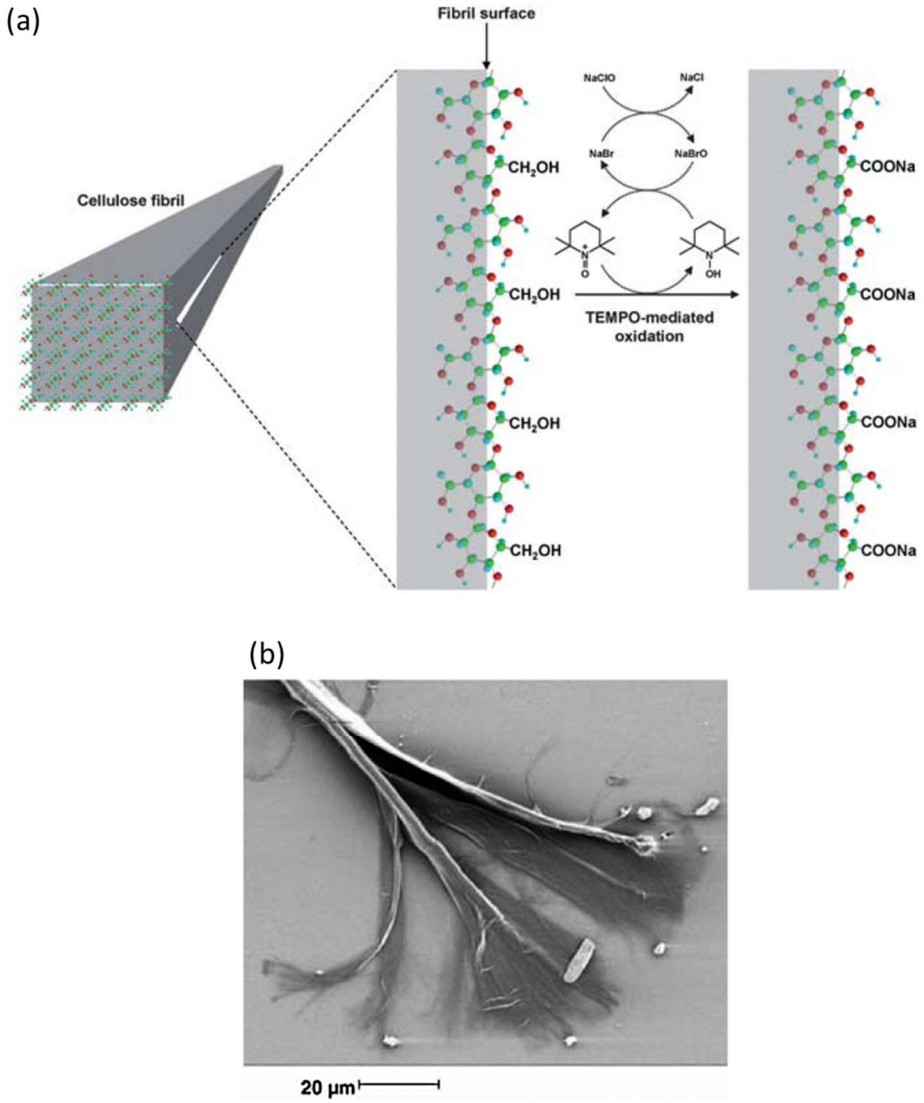

Figure 1-5. (a) Schéma de l'oxydation des hydroxyles primaires (-OH) de la surface de la NFC native en groupements carboxylates (-COO^-) par le système d'oxydation TEMPO/NaBr/NaClO[25]. (b) Micrographie MEB montrant la désintégration d'une fibre de cellulose en microfibrilles de cellulose sous l'action du prétraitement TEMPO. Figure adaptée de Moon *et coll.*[28].

- **Extraction des NCC**

Les NCC sont extraits des fibres de cellulose par hydrolyse acide contrôlée (acide sulfurique ou chlorhydrique) et traitement mécanique[4,28,29]. L'hydrolyse acide vise à dégrader les régions amorphes localisées en périphérie et au sein des macrofibrilles de cellulose (Fig. 1-1.d) en laissant les segments microcristallins intacts[4]. Les nanocristaux de cellulose (NCC) sont alors généralement libérés des segments microcristallins (en suspension) après traitement mécanique aux ultrasons[4]. Les NCC ainsi obtenus (Fig. 1-7.c) correspondent alors à des portions cristallines des mèches de fibrilles de cellulose (Fig. 1-1.e) et peuvent être vus comme une sous-entité des NFC.

1.1.2.2.3 Extraction de biopolymères

Tous les constituants présents dans la paroi des fibres végétales comme la cellulose (contour bleu de la Fig. 1-1.f), les hémicelluloses, la lignine, les pectines ainsi que les « extractibles » de natures diverses (tanins, terpènes, acides gras, antioxydants, résines) peuvent être extraits de manière sélective par des traitements principalement chimiques issus de l'industrie papetière et textile[1,7,13]. À partir des liqueurs issues des cuissons chimiques kraft et bisulfites (partie 1.1.2.2.1), il est par exemple possible d'obtenir des polymères dérivés de lignine et d'hémicelluloses. Par ailleurs, les fibres végétales qui sont délignifiées peuvent servir de pâte à dissoudre (Fig. 1-6) dans des procédés viscose ou lyocell destinés à la production de cellulose « régénérée » (également appelée cellulose II) et de dérivés de cellulose (esters et éthers de cellulose)[30,31,32]. En effet, plusieurs réactifs, parmi lesquels le N-methylmorpholine N-oxide (NMMO), la soude et les liquides ioniques ont la propriété de faire gonfler les fibres et de dissocier les chaînes de cellulose constituant les fibrilles élémentaires[33] (Fig. 1-6).

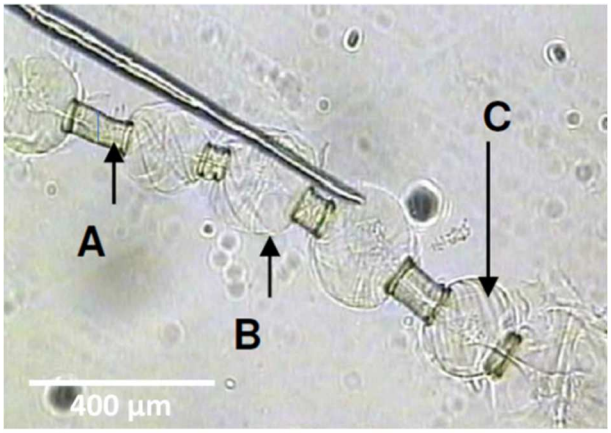

Figure 1-6. Micrographie optique d'une fibre de bois partiellement solubilisée dans un mélange de N-methylmorpholine N-oxide (NMMO) (80% en masse) et d'eau (20% en masse). Le symbole A indique une portion de fibre n'ayant pas ou peu gonflée, le symbole B une portion où la fibre a subi un gonflement important (ballon) et le symbole C une zone solubilisée à l'intérieur d'un ballon[33].

Notons qu'il est aussi possible de dépolymériser par hydrolyse acide ou enzymatique poussée, les chaînes de cellulose ou d'hémicelluloses obtenues après la dissolution des fibres. Le glucose

obtenu (monomère de base des chaînes de cellulose et d'hémicelluloses) peut être alors utilisé pour faire de l'éthanol, de l'éthylène et du polyéthylène (PE)[34].

Les fibres végétales constituent donc une matière première abondante pour la production de biopolymères thermoplastiques (cellulose régénérée, PE, PLA) mais également pour des résines thermodurcissables (résines époxydes issues de dérivées résiniques et terpéniques).

1.1.2.3 Morphologie et propriétés mécaniques

1.1.2.3.1 Propriétés microstructurales

Les caractéristiques géométriques typiques de quelques fibres naturelles ainsi que celles usuellement observées pour les NFC et NCC sont présentées dans le Tableau 1-1. Du fait de leurs dimensions nanométriques, les NCC et NFC se caractérisent généralement en utilisant des techniques microscopiques avancées telles que[4,12] :

- la microscopie électronique en transmission (MET) ;
- la microscopie électronique à balayage à émission de champ (MEB-FEG) ;
- la microscopie à force atomique (AFM).

Il est néanmoins important de noter que ces observations microscopiques sont généralement effectuées sur des suspensions préalablement diluées (concentration en masse comprise entre 0.001 *et* 0.0001% en masse) et ensuite séchées. Quelques études plus récentes ont également essayé de caractériser la microstructure des NFC en suspension dans l'eau en utilisant des techniques de diffusion des rayons X aux petits angles (SAXS)[35,36]. Cependant, la forte tortuosité des nanofibres et le caractère polydispersé des suspensions de NFC rendent l'analyse difficilement exploitable[35,36,12]. En effet, les auteurs n'ont pu estimer qu'un diamètre moyen de NFC, d'un de grandeur proche de celui déterminé par MET ou AFM.

Les micrographies MET de la Fig. 1-7.a,c montrent qu'il est plus difficile de déterminer précisément la longueur des NFC (par rapport aux NCC, Fig. 1-7.c) en raison de leur élancement et de leur enchevêtrement importants et de la difficulté à suivre les nanofibres d'une de leurs extrémités à l'autre. De manière générale, les caractéristiques géométriques des nanoparticules isolées dépendent fortement de l'espèce botanique et du traitement d'extraction utilisé. Par exemple, les suspensions de NFC extraites par voie TEMPO (Fig. 1-7.b) contiennent généralement des particules de taille inférieure (2 à 6 nm de diamètre) et bien plus élancées que les NFC issues du traitement enzymatique (10 à 500 nm de diamètre, Fig. 1-7.a). Il en résulte que les suspensions de NFC « TEMPO » (photographie de la Fig. 1-7.b) sont beaucoup plus transparentes et pâteuses que les suspensions enzymatiques (photographie de la Fig. 1-7.a).

Ces nanoparticules cellulosiques présentent des élancements $r = l/d$ importants (d et l étant respectivement le diamètre et la longueur du renfort fibreux considéré), en particulier les NFC ($100 < r < 400$). Les NFC constituent donc, au regard de leurs propriétés géométriques, des nano-renforts biosourcés intéressants pour des applications composites (nano-renforts de matrices polymères et cimentaires).

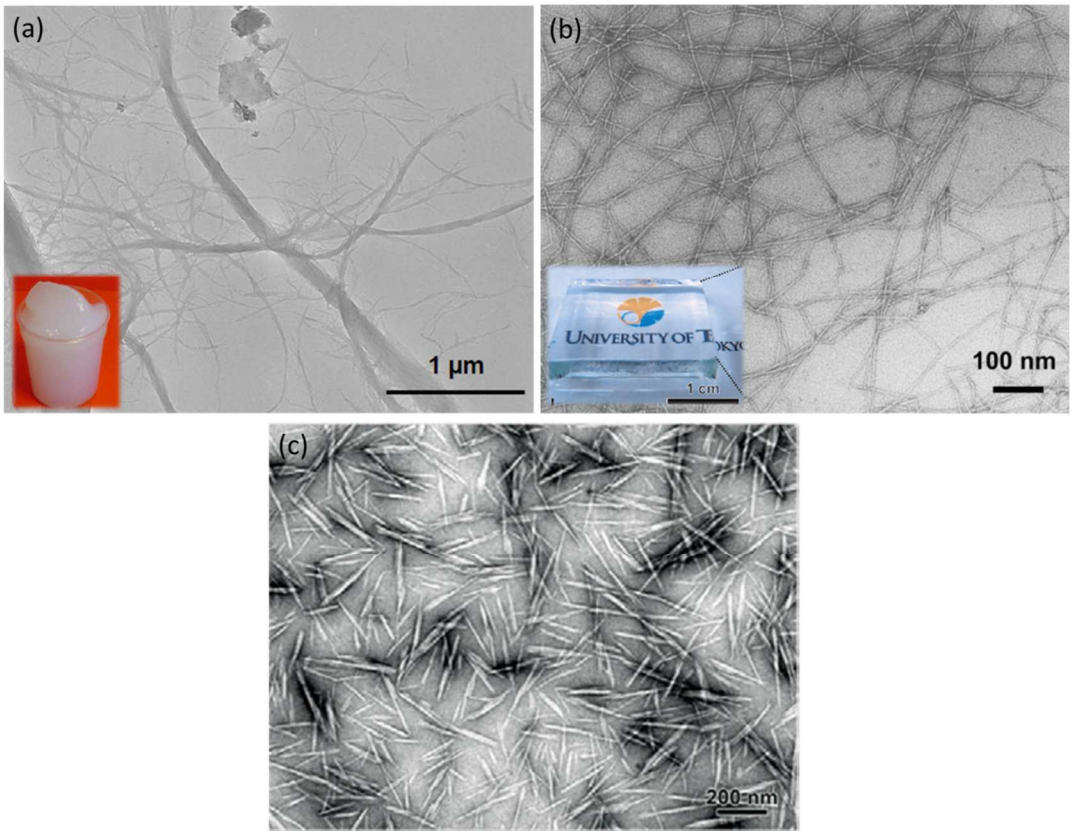

Figure 1-7. Micrographies MET d'un film de NFC extraites à partir de fibres de bois en utilisant (a) un prétraitement enzymatique[37] et (b) un prétraitement d'oxydation TEMPO[24]. Les inserts représentent des suspensions de NFC (a) enzymatique (2% en masse) et (b) TEMPO (0.8% en masse)[38]. (c) Micrographie MET d'un film de NCC obtenu à partir de fibres de ramie[39].

1.1.2.3.2 Propriétés mécaniques

Les caractéristiques mécaniques de quelques fibres naturelles et de leurs constituants aux différentes échelles sont présentées dans les diagrammes d'Ashby[6] de la Figure 1-8 ainsi que dans le Tableau 1-1. Ces figures mettent en évidence plusieurs points importants qu'il convient mettre en avant.

- Les propriétés mécaniques des fibres végétales sont assez dispersées (Tableau 1-1). Cette dispersion des propriétés est inhérente aux matériaux issus du vivant. Les propriétés mécaniques des fibres peuvent varier d'une plante à une autre en fonction des conditions de croissance, de leur maturité mais également au sein d'une même plante (en fonction de la zone de prélèvement). En effet, les fibres issues de l'écorce et de la périphérie de la tige possèdent généralement de meilleures propriétés mécaniques. En outre, les fibres végétales présentent des défauts transversaux (coudes) apparaissant au cours de leur croissance ou lors de leur extraction. À cela vient s'ajouter une dispersion induite par l'essai mécanique qui peut être hétérogène (glissement, déploiement, vrillage de la fibre parfois imprécise), associé à un dépouillement et à une analyse complexe (méthode de détermination de la section utile des fibres). Notons également que beaucoup d'essais de la littérature ont été réalisés sur des faisceaux, c'est-à-dire

sur des assemblages de fibres unitaires liées les unes aux autres par un ciment ligneux ou pectique[9]. Les fibres végétales constituent néanmoins des renforts de matrices polymères (ou cimentaires) intéressants, et une alternative aux fibres de verre, notamment en raison de leurs bonnes propriétés spécifiques (Tableau 1-1).

- Caractériser expérimentalement les propriétés mécaniques des NFC et NCC reste encore difficile à réaliser et constitue encore le sujet de plusieurs travaux de recherche[40,41,42,43]. Néanmoins, quelques études théoriques[44,45] et expérimentales[41,43] ont essayé d'évaluer les propriétés mécaniques intrinsèques des NFC et NCC. Les valeurs rapportées pour le module longitudinal E sont comprises entre 50 et 120 GPa pour les NFC et entre 120 et 140 GPa pour les NCC. À titre illustratif, en gardant à l'esprit que la masse volumique ρ de la cellulose est de l'ordre de 1.5 g cm^{-3}, cela revient à dire que les NFC et NCC ont un module spécifique $E^* = E/\rho \approx 50 - 90$ J g^{-1} largement supérieur à celui de l'acier ($E^* \approx 25$ J g^{-1}) ou du verre ($E^* \approx 27$ J g^{-1}) et similaire à celui du kevlar[4]. Ces particules constituent donc au regard de leur propriétés mécaniques intrinsèques des nano-renforts biosourcés intéressants pour des applications composites.

- Il est intéressant de noter que les constituants biochimiques des fibres végétales comme les hémicelluloses et la lignine présentent des caractéristiques mécaniques proches de celles obtenues pour certaines matrices thermoplastiques et thermodurcissables pétrosourcées (Fig. 1-8). Ces biopolymères « natifs » peuvent ainsi être utilisés comme matrices de matériaux composites pour peu que leur structure chimique ne soit pas trop altérée lors du processus d'extraction[6].

Tableau 1-1 Propriétés morphologiques et mécaniques en traction de quelques fibres végétales, des NFC et NCC et comparaison avec les fibres de Verre E et de Carbone HR[4,6,46,9].

	Densité	**Longueur**	**Diamètre**	**Module d'élasticité**	**Contrainte maximale**	**Allongement à rupture**
	ρ kg m^{-3}	l	d	E GPa	σ_r MPa	A_r %
Bois de résineux	1.2	1 à 3 mm	30 à 40 µm	3 à 15	50 à 1000	2 à 5
Bois de feuillus	1.2	0.6 à 1 mm	15 à 25 µm	5 à 15	50 à 1000	2 à 5
Lin	1.4	4 à 80 mm	5 à 40 µm	10 à 90	600 à 2000	1 à 3
Chanvre	1.4	5 à 70 mm	10 à 50 µm	10 à 90	100 à 2000	1 à 3
Coton	1.4	10 à 40 mm	10 à 60 µm	5 à 15	200 à 600	7 à 8
NFC Enz.	1.5	1 à 10 µm	10 à 500 nm	50 à 120	--	--
NFC TEMPO	1.5	0.8 à 2 µm	3 à 5 nm	50 à 120	--	--
NCC	1.5	100 à 300 nm	10 à 30 nm	100 à 140	--	--
Verre E	2.6	--	--	75	3400	4 à 5
Carbone HR	1.9	--	--	500	2300	0.5

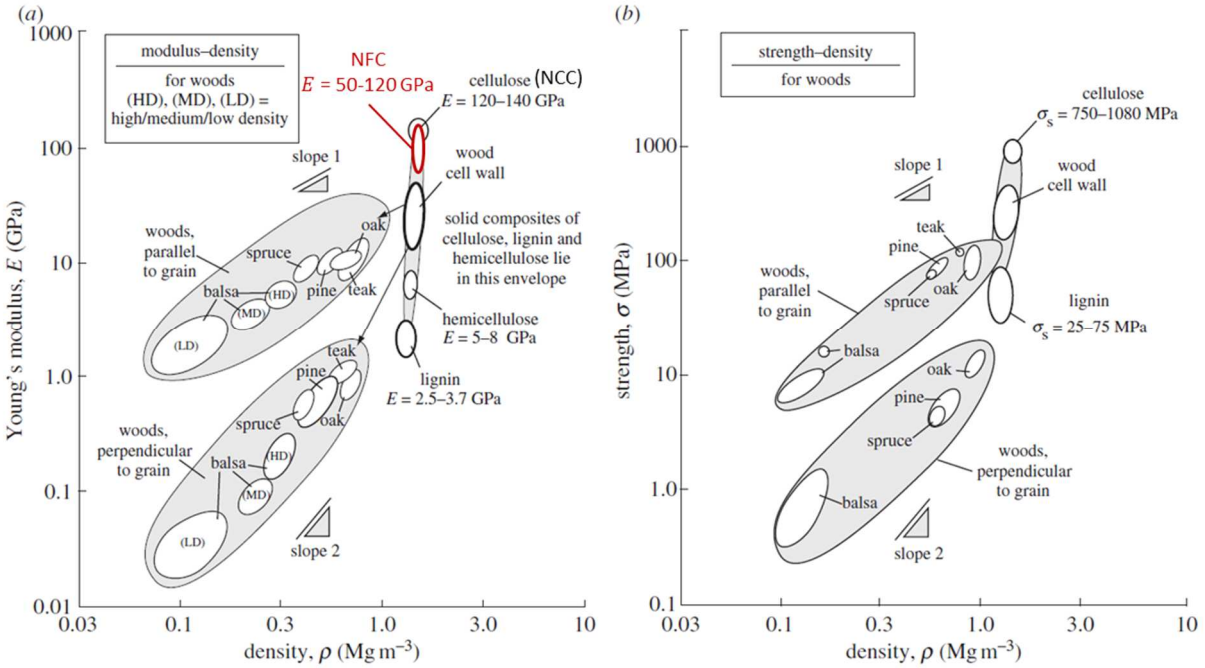

Figure 1-8. (a) Module d'élasticité E et (b) contrainte à la rupture σ en fonction de la masse volumique ρ pour le bois et ses constituants. Figure adaptée de Gibson[6].

1.1.2.4 Quelques exemples de matériaux issus des fibres végétales et de leurs constituants

Matériaux à base de fibres végétales

Les fibres végétales, principalement extraites du bois, sont utilisées dans l'industrie papetière pour former des papiers (Fig. 1-9.a) et cartons aux propriétés physiques (mécaniques, optiques, barrières, etc.) variées[47]. À titre d'exemple, l'industrie papetière produit et utilise environ 300 millions de tonnes par an de fibres blanchies. Par ailleurs, les fibres végétales peuvent être utilisées dans l'industrie des matériaux composites comme renforts de matrices polymères ou cimentaires (Fig. 1-9.b)[46,3,5,48]. De nombreuses pièces notamment automobiles telles que les garnitures intérieures de portières, les dossiers de sièges ou les habillages de coffre sont aujourd'hui renforcées par des fibres végétales (principalement issues de plantes annuelles)[46,3,5,48].

Matériaux à base de NFC et NCC

Les NCC et NFC sont des nanoparticules biosourcées abondantes et intéressantes pour de nombreuses applications[4,28,16,15]. Elles peuvent en effet être utilisées sous forme de gels dans des cosmétiques[38,26], comme agent épaississant dans les sauces de couchage pour l'industrie papetière[16], mais également ajoutées à des matrices polymères comme nano-renforts dans des nanocomposites[4,15]. À l'état sec, les NFC et NCC peuvent également être utilisées pour produire de « nouveaux » matériaux cellulosiques de densité variable ($1\ \text{kg m}^{-3} \leq \rho \leq 100\ \text{kg m}^{-3}$) tels que des films[49,50] (Fig. 1-9.c), des membranes et des mousses ou aérogels[41,51] (ces termes seront précisés dans la partie 1.4, Fig. 1-9.d).

Matériaux à base de biopolymères

La cellulose et ses dérivés (esters et éthers de cellulose) sont largement utilisés pour élaborer des matériaux aux propriétés physiques variées. On peut citer par exemple les fibres de viscose et lyocell pour le textile, les films de « cellophane » pour l'emballage et les plastiques en acétate de cellulose (lunettes de protection, Lego, filtres de cigarette, etc.)[7,13].
En outre, même si les applications industrielles sont encore peu développées, il est important de noter que de nombreuses résines thermoplastiques et thermodurcissables utilisées usuellement dans le domaine des composites (résines époxy, polyester, polyamide, polyuréthane) peuvent être partiellement ou totalement synthétisées à partir de monomères ou d'oligomères issus de la biomasse[1]. Nous avons indiquépar exemple qu'il était possible de synthétiser du polyéthylène (PE) à partir de glucose de cellulose ou d'hémicellulose, des polyamides et des polyesters à partir des acides gras insaturés présents dans les végétaux.
Par ailleurs, des travaux récents[52,53] ont montré que de nouveaux matériaux biosourcés aux propriétés physiques remarquables pouvaient être préparés en utilisant directement les biopolymères présents dans les fibres cellulosiques. À titre illustratif, la Figure 1-9.e montre une mousse super-isolante préparée simplement en utilisant la cellulose II extraite des fibres par dissolution (Fig. 1-6).

Il y a actuellement une quantité considérable de travaux sur ces matériaux[4,3,47], dont les applications sont très prometteuses. Dans la suite de ce chapitre, nous nous sommes concentrés sur quelques matériaux biosourcés émergents et prometteurs: les biocomposites (partie 1.2), les nanocomposites à renfort cellulosique (partie 1.3), et les matériaux poreux biosourcés (partie 1.4).

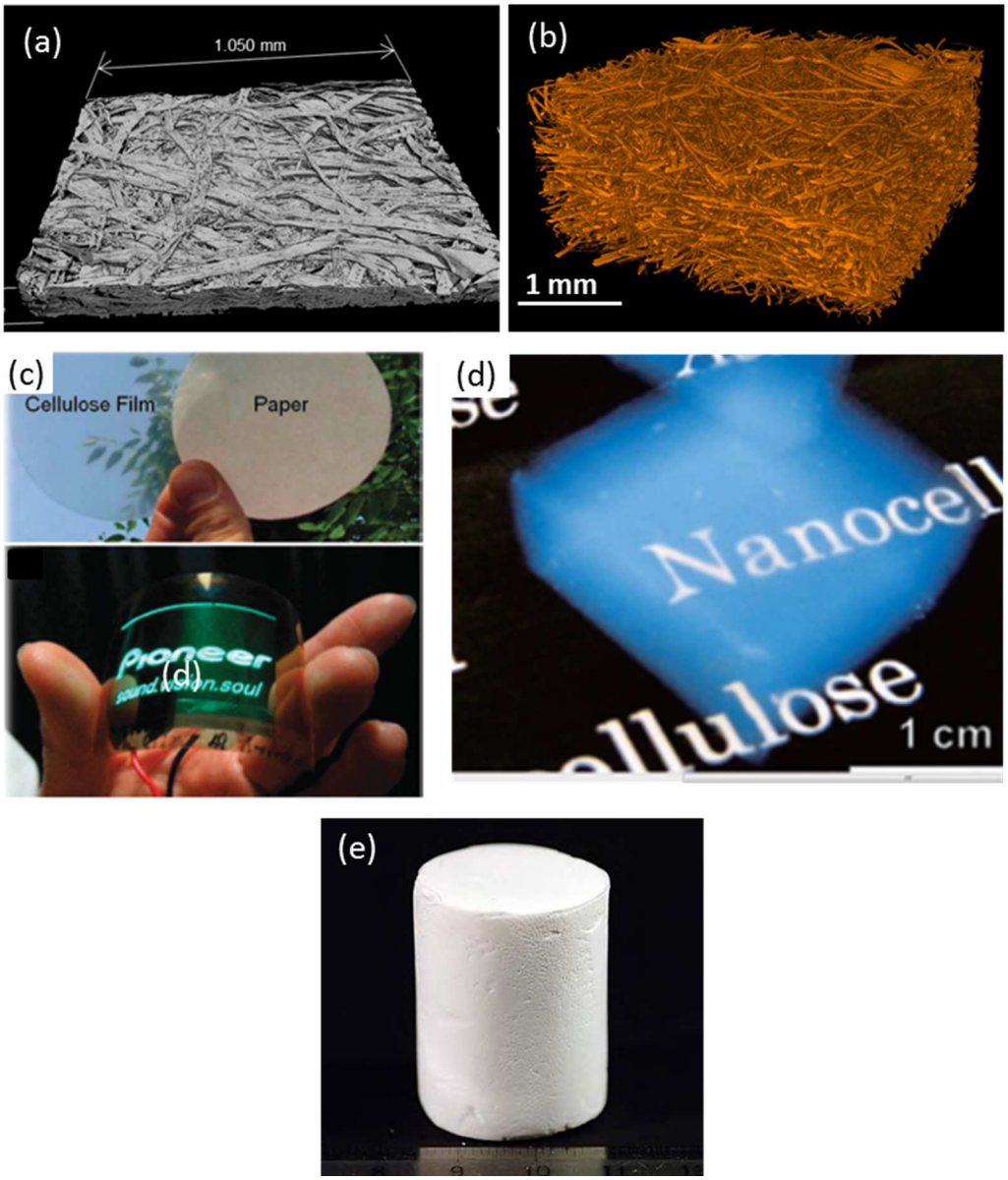

Figure 1-9. (a) Image 3D d'un papier obtenue par microtomographie à rayons X (taille de voxel : 0.7^3 µm^3)[54]. (b) Image 3D d'un mat de fibres de lin utilisé comme renfort de matériaux biocomposites obtenue par microtomographie à rayons X (taille de voxel : 2^3 µm^3). (c) Photographie d'un film transparent de NFC utilisé comme support pour l'électronique imprimé[28]. (d) Photographie d'un aérogel[55] de NFC de masse volumique $\rho = 10$ kg m^{-3}. (e) Photographie d'une mousse élaborée à partir de cellulose dissoute et régénérée[52,53].

1.2 Matériaux composites biosourcés

1.2.1 Introduction

Les matériaux composites sont des matériaux multiphasiques le plus souvent constitués de deux phases, « une matrice » et un « renfort ». En général, les principales fonctions de la matrice polymérique sont d'assurer le transfert de charges mécaniques entre les fibres et d'augmenter la ténacité du matériau, de maintenir l'orientation et la mise en forme des fibres et de protéger les fibres de l'environnement extérieur. Le renfort est l'armature assurant l'essentiel des propriétés mécaniques du composite. On parle de composites biosourcés ou de biocomposites lorsqu'au moins une des deux phases, la matrice ou le renfort, est issue de ressources renouvelables (biosourcées).

L'objectif de ce chapitre est de faire une brève présentation de ces nouveaux matériaux, des procédés de mise en forme associés ainsi que de leurs propriétés finales. La partie 1.2.2 présente les principaux constituants utilisés pour former ces matériaux. Nous nous focaliserons dans cette étude au cas des biocomposites à matrices polymères et à renforts fibreux. Nous décrions ensuite succinctement les procédés de mise en forme (partie 1.2.3). Enfin, les propriétés mécaniques de ces matériaux sont présentées et comparées à celles obtenues dans le cas de composites traditionnels (composites à fibres de verre) (partie 1.2.4). L'ensemble des données présentées dans ce chapitre reste très général. Le lecteur pourra se reporter à plusieurs ouvrages[56-59] pour des approfondissements.

1.2.2 Les biocomposites à renforts fibreux

1.2.2.1 Les matrices biosourcées ou biopolymères

Les biopolymères sont des polymères issus exclusivement d'organismes vivants ou de polymères synthétisés à partir de ressources renouvelables[1]. Cette famille de matériaux est généralement classée en quatre grandes sous-catégories[5,3,46,60]:

- **Les polysaccharides**. Ces polymères sont synthétisés par des organismes vivants et entrent notamment dans la composition de la plupart des cellules microbiennes, animales et végétales. Parmi les plus connus, on peut citer la cellulose, l'amidon, la chitine, le chitosan ;
- **Les polyesters synthétisés par des bactéries**. Parmi les plus étudiés, on peut citer les polyhydroxyalcanoates (PHA);
- **Les protéines ou polypeptides**. Ces polymères sont les constituants de la matière vivante animale (muscle, peau, cheveux, etc.) ;
- **Les polynucléotides** (ADN et ARN).

La Figure 1-10 donne un aperçu de l'ensemble des polymères partiellement ou totalement biosourcés. Les « nouveaux » biopolymères les plus utilisés comme matrice de matériaux composites semi-structurels sont l'acide polylactide (PLA) issu d'un processus de fermentation du glucose, les PHA, et les dérivées cellulosiques tels que les esters de cellulose (acétate de cellulose) présentés dans la partie 1.1.2.2.3[60]. Les matrices biosourcées sont néanmoins encore très peu utilisées dans des applications industrielles, principalement en raison de leur coût (2 à 10 fois plus important que celui des matrices pétrosourcées)[3], de leurs moins bonnes caractéristiques mécaniques et de leur faible stabilité thermique. De plus, certaines de ces matrices comme le PLA, les PHA et les polymères issus de cellulose présentent, en raison de leur structure chimique riche en oxygène, une sensibilité à l'humidité qui peut considérablement compliquer leur mise en forme (problème de dégazage) et décroître les propriétés en service des composites[3].

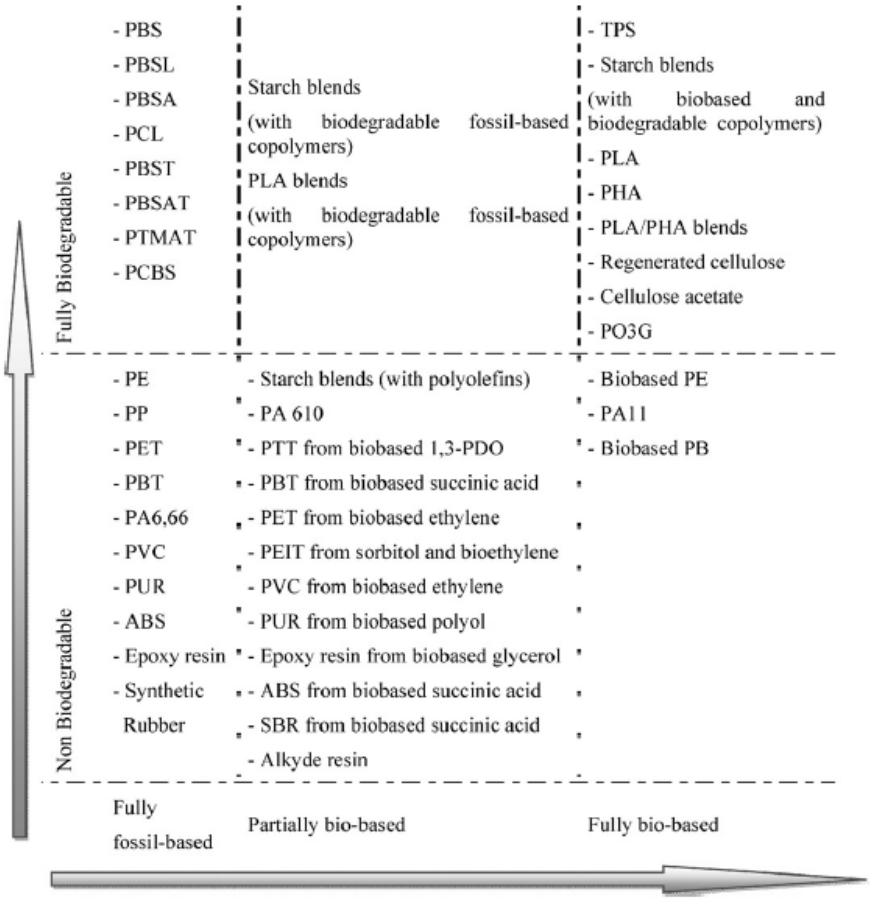

Figure 1-10. Exemples de polymères partiellement ou totalement biosourcés[48]. Le terme « Fully Biodegradable » doit être considéré avec prudence. Le PLA, par exemple, ne satisfait pas tous les critères du test de biodégradabilité (norme EN 13432), il est plutôt considéré comme biocompostable[60].

1.2.2.1 Les renforts biosourcés

Les renforts biosourcés utilisés dans les matériaux composites sont aujourd'hui principalement issus de fibres libériennes extraites des tiges des plantes annuelles. On peut citer par exemple les fibres de lin, de chanvre, d'ortie et de ramie. Ce choix est justifié par le fait que les fibres

libériennes présentent généralement des propriétés bien supérieures à celles des fibres extraites des feuilles, des graines ou même du bois (Tableau 1-1).

En général, les fibres employées dans les matériaux composites sont prélevées directement dans la chaîne de transformation de l'industrie textile[9]. Elles sont alors utilisées soit en vrac, c'est-à-dire sous forme de fibres ou faisceaux de fibres courtes de longueur calibrée (Fig.1-11.a), soit sous forme de nappes (mats hydroliés ou non, unidirectionnels, tissus, Fig.1-11.b). Les fils servant à former les tissus sont filés c'est-à-dire constitués d'un assemblage de mèches de fibres solidarisées par torsion et étirés (Fig. 1-11.a). Le caractère « discontinu » des renforts fibreux biosourcés constitue un inconvénient certain par rapport aux renforts synthétiques qui sont formés de fils continus[61]. Il est également important de signaler que les renforts biosourcés possèdent généralement une teneur en eau d'environ 5 à 10% en masse en raison du caractère hydrophile des fibres végétales (présence de groupements hydroxyles).

Figure 1-11. Quelques exemples de renforts biosourcés principalement constitués de fibres de lin. Photographies 11a extraites de www.eco-technilin.com.

1.2.3 Mise en forme

1.2.3.1 Procédés d'élaboration

En général, les procédés de fabrication et de mise en forme des matériaux composites biosourcés sont analogues à ceux utilisés pour les matériaux composites traditionnels. Ces procédés d'élaboration répondent à des besoins spécifiques tels que la forme de la pièce à produire, la taille de la série ou encore les propriétés finales. Ils peuvent être classés en différentes familles[59,57,61,62]:

- les procédés dédiés soit aux fibres courtes (où les cadences de production peuvent être élevées), soit aux fibres longues ;
- les procédés par imprégnation directe (voie humide) ou les procédés par imprégnation amont (voie sèche) ;
- les procédés de fabrication en continu ou discontinus et les procédés dédiés aux fabrications unitaires.

Ces procédés conduisent à des pièces composites présentant des performances mécaniques variées et fabriquées à différentes cadences de production (Fig. 1-12). Trois opérations indispensables, dont l'ordre chronologique dépend du procédé de mise en forme, sont généralement réalisées[63,64] :

- l'imprégnation du renfort fibreux par le polymère (forte concentration de fibres) ou la dilution des renforts dans la matrice (faible concentration de fibres) ;
- la mise en forme à la géométrie de la pièce ;
- la réticulation ou le durcissement pour les matrices thermodurcissables, la solidification par refroidissement pour les matrices thermoplastiques.

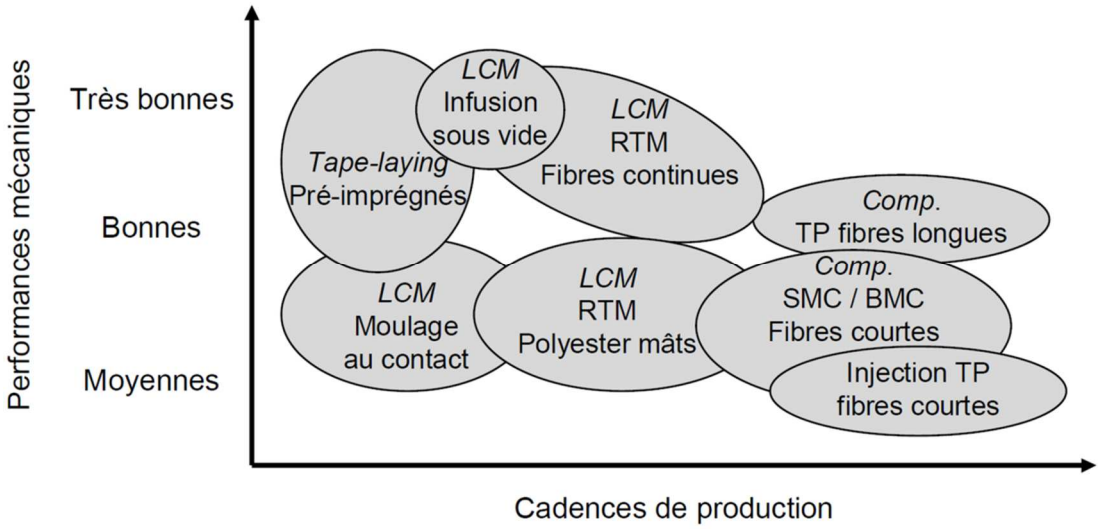

Figure 1-12. Performances mécaniques en fonction des cadences de production de quelques grands procédés de mise en forme. Les abréviations LCM désigne la famille des procédés « Liquid Composite Molding », RTM désigne les procédés de moulage par injection de résine « Resin Transfert Moulding », Comp. SMC/BMC les procédés de compression des « Sheet Molding Compounds » et « Bulk Moulding Compounds ». Reproduit d'après Harper[64].

La Figure 1-13 montre quelques exemples de réalisations de pièces composites à renforts fibreux naturels actuellement utilisées dans l'industrie automobile.

Figure 1-13. Panneau intérieur de portière de voiture et dossier de siège. Photographies extraites de www.jeccomposites.com.

1.2.3.2 Quelques problématiques de mise en forme

Même si les procédés de fabrication sont analogues à ceux utilisés pour les composites traditionnels, la mise en forme des biocomposites requiert souvent d'adapter les procédures et les conditions opératoires employées pour les composites traditionnels. L'utilisation de renforts ou de matrices biosourcés nécessite de prendre en compte la teneur en eau des matériaux (5 à 10% en masse) afin d'éviter l'apparition de défauts liés à un dégazage, la stabilité thermique limitée des fibres végétales (température de dégradation T_d autour de $180-200$°C), la géométrie complexe (corps creux) et le caractère anisotrope du comportement des fibres induit par leur nanostructure. De même, les propriétés physico-chimiques des fibres végétales (caractère hydrophile) rendent souvent l'imprégnation complexe et difficile à réaliser[46,61,62].

Notons néanmoins que plusieurs défauts et problématiques rencontrées lors de la mise en forme des composites surviennent aussi durant la fabrication des biocomposites. On peut citer par exemple :

- **Les déformations hétérogènes du renfort fibreux** (Fig. 1-14.a). Lors de la mise en forme de pièces composites à géométries complexes, des phénomènes de plissement, localisation et même de désenchevêtrement du renfort fibreux sont parfois observés (cas de réseaux fibreux très concentrés). Ces défauts sont souvent dus aux grandes déformations du renfort qu'il est nécessaires d'atteindre pour épouser les formes des pièces à fabriquer[65,66].

- **Les phénomènes de redistribution en taux et orientation de fibres** (Fig. 1-14.b. Lors de la mise en forme de pièces composites, des phénomènes de redistribution en taux et orientation de fibres peuvent se produire (cas de renforts fibreux discontinus). Le phénomène de redistribution en taux de fibres se traduit par des hétérogénéi-

tés dans la répartition spatiale des fibres (flocs, amas de fibres) tandis que le phénomène de redistribution en orientation des fibres se traduit par des directions privilégiées dans lesquelles les fibres s'orientent préférentiellement au cours de leur mise en forme[58,67]. Ces phénomènes dépendent des paramètres de mise en forme et conduisent nécessairement à des pièces composites aux propriétés physiques et mécaniques hétérogènes et anisotropes. Ce point sera tout particulièrement étudié dans ce mémoire par une étude approfondie de la rhéologie des suspensions de NFC (Chapitre 2 et 3).

- **Les phénomènes de séparation fibres-matrice** (Fig. 1-15). Pour obtenir une pièce composite aux propriétés optimisées, les fibres et le polymère doivent s'écouler de concert pour remplir l'empreinte du moule de manière homogène. Des phénomènes de séparation peuvent se produire si les paramètres du procédé (vitesse de fermeture et température du moule) ne sont pas adéquats. Ces phénomènes ne sont hélas pas encore totalement compris et restent difficiles à maîtriser en raison du très fort contraste des propriétés entre les fibres et la matrice qui possède souvent une rhéologie non-newtonienne[68]. Ainsi, certaines conditions de mise en forme aboutissent parfois à des écoulements totalement biphasiques comme cela est illustré sur la Figure 1-15.

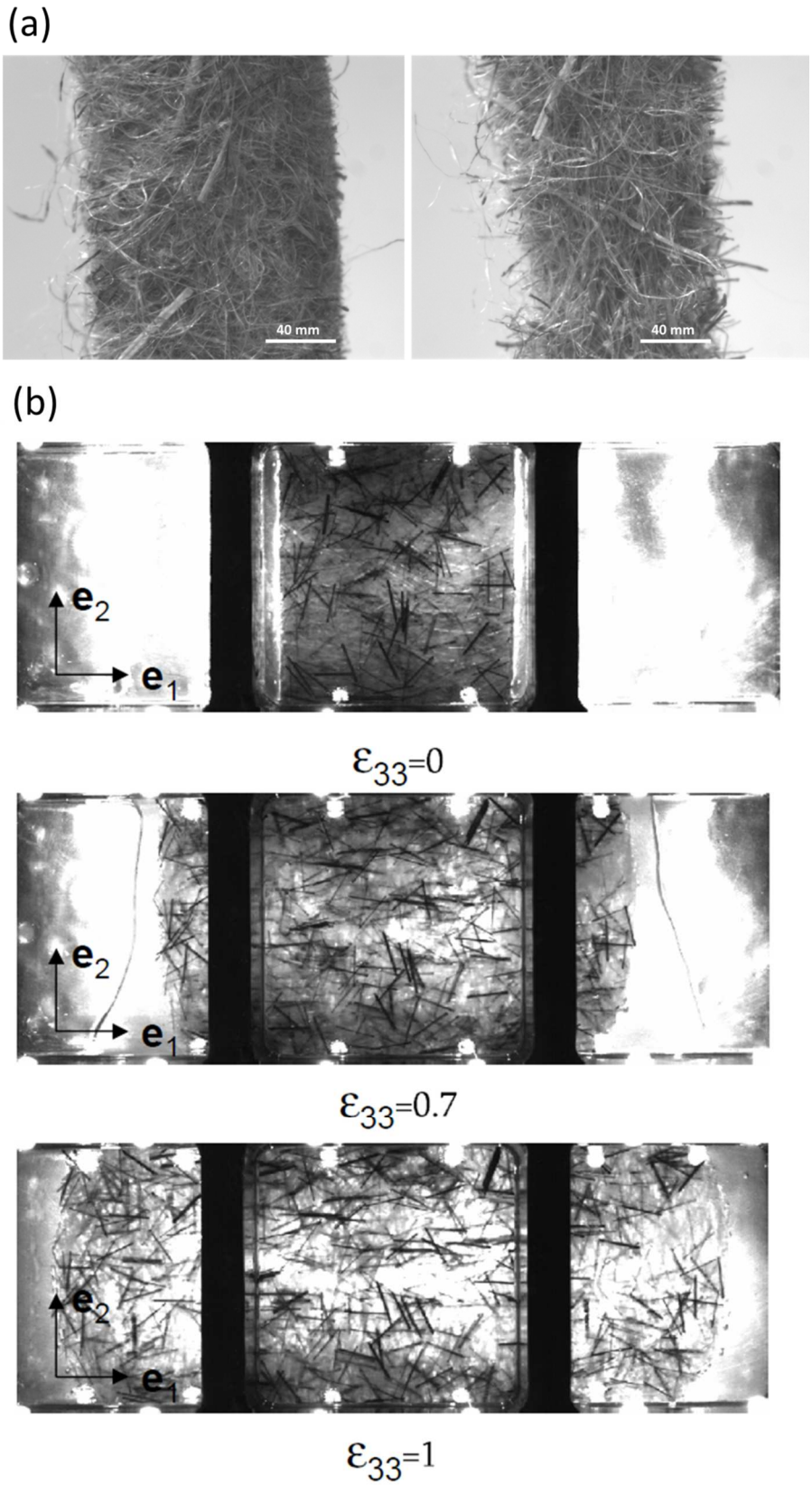

Figure 1-14. (a) Photographies de la surface d'un mat de fibres de lin sec montrant l'évolution de l'orientation des fibres lors d'un essai de traction simple et la localisation de la déformation dans le renfort. (b) Photographies de la surface d'un composite (mèches de fibres de verre imprégnées par une matrice de paraffine) montrant l'évolution de l'orientation des mèches de fibres dans le sens de l'écoulement lors d'un essai de compression en déformation plane[67].

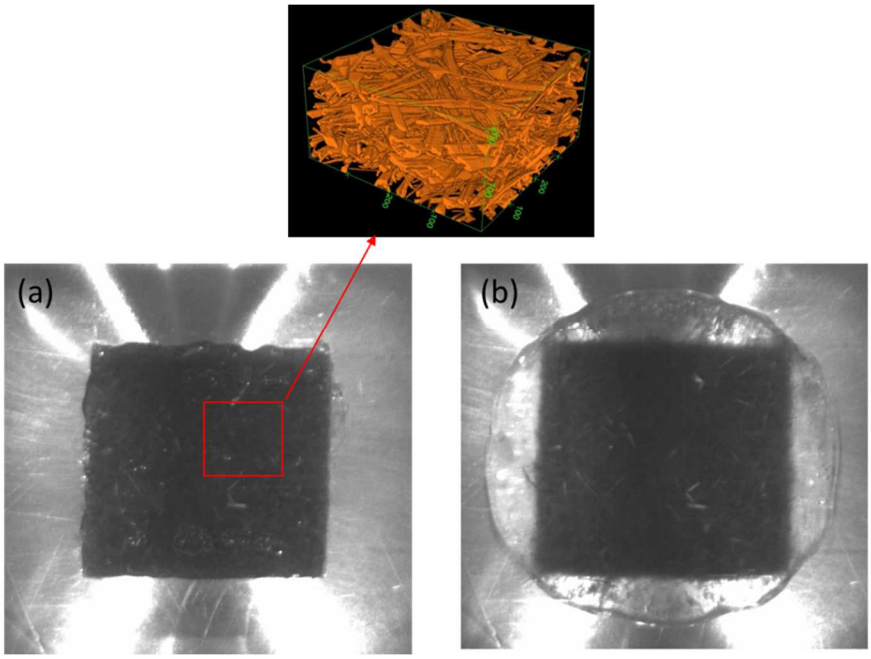

Figure 1-15. Photographies de la surface d'un composite à renfort naturel (mat de lin pré-imprégné par une matrice de paraffine) avant (a) et après (b) compression entre deux plateaux parallèles[69]. Consolidation du renfort fibreux et ségrégation de la matrice.

1.2.3.3 Propriétés microstructurales

La microstructure des matériaux composites est souvent caractérisée par microscopie électronique à balayage (MEB) sur des échantillons préalablement fracturés. Une description plus fine et en 3 dimensions peut aussi être obtenue en utilisant la microtomographie à rayons X. L'analyse de ces images permet généralement d'obtenir des informations sur la disposition et l'orientation du renfort fibreux, la nature des interactions entre fibres ainsi que sur la présence de porosité[70,71,68]. La Fig. 1-16 montre un exemple de rendu d'un volume 3D d'un composite à renfort fibreux biosourcé obtenu par microtomographie à rayons X.

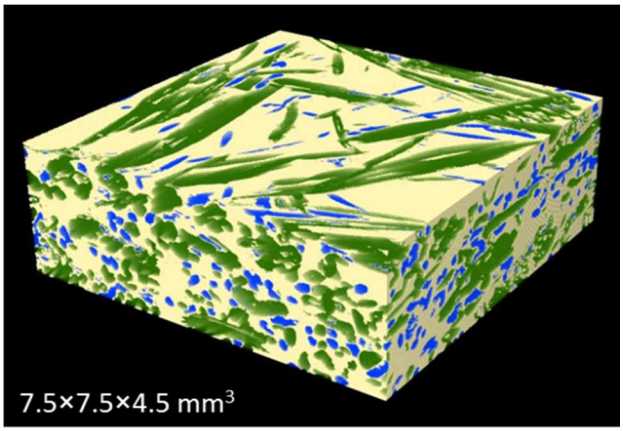

Figure 1-16. Image 3D d'un composite renforcé avec un mélange de fibres de lin et de polypropylène obtenue par microtomographie à rayons X[72]. En vert les fibres de lin, en bleu les fibres de polypropylène et en jaune la matrice de polyester.

1.2.4 Propriétés mécaniques

1.2.4.1 Comparaison avec les composites à fibres de verre

À fraction volumique et à géométrie de renfort équivalentes, les composites à renforts naturels présentent généralement des propriétés mécaniques élastiques et plastiques inférieures aux composites à fibres de verre (Fig. 1-17)[62,61,73]. Ceci constitue un verrou à lever qui nuit fortement au développement des biocomposites. À titre informatif, en 2010 les composites à renforts naturels représentaient en terme de tonnage, en Europe, seulement 1.9% du marché global des composites[61].
Plusieurs aspects relatifs aux renforts fibreux (variabilité des propriétés des fibres et de leur géométrie, présence de défauts, sensibilité à l'humidité), à l'interface entre fibres et matrice (mouillabilité, adhésion) et à la mise en forme (dispersion, agrégation, effondrement des fibres, ségrégation) sont susceptibles d'altérer les propriétés d'usage des biocomposites[62,61,73,46,3].

1.2.4.2 Quelques voies d'amélioration

De nombreux axes de recherche portent actuellement sur l'amélioration des propriétés en service des matériaux composites biosourcés. Plusieurs études sont notamment dédiées aux problématiques d'interface (mouillabilité, adhésion) entre les fibres végétales hydrophiles et les matrices polymères hydrophobes. Les principaux traitements développés sont :

- **Les traitements mécaniques**[61,74] qui consistent principalement en des opérations de raffinage, c'est-à-dire des opérations visant à modifier la « rugosité » de surface pour améliorer l'ancrage des fibres au sein de la matrice.

- **Les traitements chimiques**[75,60,76,77,78] qui consistent à greffer à la surface des fibres de cellulose des chaînes grasses. Les fibres de cellulose possèdent des groupements hydroxyles –(OH) susceptibles de réagir avec de multiples réactifs chimiques. Il est important de signaler que des techniques de chimie chromatogénique permettent désormais de réaliser ces modifications par diffusion sur des matériaux solides tels que des papiers ou des cartons, à des cadences industrielles[79].

- **Les traitements physiques** comme les traitements Corona ou plasma qui consistent à ioniser et à oxyder la surface des matériaux[80].

Notons par ailleurs que certains traitements chimiques de surface des fibres permettent également d'améliorer la stabilité thermique et de limiter les phénomènes d'hygroexpansion et d'hydroexpansion des fibres naturelles dans les composites[81].

Quelques études portent sur l'extraction des fibres et la mise en forme des biocomposites. Leur objectif est une meilleure compréhension des mécanismes de déformation et d'endommagement des fibres et des renforts fibreux naturels lors des différentes étapes de transformation

ainsi qu'un meilleur contrôle des microstructures formées. On peut citer par exemple les études dédiées :

- aux problématiques d'isolation et de séparation des fibres à partir de plantes annuelles (compromis entre traitements mécanique et chimique)[82-84];
- aux problématiques d'endommagement des fibres végétales dans les extrudeuses et compounders[85,86];
- aux problématiques de déformation des préformes sèches et imprégnées[65,69].

D'autres stratégies émergentes visent à renforcer les matrices polymères servant à imprégner les renforts fibreux par des nanoparticules cellulosiques telles que des nanofibrilles de cellulose (partie 2.3), de manière à apporter un effet de renfort à différentes échelles[87-89]. Ces stratégies s'inspirent notamment de travaux antérieurs réalisés sur des renforts de fibres de verre imprégnés par des matrices chargées par des nanotubes de carbone[90-92]. Si elles sont potentiellement intéressantes, leur mise en œuvre se heurte au problème difficile de l'imprégnation de la matrice chargée, vue comme une suspension (semi-)concentrée de nanofibres. La connaissance même de la rhéologie de ces suspensions est un des obstacles de ce problème, auquel nous essaierons de répondre dans les chapitres 2 et 3.

Enfin, ces stratégies se heurtent également aux problèmes (i) de caractérisation de leur structure multi-échelles, notamment au placement du nano-renfort, (ii) de l'estimation de leurs propriétés mécaniques. Les schémas multi-échelles dédiés à ce genre de matrice composite étant inopérants, nous essaierons de traiter ce problème dans le chapitre 4.

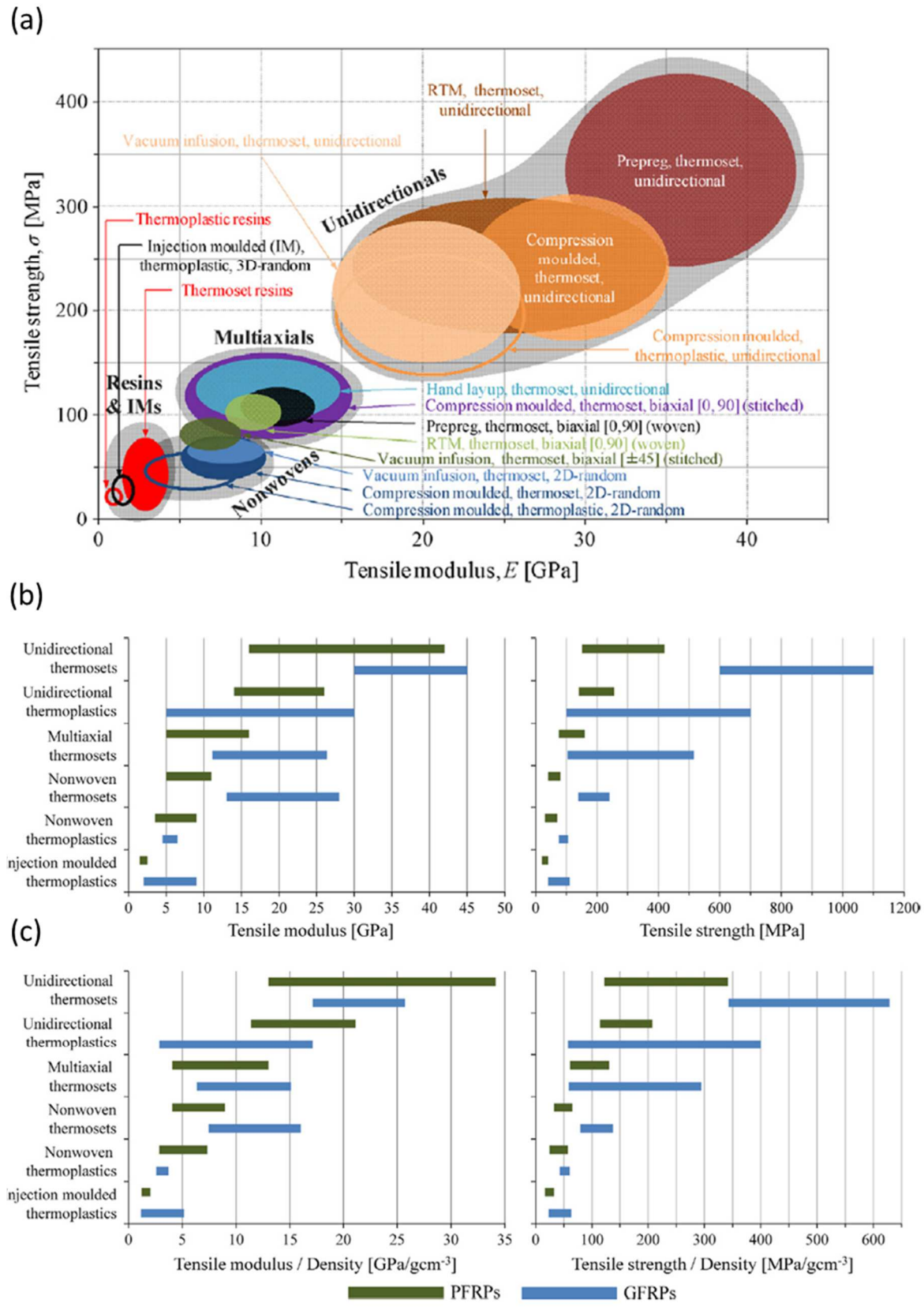

Figure 1-17. (a) Diagramme de sélection des matériaux : contrainte σ en fonction du module élastique E pour différents matériaux composites à renforts fibreux naturels. Propriétés mécaniques (E, σ) absolues (b) et spécifiques (c) pour des biocomposites (Plant Fiber Reinforced Polymer PFRP en vert) et des composites renforcés avec des fibres de verre (Glass Fiber Reinforced Polymer GFRP en vert). Figures reproduites d'après Shah[62].

1.3 Nanocomposites à renforts cellulosiques

1.3.1 Introduction

L'objectif de cette partie est de faire une brève présentation des nanocomposites à renfort cellulosique, en se focalisant plus particulièrement sur les matériaux à matrices polymères renforcées par des nanofibrilles de cellulose (NFC) qui constituent le cœur de ce travail. Ainsi, dans la partie 1.3.2, on décrit succinctement les principaux procédés d'élaboration de ces matériaux et les problématiques de mise en forme associées. On présente ensuite (partie 1.3.4) les caractéristiques mécaniques des matériaux ainsi fabriqués.

1.3.2 Mise en forme

1.3.2.1 Choix des matrices hôtes

La dispersion de ces nano-objets (en suspension dans l'eau, Fig. 1-7) dans la plupart des matrices polymères hydrophobes, constitue encore un verrou scientifique et technologique important[4,15,28]. En effet, les NFC présentent une haute surface spécifique associée à une densité importante de groupements hydroxyles et carboxylates de surface ce qui leurs confèrent une bonne affinité chimique avec l'eau (les groupements hydroxyles et carboxylates peuvent interagir avec l'eau par le biais de liaisons hydrogènes)[4]. Par conséquent, l'eau est le milieu privilégié de mise en œuvre. Ceci limite considérablement le choix de la matrice aux polymères hydrosolubles[93] (p. ex. : PEO, PVA) ou sous forme de latex[94] (p. ex. : caoutchouc naturel), c'est-à-dire sous forme de dispersion aqueuse. La dispersion des NFC en milieu non aqueux constitue encore le sujet d'une intense recherche[37,78]. Les stratégies actuellement développées visent à modifier les propriétés physico-chimiques de surface des NFC soit par l'ajout de tensioactifs[95,96], soit par greffage chimique[81] (Fig. 1-18).

1.3.2.2 Films purs de NFC ou nanopapiers

Les suspensions aqueuses de NFC (Fig. 1-7) peuvent néanmoins être utilisées pour élaborer des films de NFC purs[93,97] (aussi appelés nanopapiers, Fig. 1-9) aux propriétés mécaniques, optiques et barrières très intéressantes[98]. Lors du séchage de la suspension, les NFC se rapprochent les unes des autres sous l'action d'effets capillaires ; elles ont alors la possibilité d'interagir fortement par le biais de liaisons hydrogènes pour former un réseau d'interactions rigides[4,94,99]. Ce phénomène est similaire à celui observé lors de la formation de feuilles de papier[47].

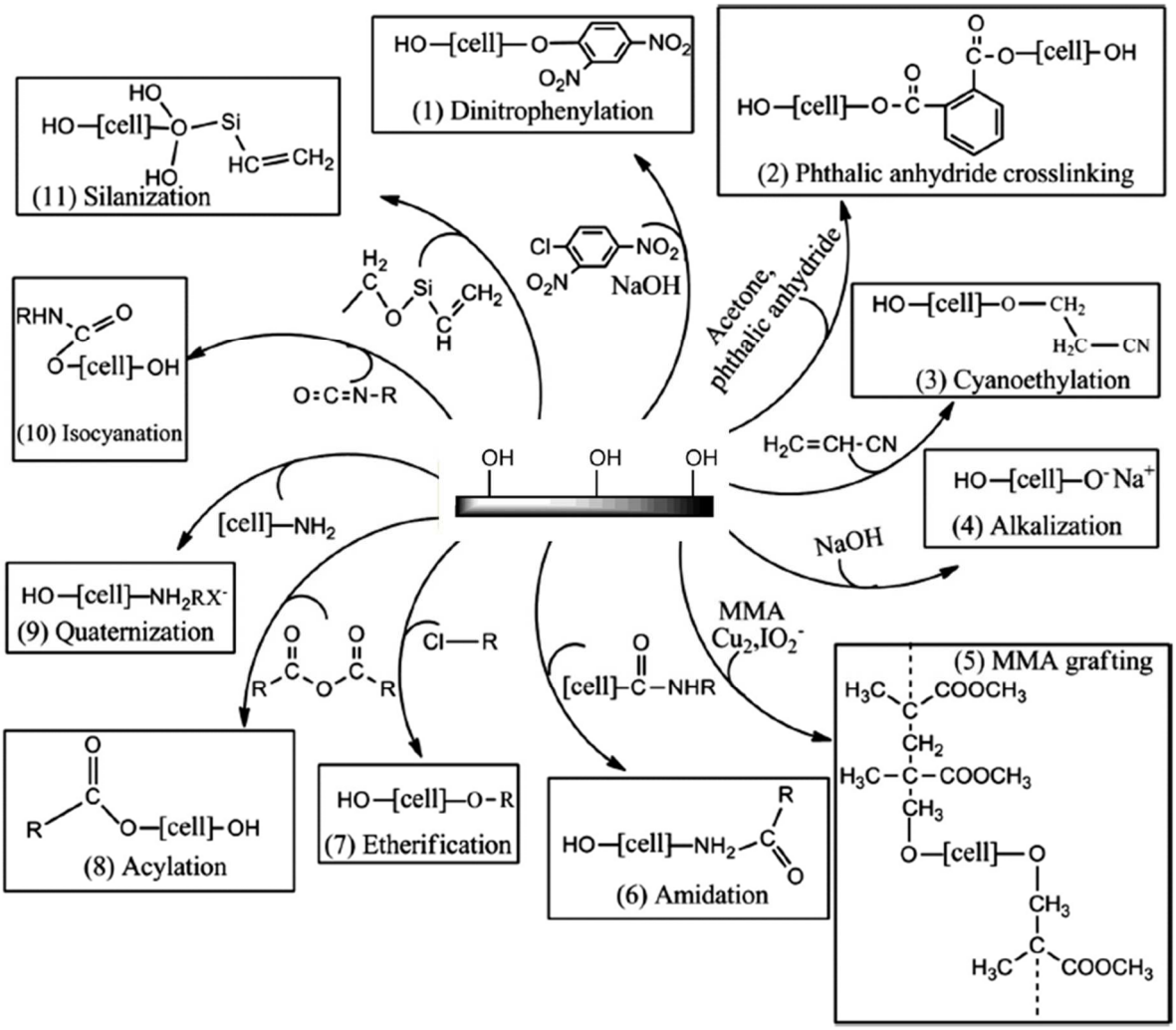

Figure 1-18. Exemples de réactions chimiques visant à modifier les propriétés physico-chimiques de surface des nanofibrilles de cellulose. Figure adaptée d'après Gurunathan *et coll.*[46].

1.3.2.3 Procédés d'élaboration

Les nanocomposites sont le plus souvent élaborés par coulée-évaporation sous forme de films minces ayant des épaisseurs comprises entre 10 et 100 µm[15]. Quelques études[30,100] ont néanmoins montré qu'il était possible de fabriquer des films nanocomposites en utilisant des procédés industriels tels que l'extrusion ou le couchage. Malheureusement, la fabrication de nanocomposites par extrusion est encore fastidieuse et requiert l'utilisation de procédures complexes visant à éliminer l'eau contenue dans les suspensions de NFC (problèmes de dégazage), à améliorer la dispersion des NFC lors du malaxage et à éluder la dégradation thermique des nanofibres[4,100].

Les films ou nanopapiers de NFC (Fig. 1-9) sont généralement élaborés par filtration[101,49,102]. Malheureusement les dimensions nanométriques, l'importante surface spécifique et le fort élancement des NFC rendent souvent le procédé de filtration extrêmement fastidieux[103]. De récents travaux[104] ont également essayé de fabriquer des films et des fils continus de NFC

(Fig. 1-19) en utilisant des techniques telles que l'induction par centrifugation[105] ou *spin-coating* en anglais.

Du point de vue procédé, il reste un nombre important de verrous technologiques et scientifiques à lever afin de pouvoir produire de manière concurrentielle et rentable ces matériaux biosourcés. Les applications industrielles les plus matures concernent le couchage de supports polymères et cellulosiques (papiers, cartons) pour l'emballage par des matrices polymères chargées en NFC, en vue d'améliorer les propriétés barrières et donc la conservation de certains produits alimentaires[106].

1.3.2.4 Quelques éléments sur la rhéologie des suspensions de NFC

Le contrôle de la microstructure des nanocomposites et films de NFC au cours de leur mise en forme est crucial pour pleinement tirer parti des caractéristiques géométriques et mécaniques intrinsèques des NFC et ainsi obtenir des matériaux aux propriétés mécaniques optimisées. Cela nécessite une bonne compréhension et maîtrise des propriétés d'écoulement des suspensions de NFC aux différentes échelles.

Aussi bien dans l'eau que dans les matrices de polymères, la rhéologie des suspensions de NFC est complexe, encore peu caractérisée, comprise et modélisée. En effet, ces suspensions se comportent comme des fluides à seuil thixotropes qui présentent un comportement rhéofluidifiant prononcé à de forts taux de cisaillement[107-109]. Les NFC sont des nanoparticules très élancées. Ainsi de manière analogue à ce qui est généralement observé pour les suspensions de fibres « classiques » (voir commentaires relatifs à la partie 1.2.3.2), les NFC translatent, se réorientent et se déforment sous écoulement (Fig. 1-19) ce qui conduit à un comportement rhéologique complexe[104]. En outre, ces suspensions ont tendance à floculer au repos ou sous l'action de forces mécaniques, pour certaines vitesses de cisaillement[110-112] (Fig. 1-20.b). Ces phénomènes de structuration par formation de flocs ou aggrégation sont sous certains aspects très similaires à ceux déjà observés dans le cas des suspensions de particules élancées de taille nanométrique telles que les suspensions de nanotubes de carbone[113,114] (Fig. 1-20.a).

L'ensemble des mécanismes d'écoulement ainsi observés aux échelles supérieures est induit à la fois par des interactions de contact (collisions, enchevêtrements) qui interviennent aux échelles fines entre les nanofibres lorsque la suspension est déformée, mais également par des interactions à courte distance de nature colloïdale (forces de van der Waals et électrostatiques) et brownienne (Fig. 1-19.b,c) qui deviennent importantes lorsque les particules sont de petite taille (1 à 1000 nm)[115,116,104]. Ainsi, le comportement des suspensions de NFC nécessite d'être caractérisé et analysé au regard de celui des suspensions de fibres « classiques » mais aussi de celui des systèmes colloïdaux concentrés (gels, matériaux vitreux mous). Nous aborderons cette problématique dans les deux prochains chapitres.

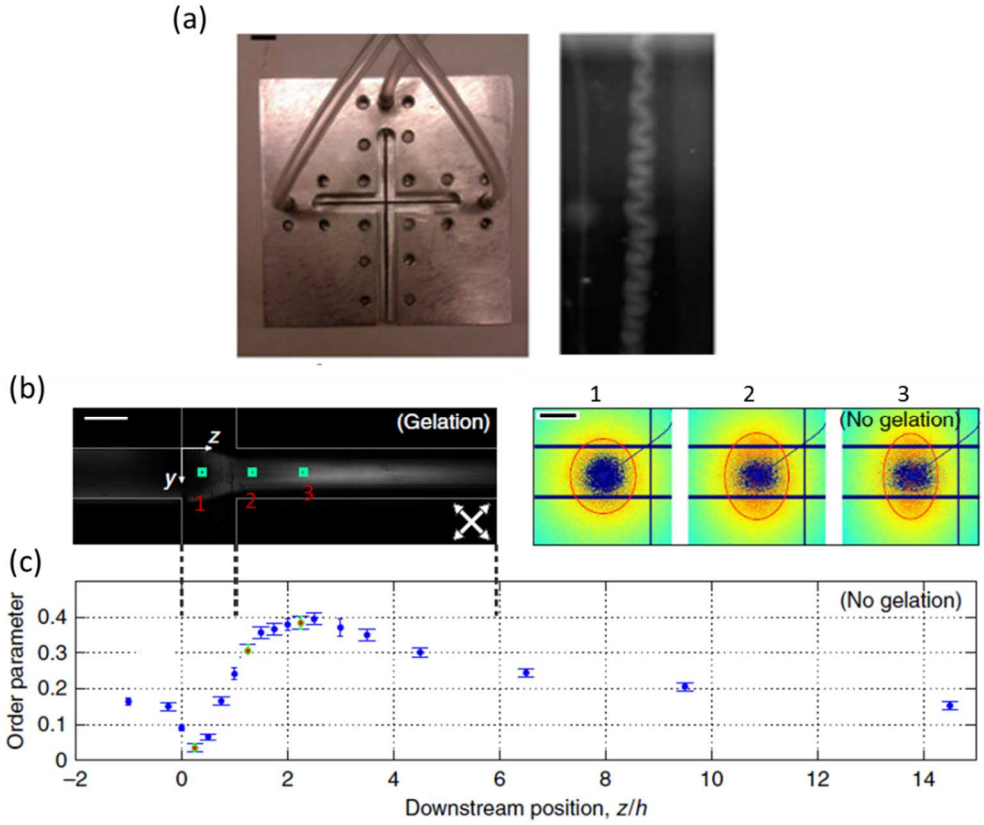

Figure 1-19. (a) Photographies montrant la filière d'un dispositif destiné à l'élaboration de fils composites renforcés avec des NFC. L'image de droite montre un fil formé par une suspension concentrée de NFC. (b) Clichés de diffraction *in situ* obtenus par SAXS à trois endroits différents dans le canal de mise en forme : 1 avant accélération et 2,3 après accélération. La barre d'échelle représente 2 mm. (c) Évolution de l'orientation globale des NFC en fonction de la position dans le canal de mise en forme. Cette figure montre (i) que les NFC s'orientent sous écoulement et (ii) que la structure au repos est rendue aléatoire sous l'effet du mouvement brownien. Figures adaptées de Hakansson *et coll.*[104].

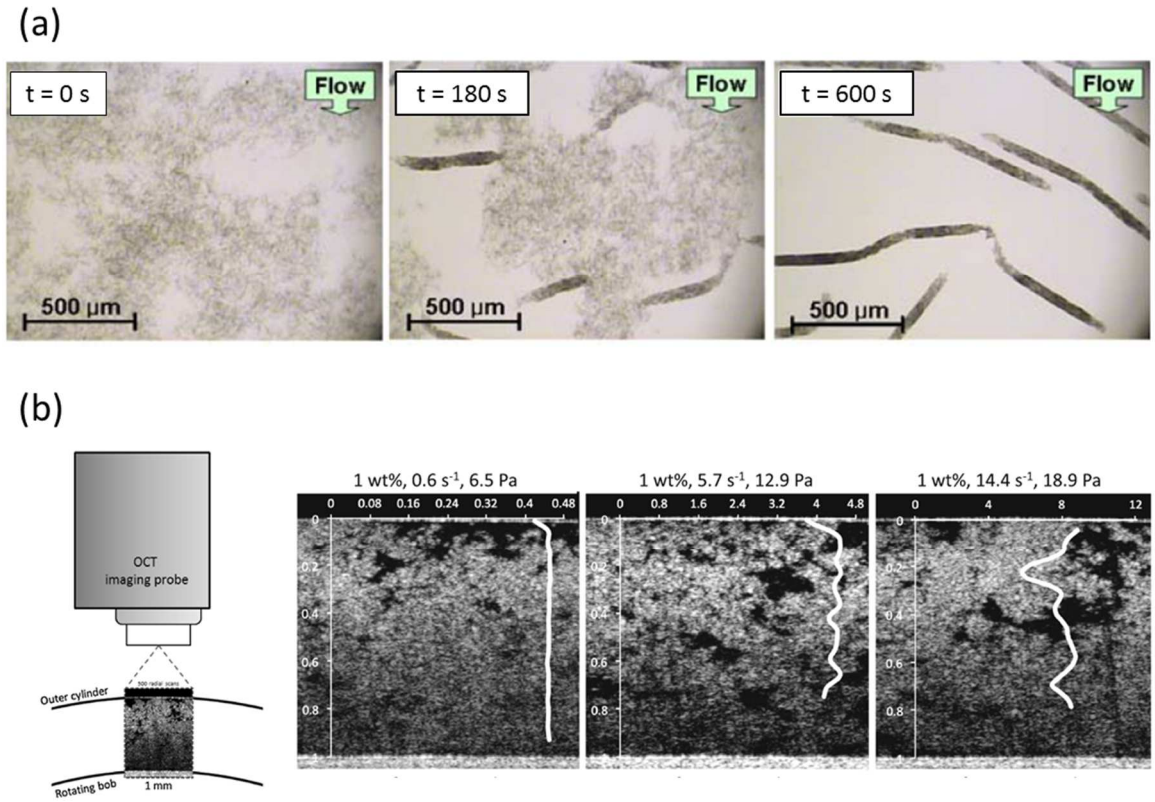

Figure 1-20. (a) Micrographies optiques montrant l'évolution de la microstructure d'une suspension diluée de nanotubes de carbone (0.03% en masse) lors d'un essai de cisaillement ($\dot{\gamma} = 0.5\ s^{-1}$) en géométrie plan-plan (entrefer de 130 µm)[113]. Les micrographies montrent la formation de rouleaux ou d'agrégats induits par l'écoulement. (b) Radiographies obtenues par tomographie optique cohérente montrant l'évolution de la microstructure d'une suspension enzymatique de NFC (1% en masse) lors d'un essai de cisaillement en géométrie de Taylor-Couette (entrefer de 870 µm). La ligne tracée en blanc correspond au profil de vitesse moyen dans l'entrefer du rhéomètre[112]. Les radiographies révèlent la présence d'hétérogénéités (flocs ou amas de flocs), de glissements aux parois ainsi que de phénomènes complexes de déchirement de la suspension.

1.3.3 Propriétés microstructurales

La caractérisation des propriétés microstructurales des nanocomposites et films de NFC est encore aujourd'hui extrêmement limitée en raison des dimensions nanométriques de la phase renforçante[4]. L'étude de la dispersion des NFC au sein de la matrice polymère consiste généralement en une inspection à l'œil nu[4]. Pour les matrices transparentes, des méthodes optiques peuvent également être employées : l'opacité suggère généralement la présence d'agrégats de taille micrométrique.

Une analyse microstructurale plus approfondie des faciès de rupture est généralement réalisée par MEB-FEG, MET ou AFM et permet de mettre en évidence :

- la présence d'agrégats ;
- la sédimentation du renfort fibreux ;
- la présence de porosité.

De même, l'orientation globale des NFC dans les matériaux peut être révélée par des techniques de diffraction à rayons X[49]. Les nanocomposites et films obtenus par coulée-évaporation

présentent généralement des microstructures fibreuses à orientation plane et aléatoire[49,97]. La Figure 1-21 montre des exemples de microstructures (section transverse) de ces matériaux.

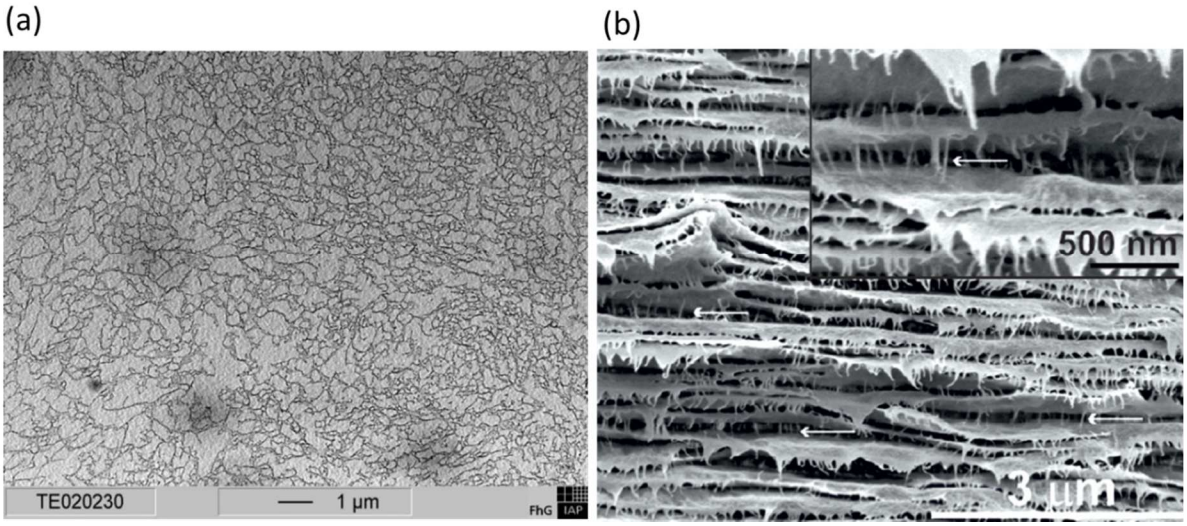

Figure 1-21. (a) Micrographie MET montrant la section fine d'un nanocomposite à matrice HPC (hydroxypropylcellulose) renforcée avec 20% en masse de NFC (traitement d'extraction mécanique)[117]. Les NFC sont en noir et la matrice en gris. (b) Micrographie MEB-FEG de la section d'un film pur de NFC TEMPO. Les clichés ont été obtenus à une humidité relative de 100% afin de mettre en évidence la structure stratifiée du matériau[97].

1.3.4 Propriétés mécaniques

Plusieurs études[99,4,93] ont montré que les propriétés mécaniques des matrices polymères hôtes pouvaient être considérablement augmentées une fois mélangées avec des NFC et ce même à de très faibles concentrations en NFC. Cela vient essentiellement du très grand élancement des NFC, de leurs très bonnes propriétés mécaniques intrinsèques et des liaisons hydrogènes que ces nanofibres peuvent former entre elles[99,118,119]. En général, l'effet de renfort apporté par les NFC (vis-à-vis de la matrice hôte) est plus marqué à haute température. En effet, comme le montre la Figure 1-22, à l'état caoutchoutique de la matrice, c'est-à-dire pour T/T_α >1, le module du composite renforcé avec un taux de charges de 4% en masse est supérieur de plus de deux ordres de grandeur à celui de la matrice non chargée. En revanche, pour T/T_α<1, l'effet de renfort est nettement moins prononcé. De plus, il est intéressant de noter que la matrice s'écoule généralement comme un fluide à l'approche d'une température critique T_e alors que le composite conserve un comportement de type solide mou jusqu'à des températures de l'ordre de 500 K (température de dégradation de la cellulose)[4]. Ce comportement inhabituel est propre aux nanocomposites renforcés avec des particules cellulosiques. Il n'est par exemple pas observé avec des nanotubes de carbone[99].

Les propriétés exceptionnelles observées pour ces systèmes sont attribuées à l'existence d'un réseau d'interaction rigide sous forme de contacts directs entre NFC[99,118,119]. Dans cette approche, le module mesuré est alors assimilé à celui « d'une feuille de papier » de fraction volumique équivalente, pour laquelle les forces de liaisons hydrogènes sont à l'origine de son comportement élastique[47]. Le scénario proposé pour expliquer cela est le suivant[4,99] : au cours de l'évaporation de l'eau, les NFC se réarrangeraient sous l'action du mouvement brownien

ou par effet capillaire dans la suspension pour former un réseau continu d'interactions directes NFC-NFC. Pour appuyer ce scénario, plusieurs études ont essayé de modifier les conditions de formation du film, par exemple en augmentant la taille des micelles de polymère ou en lyophilisant le mélange de polymère et NFC et en comprimant à chaud la poudre obtenue[99]. Les auteurs[99] ont constaté que les matériaux ainsi élaborés présentaient généralement des propriétés inférieures à celles des matériaux mis en forme par coulée-évaporation (Fig. 1-22). Ils ont attribué cet amoindrissement des propriétés à un arrangement limité des particules lors de la mise en forme du film, affectant ainsi la formation du réseau continu de NFC.

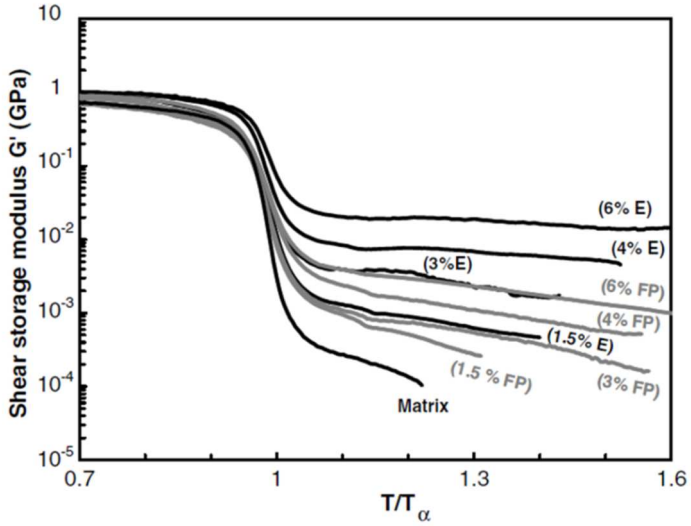

Figure 1-22. Courbes de DMA (analyse mécanique dynamique) montrant l'évolution du module de cisaillement dynamique G' en fonction de la température normalisée (T_α étant la température de relaxation) pour des nanocomposites de poly(styrène-co-buthyl acrylate) P(S-Bua) et NFC élaborés par coulée-évaporation (E) et par lyophilisation de la suspension et compression à chaud à une température de 100°C et une pression de 1 MPa (FP)[99].

Quelques études ont également essayé d'introduire les NFC dans des proportions plus importantes (10% à 100% en masse)[93,120]. Les auteurs ont pour la plupart observé des évolutions linéaires du module d'élasticité E (1 GPa $< E <$ 10 GPa) et de la contrainte d'écoulement σ_e (18 MPa $< \sigma_e <$ 100 MPa) avec la fraction volumique de fibres ϕ. Ils ont par ailleurs montré que ces évolutions pouvaient être relativement bien prédites de manière phénoménologique à partir des propriétés mécaniques des films denses, simplement en utilisant une loi des mélanges[120]. À forts taux de NFC, les propriétés mécaniques des nanocomposites sont proches de celles des films purs. Le module d'élasticité E est généralement compris entre 1 et 17 GPa, tandis que la contrainte à la rupture σ_r varie de 10 à 310 MPa[120]. Par ailleurs, d'autres travaux plus récents ont montré que les propriétés en traction (déjà remarquables) pouvaient être encore améliorées en modifiant l'orientation globale des NFC lors de la formation du film ($E \approx 30$ GPa et $\sigma_r \approx 400$ MPa)[49,121].

Comme déjà remarqué précédemment, il est intéressant de noter que les augmentations de module d'élasticité observées expérimentalement sont bien en deçà des prédictions analytiques[122,123] ou numériques[124] de la plupart des modèles mécaniques multi-échelles de la littérature. Nous reviendrons sur ce point dans le chapitre 3.

Cette description succincte du comportement mécanique des nanocomposites et films de NFC montre une fois encore qu'il est crucial de bien maîtriser le placement des NFC lors des différentes étapes de mise en forme. La répartition spatiale des NFC conditionne :

- les micromécanismes de transfert de charge fibre-matrice comme pour les composites et nanocomposites traditionnels ;
- les micromécanismes de déformation entre NFC (nombre et géométrie des contacts « directs » entre NFC).

1.4 Matériaux poreux cellulosiques

1.4.1 Introduction

1.4.1.1 Généralités

Les matériaux poreux sont constitués d'un squelette rigide entourant des cavités soit fermées, soit partiellement ou totalement ouvertes sur les cavités voisines ou sur l'extérieur[125]. Ils peuvent prendre diverses formes (nids d'abeilles, mousses, milieux plissés, enchevêtrés ou granulaires), et sont employés dans différents domaines tels que l'automobile, le transport, le bâtiment, l'emballage, le médical[125]. Les propriétés recherchées sont multiples et varient en fonction des applications dans lesquelles ces matériaux sont utilisés. On peut citer par exemple :

- les propriétés d'isolation thermique et phonique ;
- les propriétés mécaniques spécifiques et d'amortissement, de résistance aux chocs ;
- les propriétés de flottabilité ;
- les propriétés d'absorption.

De manière générale, les caractéristiques physiques dépendent de la nature du squelette solide, de son architecture (géométrie des pores, diamètre des pores et épaisseur des parois), de sa densité relative et de son procédé de fabrication[125,126]. Les matériaux poreux les plus utilisés sont les matériaux cellulaires à base de polymères pétrosourcés comme par exemple les mousses de polyuréthane, de polystyrène expansé, de polyéthylène, de PVC ou à base de latex[125,126]. Les procédés de mise en forme de ces matériaux peuvent être classés en plusieurs catégories[125,126] :

- expansion physique d'un liquide à faible température d'ébullition ;
- expansion physique d'un gaz absorbé par le polymère sous haute pression ;
- expansion d'un gaz dégagé in situ par la décomposition thermique d'un agent gonflant ;
- battage mécanique introduisant de l'air ;
- dissolution d'un ingrédient après transformation.

1.4.1.2 La voie biosourcée

Depuis une dizaine d'années, l'objectif d'un nombre croissant de travaux de recherche est de développer des matériaux poreux de substitution partiellement ou totalement biosourcés[127,128]. Ces études visent par exemple à utiliser certaines des matrices biosourcées présentées dans la partie 1.2.2.1 comme le PLA[129] (Fig. 1-23) pour élaborer de nouveaux matériaux cellulaires. D'autres études cherchent à substituer certains réactifs ou produits classiquement utilisés dans la synthèse de matériaux polymères cellulaires par des constituants issus de la biomasse végétale. À titre d'exemple, certains constituants des mousses de polyuréthane peuvent être remplacés par des dérivés de lignine[130,131] ou de tanin[132] (Fig. 1-14.b). Ces stratégies sont

décrites et précisées dans plusieurs ouvrages[60,3]. Le lecteur intéressé pourra s'y reporter pour des approfondissements.

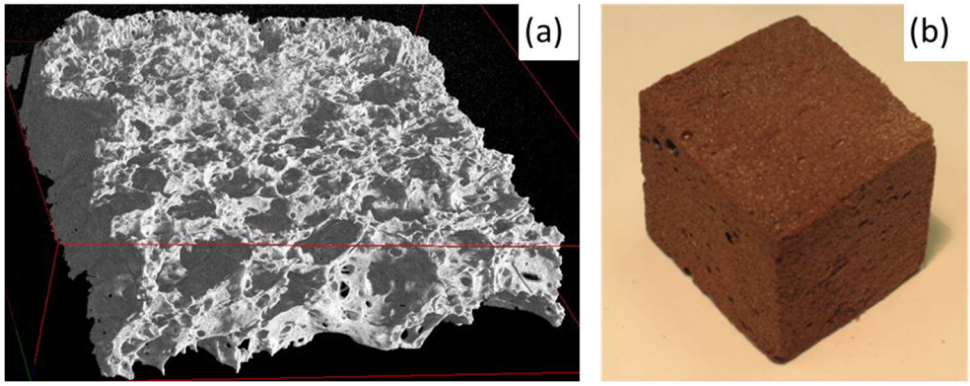

Figure 1-23. (a) Image 3D d'une mousse de PLA obtenue par microtomographie à rayons X. (b) Photographie d'une mousse de polyuréthane élaborée à partir de lignine oxypropylée[131].

Ces dernières années, de nouvelles stratégies visant à exploiter les propriétés remarquables de la cellulose ont été développées[93,52]. De nouveaux matériaux ont émergé, parmi lesquelles :

- les matériaux formés d'un assemblage de nanofibres de cellulose[93,133,134];
- les matériaux issus de cellulose régénérée[52,53,135].

L'objectif de cette partie est de présenter brièvement ces nouvelles stratégies, les matériaux obtenus ainsi que leurs propriétés, en se focalisant principalement sur les propriétés mécaniques.

1.4.2 Quelques stratégies émergentes

1.4.2.1 Matériaux issus de suspensions de NFC

Les suspensions de NFC peuvent être utilisées pour former des matériaux cellulosiques de faible voire très faible densité (7 à 100 kg m^{-3}) tels que des mousses et des aérogels[93,133,134,136]. Dans cette étude, on utilisera le terme « mousse » pour les matériaux cellulaires ayant un diamètre moyen de pores supérieur au micromètre (micropores) et « aérogel » pour les matériaux de très faible densité ayant un diamètre moyen de pores inférieur au micromètre (nanopores).

L'objectif de ces travaux de recherche est de sécher les suspensions colloïdales aqueuses de NFC tout en évitant l'effondrement et la densification de la structure sous l'effet de forces capillaires. Deux méthodes de séchage sont fréquemment utilisées pour extraire l'eau contenue dans ces suspensions : la cryodessiccation[137] (ou lyophilisation) et le séchage par fluide supercritique[136].

La cryodessiccation est un procédé classiquement utilisé dans l'industrie agroalimentaire et pharmaceutique. Il s'effectue généralement en deux étapes. La première étape consiste à solidifier le fluide suspensif en abaissant sa température (Fig. 1-24). Durant la solidification, les

particules en suspension sont séparées et redistribuées par le front de glace se déplaçant[138,139]. Les cristaux de glace formés sont ensuite sublimés à basse température ($\approx -50°C$) dans des conditions de faible vide (0.020 mbar)[137].

Le séchage par voie supercritique consiste à faire subir au fluide une variation de température et de pression l'amenant à contourner le point critique qui limite la courbe de vaporisation (Fig. 1-24). Au-delà de ce point les états liquides et vapeur ne sont plus discernables et les forces capillaires sont alors inexistantes[140]. Cette technique de séchage nécessite de passer par une procédure d'échange de solvant : l'eau possède une température et une pression critique très élevée ($T_c \approx 374°C$, $P_c \approx 218$ bars). Parmi les fluides adaptés au séchage supercritique, on compte le dioxyde de carbone CO_2 ($T_c = 31°C$, $P_c = 74$ bars), ou certains fréons ($T_c = 27°C$, $P_c = 30$ à 40 bars).

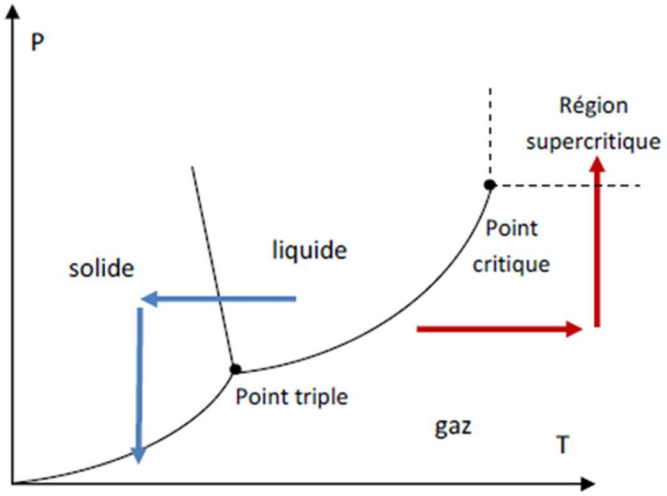

Figure 1-24. Diagramme de phase (pression P en fonction de la température T) montrant les chemins suivis lors du séchage par cryodessiccation (flèches bleues) et du séchage par voie supercritique (flèches rouges). Figure reproduite d'après Sescousse[140].

1.4.2.2 Matériaux issus de cellulose régénérée

Dans cette approche, les chaînes de cellulose sont dissociées des fibres végétales délignifiées en utilisant un solvant approprié (voir les commentaires relatifs à la partie 1.1.2.2.3 et la Fig. 1-6). Les solutions de cellulose ainsi obtenues sont ensuite coulées dans un moule et régénérées[52]. La régénération consiste à introduire la solution de cellulose dans un bain coagulant (eau, acide alcool). Il apparaît alors un phénomène de séparation de phases : le solvant contenu dans la solution de cellulose diffuse vers le coagulant, tandis que le coagulant diffuse vers le gel de cellulose. Ce phénomène participe à la formation d'un gel, c'est-à-dire d'un réseau enchevêtré de macromolécules de cellulose gonflées. La dernière étape consiste ensuite à retirer le coagulant présent à l'intérieur du gel sans altérer sa structure tridimensionnelle. Cette étape est généralement réalisée par cryodessiccation ou par voie supercritique (CO_2)[53,52].

De nombreuses études actuelles sont dédiées au développement de procédures de séchage alternatives[135,141]. Plusieurs travaux de recherche récents[135,141] ont montré qu'il était possible

en modifiant le système (ajout de tensioactifs, hydrophobisation de la cellulose) de conserver une structure aérée par simple séchage à l'air libre.

1.4.3 Propriétés microstructurales

La microstructure des mousses et aérogels de cellulose est souvent caractérisée par MEB-FEG. La Figure 1-25 montre quelques exemples de mousses et aérogels obtenus à partir de suspensions de NFC ou de solutions de cellulose régénérées. Les microstructures des matériaux obtenus sont très différentes et varient en fonction du procédé de séchage (séchage par cryo-dessiccation ou séchage par voie supercritique).

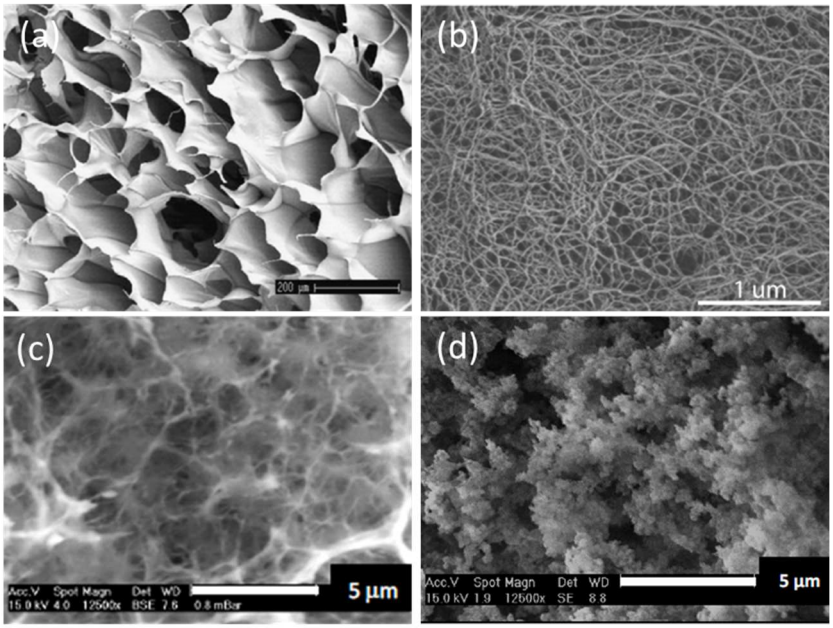

Figure 1-25. (a) Structure obtenue après séchage par cryodessiccation d'une suspension de NFC TEMPO (2.4% en masse)[142]. (b) Structure obtenue après séchage par voie supercritique d'une suspension enzymatique (2% en masse)[136]. (c) Structure obtenue après séchage par cryodessiccation d'une solution de cellulose régénérée[140]. (d) Structure obtenue après séchage par voie supercritique d'une solution de cellulose régénérée (15% en masse)[140].

Notons qu'il est encore difficile à partir des micrographies obtenues (Fig. 1-25) d'extraire des descripteurs quantitatifs ou statistiques de la microstructure de ces matériaux. Des méthodes indirectes par intrusion ou adsorption de gaz sont parfois utilisées afin d'estimer la porosité et la surface spécifique de ces matériaux[140].

1.4.4 Propriétés mécaniques

Le comportement mécanique des mousses et aérogels de cellulose est encore peu caractérisé[136,142,133]. Les premières études tendent néanmoins à montrer que les propriétés élastiques et plastiques de ces matériaux biosourcés sont bien inférieures à celles classiquement obtenues pour des mousses de polymères standards. Quelques valeurs typiques de module d'élasticité issues de la littérature sont reportées dans le diagramme de la Fig. 1-26. Les faibles caractéristiques mécaniques de ces matériaux sont souvent attribuées à la présence de défauts struc-

turels (fissures, hétérogénéité dans la répartition de la phase solide)[139,138]. Une meilleure compréhension ainsi qu'un meilleur contrôle des architectures formées par ces matériaux (Fig. 1-25) devrait permettre d'accroître considérablement leurs performances[139,138].

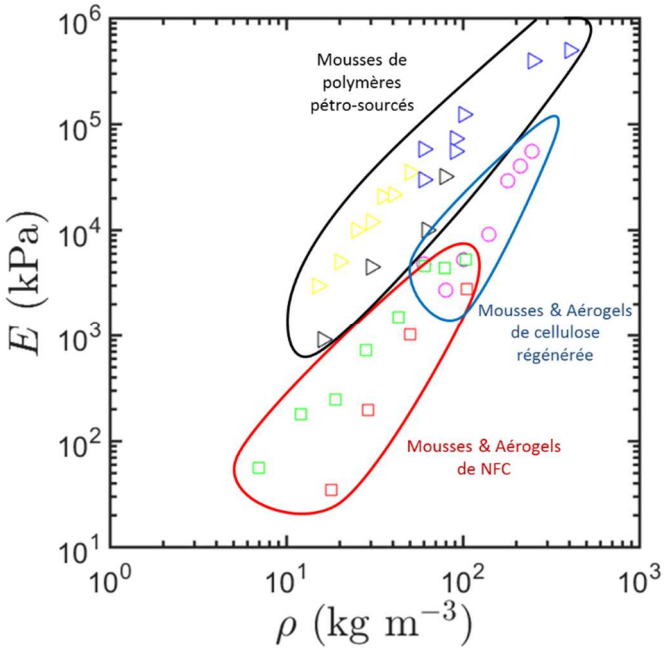

Figure 1-26. Module élastique E (en compression) en fonction de la masse volumique ρ pour des mousses polymères classiques[125,126] (triangles noirs : PU, triangles jaunes : PSE, triangles bleus : PVC), des mousses et aérogels de NFC[136,51,134,133] (carrés rouges : séchage par voie supercritique, carrés verts : cryodessiccation), et des mousses et aérogels de cellulose régénérée[53,52,140] (ronds magenta : séchage par voie supercritique).

Ces matériaux cellulosiques ont un avenir très prometteur dans la « super-isolation » thermique[55,143,144]. En effet, plusieurs études récentes ont montré que les aérogels de NFC et de cellulose régénérée préparés par voie supercritique, présentent des conductivités thermique λ de l'ordre de 0.02 W m^{-1} K^{-1}), c'est-à-dire des conductivités proches de celles mesurées pour l'air. Néanmoins, pour pouvoir utiliser pleinement ces matériaux, par exemple dans le bâtiment comme âmes de structures sandwich, il est crucial d'accroître encore leurs performances mécaniques. Nous reviendrons sur la problématique de mise en forme des mousses de NFC dans le chapitre 5.

1.5 Conclusion

1.5.1 Bilan de l'étude bibliographique

Dans la partie 1.1, nous avons montré que les fibres végétales constituent en raison de leur structure hiérarchisée et leur composition biochimique riche et variée une matière première renouvelable abondante pour de multiples matériaux. À partir des fibres végétales, il est possible d'extraire au moyen de procédés chimiques et mécaniques, deux types de nanorenforts biosourcés : les nanofibrilles de cellulose (NFC) et les nanocristaux de cellulose (NCC). Les NFC se présentent généralement sous la forme de nanoparticules fibreuses semi-flexibles très élancées ayant un diamètre compris entre 3 et 500 nm et une longueur comprise entre 1 et 10 µm. En revanche, les NCC sont des bâtonnets rigides plus ramassés dont le diamètre est compris entre 20 et 30 nm et la longueur entre 200 et 400 nm. Les propriétés morphologiques et physico-chimiques des particules extraites dépendent fortement du traitement d'extraction et de l'espèce botanique considérée.
En outre, nous avons montré qu'il est aussi possible d'extraire de manière sélective les constituants chimiques majoritaires des fibres végétales tels que la cellulose, la lignine et les hémicelluloses.

Dans la partie 1.2, nous avons montré que les fibres végétales peuvent être utilisées pour renforcer des matrices polymères. Les matériaux composites biosourcés à renforts naturels présentent généralement de bonnes propriétés mécaniques spécifiques. Ces propriétés restent néanmoins assez dispersées, difficiles à contrôler et sont généralement encore inférieures à celles des composites classiques à fibres de verre. Plusieurs aspects relatifs aux renforts naturels (variabilités des propriétés géométriques et mécaniques des fibres, sensibilité à l'humidité), aux interfaces fibres-matrice (mouillabilité, adhésion) et aux conditions d'élaboration (contrôle difficile de la microstructure au cours de la mise en forme) sont susceptibles d'altérer les propriétés en service des biocomposites. Ainsi, plusieurs voies d'amélioration sont étudiées pour accroître leurs performances mécaniques. Beaucoup de travaux de recherche actuels portent sur l'optimisation des propriétés d'interface entre les fibres et la matrice (p. ex. greffage chimique de surface). Encore très peu de travaux portent sur l'élaboration de composites biosourcés à double échelle de renforts à base de nanofibrilles de cellulose.

Dans la partie 1.3, nous avons montré que les NFC constituent en raison de leurs propriétés géométriques ($100 < l/d < 500$) et mécaniques ($80\ \text{GPa} < E < 100\ \text{GPa}$) remarquables, des nano-renforts intéressants pour des matrices polymères ou cimentaires. En effet, les NFC peuvent apporter un effet de renfort extrêmement important aux matrices dans lesquelles elles sont introduites (et ce même à de faibles concentrations) pour peu que leur dispersion lors des étapes de mise en forme soit maîtrisée. Malheureusement, nous avons vu que le mélangeage et la dispersion des NFC (et NCC) extraites sous forme de suspensions aqueuses avec la plupart des résines polymères hydrophobes était encore difficile à réaliser et constituait un

frein majeur à leur utilisation dans des composites. En revanche, nous avons vu que ces particules pouvaient être plus facilement mélangées et dispersées au sein de matrices hydrosolubles et de polymères sous forme de latex. Les propriétés mécaniques des films nanocomposites ainsi obtenus dépendent de la répartition spatiale en taux et orientation de nanofibres comme pour les composites classiques, mais également de la micromécanique se produisant aux interfaces entre NFC. En effet, contrairement aux charges et nano-charges plus classiquement utilisées (nanotubes de carbone), les NFC peuvent interagir fortement entres elles par le biais de liaisons hydrogènes pour former des réseaux connectés cohésifs capables de supporter et transmettre les efforts. Encore peu de travaux expérimentaux et théoriques se sont penchés sur l'étude des nanostructures de ces matériaux et sur les micro-mécanismes de déformation et de transfert de charge se produisant à l'échelle des NFC et du réseau de NFC.

Dans la partie 1.4, nous avons vu qu'un nombre croissant de travaux de recherche visent à utiliser les constituants élémentaires de la paroi des fibres végétales (NFC et dérivés de cellulose) pour élaborer des matériaux poreux biosourcés de faible voire très faible densité. D'une manière générale, les propriétés microstructurales de ces matériaux sont encore peu caractérisées et comprises. En outre, ces matériaux présentent des performances mécaniques inférieures à la plupart des mousses polymères standards ce qui constitue un frein important à leur utilisation, par exemple dans la conception de matériaux de structure.

1.5.2 Approche adoptée

Dans ce projet de thèse nous avons fait le choix de travailler avec des nanofibrilles de cellulose qui nous paraissaient être, au vu de leur élancement important et de leurs très bonnes propriétés mécaniques intrinsèques, des nanorenforts biosourcés intéressants pour des composites à double échelle de renforts.

Ainsi, dans le **chapitre 2** nous avons extrait à partir de fibres de bois, deux types de suspensions de NFC : des NFC enzymatiques et des NFC TEMPO. Ensuite, nous avons caractérisé leur rhéologie (en cisaillement) aux échelles macroscopique et mésoscopique en utilisant une méthodologie originale et complémentaire à celles présentées dans la partie bibliographique (partie 1.3.2.4). Cette première étude nous a permis de mettre en évidence l'influence de la microstructure et des propriétés physico-chimiques des NFC ainsi que celle de la vitesse de sollicitation sur leur propriété d'écoulement et sur leur mésostructure. Ensuite (**chapitre 3**), comme il est encore relativement difficile d'obtenir par l'expérience des descripteurs pertinents de la microstructure des suspensions de NFC (et de son évolution) en écoulement (partie 1.3.2.4), nous avons fait le choix de passer par une approche de modélisation multi-échelles s'appuyant fortement sur les travaux expérimentaux, théoriques et numériques dédiés aux suspensions de fibres, nanofibres et colloïdes, pour expliquer le comportement macroscopique des suspensions de NFC à partir des mécanismes de déformation et d'écoulement aux échelles fines (micro et nanoscopiques).

Ce premier volet sur la rhéologie multi-échelles des suspensions aqueuses de NFC a pour objectif une meilleure compréhension et maîtrise de ces nouveaux renforts biosourcés lors des procédés d'élaboration de composites ou de mousses qui passent généralement par des étapes de mise de mise en œuvre ou les renforts fibreux sont présents dans des suspensions au comportement rhéologique complexe.

Dans le **chapitre 4,** nous nous sommes intéressés aux propriétés microstructurales et mécaniques de nanocomposites renforcés avec des nanofibrilles de cellulose ainsi qu'à leur modélisation. Comme il est encore difficile de mélanger efficacement les NFC à des résines polymères standards (partie 1.3.2), nous avons utilisé une matrice modèle hydrosoluble de PEO. Une modélisation originale du comportement élastique macroscopique équivalent de ces milieux a ensuite été réalisée en tenant compte d'hypothèses simplifiées s'appuyant très fortement sur les analyses microstructurales des nanofibres et de leurs composites.

Enfin, dans le **chapitre 5** nous avons cherché à améliorer l'élaboration des mousses de NFC (partie 1.4.2.1) en vue de les utiliser (plus tard) comme âmes de matériaux sandwich. Nous avons pour cela cherché à optimiser les procédures d'élaboration actuelles (partie 1.4.2.1). Une nouvelle voie d'élaboration impliquant un brassage mécanique des suspensions a également été proposée.

Références

1 A. Gandini and M. N. Belgacem, in Monomers, *Polymers and Composites from Renewable Resources*, Elsevier, Amsterdam, 2008, pp. 1–16.

2 N. Berezina and S. M. Martelli, *in Chapter 1:Bio-based Polymers and Materials*, 2014.

3 A. K. Mohanty, M. Misra and L. T. Drzal, *Natural Fibers, Biopolymers, and Biocomposites*, CRC Press, 2005.

4 A. Dufresne, *Nanocellulose: From Nature to High Performance Tailored Materials*, Walter de Gruyter, 2013.

5 A. K. Mohanty, M. Misra and G. Hinrichsen, *Macromol. Mater. Eng.*, 2000, 276-277, 1–24.

6 L. J. Gibson, *J. R. Soc. Interface*, 2012, 9, 2749–2766.

7 D. Fengel and G. Wegener, *Wood: chemistry, ultrastructure, reactions*, Walter de Gruyter, 1983.

8 M. Toungara, P. Latil, P.J.J. Dumont, S. Rolland du Roscoat, L. Orgéas, T. Joffre, and R. Passas, *Review of Scientific Instruments,* 2015 (submitted).

9 C. Baley, *Tech. Ing.*, 2013.

10 L. Donaldson, *Wood Sci. Technol.*, 2007, 41, 443–460.

11 G. Chinga-Carrasco, *Nanoscale Res. Lett.*, 2011, 6, 1–7.

12 I. Usov, G. Nyström, J. Adamcik, S. Handschin, C. Schütz, A. Fall, L. Bergström and R. Mezzenga, *Nat. Commun.*, 2015, 6, 7564.

13 D. N.-S. Hon and N. Shiraishi, *Wood and Cellulosic Chemistry, Second Edition, Revised, and Expanded*, CRC Press, 2000.

14 E. Retulainen, K. Niskanen and N. Nilsen, *Pap. Phys.*, 1998, 16.

15 I. Siró and D. Plackett, *Cellulose*, 2010, 17, 459–494.

16 N. Lavoine, I. Desloges, A. Dufresne and J. Bras, *Carbohydr. Polym.*, 2012, 90, 735–764.

17 K. Abe, S. Iwamoto and H. Yano, *Biomacromolecules*, 2007, 8, 3276–3278.

18 O. Nechyporchuk, F. Pignon and M. N. Belgacem, *J. Mater. Sci.*, 2014, 50, 531–541.

19 L. H. Rees, *Chem. Eng.*, 1974, 81, 86–92.

20 T. Taniguchi and K. Okamura, *Polym. Int.*, 1998, 47, 291–294.

21 K. L. Spence, R. A. Venditti, O. J. Rojas, Y. Habibi and J. J. Pawlak, *Cellulose*, 2010, 17, 835–848.

22 M. Henriksson, G. Henriksson, L. A. Berglund and T. Lindström, *Eur. Polym. J.*, 2007, 43, 3434–3441.

23 M. Pääkkö, M. Ankerfors, H. Kosonen, A. Nykänen, S. Ahola, M. Österberg, J. Ruokolainen, J. Laine, P. T. Larsson, O. Ikkala and T. Lindström, *Biomacromolecules*, 2007, 8, 1934–1941.

24 T. Saito, S. Kimura, Y. Nishiyama and A. Isogai, *Biomacromolecules*, 2007, 8, 2485–2491.

25 A. Isogai, T. Saito and H. Fukuzumi, *Nanoscale*, 2011, 3, 71–85.

26 A. B. Fall, S. B. Lindström, O. Sundman, L. Ödberg and L. Wågberg, *Langmuir,* 2011, 27, 11332–11338.

27 A. Olszewska, P. Eronen, L.-S. Johansson, J.-M. Malho, M. Ankerfors, T. Lindström, J. Ruokolainen, J. Laine and M. Österberg, *Cellulose*, 2011, 18, 1213–1226.

28 R. J. Moon, A. Martini, J. Nairn, J. Simonsen and J. Youngblood, *Chem. Soc. Rev.*, 2011, 40, 3941–3994.

29 Y. Habibi, L. A. Lucia and O. J. Rojas, *Chem. Rev.*, 2010, 110, 3479–3500.

30 S. Wang, A. Lu and L. Zhang, *Prog. Polym. Sci.*, 2015.

31 T. Rosenau, A. Potthast, H. Sixta and P. Kosma, *Prog. Polym. Sci.*, 2001, 26, 1763–1837.

32 H.-P. Fink, P. Weigel, H. J. Purz and J. Ganster, *Prog. Polym. Sci.*, 2001, 26, 1473–1524.

33 C. Cuissinat and P. Navard, *Macromol. Symp.*, 2006, 244, 1–18.

34 J. Boucher, C. Chirat and D. Lachenal, *Energy Convers. Manag.*, 2014, 88, 1120–1126.

35 Y. Su, C. Burger, H. Ma, B. Chu and B. S. Hsiao, *Biomacromolecules*, 2015, 16, 1201–1209.

36 Y. Su, C. Burger, B. S. Hsiao and B. Chu, *J. Appl. Crystallogr.*, 2014, 47, 788–798.

37 K. Missoum, M. N. Belgacem and J. Bras, *Materials*, 2013, 6, 1745–1766.

38 T. Saito, T. Uematsu, S. Kimura, T. Enomae and A. Isogai, *Soft Matter*, 2011, 7, 8804–8809.

39 Y. Habibi and A. Dufresne, *Biomacromolecules*, 2008, 9, 1974–1980.

40 S. J. Eichhorn and R. J. Young, *Cellulose*, 2001, 8, 197–207.

41 T. Saito, R. Kuramae, J. Wohlert, L. A. Berglund and A. Isogai, *Biomacromolecules*, 2013, 14, 248–253.

42 I. Sakurada, Y. Nukushina and T. Ito, *J. Polym. Sci.*, 1962, 57, 651–660.

43 S. Iwamoto, W. Kai, A. Isogai and T. Iwata, *Biomacromolecules*, 2009, 10, 2571–2576.

44 S. Neyertz, A. Pizzi, A. Merlin, B. Maigret, D. Brown and X. Deglise, *J. Appl. Polym. Sci.*, 2000, 78, 1939–1946.

45 K. Tashiro and M. Kobayashi, *Polym. Bull.,* 1985, 14, 213–218.

46 T. Gurunathan, S. Mohanty and S. K. Nayak, *Compos. Part Appl. Sci. Manuf.,* 2015, 77, 1–25.

47 K. Niskanen, *Mechanics of Paper Products*, Walter de Gruyter, 2012.

48 O. Faruk, A. K. Bledzki, H.-P. Fink and M. Sain, Prog. *Polym. Sci.*, 2012, 37, 1552–1596.

49 H. Sehaqui, N. Ezekiel Mushi, S. Morimune, M. Salajkova, T. Nishino and L. A. Berglund, *ACS Appl. Mater. Interfaces*, 2012, 4, 1043–1049.

50 R. Bardet, M. N. Belgacem and J. Bras, *Cellulose*, 2013, 20, 3025–3037.

51 H. Sehaqui, M. Salajková, Q. Zhou and L. A. Berglund, *Soft Matter*, 2010, 6, 1824–1832.

52 R. Gavillon and T. Budtova, *Biomacromolecules*, 2008, 9, 269–277.

53 R. Sescousse, R. Gavillon and T. Budtova, *Carbohydr. Polym.,* 2011, 83, 1766–1774.

54 C. Marulier, P. J. J. Dumont, L. Orgéas, S. R. du Roscoat and D. Caillerie, *Cellulose*, 2015, 22, 1517–1539.

55 Y. Kobayashi, T. Saito and A. Isogai, *Angew. Chem.,* 2014, 126, 10562–10565.

56 L. Orgéas, P. J. J. Dumont and L. Nicolais, in *Wiley Encyclopedia of Composites, John Wiley & Sons, Inc.*, 2011.

57 M. M. Schwartz, *Composite Materials Handbook*, 1997.

58 S. G. Advani, Flow and Rheology in *Polymer Composites Manufacturing*, Elsevier, 1994.

59 D. Gay, *Matériaux composites.* : 5e edition, Hermes Science Publications, 2005.

60 M. N. Belgacem and A. Gandini, *Monomers, Polymers and Composites from Renewable Resources*, Elsevier, 2011.

61 D. U. Shah, *J. Mater. Sci.*, 2013, 48, 6083–6107.

62 D. U. Shah, *Mater. Des.*, 2014, 62, 21–31.

63 P. Latil, *Micro-mécanismes de déformation de mèches de fibres saturées*, Thèse de doctorat de l'Université Grenoble Alpes, 2012.

64 L. T. Harper, *Discontinuous carbon fibre composites for automotive applications*, Ph.D. thesis, University of Nottingham 2006.

65 P. Ouagne, D. Soulat, J. Moothoo, E. Capelle and S. Gueret, *Compos. Part Appl. Sci. Manuf.*, 2013, 51, 1–10.

66 P. Ouagne, D. Soulat, C. Tephany, D. Duriatti, S. Allaoui and G. Hivet, *J. Compos. Mater.*, 2013, 47, 3501–3515.

67 P. Dumont, J.-P. Vassal, L. Orgéas, V. Michaud, D. Favier and J.-A. E. Månson, *Rheol. Acta*, 2007, 46, 639–651.

68 L. Orgéas, P. J. J. Dumont, V. Michaud and D. Favier, *Int. J. Mater. Form.*, 2008, 1, 929–932.

69 P.J.J. Dumont, L. Orgéas, M. Hubert, B. Vermeulen, P. Vromant, S. Rolland du Roscoat and J.-F. Bloch, 10th Int. Conf. Process. Compos. Mater. FPCM10, 2010.

70 J. Viguié, P. Latil, L. Orgéas, P. J. J. Dumont, S. Rolland du Roscoat, J.-F. Bloch, C. Marulier and O. Guiraud, *Compos. Sci. Technol.*, 2013, 89, 202–210.

71 O. Guiraud, L. Orgéas, P. J. J. Dumont and S. R. du Roscoat, *J. Rheol.*, 2012, 56, 5 93–623.

72 P.J.J. Dumont and J. Viguié, *Compos. Part. A*, 2015 (submitted).

73 D. U. Shah, P. J. Schubel and M. J. Clifford, *Compos. Part B Eng.*, 2013, 52, 172–181.

74 M. D. H. Beg and K. L. Pickering, *Compos. Part Appl. Sci. Manuf.*, 2008, 39, 1748–1755.

75 M. N. Belgacem and A. Gandini, *Compos. Interfaces*, 2005, 12, 41–75.

76 M. Abdelmouleh, S. Boufi, M. N. Belgacem and A. Dufresne, *Compos. Sci. Technol.*, 2007, 67, 1627–1639.

77 B. Ly, W. Thielemans, A. Dufresne, D. Chaussy and M. N. Belgacem, *Compos. Sci. Technol.*, 2008, 68, 3193–3201.

78 A. Gandini and M. N. Belgacem, *Springer Berlin Heidelberg*, 2015, pp. 1–38.

79 N. C. Stinga, *Utilisation de la chimie chromatogénique pour la conception et la réalisation de matériaux cellulosiques barrières à l'eau, aux graisses et aux gaz*, Thèse de doctorat de l'Université Grenoble Alpes, 2008.

80 M. N. Belgacem, P. Bataille and S. Sapieha, *J. Appl. Polym. Sci.*, 1994, 53, 379–385.

81 K. Missoum, J. Bras and M. N. Belgacem, *Cellulose*, 2012, 19, 1957–1973.

82 A. Bourmaud, C. Morvan and C. Baley, *Ind. Crops Prod.*, 2010, 32, 662–667.

83 K. Charlet, J. P. Jernot, M. Gomina, J. Bréard, C. Morvan and C. Baley, *Compos. Sci. Technol.*, 2009, 69, 1399–1403.

84 G. Coroller, A. Lefeuvre, A. Le Duigou, A. Bourmaud, G. Ausias, T. Gaudry and C. Baley, *Compos. Part Appl. Sci. Manuf.*, 2013, 51, 62–70.

85 N. L. Moigne, M. van den Oever and T. Budtova, *Compos. Part Appl. Sci. Manuf.*, 2011, 42, 1542–1550.

86 C. Grande and F. G. Torres, *Adv. Polym. Technol.*, 2005, 24, 145–156.

87 K. Okubo, T. Fujii and E. T. Thostenson, *Compos. Part Appl. Sci. Manuf.*, 2009, 40, 469–475.

88 M. H. Gabr, M. A. Elrahman, K. Okubo and T. Fujii, *Compos. Part Appl. Sci. Manuf.*, 2010, 41, 1263–1271.

89 M. H. Gabr, M. A. Elrahman, K. Okubo and T. Fujii, *Compos. Struct.*, 2010, 92, 1999–2006.

90 E. T. Thostenson, W. Z. Li, D. Z. Wang, Z. F. Ren and T. W. Chou, *J. Appl. Phys.*, 2002, 91, 6034–6037.

91 E. Bekyarova, E. T. Thostenson, A. Yu, H. Kim, J. Gao, J. Tang, H. T. Hahn, T.-W. Chou, M. E. Itkis and R. C. Haddon, *Langmuir*, 2007, 23, 3970–3974.

92 M. Kim, Y.-B. Park, O. I. Okoli and C. Zhang, *Compos. Sci. Technol.*, 2009, 69, 335–342.

93 H. Sehaqui, Q. Zhou and L. A. Berglund, *Soft Matter*, 2011, 7, 7342–7350.

94 V. Favier, H. Chanzy and J. Y. Cavaille, *Macromolecules*, 1995, 28, 6365–6367.

95 L. Heux, G. Chauve and C. Bonini, *Langmuir*, 2000, 16, 8210–8212.

96 I. Kvien, B. S. Tanem and K. Oksman, *Biomacromolecules*, 2005, 6, 3160–3165.

97 A. J. Benítez, J. Torres-Rendon, M. Poutanen and A. Walther, *Biomacromolecules*, 2013, 14, 4497–4506.

98 C. Aulin, G. Salazar-Alvarez and T. Lindström, *Nanoscale*, 2012, 4, 6622–6628.

99 F. Dalmas, J.-Y. Cavaillé, C. Gauthier, L. Chazeau and R. Dendievel, *Compos. Sci. Technol.*, 2007, 67, 829–839.

100 M. Pereda, N. E. Kissi and A. Dufresne, *ACS Appl. Mater. Interfaces*, 2014, 6, 9365–9375.

101 A. N. Nakagaito, A. Fujimura, T. Sakai, Y. Hama and H. Yano, *Compos. Sci. Technol.*, 2009, 69, 1293–1297.

102 M. Henriksson, L. A. Berglund, P. Isaksson, T. Lindström and T. Nishino, *Biomacromolecules*, 2008, 9, 1579–1585.

103 K. Dimic-Misic, A. Puisto, P. Gane, K. Nieminen, M. Alava, J. Paltakari and T. Maloney, *Cellulose*, 2013, 20, 2847–2861.

104 K. M. O. Håkansson, A. B. Fall, F. Lundell, S. Yu, C. Krywka, S. V. Roth, G. Santoro, M. Kvick, L. Prahl Wittberg, L. Wågberg and L. D. Söderberg, *Nat. Commun.*, 2014, 5, 4018.

105 A. Walther, J. V. I. Timonen, I. Díez, A. Laukkanen and O. Ikkala, *Adv. Mater.*, 2011, 23, 2924–2928.

106 N. Lavoine, I. Desloges, B. Manship and J. Bras, *J. Food Sci. Technol.*, 2015, 52, 5590–5600.

107 M. Mohtaschemi, K. Dimic-Misic, A. Puisto, M. Korhonen, T. Maloney, J. Paltakari and M. J. Alava, *Cellulose*, 2014, 21, 1305–1312.

108 M. Iotti, Ø. W. Gregersen, S. Moe and M. Lenes, *J. Polym. Environ.*, 2010, 19, 137–145.

109 E. Lasseuguette, D. Roux and Y. Nishiyama, *Cellulose*, 2007, 15, 425–433.

110 E. Saarikoski, T. Saarinen, J. Salmela and J. Seppälä, *Cellulose*, 2012, 19, 647–659.

111 A. Karppinen, T. Saarinen, J. Salmela, A. Laukkanen, M. Nuopponen and J. Seppälä, *Cellulose*, 2012, 19, 1807–1819.

112 T. Saarinen, S. Haavisto, A. Sorvari, J. Salmela and J. Seppälä, *Cellulose*, 2014, 21, 1261–1275.

113 A. W. K. Ma, M. R. Mackley and F. Chinesta, *Int. J. Mater. Form.*, 2008, 1, 75–81.

114 A. W. K. Ma, F. Chinesta and M. R. Mackley, *J. Rheol.*, 2009, 53, 547–573.

115 J. Mewis and N. J. Wagner, *Colloidal Suspension Rheology*, Cambridge University Press, 2012.

116 W.B. Russel, D.A. Saville, W.R. Schowalter, *Colloidal Dispersions*, Cambridge University Press, 1992.

117 T. Zimmerman, E. Pohler and P. Schwaller, *Adv Eng Mater*, 2005, 7, 1156–1161.

118 V. Favier, J. Y. Cavaille, G. R. Canova and S. C. Shrivastava, *Polym. Eng. Sci.*, 1997, 37, 1732–1739.

119 V. Favier, R. Dendievel, G. Canova, J. Y. Cavaille and P. Gilormini, *Acta Mater.*, 1997, 45, 1557–1565.

120 K.-Y. Lee, Y. Aitomäki, L. A. Berglund, K. Oksman and A. Bismarck, *Compos. Sci. Technol.*, 2014, 105, 15–27.

121 J. G. Torres-Rendon, F. H. Schacher, S. Ifuku and A. Walther, *Biomacromolecules*, 2014, 15, 2709–2717.

122 H. L. Cox, *Br. J. Appl. Phys.*, 1952, 3, 72–79.

123 C. L. Tucker III and E. Liang, *Compos. Sci. Technol.*, 1999, 59, 655–671.

124 A. Kulachenko, T. Denoyelle, S. Galland and S. B. Lindström, *Cellulose*, 2012, 19, 793–807.

125 L. J. Gibson and M. F. Ashby, *Cellular Solids: Structure and Properties*, Cambridge University Press, 1997.

126 N. Mills, *Polymer Foams Handbook: Engineering and Biomechanics Applications and Design Guide*, Butterworth-Heinemann, 2007.

127 M. Zhang, Y. H. Zhou, X. H. Yang and L. H. Hu, *Adv. Mater. Res.*, 2011, 250-253, 974–979.

128 X. Luo, A. Mohanty and M. Misra, *Ind. Crops Prod.*, 2013, 47, 13–19.

129 S. T. Lee, L. Kareko and J. Jun, *J. Cell. Plast.*, 2008, 44, 293–305.

130 C. A. Cateto, M. F. Barreiro, A. E. Rodrigues and M. N. Belgacem, *Ind. Eng. Chem. Res.*, 2009, 48, 2583–2589.

131 S. Laurichesse and L. Avérous, *Prog. Polym. Sci.*, 2014, 39, 1266–1290.

132 G. Tondi and A. Pizzi, *Ind. Crops Prod.*, 2009, 29, 356–363.

133 Z. M. Ali and L. J. Gibson, *Soft Matter*, 2013, 9, 1580–1588.

134 A. E. Donius, A. Liu, L. A. Berglund and U. G. K. Wegst, *J. Mech. Behav. Biomed. Mater.*, 2014, 37, 88–99.

135 G. Pour, C. Beauger, A. Rigacci and T. Budtova, *J. Mater. Sci.*, 2015, 50, 4526–4535.

136 H. Sehaqui, Q. Zhou and L. A. Berglund, *Compos. Sci. Technol.*, 2011, 71, 1593–1599.

137 J. G. Day and G. Stacey, *Cryopreservation and Freeze-Drying Protocols*, Springer Science & Business Media, 2007.

138 S. Deville, *Materials*, 2010, 3, 1913–1927.

139 S. Deville, *J. Mater. Res.*, 2013, 28, 2202–2219.

140 R. Sescousse, *Nouveau matériaux cellulosiques ultra-poreux et leurs carbones à partir de solvants verts*, Thèse de doctorat Mines ParisTech, 2010.

141 N. T. Cervin, L. Andersson, J. B. S. Ng, P. Olin, L. Bergström and L. Wågberg, *Biomacromolecules*, 2013, 14, 503–511.

142 J. Han, C. Zhou, Y. Wu, F. Liu and Q. Wu, *Biomacromolecules*, 2013, 14, 1529–1540.

143 Y. Habibi and L. A. Lucia, *Polysaccharide Building Blocks: A Sustainable Approach to the Development of Renewable Biomaterials*, John Wiley & Sons, 2012.

144 A. Demilecamps, C. Beauger, C. Hildenbrand, A. Rigacci and T. Budtova, *Carbohydr. Polym.*, 2015, 122, 293–300.

Chapitre 2

Heterogeneous flow kinematics of cellulose nanofibril suspensions under shear

Ce chapitre est basé sur un article paru en 2015, F. Martoïa, C. Perge, P.J.J. Dumont, L. Orgéas, M.-A. Fardin, S. Manneville, M.N. Belgacem, « Heterogeneous flow kinematics of cellulose nanofibril suspensions under shear », *Soft Matter*, vol. 11, p. 4742-4755.

Abstract

The rheology of NFC suspensions that exhibited different microstructures and colloidal stability, namely TEMPO-oxidized and enzymatic NFC suspensions, were investigated at the macro and mesoscales using a transparent Couette rheometer combined with optical observations and ultrasonic speckle velocimetry (USV). Both NFC suspensions showed a complex rheology, which was typical of yield stress, non-linear and thixotropic fluids. Hysteresis loops and erratic evolutions of the macroscale shear stress were also observed, thereby suggesting important mesostructural changes and/or inhomogeneous flow conditions. The *in situ* optical observations revealed drastic mesostructural changes for the enzymatic NFC suspensions, whereas the TEMPO-oxidized NFC suspensions did not exhibit mesoscale heterogeneities. However, for both suspensions, USV measurements showed that the flow was heterogeneous and exhibited complex situations with the coexistence of multiples flow bands, wall slippage and possibly multidimensional effects. Using USV measurements, we also showed that the fluidization of these suspensions could presumably be attributed to a progressive and spatially heterogeneous transition from a solid-like to a liquid-like behavior. As the shear rate was increased, the multiple coexisting shear bands progressively enlarged and nearly completely spanned over the rheometer gap, whereas the plug-like flow bands were eroded.

2.1 Introduction

Cellulose nanofibrils (NFCs) are the main reinforcing constituents of plant cell walls. They can be extracted from cellulosic fibers by mechanical and/or chemical processing routes in the form of aqueous colloidal suspensions. Because of their intrinsic outstanding mechanical properties[1,2,3] (Young's Modulus $E \approx$ 80-100 GPa and ultimate tensile stress $\sigma \approx$ 1-3 GPa) and their reactive surface chemistry, NFCs constitute attractive renewable nanoscale fibrous reinforcements for several applications. They can be used in cosmetics as gelling agents or in papermaking industry as coating to reinforce or to functionalize substrates[4] or even as transparent films/nanopapers for packaging[5,6]. They are also used as slender nano-reinforcements in polymer matrix composites[7,8] that have been in development in the last ten years. Understanding the rheology of NFC suspensions is crucial either to fully exploit the end-use properties or to optimize the forming processes of the aforementioned materials, and more precisely the placement of the nanoscale fibrous reinforcements[9].

To reduce energy demand during the NFC extraction processes and to make these processes more environmentally friendly, enzymatic or oxidation pre-treatments are used prior to mechanical treatments. Enzymatic treatment[10,11] consists of a mild hydrolysis of cellulosic fibers, whereas TEMPO oxidation[12,13,14] is a chemical modification of hydroxyl groups (-OH) at the surface of the microfibrils into carboxylate ones ($-COO^-$). Depending on the extraction processes, the morphology as well as the physico-chemical surface properties of NFCs are different. NFC suspensions produced by mechanical disintegration with or without enzymatic pretreatment are polydisperse suspensions[15,16], *i.e.*, they contain both microscale elements such as partially fibrillated cellulose fibers but also nanoscale elements in the form of elementary fibrils or bundles of fibrils with a diameter that ranges between 5 and 100 nm and a length that ranges between 1 and 10 µm[17]. Because of the low surface charge of the native extracted cellulose nanofibrils (zeta potential $\xi = -15$ mV), mechanical and enzymatic NFC suspensions often exhibit flocs whose size ranges between 50 µm and 1000 µm and displays opaque textures even at very low NFC concentrations[18,19]. TEMPO-oxidized NFC suspensions are less polydisperse suspensions[13,20] and contain few fibril bundles and mostly individualized fibrils having a diameter ranging from 3 to 6 nm and a length from 1 to 2 µm. These suspensions are commonly much more transparent and are not flocculated because of their more homogenous structures that contain small highly charged slender nanoparticles ($\xi = -15$ mV)[13].

Regardless of the extraction routes, the rheology of NFC suspensions is complex, poorly characterized and still not well understood and modeled, which limits the use of NFCs. At the macroscale, *i.e.,* at the rheometer scale, mechanical, enzymatic or TEMPO-oxidized NFC suspensions are commonly regarded as thixotropic yield stress fluids[21]. These suspensions exhibit a macroscale yield stress $\bar{\tau}_0$ at low macroscale shear rates ($0.001\ s^{-1} \leq \bar{\dot{\gamma}} \leq 0.1\ s^{-1}$) and a shear thinning behavior at higher shear rates[22,23,24] ($10\ s^{-1} \leq \bar{\dot{\gamma}} \leq 1000\ s^{-1}$). In addition, at intermediate shear rates ($0.1\ s^{-1} \leq \bar{\dot{\gamma}} \leq 10\ s^{-1}$) several studies[24,18,25,26] reported macroscale rheograms $\bar{\tau}(\bar{\dot{\gamma}})$ with the presence of hysteresis regions with shear stress plateaus. At the mesoscale,

i.e., at sizes above or of the order of the representative volume of the suspensions, *i.e.*, approximately five to ten NFC lengths, the rheology is complex and strongly affected by the extraction process[27]. By investigating the shear rheology of enzymatic suspensions with a combination of a rotational dynamic rheometer and digital imaging techniques, several authors[18,25] reported the presence of flocculated structures in enzymatic NFC suspensions. The complex aggregation-disaggregation kinetics of flocs was correlated with the complex macroscale rheograms recorded at intermediate and high shear rates. Surprisingly, the rheology of TEMPO-oxidized NFC suspensions for which NFCs are electrostatically stabilized by the presence of carboxylate groups at their surface, has been less investigated. The shear rheology of these suspensions was mainly studied in "stationary state" and in a narrow shear rate range[23,28].

Although this point has not yet been deeply discussed in the literature[19,21,29,30], the complex macroscale shear rheology of NFC suspensions may be related to rheometry problems that are often reported while shearing other yield stress fluids[31,32,33,34,35]: wall slippage resulting from the geometric characteristics of rheometers (*e.g.* with non-ideal boundary conditions), mesoscale flow heterogeneities such as shear strain localization, shear banding or other material heterogeneities such as migration–segregation. For example, when subjected to shear flow, soft glassy materials (clay suspensions, concentrated emulsions, colloidal gels) exhibit a variety of complex rheological behaviors because the applied shear strain may disrupt and rearrange the microstructure over a wide range of spatial and temporal scales leading to heterogeneous flow properties[34,36,37]. More particularly, in thixotropic yield stress fluids such as in colloidal suspensions, the coexistence of two phenomena in competition, *i.e.*, a shear-induced rejuvenation or destructuration and an aging-induced restructuration, leads to heterogeneous flows such as shear banding. All the aforementioned problems hinder proper assessment of the "true" rheology, and are often the source of complex macroscale rheograms, showing for example the presence of stress minimum in flow curves[38] or complex hysteresis loops[39,40] when measurements are performed by sweeping up then down (or vice versa) the apparent shear rate. It is also important to note that in the case of semi-flexible slender fiber suspensions as for example in carbon nanotube suspensions[41] or even in non-colloidal glass fiber suspensions[42], the flow may reorient and deform (bend, stretch the particles, which also leads to complex flow properties.

To overcome the aforementioned rheometry difficulties, proper rheometry techniques have to be used. For instance, the use of rheometers coupled with 2D surface and bulk visualization setups[25,38] (transparent measuring cell) enables a link between complex macroscale rheology and mesoscale heterogeneous flows to be experimentally established. However, even if these techniques are extremely informative, they cannot provide local velocity measurements, so that the "true" rheology of the material cannot be precisely estimated from the global rheological data.

To better understand the local flow behavior of many complex fluids, several rheometry setups dedicated to local velocity measurements have recently emerged[32]. A first approach, the so called Particle Imaging Velocimetry[43] (PIV) consists of adding particles to the investigated fluid and measuring their displacements using optical microscopy or laser sheet techniques. Unfortunately, these techniques can only be used for transparent fluids. Other advanced rheometry setups based on Magnetic Resonance Imaging[44,41,45] (MRI) or high frequency Ultrasonic Speckle Velocimetry[46,47] (USV) enable space and time-resolved velocity profiles to be measured for a wide range of fluids. In addition, rheometry setups based on scattered-radiation methods[48] (Small Angle X-rays Scattering SAXS, Small Angle Neutron Scattering SANS, Static Light Scattering SLS) can provide a multiscale space and time-resolved description of the structure of the sheared materials. Note that none of the aforementioned techniques has already been used to study the rheology of NFCs.

Thus, the objectives of this study were (i) to experimentally investigate the shear rheology of colloidal enzymatic and TEMPO-oxidized NFC water suspensions, (ii) to describe the temporal and spatial heterogeneities that were encountered during rheological testing, and (iii) to outline the potential mesostructural and microstructural origins of the observed flow phenomena.
Bearing in mind the aforementioned difficulties, two types of techniques were used to investigate the rheology of these suspensions while sweeping down and then up the applied macroscopic shear rate, and *vice versa.* First, a transparent Couette rheometer enabled potential flow-induced mesostructural changes to be observed. In addition, the use of an ultrasonic speckle velocimetry (USV) setup enabled a two-dimensional time-resolved characterization of the mesoscale flow of the considered suspensions, *i.e.*, the evolution of the local velocity field within the Couette cell.

2.2 Materials and experimental procedure

2.2.1 Extraction of NFCs

Enzymatic and TEMPO-oxidized NFCs were extracted from a commercial bleached eucalyptus kraft pulp (Celbi, Portugal) following the two extraction routes shown in Figure 2-1. The used bleached eucalyptus fibers had a mean diameter of 25 µm and a mean length of 600 µm. For the enzymatic NFCs, fibers in water suspension (1.7 $wt\%$) were first refined using a Valley beater for 6 h and then hydrolyzed in mild conditions by adding 20 mg of enzymes per gram of fibers (Celluclast ATCC 26921, Sigma-Aldrich, France). The ensuing suspension was then maintained at pH 5 using a 0.8 M acetate buffer solution at a temperature of 50°C for 2 h. In the case of the TEMPO treatment, fibers were first oxidized by the addition of 5 mmol of NaClO per gram of fibers in presence of TEMPO (0.1 mmol per gram of fibers) and NaBr (1mmol per gram of fibers) catalysts at pH 10 for 3 h. To remove all chemicals, enzyme and TEMPO treated fibers were then centrifuged three times at 10,000 rpm for 10 min and redispersed three times using a homogenizer (Ultra Turrax T65, IKA, France) at 10,000 rpm for

30 s. Suspensions were at pH ranging from 7 to 8 after this operation and were then fibrillated 70 times through a grinder (model MKCA6-2, disk model MKGA6-80#, Masuko Sangyo Co. Ltd, Japan) revolving at a rotation speed of 2500 rpm and with a clearance gauge of 0.

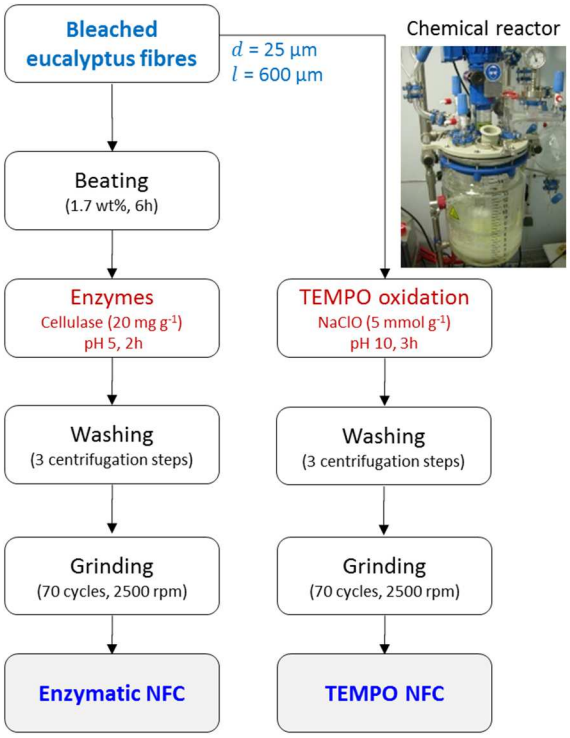

Figure 2-1. Simplified scheme of the two extraction routes used for obtaining enzymatic and TEMPO-oxidized NFC suspensions.

2.2.2 Morphology of processed NFCs

The morphology of NFCs was investigated using an optical microscope (Axio imager M1m, Zeiss) and an atomic force microscope (AFM, Nanoscope III, Veeco, Canada). The qualitative study of the microstructure revealed that enzymatic NFC suspensions were polydisperse suspensions containing (i) partially fibrillated eucalyptus fibers (diameter ≈ 20 µm and length ≈ 250 µm, Fig. 2-1.a), (ii) bundles of fibrils having a diameter ranging between 100 and 500 nm, and (iii) nanoscale elements in the form of individualized fibrils with a diameter ranging from 20 to 50 nm.

The isolated NFCs shown in Figure 2-2.b had lengths that ranged between 1 and 10 µm. However, note that a more precise determination of the length distribution of these very polydisperse suspensions still remains a challenging problem. In contrast, TEMPO-oxidized NFC suspensions were much less polydisperse, as they contained few fibers close to their original dimensions (Fig. 2-2.d) and very small slender individualized fibrils with a diameter and length ranging between 3 and 6 nm and between1 and 1.5 µm, respectively (Fig. 2-2.e,f). The content of carboxyl groups (-COOH) Γ_{NFC} determined by conductimetric titration was was 0.05 mmol $g^{-1}$for enzymatic NFC (close to the value obtained for bleached eucalyptus fibers), whereas this content was 1.45 mmol g^{-1} for NFC obtained after TEMPO-mediated

oxidation. Thus, TEMPO-oxidized NFCs were much more electrically charged and stable in water suspension.

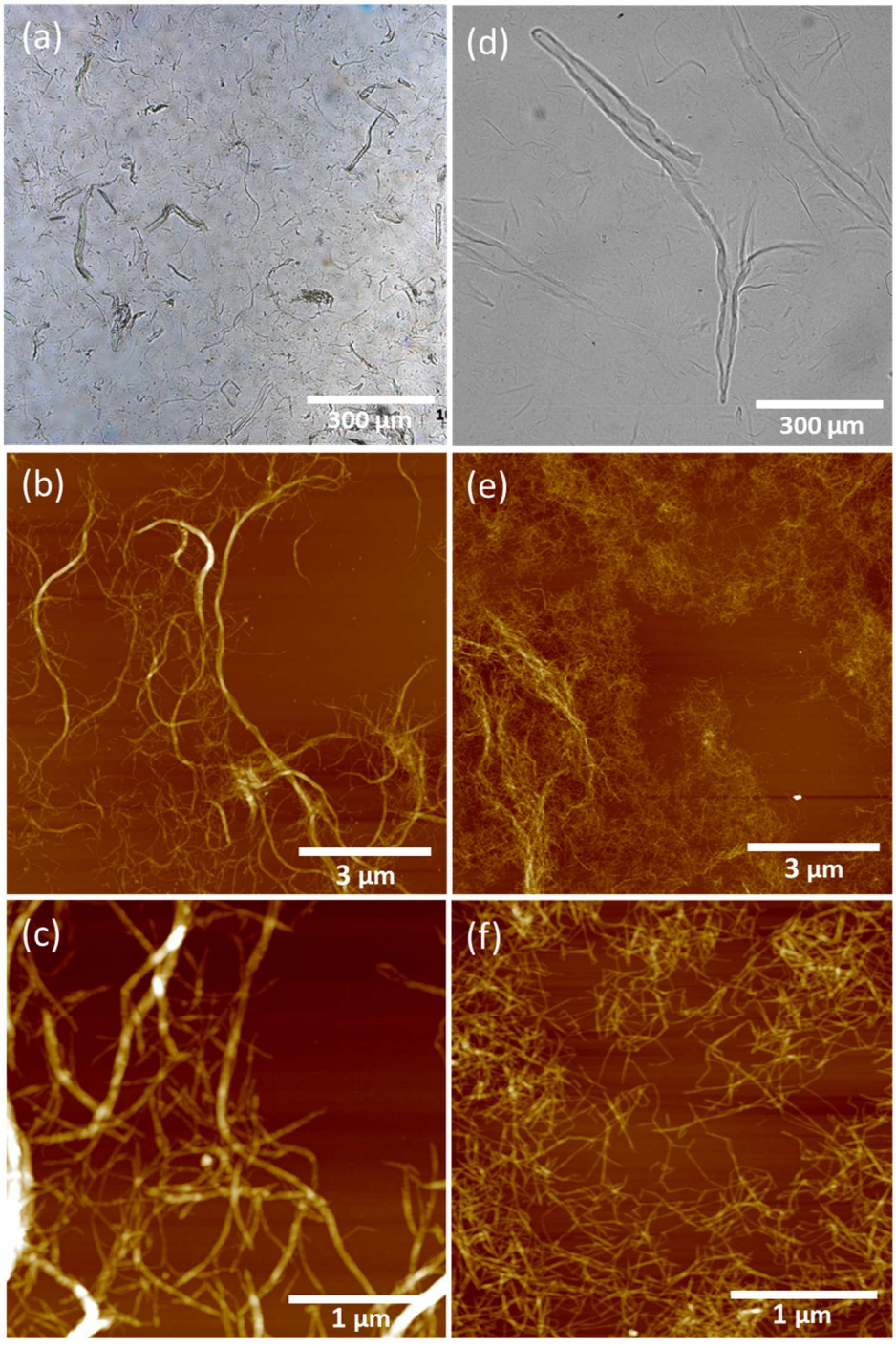

Figure 2-2. Light optical micrographs of (a) enzymatic NFCs and (d) TEMPO-oxidized NFCs in suspension at 0.1 *wt*%. AFM micrographs of (b,c) enzymatic NFC films, and (e,f) TEMPO-oxidized NFC films obtained after drying the suspensions diluted at 0.001 *wt*%.

2.2.3 Rheometry

2.2.3.1 Taylor-Couette rheometry

The rheology of NFC suspensions was first studied using a stress-controlled rheometer (ARG2, TA Instruments) equipped with a transparent Taylor-Couette cell of height $H = 60$ mm (inner polished PEEK rotating cylinder of radius $R_1 = 23$ mm, fixed sand-blasted PMMA stator of radius $R_2 = 25$ mm, gap $e = R_2 - R_1 = 2$ mm), which enabled potential macro and mesoscale flocs or flow heterogeneities to be observed while shearing the NFC suspensions. The photographs were taken every 5 s using a 36.2 megapixels camera (Nikon D800) equipped with a 100 mm macro lens, the observed zone being illuminated with two LED light sources positioned at $+/-90°$. All the measurements were performed at 20°C using suspensions that were pre-sheared at 1000 s^{-1} for 60 s. A solvent trap was also systematically used to prevent water evaporation.

From the imposed rotor rotation velocity Ω around the $\mathbf{e}_z$-direction and the measured reaction torque Γ, and assuming a homogeneous flow in a gap e sufficiently small compared to R_1, the rheograms showing the macroscale shear stress:

$$\bar{\tau} = \frac{R_1^2+R_2^2}{4\pi H R_1^2 R_2^2}\,\Gamma. \tag{1}$$

as a function of the macroscale shear rate $\bar{\dot{\gamma}}$:

$$\bar{\dot{\gamma}} = \frac{R_1^2+R_2^2}{R_2^2-R_1^2}\,\Omega \tag{2}$$

were obtained by decreasing $\bar{\dot{\gamma}}$ from 1000 to 0.001 s^{-1} in 45 logarithmically-spaced steps of duration $\delta t = 50$ s and then by increasing $\bar{\dot{\gamma}}$ over the same range, and *vice versa*.

2.2.3.2 Ultrasonic speckle velocimetry (USV) rheometry

Rheo-ultrasonic velocimetry (rheo-USV) measurements were performed using the same measuring Taylor-Couette cell which was immersed in a large water tank (total volume 2.2 l) connected to a water bath thermostat (230-CCNR Huber Ministat) maintaining a test temperature of 20°C and providing proper acoustic coupling with a fair impedance matching between the sample contained in the cell and the ultrasonic transducer array (Fig. 2-3). A detailed explanation of the rheo-USV setup is given elsewhere[46]. In short, the heterogeneous structure of the NFC suspensions under study scatters high-frequency ultrasound (15 MHz in the present case) efficiently enough to allow for ultrasonic images to be recorded with a custom-made ultrafast scanner[46]. Velocity maps within a vertical cross-section of the Taylor-Couette cell are obtained by cross-correlating successive ultrasonic images of the NFC suspensions.

More precisely, as sketched in Figure 2-3, our rheo-ultrasonic setup enables the projection $v_y(x,y,z,t)$ of the velocity vector $\mathbf{v}(\mathbf{x},\mathrm{t}) = v_x\mathbf{e}_x + v_y\mathbf{e}_y + v_z\mathbf{e}_z = v_r\mathbf{e}_r + v_\theta\mathbf{e}_\theta + v_z\mathbf{e}_z$ of mesoscale points flowing at a position $\mathbf{x} = x\mathbf{e}_x + y\mathbf{e}_y + z\mathbf{e}_z = r\mathbf{e}_r + z\mathbf{e}_z$ to be recorded along the ultrasonic

propagation direction $\mathbf{e}_y$ over a region of interest (centered in the total height H of the cell) which had a height $h = 32$ mm, a width $e' \approx e = 2$ mm and a thickness $t = 300$ µm, simultaneously with macroscopic rheological data. In the following sections, the time-space velocity maps have a spatial resolution of 70 µm along r and of 250 µm along z as well as a time resolution of 0.5 s. By noting $\varphi = (\widehat{\mathbf{e}_r, \mathbf{e}_y})$ the inclination angle of the ultrasonic transmitters-receivers with respect to the mean radial direction of the region of interest ($\varphi = 5°$, see Gallot et al.[46] for the calibration procedure), v_y can be expressed as a function of the radial v_r and orthoradial v_θ components of $\mathbf{v}$ as follows (Fig. 2-3):

$$v_y = v_r \cos\varphi + v_\theta \sin\varphi \ . \tag{3}$$

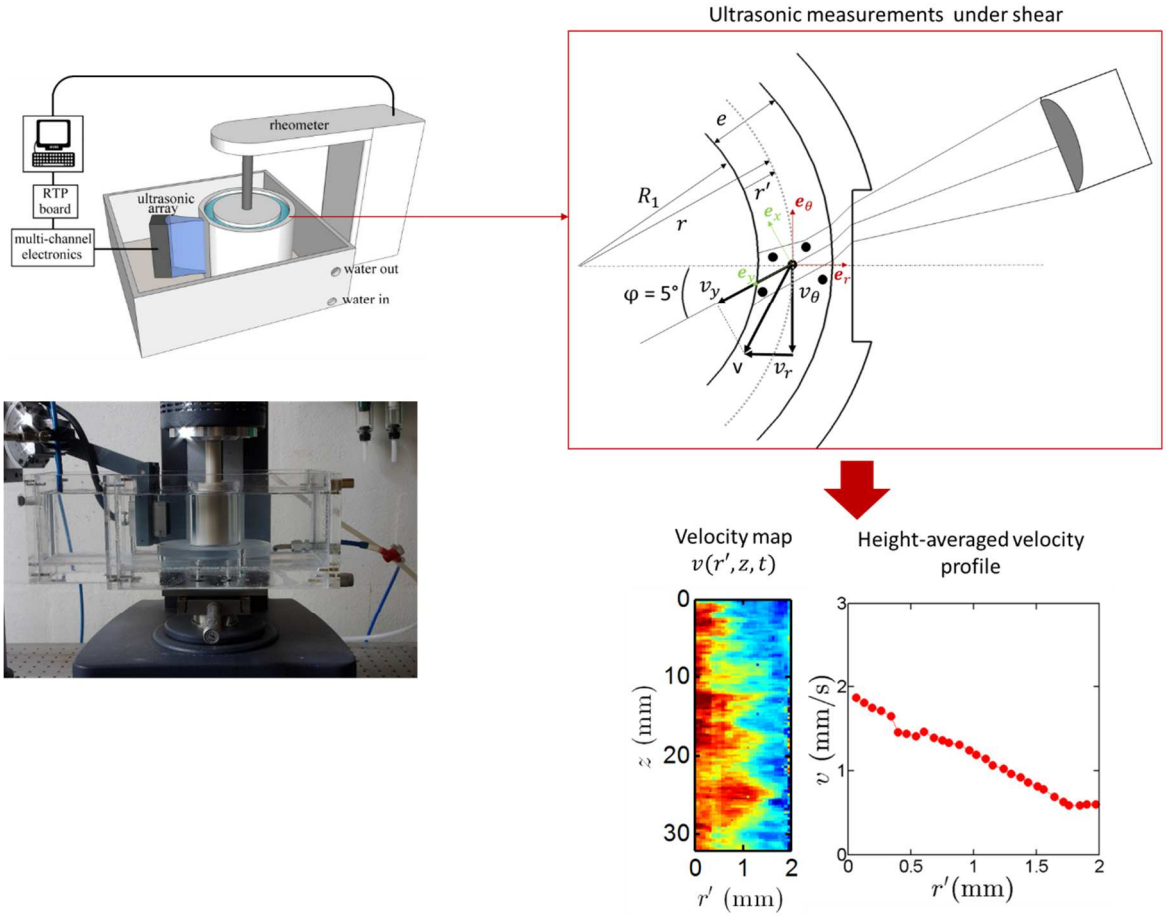

Figure 2-3. Schematic presentation of the ultrafast ultrasonic speckle velocimetry (USV) setup from the Taylor-Couette cell used (top left) to the velocity map $v(r', z, t)$ given in Equation (4) and the height-averaged velocity profile obtained during the shear test (bottom right). Note also that in this sketch, the rotor is located at $r' = 0$ mm and the stator at $r' = 2$ mm.

The use of a small incident angle φ and a narrow gap e lead to a low variation of the θ angle across the ultrasonic propagation direction $\mathbf{e}_y$ (Fig. 2-3), so that, all the velocity profiles presented in this study mainly correspond to the velocity $v(r', z)$ calculated from the ratio $\frac{v_y(y,z)}{\sin\varphi}$ as follows:

$$v(r', z) = \frac{v_y(y,z)}{\sin\varphi} \simeq v_\theta(r', z) + \frac{v_r(r', z)}{\tan\varphi}. \tag{4}$$

It is worth noting that in these conditions, the use of the USV technique does not allow the orthoradial component v_θ to be measured independently from the radial component v_r, and do not provide any information on the presence of a vertical component v_z in the vorticity direction. However, the information gathered by this technique, *i.e.*, the velocity maps and profiles (Fig. 2-3), and their temporal evolution are very informative and provide a powerful framework for understanding the flow kinematics of complex fluids:

(i) The velocity maps, as those shown in Figure 2-3, provide useful information on the dependence of the velocity v along the vorticity direction $\mathbf{e}_z$. These maps are very useful for (i) assessing the presence of multi-dimensional flows arising, for example, from hydrodynamic or elastic instabilities, and (ii) studying their kinematics under shear[46,49].

(ii) The use of the height-averaged velocity profiles enable the existence of multiple flow regimes along the gap to be detected. The transition from a flow band to another is generally accompanied by a pronounced slope change in the velocity profile[50].

(iii) Note also that at the vicinity of the rotor and stator respectively, the contribution of the radial component v_r in eqn (4) vanishes, so that v is equal to the orthoradial velocity v_θ. This enables wall slippage to be assessed.

For information, the experimental velocity profiles were systematically compared with theoretical velocity profiles $v_{th}(r)$ obtained for a Newtonian fluid under no slip and purely orthoradial flow conditions. At a given macroscopic shear rate $\bar{\dot{\gamma}}$ (*i.e.*, at an imposed rotor rotation velocity Ω), $v_{th}(r)$ is defined as follows:

$$v_{th}(r) = \Omega(1+\tfrac{r}{R_1})\left[\frac{\left(\frac{R_2}{R_1+r}\right)^2-1}{\left(\frac{R_2}{R_1}\right)^2-1}\right] \simeq \Omega(1-\tfrac{r}{R_2}). \qquad (5)$$

2.3 Results and discussion

2.3.1 Macroscale rheology coupled with optical flow visualization

The macroscale rheograms obtained for enzymatic and TEMPO-oxidized NFC suspensions were complex and very sensitive to the experimental procedure. In Figures 2-4 and 2-5, the macroscale rheograms obtained for the enzymatic and TEMPO-oxidized NFC suspensions showed that these two suspensions behaved as thixotropic yield stress fluids. These suspensions exhibited a pronounced shear-thinning behavior at high shear rates ($50\ s^{-1} < \bar{\dot{\gamma}} < 1000\ s^{-1}$). In this regime, the stress $\bar{\tau}$ was a power-law function of the applied shear rate $\bar{\dot{\gamma}}$, *i.e.*, $\bar{\tau} \propto \bar{\dot{\gamma}}^n$, with a macroscale power-law exponent n below 1 ($n = 0.29$ and 0.28 for the enzymatic and TEMPO-oxidized suspensions shown in Figure 2-4 and Figure 2-5, respectively), whereas the suspensions exhibited an apparent yield stress $\bar{\tau}_0$ at low shear rates ($0.001\ s^{-1} < \bar{\dot{\gamma}} < 0.1\ s^{-1}$). For both types of suspensions, the flow curves obtained by sweeping up then down the shear rate $\bar{\dot{\gamma}}$ (Figures 2-4.a and 2-5.a) were much more erratic and did not superimpose, particularly at low and intermediate shear rates ($0.001\ s^{-1} < \bar{\dot{\gamma}} < 10\ s^{-1}$). On the contrary, the flow curves obtained for sweeping down then up testing conditions (Fig. 2-4.b and Fig. 2-5.b) systematically displayed closed hysteresis loops within intermediate shear rates ($1\ s^{-1} < \bar{\dot{\gamma}} < 10\ s^{-1}$) for enzymatic NFC suspensions and ($0.01\ s^{-1} < \bar{\dot{\gamma}} < 0.1\ s^{-1}$) for TEMPO-oxidized NFC suspensions), but were superimposed both at very low and high shear rates. Note also that the flow curves displayed several sudden drastic slope changes both during the upward and downward sweeps for all suspensions and testing conditions.

Some of the 2D mesoscale optical observations of the suspensions that were obtained simultaneously to rheological measurements are vizualized in Figures 2-4 and 2-5. In particular, Figure 2-4 showed that enzymatic NFC suspensions exhibited complex flocculated mesostructures. The evolution of these mesostructures could be related to some of the aforementioned complex variations of the flow curve. At low applied shear rates ($0.001\ s^{-1} < \bar{\dot{\gamma}} < 1\ s^{-1}$), the obtained mesostructures were dependent on the sweeping direction. Indeed, for sweeping up then down testing conditions (Fig. 2-4.a), the suspensions exhibited textures in the form of individual flocs ($<$ 100 µm, Fig. 2-4.a) during the upward sweep and textures in the form of floc chains ($\simeq 100 - 300$ µm) during the downward sweep. These considerable mesostructural changes could explain the differences in yield stress levels that were recorded on the macroscopic flow curves. However, for sweeping down then up testing conditions (Fig. 2-4.b) the suspensions displayed the same type of mesostructures both during the upward and downward sweeps. Within the intermediate shear rates ($1\ s^{-1} < \bar{\dot{\gamma}} < 10\ s^{-1}$) and for all testing conditions, the viscosity plateaus were linked to drastic mesostructural changes. As previously reported by Saarikoski *et al.*[25] and Karppinen *et al.*[18] for enzymatic NFC suspensions or by Björkman[51] for pulp fiber suspensions, within this shear rates range the flow of the suspension in the gap was very complex: large clusters of flocs in the form of rolls and regions or voids free of fibers appeared. It is also important to note that in these conditions, any analysis of the macroscale

rheograms in terms of continuous mechanisms should be considered cautiously because the size of the suspension heterogeneities can be of the same order of magnitude as the thickness of the sheared fluid. In the shear thinning branch of the flow curves ($10\ s^{-1} < \bar{\dot{\gamma}} < 1000\ s^{-1}$), floc chains were totally disaggregated or split into individual and detached flocs ($<\ 100$ µm). However, for all testing conditions, no drastic evolution in the floc size were clearly observed between the suspensions sheared at $100\ s^{-1}$ and $1000\ s^{-1}$, so that the mechanisms involved in the shear thinning behavior may have occurred at a finer scale, *i.e.*, at the floc scale or even at the NFC scale. These last observations could explain why the stress levels recorded at high shear rates were very similar for all testing conditions.

The mesoscale structures of TEMPO-oxidized NFC suspensions shown in Figure 2-5 were very different from those of enzymatic suspensions. TEMPO-oxidized NFC suspensions were nearly transparent, stable and non-flocculated either at rest or during shearing. Hence, the complexity of the macroscale rheograms shown in Figure 2-5 cannot be explained using these 2D mesoscale observations, and may also be related to other potential sources commonly reported for other soft-glassy materials, *i.e.*, to mesoscale heterogeneous flow conditions associated to slippage at wall (stick-slip) and shear banding. For that purpose, a bulk analysis of kinematical fields is required (see next subsection).

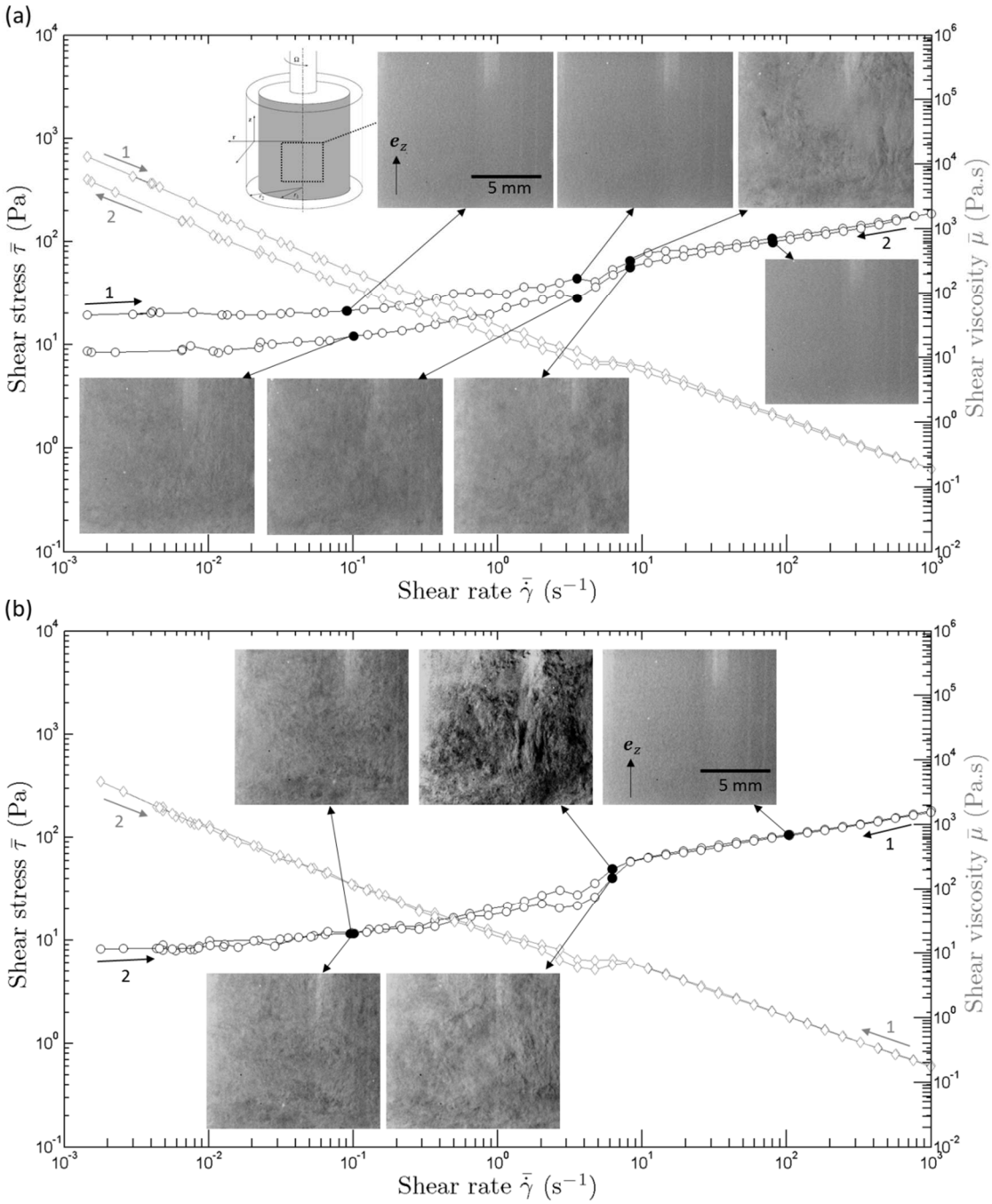

Figure 2-4. Macroscale rheograms: macroscopic shear stress $\bar{\tau}$ (black circle symbols) and viscosity $\bar{\mu}$ (gray diamond symbols) as a function of the macroscopic shear rate $\dot{\bar{\gamma}}$ for a 2 *wt*% enzymatic NFC suspension obtained by first increasing the shear rate $\dot{\bar{\gamma}}$ from 0.001 to 1000 s^{-1} in 45 logarithmically spaced steps of duration $\delta t = 50$ s and then decreasing $\dot{\bar{\gamma}}$ over the same range (a), or *vice versa* (b). Insets: visualizations of the mesostructures of the suspensions at different macroscopic shear rates $\dot{\bar{\gamma}} = 0.1, 5, 8$ and 100 s^{-1}.

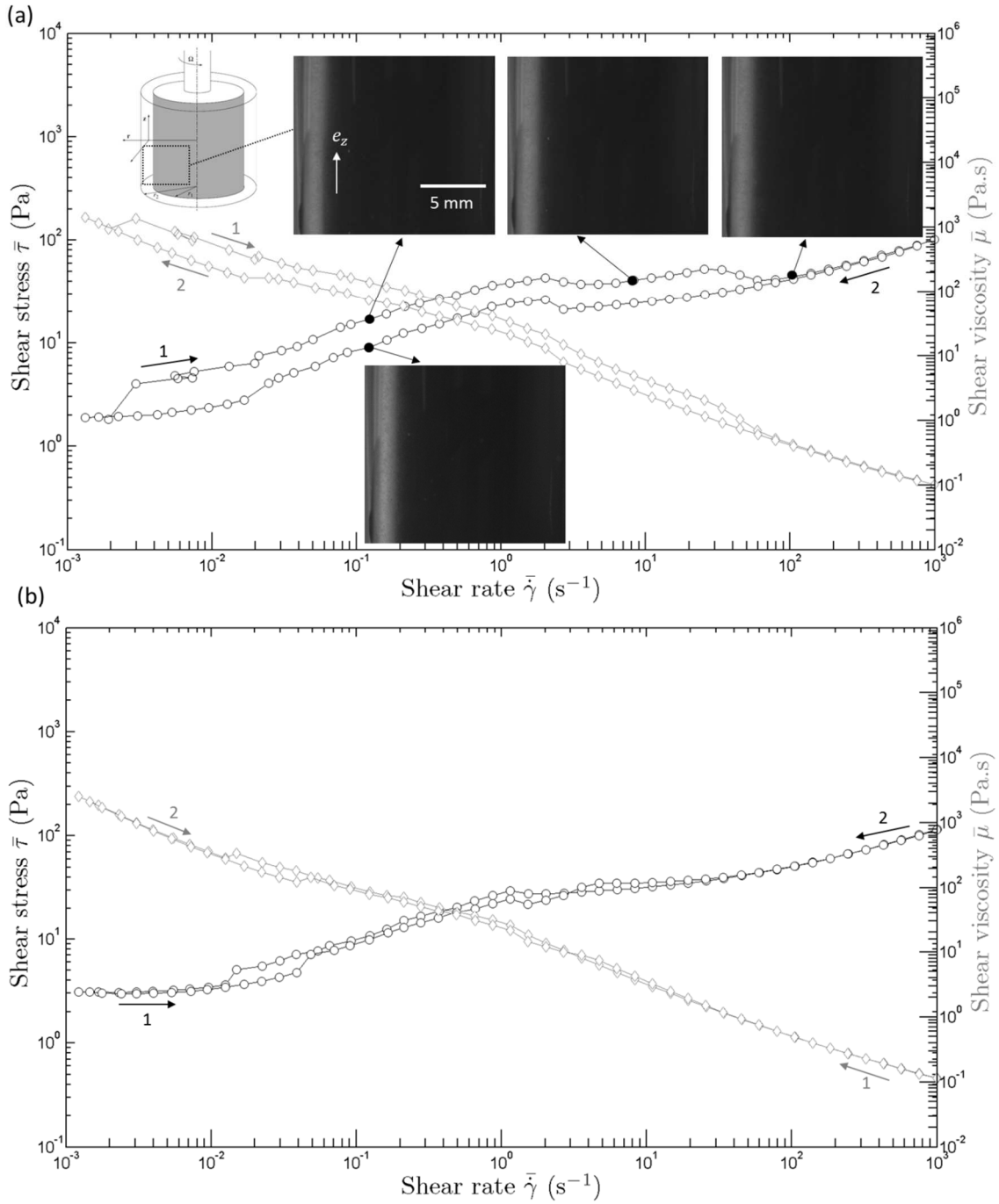

Figure 2-5. Macroscale rheograms: macroscopic shear stress $\bar{\tau}$ (black circle symbols) and viscosity $\bar{\mu}$ (gray diamond symbols) as a function of the macroscopic shear rate $\dot{\bar{\gamma}}$ for a $1wt\%$ TEMPO-oxidized NFC suspension, obtained by first increasing the shear rate $\dot{\bar{\gamma}}$ from $\dot{\bar{\gamma}}$ from 0.001 to 1000 s^{-1} in 45 logarithmically spaced steps of duration $\delta t = 50$ s and then decreasing $\dot{\bar{\gamma}}$ over the same range (a), or *vice versa* (b). Insets: visualizations of the mesostructures of the suspensions at different macroscopic shear rates $\dot{\bar{\gamma}} = 0.1, 5, 8$ and 100 s^{-1}.

2.3.2 Mesoscale rheology: description of the flow dynamics using rheo-USV

Presumably because of the presence of flocs or aggregates (Fig. 2-2.a,b,c and Fig. 2-4.a,b in the case of enzymatic NFC suspensions) and some rare macroscale fibers (Fig. 2-2.d,e,f in the case of TEMPO-oxidized NFC suspensions), enzymatic and TEMPO-oxidized NFC suspensions naturally scatter ultrasound when subjected to incident ultrasonic pulses. Hence, it was possible to use the USV technique directly for the NFC suspensions to obtain the 2D spatial and time-resolved characterization of the shear flow, *i.e.*, to acquire simultaneously both global rheological data and ultrasonic images of the phenomena that occurred inside the sheared suspensions (see the example in Figure 2-3).

Figure 2-6 and Figure 2-7 give two significant examples of the typical information that was obtained by coupling standard rheometry with the USV technique during quick start-up shear tests from 0 to constant imposed shear rates for the enzymatic and TEMPO-oxidized suspensions, respectively.

For both suspensions, graphs (a) in Figure 2-6 and Figure 2-7 showed that the time evolution of the macroscale shear stress $\bar{\tau}$ first exhibited a short and sharp increase up to a peak flow stress that was followed by a slower decrease down to a steady state regime over a few tens of seconds, a feature typical of thixotropic systems. The first regime was induced by the sudden shear rate jump from 0 to the imposed constant values. This behavior was probably related to the heterogeneous elastoviscoplastic deformation (see below) of the initially entangled nanostructure of the NFC suspensions. In the second stress regime, additional deformation mechanisms may have occurred so that the suspensions accommodated the imposed shear deformation: in the deformed zones of the suspensions (Fig. 2-6.c and Fig. 2-7.c below and the related comments), NFC may have progressively disentangled and deformed, which resulted in the formation of a new steady state structure where NFC continuously lost and recreated their contacts. This phenomenon is illustrated in graphs (c) in Figures 2-6 and 2-7 where the r'-profiles of the height-averaged value of the velocity field v, evolved towards stabilized profiles after several tens of seconds.

For enzymatic NFC suspensions, the lower spatiotemporal diagram shown in Figure 2-6.a and the spatial velocity maps taken at different times shown in Figure 2-6.b were very erratic. The velocity v was heterogeneous over the entire height h of the Couette cell. These large spatial heterogeneities, the size of which was of the order of magnitude of the gap e, also evolved in time, which suggested the occurrence of complex 2D or 3D flow phenomena. These bulk observations were in accordance with those made using the optical images shown in section 3.1 and confirmed the presence of flocs having complex kinetics and kinematics under shear. These observations were also in agreement with surface and bulk observations made by Karppinen *et al.*[18] using an optical system and by Saarinen *et al.*[19] using optical coherence tomography, respectively. These results show once again that the dimensions of classical rheometers are probably not suitable for a relevant study of the bulk rheology of these unstable

and flocculated suspensions in the framework of continuum mechanics. However, these rheometers can be used to study shear flow phenomena occurring in confined geometries.

For TEMPO-oxidized NFC suspensions, recorded spatiotemporal diagrams (Fig. 2-7.a) and spatial velocity maps (Fig. 2-7.b) were very different from those observed for enzymatic NFC suspensions (Fig. 2-6.a,b). Indeed, even if the velocity field v was also heterogeneous, (i) its spatial and temporal variations were smoother and much less erratic, (ii) and this field was only weakly z-dependent. Thus, point (i) confirms the optical observations made in the previous section for TEMPO-oxidized NFC suspensions: these suspensions did not exhibit mesoscale flocs at the micrometric scale. Point (ii) tends to prove that the flow of TEMPO-oxidized NFC suspensions was mainly 2D and contained in the $(\mathbf{e}_r, \mathbf{e}_\theta)$ plane. Therefore, a deeper quantitative analysis of the rheometry experiments for TEMPO-oxidized NFC suspensions can be more easily done compared to the case of enzymatic NFC suspensions. As shown in section 3.4, more information on the bulk rheology of TEMPO-oxidized NFC suspensions can also be extracted from the USV rheometry experiments.

Maps and profiles of the velocity field v (local or height-averaged) shown in Figure 2-6.b,c and Figure 2-7.b,c for enzymatic and TEMPO-oxidized NFC suspensions, respectively, showed that in general, their flow was heterogenous and exhibited complex situations with the coexistence of multiple flow bands, and wall slippage. The complex flow patterns were far from those expected with a Newtonian fluid in a small-gap Couette rheometer (eqn (5)), as illustrated in Figure 2-6.c and Figure 2-7.c. For example, the mesoscale velocity profiles obtained for the enzymatic NFC suspension (Fig. 2-6.c) revealed that a plug flow ($\mathrm{d}v/\mathrm{d}r \approx 0$) that nearly spanned over the entire gap probably occurred at the very beginning of the shear test. This phenomenon was accompanied by important wall slippage that could be observed both at the stator and the rotor. This phenomenon could also result in a progressive loading and a subsequent progressive strengthening or strain-hardening of the NFC network in the plug flow zone (see also our previous remark on the heterogeneous elastoviscoplastic deformation of the entangled NFC network before the peak stress). At $t = 73$ s, wall slippage increased on the rotor side ($r' = 0$) and two flow bands coexisted. A first flow band where $\mathrm{d}v/\mathrm{d}r \neq 0$ was formed near the rotorv ($0 \text{ mm} \leq r' \leq 0.4$ mm) and coexisted with a flow band where $\mathrm{d}v/\mathrm{d}r \approx 0$ near the stator ($0.4 \text{ mm} \leq r' \leq 2$ mm). Upon increasing the shearing time, the height-averaged velocity profiles revealed an increase of the width of the first flow band that progressively filled the entire gap. This transient behavior is reminiscent of the transient shear banding reported in carbopol microgels[39,52]. At "steady state" ($t \geq 73$ s), in spite of the strong heterogeneity of the velocity map along the vertical direction (Fig. 2-6.b), the suspension was roughly deformed in the entire gap, as shown by the last height-averaged velocity profile in Figure 2-6.c. Figure 2-7.c shows that the mesoscale velocity profiles for the TEMPO-oxidized NFC suspension were also very complex. Before and after the stress peak at $t = 1$ s, the flow exhibited a large central flow band where $\mathrm{d}v/\mathrm{d}r \approx 0$ that coexisted with a second flow band where $\mathrm{d}v/\mathrm{d}r \neq 0$ next to the stator. At short times ($t < 1.5$ s), nearly perfect no slip boundary conditions were observed on both sides (rotor and stator), while in the longer run

($t > 1.5$ s), pronounced wall slippage was recorded near the rotor. The width of the flow band where $\mathrm{d}v/\mathrm{d}r \approx 0$ remained approximately constant and equal to 1.5 mm.

A careful inspection of the velocity profiles (Fig. 2-7.c) also revealed an even more striking phenomenon. At the beginning of the shear test, *i.e.*, from $t = 0.5$ s to $t = 1.5$ s, the velocity of flow band where $\mathrm{d}v/\mathrm{d}r \approx 0$ passed through a maximum and reached values higher than the rotor velocity (≈ 10 mm s^{-1}). This transient phenomenon has already been reported for other systems such as wormlike micellar solutions[49] or organogels[50]. The authors attributed it to the signature of a multi-dimensional flow induced by transient elastic-like effects[49], suggesting that this phenomenon cannot be understood in the standard kinematic framework of the Couette flow, *i.e.*, 2D orthoradial flow $v_\theta(r)$. As inferred from eqn (4), a radial component v_r in the velocity field leads to an additional contribution $v_r/\tan\varphi$ to v. Note that since $\tan\varphi \approx 0.08$ for the present rheo-USV system, the effect of v_r on v was amplified by a factor of about 12. Hence, radial flow phenomena were also potentially at the origin of the aforementioned astonishing evolution of v.

These two examples show that rheo-USV provides a suitable and powerful framework for understanding the rheology of cellulose nanofibrils suspensions. They emphasize the difficulty to properly assess the "true" shear rate of these particular fiber suspensions from standard rheological measurements alone.

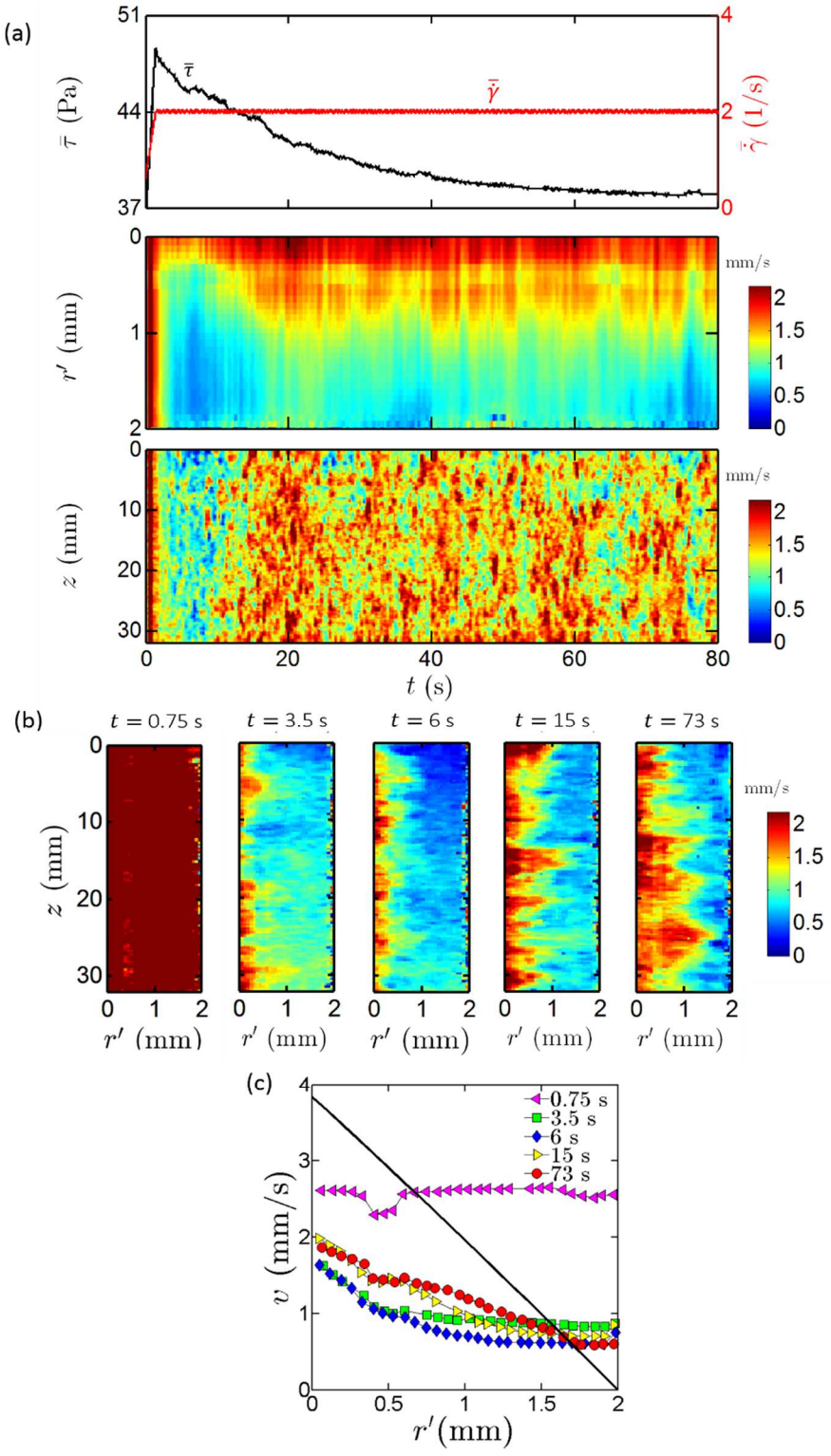

Figure 2-6. Start-up of shear from 0 to 2 s^{-1} obtained for a 2 *wt*% enzymatic NFC suspension. (a) Time-evolution of the macroscale shear stress $\bar{\tau}$ (upper graph, black line) and the targeted macroscale shear rate $\dot{\bar{\gamma}}$ applied by the rheometer (upper graph, red line), and spatiotemporal diagrams of the height-averaged mesoscale velocity field $v(r', t)$ (middle graph) and of the local mesoscale velocity field $v(z, t)$ at $r' = 0.4$ mm. (b) Spatial velocity maps $v(r', z)$ taken at times $t =$ 0.75 s, 3.5 s, 6 s, 15 s and 73 s. Each map corresponds to an average over 50 pulses sent every 0.5 ms. (c) Height-averaged velocity profiles obtained for the different times t as well as the theoretical profile (line in black) expected at 2 s^{-1} in the case of no slip 2D orthoradial flow.

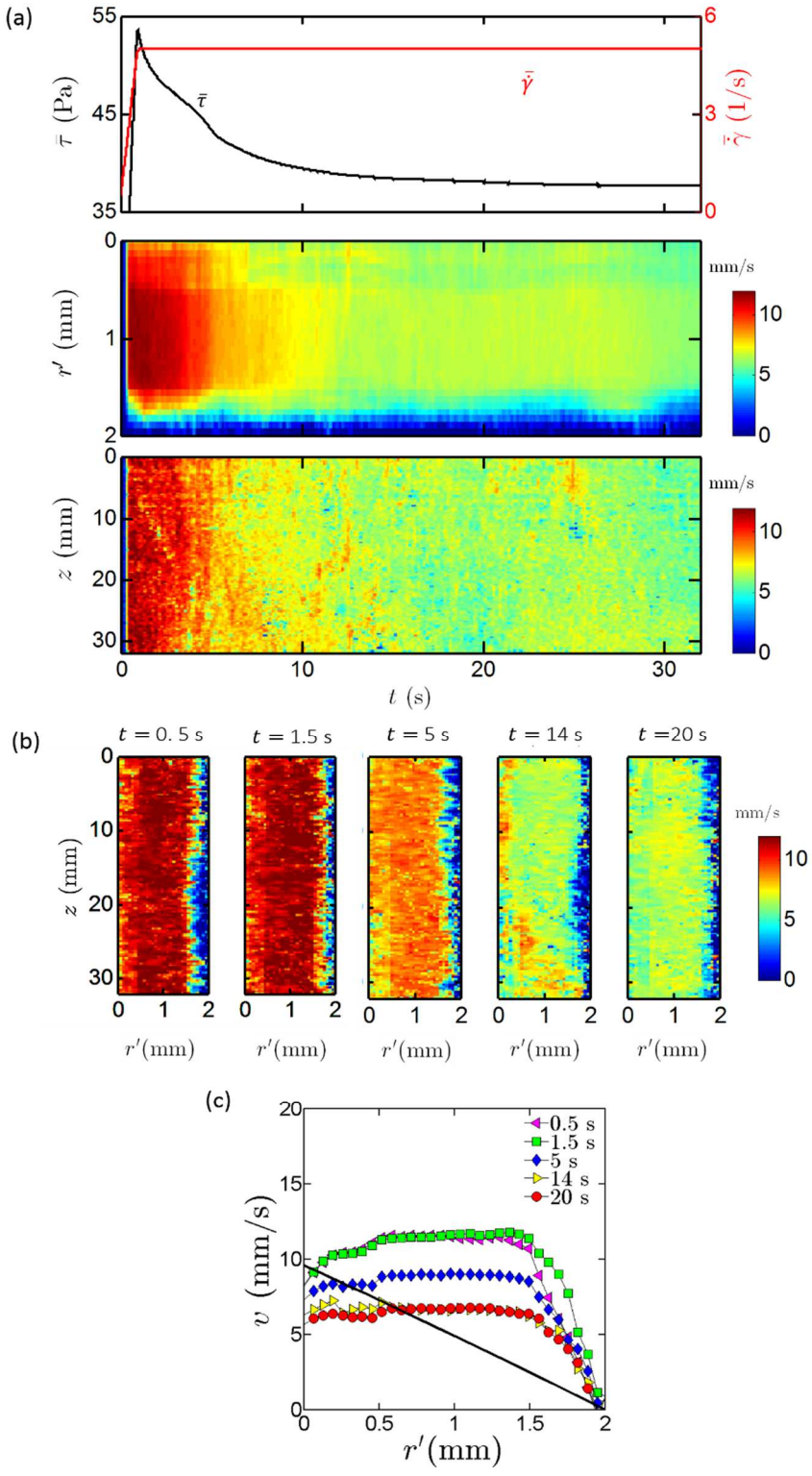

Figure 2-7. Start-up of shear from 0 to 5 s^{-1} obtained for a 1 $wt\%$ TEMPO-oxidized NFC suspension. (a) Time-evolution of the macroscale shear stress $\bar{\tau}$ (upper graph, black line) and the targeted macroscale shear rate $\dot{\bar{\gamma}}$ applied by the rheometer (upper graph, red line), and spatiotemporal diagrams of the height-averaged mesoscale velocity field $v(r', t)$ (middle graph) and of the local mesoscale velocity field $v(z, t)$ at $r' = 0.4$ mm. (b) Spatial velocity maps $v(r, z)$ taken at times $t =$ 0.5 s, 1.5 s, 5 s, 14 s and 20 s. Each map corresponds to an average over 50 pulses sent every 0.5 ms. (c) Height-averaged velocity profiles obtained for the different times t as well as the theoretical profile (line in black) expected at 5 s^{-1} in the case of no slip 2D orthoradial flow.

2.3.3 Multiscale rheology of TEMPO-oxidized suspensions

In this section, we describe in detail a set of results obtained for the unflocculated and stable TEMPO-oxidized NFC suspensions, *i.e.*, suspensions for which a mesoscale analysis remained meaningful. More precisely, the complex macroscopic rheogram that was obtained for a 0.9 $w\%$ TEMPO-oxidized NFC suspension was studied simultaneously to the USV measurements. This is illustrated in Figure 2-8 which shows the height-averaged steady-state velocity profiles obtained by sweeping up and then down the macroscopic shear rates ranging between 0.1 s^{-1} and 1000 s^{-1}.

All the plotted velocity profiles showed that the flow was inhomogeneous for both the upward and downward sweeps. Besides, the velocity profiles were also different showing that the flow was affected by the history of the macroscale applied shear rate $\bar{\dot{\gamma}}$. In addition, Figure 2-8 also shows that wall slippage systematically occurred either on the rotor side or the stator side or on both sides. Lastly, two distinctive classes of flow bands also appeared while shearing the suspension: a first class where $\mathrm{d}v/\mathrm{d}r \approx 0$ and a second class where $\mathrm{d}v/\mathrm{d}r \neq 0$.

For the upward sweep and ($0.1\ s^{-1} < \bar{\dot{\gamma}} < 1\ s^{-1}$), the suspension flow exhibited only two flow bands: a first flow band where $\mathrm{d}v/\mathrm{d}r \approx 0$ near the rotor ($0\ \mathrm{mm} \leq r' \leq 1.5\ \mathrm{mm}$) and a second flow band where $\mathrm{d}v/\mathrm{d}r \neq 0$ located near the stator ($1.5\ \mathrm{mm} \leq r' \leq 2\ \mathrm{mm}$).
For ($2\ s^{-1} < \bar{\dot{\gamma}} < 10\ s^{-1}$), the flow exhibited three bands: two flow bands where $\mathrm{d}v/\mathrm{d}r \neq 0$ near the rotor ($0\ \mathrm{mm} \leq r' \leq 0.3\ \mathrm{mm}$) and the stator ($1.4\ \mathrm{mm} \leq r' \leq 2\ \mathrm{mm}$) coexisted with a flow band where $dv/dr \approx 0$ ($0.3\ \mathrm{mm} \leq r' \leq 1.4\ \mathrm{mm}$).
At $\bar{\dot{\gamma}} = 50\ s^{-1}$, the suspension displayed two flow bands having two different non-zero slopes: a first band close to the rotor ($0\ \mathrm{mm} \leq r' \leq 0.7\ \mathrm{mm}$) and a second flow band close to the stator ($0.7\ \mathrm{mm} \leq r' \leq 2\ \mathrm{mm}$).
In summary, as the macroscale shear rate $\bar{\dot{\gamma}}$ was increased, the size of the flow band where $\mathrm{d}v/\mathrm{d}r \approx 0$ that was initially located near the rotor and then only in the middle of the gap progressively disappeared for the highest macroscale shear rates $\bar{\dot{\gamma}}$ (Table 2-1). These evolutions of the mesoscale velocity maps also corresponded to a complex evolution of the macroscale stress as shown in Figure 2-8. For instance, the macroscale shear stress reached a local maximum at a macroscale shear rate $\bar{\dot{\gamma}} = 1\ s^{-1}$ that was followed by a drop at $\bar{\dot{\gamma}} = 2\ s^{-1}$. This behavior corresponded to a transition between a flow that exhibited two bands towards a flow where three bands coexisted (Table 2-1).

For the downward sweep, heterogeneous velocity profiles were also recorded. The situation seems even more complicated than for the upward sweep. For instance, at $\bar{\dot{\gamma}} = 50\ s^{-1}$, a bumpy velocity profile was recorded. As the shear rate was further decreased, the strong heterogeneity of the velocity profile persisted. The velocity profiles revealed a progressive transition between flow regimes with noisy, bumpy velocity profiles for ($0.5\ s^{-1} < \bar{\dot{\gamma}} < 50\ s^{-1}$) to a situation where only two bands coexisted at $\bar{\dot{\gamma}} = 0.1\ s^{-1}$: a narrow flow band where $\mathrm{d}v/\mathrm{d}r \neq 0$ near the stator ($1.7\ \mathrm{mm} \leq r' \leq 2\ \mathrm{mm}$) and a large band where $\mathrm{d}v/\mathrm{d}r \approx 0$ near the rotor ($0\ \mathrm{mm} \leq r' \leq 1.7\ \mathrm{mm}$).

While decreasing the shear rate $\bar{\dot{\gamma}}$ in a range varying from 10 s^{-1}, to 0.5 s^{-1}, a flow band where $dv/dr \approx 0$ progressively enlarged and connected in the middle of the Couette cell (0.5 mm $\leq r' \leq$ 1.7 mm). This transition was accompanied by a nonmonotonic evolution of the macroscale shear stress. In particular, as for the upward sweep, a local maximum in the macroscale stress was observed at $\bar{\dot{\gamma}} = 1$ s^{-1}. Here it corresponded to a situation where the number of bands in the velocity profile progressively turned from three to two at $\bar{\dot{\gamma}} = 0.1$ s^{-1} (Fig. 2-8 and Table 2-2).

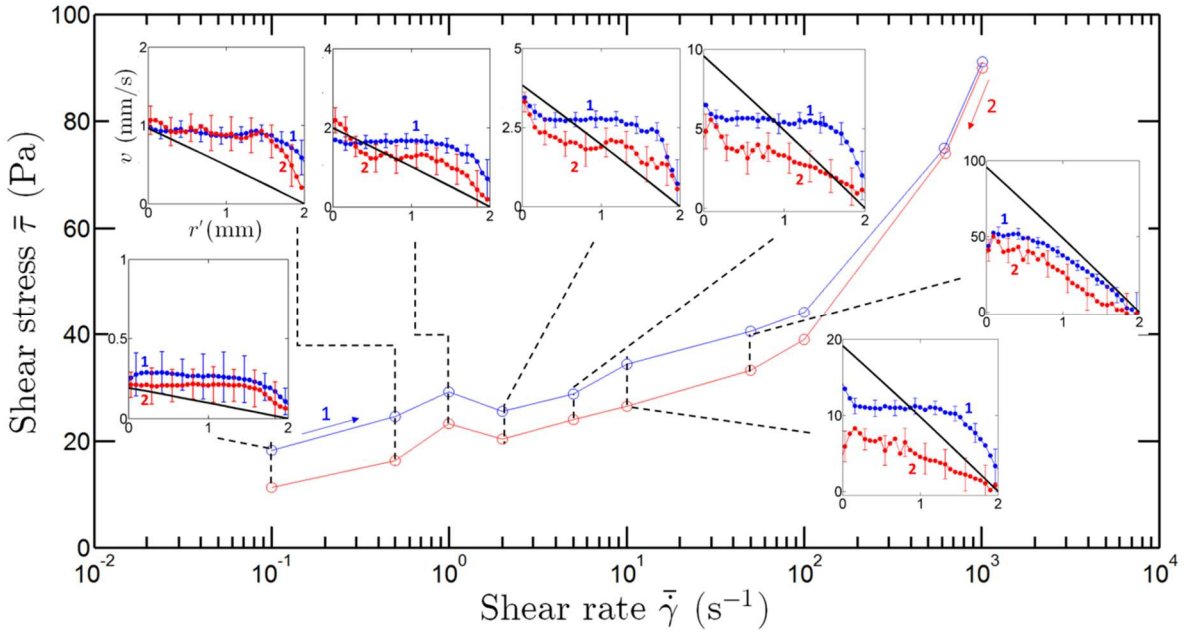

Figure 2-8. Macroscale rheogram of a 0.9 *wt*% TEMPO-oxidized NFC suspension obtained in a Couette rheometer first by sweeping up the shear rate $\bar{\dot{\gamma}}$ from 0.1 to 1000 s^{-1} in 10 steps of $\delta_t = 40$ s. Insets: velocity profiles inside the gap of the Couette cell at $\bar{\dot{\gamma}} = 0.1, 0.5, 1, 2, 5, 10$ and 50 s^{-1} recorded during the upward (blue dots) and downward (red dots) sweeps after 50 s of shear. Number 1 denotes upward sweeps, whereas number 2 denotes downward sweeps.

2.3.4 Discussion

For TEMPO-oxidized NFC suspensions, the use of the USV measurements enabled a link between the events from the macroscale flow curves and the mesoscale flow kinematics to be quantitatively established. These USV measurements showed that the flow was affected by the presence of wall slippage and multiple flow bands that evolved with the macroscopic shear rate. In addition, the optical observations shown in section 3.1 did not reveal clear evidence of mesostructural changes in the TEMPO-oxidized NFC suspensions. Hence, the phenomena leading to both wall slippage and the coexistence of multiple flow bands may occur at a lower scale, *i.e.*, at the microscale and may be related to microstructural changes in the network of NFC, deformation of NFC and/or concentration gradients within the gap.

The phenomenon of wall slippage has often been reported for a variety of systems including pastes, colloids and polymers[38,45,53]. This phenomenon is affected by the geometry (*e.g.* surface roughness) and the physico-chemical nature of the solid-fluid interface. However, the origin

of this phenomenon at finer scales and its effects on the flow kinematics and the microstructures still remain poorly understood. In the case of heterogeneous and polydisperse systems, wall slippage is often considered as resulting from a natural particle depletion phenomenon[19,53], *i.e.*, a sudden decrease in the concentration of elements near the rheometer walls. The depletion of the particles can be enhanced by the flow, which can induce a migration from the high-shear regions towards the low-shear regions. For the negatively charged TEMPO-oxidized NFC suspensions, the use of positively charged solid interfaces (for example, the rheometer walls in this study) would probably enhance the adhesion, leading to a decrease of the wall depletion effects.

The difference in macroscopic stress levels recorded during the upward and downward sweeps (Fig. 2-8) could be attributed to the coexistence of multiple flow bands having different kinetics and kinematics under shear. These types of heterogeneous velocity profiles have already been reported for a variety of soft systems ranging from surfactant, wormlike micelles[50,54,55], organogels[49], triblock copolymers[56] and clay suspensions[57]. By varying the sweep rates, the authors[39,40] have shown that the kinetic of the multiple mesoscale bands could be interpreted using a characteristic time resulting from the competition between physical aging (restructuring mechanisms) and shear rejuvenation (structure breakup).

As pointed out in section 2.3.2, the rheo-USV setup provides a rich but incomplete description of the flow dynamics. Note that similar problems also occur using other advanced velocimetry techniques such as those based on Magnetic Resonance Imaging (MRI). Thus, to further analyze the rheology of TEMPO-oxidized NFC suspensions, several assumptions on the flow in the Taylor-Couette cell must be considered:

- For instance, it may reasonably be assumed that the flow kinematics were independent of the vorticity direction $\mathbf{e}_z$, *i.e.*, that the TEMPO-oxidized NFC suspensions did not exhibit any vertical recirculating flows ($v_z \approx 0$). This assumption is supported by the visualizations shown in Figure 2-5 which tend to prove that the suspension flow was mainly contained in the $(\mathbf{e}_r, \mathbf{e}_\theta)$ plane, as the macroscale fibers that were present in the TEMPO-oxidized NFC suspensions did not display any noticeable vertical displacements under shear.
- Further, the derivative of the velocity v with respect to r can be expressed from eqn(4) as follows:

$$\frac{dv}{dr} = \frac{dv_\theta}{dr} + \frac{1}{tan(\varphi)}\frac{dv_r}{dr}. \quad (6)$$

Then, two typical flow situations corresponding to $dv/dr \approx 0$ and $dv/dr \neq 0$ can be considered. As shown in the velocity profiles of Figure 2-8, flow situations where $dv/dr \approx 0$ occurred within bands of several hundred microns in width. In these bands, it seems unlikely that the two terms of eqn(6) systematically balance each other out. Presumably in these flow situations $dv_r/dr \approx 0$ and $dv_\theta/dr \approx 0$, *i.e.*, the radial and orthoradial components of the velocity are constant over the gap width. However, in the absence of any recirculation phenomena, a flow

condition where the radial component v_r is a non-zero constant across the gap is unphysical (the fluid cannot go out of the measuring cell). Note also that in these "plug-like" flow bands; v_θ is probably constant, thus, meaning that the suspension is actually very weakly sheared. Similarly, a flow where $dv/dr \neq 0$ leads to $dv_r/dr \neq 0$ and $dv_\theta/dr \neq 0$: in this case the suspension is much more deformed.

Bearing in mind the aforementioned remarks, Figure 2-8 shows that the plug-like flow zones where $dv/dr \approx 0$ were located close to the rotor, whereas the deformed zones where $dv/dr \neq 0$ were surprisingly located near the stator. Taking into account the slight decrease (15% in our case) in the shear stress τ along the rheometer radius r from the rotor to the stator:

$$\tau(r) = \frac{\Gamma}{2\pi h r^2}, \quad (7)$$

it is worth noting that the deformed bands appeared in the lowest shear stress zones. For simpler yield stress fluids, the opposite situation has usually been reported, in general, deformed zones are observed near the rotor, *i.e.*, in the highest shear stress zones. As for the studied TEMPO-oxidized NFC suspensions, Saarinen *et al.*[19] have also reported for enzymatic NFC suspensions the presence of deformed bands in the lowest shear stress zone. The authors associated this phenomenon to wall depletion, *i.e.*, a drop in the NFC concentration profile near the stator. Here for the stable and unflocculated TEMPO-oxidized NFC suspensions, similar particle depletion phenomenon may have occurred. This phenomenon could be related to a potential strain-induced contraction of the NFC network. This contraction/consolidation could induce a migration of the fluid phase (water) towards regions where the stress is lower, *i.e.*, close to the stator. This scenario would have to be confirmed by additional investigations.

Figure 2-8 also shows that the transition from a solid to a liquid-like behavior of the studied TEMPO-oxidized NFC suspensions was heterogeneous as plug-flow zones and much more deformed zones coexisted over a wide range of macroscopic shear rate. We note also that the size of these zones evolved as a function of the macroscopic shear rate. Therefore, we propose to interpret the evolution of the shear stress as a function of the shear rate during the upward sweep in terms of suspension fluidization involving several deformation mechanisms at the microscale. The first mechanism could be a progressive strengthening or strain-hardening of the NFC network in plug-like flow zones. In the insets of Figure 2-8 for shear rates $\overline{\dot{\gamma}} < 1\ s^{-1}$, note that the width of the plug-like flow zones almost remained the same. However, from 0.1 to 1 s^{-1}, the induced deformation in these zones slightly increased. If the plug like flow zones could sustain this increase in shear, a potential reason for that could be that the suspension strengthened because of a potential strain hardening elastoviscoplastic behavior of the entangled NFC network (see also our previous remark in section 3.2). Then, while increasing the shear rate, this mechanism could be followed by the fracture and the progressive disentanglement of the NFC network (for instance, see the drops in the macroscale stress in Figure 2-5b and Figure 2-8 for $\overline{\dot{\gamma}} > 1\ s^{-1}$). At the highest shear rates, shear-induced alignment and stretching of NFC slender particles could eventually occur (predominance of viscous effects on restructuring effects).During the downward sweep, the suspension did not remain fluidized as

shown by the progressive and successive formation of plug-like flow bands, which spanned nearly completely over the Couette cell width (see the velocity profiles in Fig. 2-8). This phenomenon may be related to fast restructuring phenomena, *i.e.*, fast formation of a network of colloidal interactions between NFC, dominating the viscous effects[40] and leading to plug-like flow bands.

Even if the radial component v_r cannot be assessed using the rheo-USV nor the optical observations, we make the assumption that this component was small for the steady-state velocity profiles that are shown in Figure 2-8. Thus, a rough estimate of the mesoscale shear rate $\dot{\gamma}(r)$ within each flow bands was obtained from the height-averaged velocity profile $v(r)$ as follows:

$$\dot{\gamma}(r) \approx \frac{v(r)}{r} - \frac{dv(r)}{dr}. \tag{8}$$

The estimated values of the mean mesoscale shear rate $\dot{\gamma}$ within each flow bands, and their associated mesoscale mean shear stress τ (calculated from eqn(7)), are shown in the rheograms of Figure 2-9. This figure shows that the as-estimated mesoscale flow curves were multivalued, *i.e.*, a mesoscale shear stress could correspond to several mesoscale shear rates. The difference between the shear rates in each band (Fig. 2-8,9 and Tables 2-1,2) was probably responsible for this phenomenon as each band did not reach the same level of shear strain during the sweep duration, and presumably did not acquire a similar microstructure. However, these mesoscale flow curves tend to show that the TEMPO-oxidized NFC suspension behaved as a thixotropic non-linear fluid having a steady state yield stress τ_0 close to $15-25$ Pa, *i.e.*, a much higher yield stress value than the apparent yield stress $\bar{\tau}_0$ measured in the macroscale flow curves ($\bar{\tau}_0 \approx 3$ Pa). For pasty materials, the phenomenon of wall slip often leads to underestimate the macroscale shear stress, especially at low macroscale shear rates[45,58].

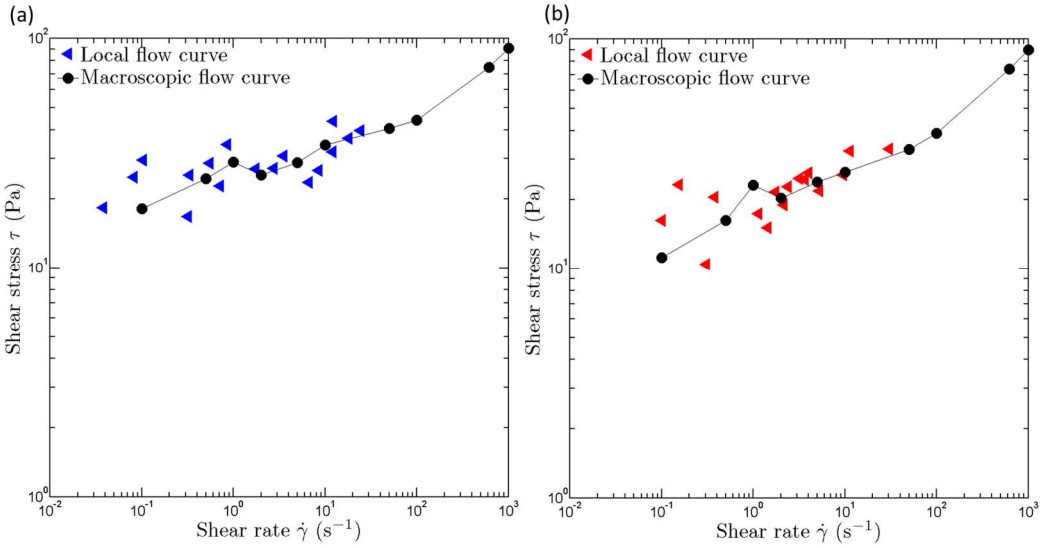

Figure 2-9. Flow curves showing the evolution of the mesoscale shear stress τ (calculated from Equation 7) as a function of the mesoscale shear rate $\dot{\gamma}$ given in Tables 1 and 2: (a) results obtained for upward sweep of the macroscale shear rate (blue dots) and (b) results obtained for downward sweep (red dots). The macroscale flow curve is shown for comparison (black curve).

Tableau 2-1. Summary of the macro and mesoscale data obtained by sweeping up the macroscale shear rate $\bar{\dot{\gamma}}$ from 0.1 to 1000 s^{-1}.

Macroscale shear rate $\bar{\dot{\gamma}}$ (s^{-1})	**Total number of bands**	**Thickness of the bands (mm)**	**Mesoscale shear rate $\dot{\gamma}$ (s^{-1})**
0.1	2	$0 \leq r' \leq 1.6$ $1.6 \leq r' \leq 2$	0.04 0.3
0.5	2	$0 \leq r' \leq 1.6$ $1.6 \leq r' \leq 2$	0.08 0.7
1	2	$0 \leq r' \leq 1.5$ $1.5 \leq r' \leq 2$	0.1 1.7
2	3	$0 \leq r' \leq 0.3$ $0.3 \leq r' \leq 1.6$ $1.6 \leq r' \leq 2$	2.7 0.3 6.6
5	3	$0 \leq r' \leq 1.6$ $0 \leq r' \leq 1.6$ $0 \leq r' \leq 1.6$	3.5 0.5 8.4
10	3	$0 \leq r' \leq 0.2$ $0.2 \leq r' \leq 1.4$ $1.4 \leq r' \leq 2$	18 0.9 32.1
50	2	$0 \leq r' \leq 0.7$ $0.7 \leq r' \leq 2$	12.2 24.2

Tableau 2-2. Summary of the macro and mesoscale data obtained by sweeping down the macroscale shear rate $\bar{\dot{\gamma}}$ from 1000 to 0.1 s^{-1}.

Macroscale shear rate $\bar{\dot{\gamma}}$ (s^{-1})	**Total number of bands**	**Thickness of the bands (mm)**	**Mesoscale shear rate $\dot{\gamma}$ (s^{-1})**
50	2	$0 \leq r' \leq 1.4$ $1.4 \leq r' \leq 2$	11.3 30.1
10	1	$0 \leq r' \leq 2$	4
5	3	$0 \leq r' \leq 0.3$ $0.3 \leq r' \leq 0.9$ $0.9 \leq r' \leq 2$	9.5 3.7 2.4
2	3	$0 \leq r' \leq 0.2$ $0.2 \leq r' \leq 1.4$ $1.4 \leq r' \leq 2$	5.3 0.4 2.1
1	3	$0 \leq r' \leq 0.3$ $0.3 \leq r' \leq 1.4$ $1.4 \leq r' \leq 2$	3.1 0.2 1.7
0.5	3	$0 \leq r' \leq 0.3$ $0.3 \leq r' \leq 1.5$ $1.5 \leq r' \leq 2$	1.1 0.1 1.4
0.1	2	$0 \leq r' \leq 1.7$ $1.7 \leq r' \leq 2$	0.007 0.3

2.4 Conclusion

The shear rheology of colloidal enzymatic and TEMPO-oxidized NFC suspensions was experimentally investigated using a Couette rheometer equipped with (i) a transparent cell that enabled optical observations and (ii) an ultrasonic speckle velocimetry (USV) setup. The rheo-USV technique enabled an unprecedented description of the spatiotemporal evolution of mesoscale flow kinematics that occurred in shear rheometry experiments for suspensions of NFC in water.

Macroscale rheograms showed that both suspensions behaved as yield stress fluids that exhibited a pronounced shear-thinning behavior at high shear rates. These suspensions also showed significant history dependence (thixotropy), hysteresis loops during upward and downward sweeps and complex phenomena such as, for instance, abrupt shear stress decrease as the shear rate was increased. All these phenomena suggested a strong coupling between flow and the structural properties of the studied NFC suspensions, but also inhomogeneous flow conditions.

The *in situ* optical observations revealed that the enzymatic NFC suspensions exhibited flocculated textures that evolved with the applied macroscopic shear rate and sweeping history. These observations, which are in accordance with previous studies[18], also showed that some of the complex evolutions observed in the macroscale flow curves corresponded to erratic mesostructural changes. These mesostructural changes were not observed for TEMPO-oxidized NFC suspensions.

For both types of suspensions, the spatiotemporal velocity diagrams and the velocity profiles obtained with the USV technique revealed that the flow was inhomogeneous for a wide range of applied shear rates and was affected by the presence of wall slip, multiple flow bands, as well as possibly two-dimensional or three-dimensional flows, resulting either from spatial heterogeneity of enzymatic NFC suspension or from elastic-like instabilities for TEMPO-oxidized NFC suspensions as those encountered in other soft materials[19,49,50,51,55,57].

For enzymatic NFC suspensions, the spatiotemporal velocity diagrams obtained using USV showed complex transient flow initiation and erratic events that occurred even if the macroscopic shear stress and the height-averaged velocity profile were apparently stabilized, suggesting that the steady-state flow conditions were not attained. These phenomena could result from the presence of floc chains or individual flocs the size of which was of the order of the rheometer gap that were moving apart under shear. Hence, using these types of rheometers is certainly not suitable for a proper rheology analysis based on a standard continuum framework. Therefore, the rheological models that have been established for enzymatic NFC suspensions using these types of rheometers are questionable: the gap is not large enough to obtain relevant rheological bulk properties.

For TEMPO-oxidized NFC suspensions, spatiotemporal velocity diagrams were very different from those of enzymatic NFC suspensions. Indeed, even if the velocity field was also heterogeneous, its spatial and temporal variations were smoother and much less erratic. This suggests that for TEMPO-oxidized NFC suspensions the flow was only weakly z-dependent. Thus, it was possible to carry out a deeper analysis of the bulk kinematic fields, revealing that, in the investigated shear rate $0.1\ \mathrm{s}^{-1} < \bar{\dot{\gamma}} < 50\ \mathrm{s}^{-1}$), the flow was heterogeneous for both the upward and downward sweeps. The height-averaged velocity profiles showed that the flow was affected by wall slippage and the presence of multiple flow bands. Two distinctive classes of bands appeared while shearing the suspension: a first class where $\mathrm{d}v/\mathrm{d}r \approx 0$ and a second class where $dv/dr \neq 0$. The number and the kinetics of the different flow bands varied as function of the applied macroscopic shear rate and the sweeping history.
In the probable absence of recirculating flows in the vorticity direction, the coexistence of these two types of bands could be related to a spatially heterogeneous transition from a solid-like to a liquid-like behavior of the TEMPO-oxidized NFC suspensions. These phenomena could result from a competition between structuration phenomena that involve colloidal interactions between NFCs and that are predominant at low shear rates and destructuration phenomena that involve predominant viscous forces at higher shear rates.

This study provides a comprehensive framework for understanding the rheology of NFC suspensions. However, new experimental investigations should be performed to confirm that the flow is not affected by the presence of vertical recirculation phenomena, and that the contribution of the radial component is low compared to the orthoradial component of the velocity field. It would also be of great interest to complement this study by finer local measurements to observe potential changes in the suspension microstructures within the gap (migration, orientation, variations of volume fraction of NFC, deformation of NFC) to explain the origin of phenomena such as shear banding and wall slippage.

References

1 L. J. Gibson, *J. R. Soc. Interface*, 2012, 9, 2749–2766.

2 Q. Cheng and S. Wang, *Compos. Part Appl. Sci. Manuf.*, 2008, 39, 1838–1843.

3 S. Tanpichai, F. Quero, M. Nogi, H. Yano, R. J. Young, T. Lindström, W. W. Sampson and S. J. Eichhorn, *Biomacromolecules*, 2012, 13, 1340–1349.

4 R. Bardet and J. Bras, in *Handbook of Green Materials*, World Scientific, 2014, 5, 207–232.

5 C. Aulin, G. Salazar-Alvarez and T. Lindström, *Nanoscale*, 2012, 4, 6622–6628.

6 H. Sehaqui, N. Ezekiel Mushi, S. Morimune, M. Salajkova, T. Nishino and L. A. Berglund, *ACS Appl. Mater. Interfaces*, 2012, 4, 1043–1049.

7 I. Siró and D. Plackett, *Cellulose*, 2010, 17, 459–494.

8 A. Dufresne, *Nanocellulose: from nature to high performance tailored materials*, Walter de Gruyter, 2012.

9 T. Saito, T. Uematsu, S. Kimura, T. Enomae and A. Isogai, *Soft Matter*, 2011, 7, 8804–8809.

10 M. Henriksson, G. Henriksson, L. A. Berglund and T. Lindström, *Eur. Polym. J.*, 2007, 43, 3434–3441.

11 M. Pääkkö, M. Ankerfors, H. Kosonen, A. Nykänen, S. Ahola, M. Österberg, J. Ruokolainen, J. Laine, P. T. Larsson and O. Ikkala, *Biomacromolecules*, 2007, 8, 1934–1941.

12 T. Saito, S. Kimura, Y. Nishiyama and A. Isogai, *Biomacromolecules*, 2007, 8, 2485–2491.

13 A. Isogai, T. Saito and H. Fukuzumi, *Nanoscale*, 2011, 3, 71–85.

14 T. Saito and A. Isogai, *Biomacromolecules*, 2004, 5, 1983–1989.

15 Y. Qing, R. Sabo, J. Y. Zhu, U. Agarwal, Z. Cai and Y. Wu, *Carbohydr. Polym.*, 2013, 97, 226-234.

16 K. L. Spence, R. A. Venditti, O. J. Rojas, Y. Habibi and J. J. Pawlak, *Cellulose*, 2011, 18, 1097–1111.

17 G. Chinga-Carrasco, *Nanoscale Res. Lett.*, 2011, 6, 1–7.

18 A. Karppinen, T. Saarinen, J. Salmela, A. Laukkanen, M. Nuopponen and J. Seppälä, *Cellulose*, 2012, 19, 1807–1819.

19 T. Saarinen, S. Haavisto, A. Sorvari, J. Salmela and J. Seppälä, *Cellulose*, 2014, 21, 1261–1275.

20 S. Fujisawa, Y. Okita, H. Fukuzumi, T. Saito and A. Isogai, *Carbohydr. Polym.*, 2011, 84, 579–583.

21 M. Mohtaschemi, K. Dimic-Misic, A. Puisto, M. Korhonen, T. Maloney, J. Paltakari and M. J. Alava, *Cellulose*, 2014, 21, 1305–1312.

22 C. Goussé, H. Chanzy, M. L. Cerrada and E. Fleury, *Polymer*, 2004, 45, 1569–1575.

23 E. Lasseuguette, D. Roux and Y. Nishiyama, *Cellulose*, 2008, 15, 425–433.

24 M. Iotti, Ø. W. Gregersen, S. Moe and M. Lenes, *J. Polym. Environ.*, 2010, 19, 137–145.

25 E. Saarikoski, T. Saarinen, J. Salmela and J. Seppälä, *Cellulose*, 2012, 1–13.

26 M. Mohtaschemi, A. Sorvari, A. Puisto, M. Nuopponen, J. Seppälä and M. J. Alava, *Cellulose*, 2014, 1–13.

27 P. Chen, H. Yu, Y. Liu, W. Chen, X. Wang and M. Ouyang, *Cellulose*, 2013, 20, 149–157.

28 H. Fukuzumi, R. Tanaka, T. Saito and A. Isogai, *Cellulose*, 2014, 21, 1553–1559.

29 T. Saarinen, M. Lille and J. Seppälä, *Annu Trans Nord Rheol Soc*, 2009, 17, 121–128.

30 F. Martoïa, P.J.J. Dumont, L. Orgéas, M. N. Belgacem, C. Perge, M.-A. Fardin and S. Manneville, oral communication in GFR, Nantes, 2013.

31 P. Coussot, L. Tocquer, C. Lanos and G. Ovarlez, *J. Non-Newton. Fluid Mech.*, 2009, 158, 85–90.

32 S. Manneville, *Rheol. Acta*, 2008, 47, 301–318.

33 P. C. F. Møller, S. Rodts, M. A. J. Michels and D. Bonn, *Phys. Rev. E*, 2008, 77, 041507.

34 G. Ovarlez, S. Rodts, X. Chateau and P. Coussot, *Rheol. Acta*, 2009, 48, 831–844.

35 G. Ovarlez, S. Cohen-Addad, K. Krishan, J. Goyon and P. Coussot, *J. Non-Newton. Fluid Mech.*, 2013, 193, 68–79.

36 P. Moller, A. Fall, V. Chikkadi, D. Derks and D. Bonn, *Philos. Trans. R. Soc. Math. Phys. Eng. Sci.*, 2009, 367, 5139–5155.

37 T. Gibaud, D. Frelat and S. Manneville, *Soft Matter*, 2010, 6, 3482–3488.

38 F. Pignon, A. Magnin and J.-M. Piau, *J. Rheol.*, 1996, 40, 573–587.

39 T. Divoux, C. Barentin and S. Manneville, *Soft Matter*, 2011, 7, 8409–8418.

40 T. Divoux, V. Grenard and S. Manneville, *Phys. Rev. Lett.*, 2013, 110, 018304.

41 E. K. Hobbie, *Rheol. Acta*, 2010, 49, 323–334.

42 P. Dumont, J.-P. Vassal, L. Orgéas, V. Michaud, D. Favier and J.-A. E. Manson, *Rheol. Acta*, 2007, 46, 639–651.

43 R. J. Adrian, *Exp. Fluids*, 2005, 39, 159–169.

44 P. T. Callaghan, *Rep. Prog. Phys.*, 1999, 62, 599–670.

45 P. Coussot, *Rheometry of pastes, suspensions, and granular materials: applications in industry and environment*, John Wiley & Sons, 2005.

46 T. Gallot, C. Perge, V. Grenard, M.-A. Fardin, N. Taberlet and S. Manneville, *Rev. Sci. Instrum.*, 2013, 84, 045107.

47 S. Manneville, L. Bécu and A. Colin, *Eur. Phys. J. - Appl. Phys.*, 2004, 28, 361–373.

48 J. A. Pople, I. W. Hamley and G. P. Diakun, *Rev. Sci. Instrum.*, 1998, 69, 3015–3021.

49 M. A. Fardin, C. Perge, N. Taberlet and S. Manneville, *Phys. Rev. E*, 2014, 89, 011001.

50 P. Grondin, S. Manneville, J.-L. Pozzo and A. Colin, *Phys. Rev. E*, 2008, 77, 011401.

51 U. Björkman, *Nord. Pulp Pap. Res. J.*, 2003, 18, 32–37.

52 T. Divoux, D. Tamarii, C. Barentin, S. Teitel and S. Manneville, *Soft Matter*, 2012, 8, 4151–4164.

53 H. A. Barnes, *J. Non-Newton. Fluid Mech.*, 1995, 56, 221–251.

54 J. P. Decruppe, O. Greffier, S. Manneville and S. Lerouge, Phys. Rev. E, 2006, 73, 061509.

55 M. A. Fardin, C. Perge, N. Taberlet and S. Manneville, Phys. Rev. E, 2014, 89, 011001(R).

56 S. Manneville, A. Colin, G. Waton and F. Schosseler, *Phys. Rev. E*, 2007, 75, 061502.

57 T. Gibaud, C. Barentin, N. Taberlet and S. Manneville, *Soft Matter*, 2009, 5, 3026–3037.

58 V. Bertola, F. Bertrand, H. Tabuteau, D. Bonn and P. Coussot, *J. Rheol.*, 2003, 47, 1211–1226.

Acknowledgements

This research was made possible thanks to the facilities of the TekLiCell platform funded by the Région Rhône-Alpes (ERDF: European regional development fund). LGP2 and 3SR laboratories are parts of the LabEx Tec 21 (Investissements d'Avenir - grant agreement n°ANR-11-LABX-0030) and of the Énergies du Futur and PolyNat Carnot Institutes (Investissements d'Avenir - grant agreements n°ANR-11-CARN-007-01 and ANR-11-CARN-030-01). C. Perge, M.-A. Fardin and S Manneville acknowledge funding from the Institut Universitaire de France and from the European Research Council under the European Union's Seventh Framework Programme No. FP7/2007-2013 and ERC Grant No. 258803. The authors gratefully acknowledge C. Sillard (LGP2) for the technical support in the use of the atomic force microscope.

Chapitre 3

Micro-mechanics of electrostatically stabilized suspension of cellulose nanofibrils under steady shear flow

Ce chapitre est basé sur un article actuellement soumis dans le journal *Soft Matter*, F. Martoïa, P.J.J. Dumont, L. Orgéas, M.N. Belgacem, J.-L. Putaux (en révision le 11/12/15).

Abstract

In this study, we characterized and modeled the rheology of TEMPO-oxidized cellulose nanofibril (NFC) aqueous suspensions with electrostatically stabilized and unflocculated nanofibrous structures. These colloidal suspensions of slender and wavy nanofibers exhibited a yield stress and a shear thinning behavior at low and high shear rates, respectively. Both the shear yield stress and the consistency of these suspensions were power-law functions of the NFC volume fraction. We developed an original multiscale model for the prediction of the rheology of these suspensions. At the nanoscale, the suspensions were described as concentrated systems where NFCs interacted with the Newtonian suspending fluid through Brownian motion and long range fluid-NFC hydrodynamic interactions, as well as with each other through short range hydrodynamic and repulsive colloidal interaction forces. These forces were estimated using both the experimental results and 3D networks of NFCs that were numerically generated to mimic the nanostructures of NFC suspensions under shear flow. They are in good agreement with theoretical and measured forces for model colloidal systems. The model showed the primary role played by short range hydrodynamic and colloidal interactions on the rheology of NFC suspensions. At low shear rates, the origin of the yield stress of NFC suspensions was attributed to the combined contribution of repulsive colloidal interactions and the topology of the entangled NFC networks in the suspensions. At high shear rates, both concurrent colloidal and short (in some cases long) range hydrodynamic interactions could be at the origin of the shear thinning behavior of NFC suspensions.

3.1 Introduction

Cellulose nanofibrils (NFCs) are interesting biosourced building blocks, isolated from cellulose fibers in the form of slender nanofibers with outstanding mechanical properties[1]. These nanofibers can be used to manufacture many promising materials including yarns[2,3], films[4], aerogels[5] and (nano-)composites[1,6]. NFCs can be extracted from their native cellulosic fibers using various chemical and mechanical treatments[1]. Among them, one of the most efficient extraction routes is TEMPO-mediated oxidation[7,8] which yields well-individualized NFCs while preserving a significant content of native crystalline cellulose. At low pH and high ionic strength, TEMPO-oxidized NFC aqueous suspensions exhibit heterogeneous and flocculated textures[9,10,4,11]. Materials processed with these NFCs have altered physical and mechanical properties[4]. On the contrary, at high pH and low ionic strength, NFC aqueous suspensions are homogeneous, nearly transparent and electrostatically stabilized by the presence of negatively charged carboxyl groups[9,10,4]. In these situations, NFC-based materials exhibit significantly enhanced[4] but not optimized end-used properties. Thus, it is crucial to understand and to control macroscale flow properties and flow-induced nanostructures of stabilized TEMPO-oxidized NFC suspensions during processing[12,3,2,13].

Electrostatically stabilized TEMPO-oxidized NFC suspensions exhibit a very complex rheology[14]. These suspensions usually behave like thixotropic shear thinning and anisotropic yield stress fluids[14,15,16]. They combine typical rheological features of soft glassy materials[17] such as clay suspensions, concentrated emulsions and colloidal gels, but also typical features of colloidal and non-colloidal fiber suspensions such as carbon nanotube and glass or biosourced fiber suspensions[18]. For example, during shearing, stabilized TEMPO-oxidized NFC suspensions exhibit heterogeneous flow properties[14,16], which involves strain localization, shear banding, migration, segregation, and wall depletion, as well as potential structural rearrangement such as fiber orientation[12] and deformation, shear-induced rejuvenation and destructuration. The situation is even more complicated when NFC suspensions exhibit flocculated textures[14,19]. These suspensions are unstable and exhibit complex and heterogeneous flow kinematics under shear[14,19]. Hence, for all the aforementioned NFC suspensions, advanced rheometry setups and procedures are required to properly characterize their intrinsic bulk flow properties[20,21,22,23].

Recent studies on NFC suspension rheology have reported that stabilized TEMPO-oxidized NFC suspensions behave at first order as Hershel-Bulkley fluid at the macroscale[15,24]:

$$\tau = \tau_0 + K\dot{\gamma}^n, \tag{1}$$

where τ_0, K and n are the macroscale shear yield stress, shear consistency and flow index, respectively, and where τ_0 and K are power-law functions of the volume fraction of NFC ϕ:

$$\tau_0 \propto \phi^e \qquad \text{and} \qquad K \propto \phi^g, \tag{2}$$

where $2 < e < 3.5$ and $2 < g < 2.5$.

These approaches provide important general phenomenological trends but do not relate the macroscale rheology of NFC suspensions to their complex nanostructure and deformation nano-mechanisms. For that purpose, rare but interesting multiscale analyses have been developed for these biosourced fibrous systems[24,25]. For example, by performing shear tests with a vane rheometer at low shear rates with NFC suspensions (concentration ranging between 0.5 and 10 wt%), Varanasi *et al.*[25] used an excluded volume theory, namely the Crowded Number theory[26], to estimate the mean NFC aspect ratio $r = l/d$ (where l and d are the NFC length and diameter, respectively) at the gel point, *i.e.*, at the critical NFC volume fraction ϕ_c for which a yield stress τ_{0c} is first observed and for which NFCs form a cohesive connected fibrous network. This model enables the critical macroscale yield stress τ_{0c} to be related to the underlying nanoscale fibrous reinforcements of the NFC suspensions. However, this approach does not take into account neither the wavy nature of NFCs, nor their potential orientation[12] and deformation that could be induced during suspension flow (the Crowded Number being used in the isotropic case with the assumption of straight fibers[26]). Further, this model cannot explain the experimental trends that are observed in the concentrated regime, *i.e.,* above the critical NFC concentration ϕ_c (see eqn (2)). It is also based on the extension of a theory initially developed for pulp fiber suspensions, *i.e.*, for flocculated suspensions made of micrometric fibers. Thus, a more appropriate framework is required to analyze the rheology of stabilized colloidal NFC suspensions such as TEMPO-oxidized NFC suspensions.

Colloidal interactions are known to play a central role in the non-Newtonian behavior of soft-glassy systems, especially in the low shear strain regime or low shear rate regimes where these systems exhibit solid-like properties[17,20,27,28,29,30]. For instance, for sufficiently high concentration of colloids, the macroscale yield stress τ_0 is often attributed to the formation of networks of strong colloidal interaction forces $\mathbf{f}^{col}$ that are able to restrain the Brownian forces $\mathbf{f}^{B}$ exerted by the suspending fluid on the elastic colloidal particles. In the case of repulsive colloidal systems such as the studied NFC suspensions, solid-like properties are closely related both to the topological arrangement and the geometry of colloids[31,13]. For slender wavy and entangled semi-flexible fibers, geometrical and topological effects are of great importance like in non-colloidal fibrous materials[32,33]. Hence, τ_0 is often related to a number of particle "bonds" B per unit area A of the sample and to a characteristic force f_c^{col} required to pull these bonds apart[27,28]:

$$\tau_0 \propto \frac{B f_c^{col}}{A}. \tag{3}$$

In general, the number of particle "bonds" B is estimated geometrically by using excluded volume approaches. This method was used in the Random Contact Equation that was developed by Philipse[34] to estimate the average number of contacts per particles z in suspensions of randomly oriented rods. In addition, it is worth noting that other studies[28,35,36] showed that the range of characteristic forces f^c is in good agreement with the colloidal forces that are

predicted by the classical DLVO theory developed by Derjaguin, Landau, Verwey and Overbeek.

At higher shear rates, *i.e.,* in the liquid-like regime, other interaction forces also become significant during suspension flow[27,28,20,29]. Long-range hydrodynamic interactions $\mathbf{f}^{hl}$ occur between the suspending fluid and the particles far from particle contact zones and short-range hydrodynamic interactions $\mathbf{f}^{hs}$ occur when the particles are sufficiently close to each other, *i.e.*, if their interparticle distance is in the order of the particle diameter.
For the two aforementioned flow regimes, the macroscale rheology depends both on the current microstructure of the suspension and its evolution during flow. A complete analytical treatment would be quite difficult, requiring a fine description of the microstructure and flow micro-mechanisms. For concentrated suspensions of anisotropic slender and semi-flexible particles such as NFCs, the situation is even more complicated because of the potential flow-induced deformation and rotation of these particles.

In parallel to studies dedicated to colloidal systems, other multiscale theories have been developed in the field of fiber-reinforced composite materials to predict the rheology of concentrated polymer and non-colloidal fiber suspensions. The resulting rheological models relate the macroscopic rheological behavior of the suspensions to the fiber geometry and the fibrous architecture, *i.e.*, the content, distribution and orientation of fibers. These microstructural parameters are of first importance since they determine for example the number of fiber-fiber contacts per unit volume. These models also emphasize the role of contact micromechanisms in the regions of inter-fiber contacts. In non-colloidal fiber suspensions, these local forces result from potential (i) elastic deformation of the fibrous network, *i.e.*, bending or twisting deformation of fibers between contact points, (ii) dry Coulombic friction phenomena that are induced by the contacts between fibers, and (iii) lubrication interactions that are induced by shearing of thin suspending fluid zones in the vicinity of contact zones. These suspensions exhibit a highly anisotropic response that depends on the orientation state. Thus, the aforementioned models must be also accompanied by a set of fiber orientation equations for the prediction of the evolution of the anisotropy. Several theories have been purposely developed in the literature[37,38,39]. Most of them are based on the well-known Jeffery's equations[40].

Recent studies have expanded these multiscale models to colloidal fibrous systems, for example carbon nanotube suspensions[39]. However, to the best of our knowledge, none of them properly encompasses the particular physics of colloidal forces between particles, and their critical role, in particular at low and moderate shear rates. Thus, the objective of the study was to build, from an experimental database and a theoretical framework inspired from those developed for non-colloidal and concentrated fibrous systems, a multiscale rheological model to emphasize the impact of the particular fibrous nanostructure and colloidal interactions of TEMPO-oxidized NFC suspensions on their shear rheology. The developed model is restricted to unflocculated suspensions, *i.e.*, NFC suspensions at high pH and low ionic strength that

are stabilized by repulsive colloidal interaction forces. In this context, we processed electrostatically stabilized TEMPO-oxidized NFCs[14] (section 2). The geometry of these particles was finely characterized, and the macroscale shear rheology of TEMPO-oxidized NFCs suspensions was investigated for various fiber contents (section 3). This experimental database enabled a multiscale rheological model to be built, accounting for the fibrous nature of the considered suspensions and for the interaction forces between the fluid and the NFCs, namely Brownian and long range hydrodynamic interactions, and between contacting NFCs, namely repulsive colloidal and short range hydrodynamic interactions (section 4). The nanoscale constitutive parameters of the model were identified using realistic elementary volumes of the fibrous nanostructures of NFC suspensions that were numerically generated. Finally, the suitability of the model prediction was discussed (section 5).

3.2 Materials and experimental procedures

3.2.1 Extraction of NFCs

TEMPO-oxidized NFC suspensions with 1 wt% of NFCs were obtained from a commercial eucalyptus bleached kraft pulp (Celbi, Portugal) using a processing route that has already been used by Martoïa *et al.*[14]. A chromatography analysis of the suspending fluid showed that the solid content of residual sugars and oligomers (mainly hemicelluloses) was very low, *i.e.*, approximately 70 mg L^{-1}. This suggests that only few residual oligomers were liberated during mechanical grinding, and that the studied NFCs could be considered to be suspended in a Newtonian matrix of water with a shear viscosity μ of 10^{-3} Pa s. Then, NFC suspensions at various concentrations ranging from 0.2 to 1 wt%, *i.e.*, NFC volume fraction ϕ ranging from 0.0013 to 0.0067 (ϕ was estimated assuming a cellulose density ρ of 1500 kg m^{-3}), were prepared by diluting the initial NFC suspension with deionized water. All the suspensions were at pH = 8.

3.2.2 Microscopy

The macro-, micro- and nano-scale morphologies of NFCs and NFC suspensions were investigated using various optical and electronic imaging techniques. Natural and cross-polarized optical sources were used at meso- and micro-scales to assess the homogeneity of the processed suspensions. Micrographs were recorded in transmission mode on NFC aqueous suspensions diluted to 0.1 wt%, using an optical microscope (Axio Imager M1m, Zeiss) equipped with a camera (AxioCAM MRC5, Zeiss). A drop of the suspension was deposited into a cavity microslide (L4090 Agar Scientific, UK) that had a 18-mm diameter and a 15-mm depth. TEM observations were also carried out to analyze the nanoscale morphology of NFCs. TEM specimens were prepared by depositing a drop of NFC suspension at a concentration of 0.001 wt% onto glow-discharged carbon-coated electron microscope grids. These specimens were then negatively stained with 2 wt% uranyl acetate and air-dried for a few minutes before being imaged using a Philips CM200 microscope operating at an accelerating voltage of 80 kV. Images were recorded on Kodak SO163 films

3.2.3 Rheometry

The rheology of NFC suspensions was studied using a stress-controlled rheometer (MCR 301, Anton Paar Physica, Austria) equipped with a plate-plate geometry (diameter 25 mm, gap 1 mm) for the most concentrated suspensions ($\geq$ 0.3 wt%) and with a cone-plate geometry (diameter 50mm, gap 150 µm) for the less concentrated suspensions ($<$ 0.3 wt%). To minimize wall slippage that often occurs when pasty materials are sheared[20,17], the rheometer walls were covered with sandpaper (surface roughness 120 µm). All the measurements were performed at 20°C with pre-sheared, at 10^3 s^{-1} for 60 s, suspensions. A glass solvent trap was systematically used to prevent water evaporation. As described by Martoïa *et al.*[14], macroscale

rheograms were obtained by sweeping down the macroscopic shear rate $\dot{\gamma}$ from 10^3 s^{-1} to 10^{-3} s^{-1} in 90 logarithmically-spaced steps for times of $\delta t = 50$ s (Fig. 3-2). This time resulted in a steady state response of the suspensions for each step[14].

A typical macroscale flow curves that were obtained by following this procedure is shown in Fig. 3-2.a. These flow curves exhibit a peculiar shape with two distinct regimes already observed in other colloidal systems[41,42,43]. As the macroscale shear rate is decreased from the high shear rate region, the macroscale shear stress progressively decreases to reach a horizontal plateau up to $\approx 10^{-1} - 10^{0}$ s^{-1}. This plateau is usually considered to be close to the steady state macroscale yield stress τ_0[20,17,44]. In addition, it is interesting to notice that, within this first regime, the same suspension behaves identically when it is sheared inside a Couette geometry. Lowering the shear rate beyond the plateau yields a second regime with a remarkable decrease of the macroscale shear stress that depends on the geometry of the rheometer (Fig. 3-2.a).

To elucidate mesoscale flow mechanisms related to the macroscale rheology, we previously used the same Couette geometry coupled with an ultrasonic speckle velocimetry system (rheo-USV)[14,45]. Regardless of the considered regime, the studied TEMPO-oxidized NFC suspensions were shown to exhibit heterogeneous mesoscale flows, with the occurrence of wall slippage, shear bands and in some cases plug-like flow bands. In the first flow regime, shear banding was moderate and no pronounced plug-like flow band was observed while sweeping down the shear rate: the recorded macroscale flow curves coincided, as a first order approximation, with that obtained using rheo-USV at the mesoscale. In the second flow regime, the decrease of the macroscopic shear stress τ was correlated with marked plug-like flow zones bands that spanned over the cell gap, as observed in other soft glassy materials[17,44,42, 46].

Thus, in light of these observations, only the first regime of the rheological data will be examined in the following sections, (i) assuming as a first approximation that the macroscale flow curves are sufficiently representative of the bulk rheology of the NFC suspensions, (ii) adopting the methodology reported in other studies[20,47] to analyze and discuss, from a phenomenological standpoint, rheograms using a Herschel-Bulkley approach, (eqn (1), Fig.3-2.a-b).

3.3 Experimental results

3.3.1 Multiscale structure of the processed NFCs

From the multiscale observations performed on the TEMPO-oxidized NFC suspensions (Fig. 3-1), several relevant remarks can be drawn. First, as shown in the inset picture in Fig. 3-1.a, the processed TEMPO-oxidized NFC suspensions were stable, *i.e.*, they did not exhibit flocculated textures. This stability was ensured by the presence of carboxylate groups [-COO^-] introduced at the surface of NFCs during the TEMPO treatment: the content of carboxyl groups [-COOH] determined by conductimetric titration Γ_{COOH} was 1.45 mmol g^{-1},

whereas it was only 0.05 mmol g^{-1} for native eucalyptus fibers. Thus, at the suspension pH, *i.e.* at pH 8, close to the pKa of the acid-base pair (pKa $\approx$ 8), carboxyl groups were partially dissociated into carboxylate groups. Note also that these suspensions remained stable and unflocculated under shear flow[14,16]. In addition, the observations under cross-polarized light shown in Fig. 3-1.b revealed that the studied NFC suspensions did not exhibit pronounced birefringent textures. This was likely due to the very high aspect ratio of NFCs and their kinks (for example, see the micrographs shown in Fig. 3-1.c-d) that did not enable the particles to easily self-assemble into well-ordered domains.

A finer analysis of the microstructures showed that the processed NFC suspensions were bi-disperse in size: they contained (i) sparse fibers close to their original dimensions (diameter $\approx$ 20 µm and length $\approx$ 600 µm, Fig. 3-1.a), and (ii) a very large amount of small and slender individualized fibrils. Even if the precise determination of the size of these very slender elements is still challenging, the dimensions of the NFCs were determined from the TEM images (Fig. 3-1.c-d). We measured a mean diameter d of 4 nm and a mean length l of 1200 nm, *i.e.,* a mean aspect ratio $r = l/d \approx 300$. It is worth noting that the diameter d and length l are in the same order of magnitude than that determined by Usov *et al.*[48] using AFM and TEM images from TEMPO-oxidized NFC suspensions extracted from wood fibers. Finally, TEM micrographs shown in Fig. 3-1.c-d also revealed that the NFCs were tortuous and consisted of an assembly, on the average, of $n_{seg} = 7$ slender straight segments with a mean length $l_{seg} =$ 169 nm interspersed with kinks or curved regions[48]. The mean misorientation angle θ_{seg} between each consecutive segment of a NFC was close to $\pi/8$ rad[48].

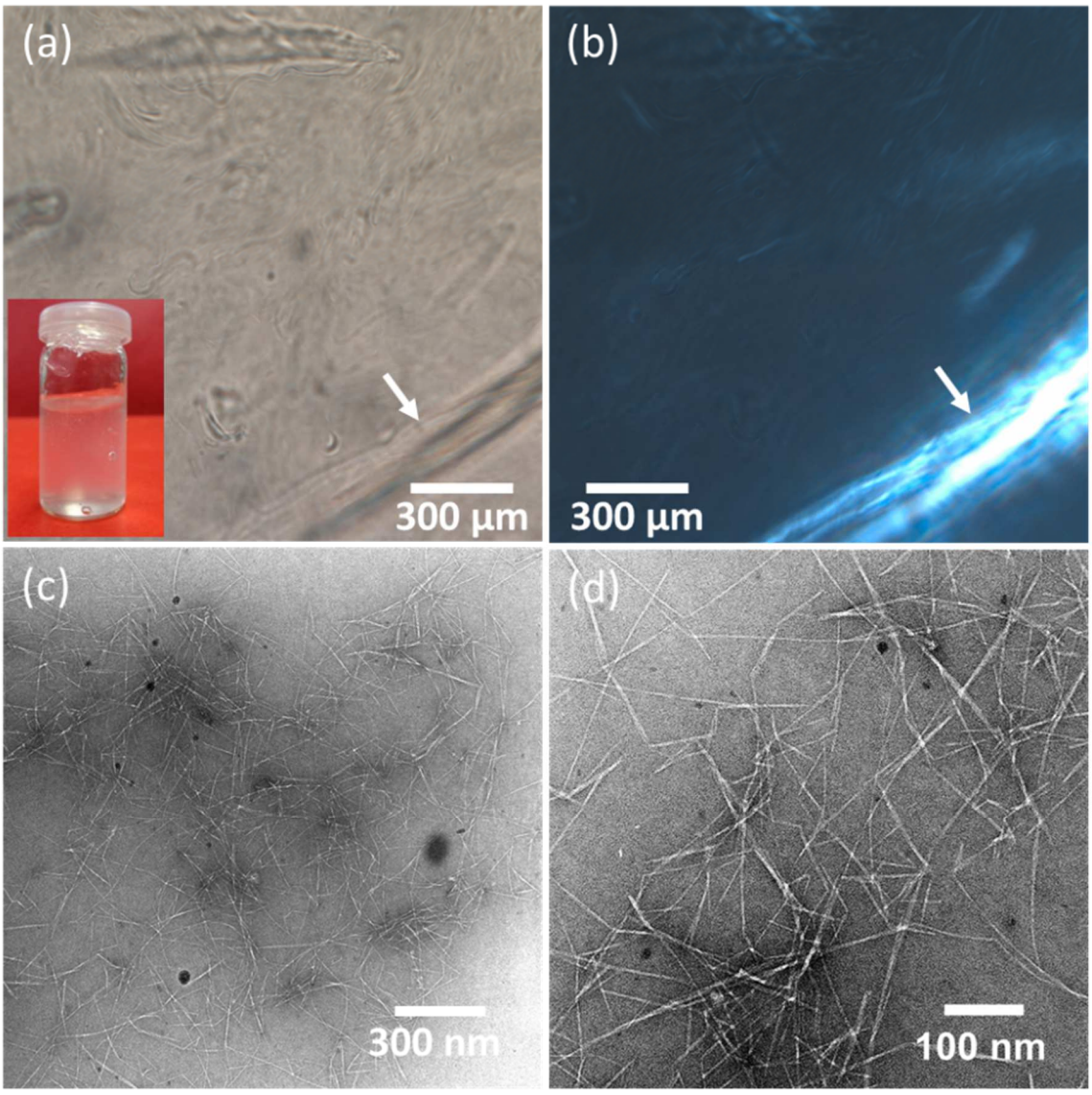

Figure 3-1. Optical (a) and cross-polarized light micrographs (b) of a 0.1 *wt*% TEMPO-oxidized NFC suspension. The white arrow indicates a partially fibrillated cellulose fiber. (c-d) TEM micrographs of the dry suspensions after negative staining.

3.3.2 Macroscale shear rheology

The values of τ_0, K, n of the Herschel-Bulkley model were fitted from the rheograms in Fig. 3-2.b. They are reported in Fig. 3-3 as a function of the volume fraction of NFCs ϕ. The steady state yield stress τ_0 and the consistency K were power-law functions of ϕ (eqn (2)) with power-law exponents e and g of 3.1 and 1.8, respectively. Keeping in mind the very small NFC volume fraction ϕ, these tendencies clearly emphasize a noteworthy thickening effect that can be directly related to the pronounced aspect ratio r of the studied NFCs ($\approx$ 300). These power-law exponents are in agreement with those previously reported for sheared TEMPO NFC suspensions[15,24]. However, some differences can be noticed. Particularly, the yield stress values shown in Fig. 3-3 are twice as large as those reported by Mohtaschemi *et*

al.[24] This could be related to different rheometry procedures and/or differences in (i) the NFC microstructures and (ii) ionic strength of the suspensions that control the aggregation state and stability of the ensuing colloidal systems. Finally, Fig. 3-3.c shows that the flow index n was nearly independent of the NFC volume fraction ϕ and close to 0.6. In comparison, Mohtaschemi *et al.*[24] reported a slight decrease in the flow index n ($0.4 \leq n \leq 0.2$) as a function of ϕ ($0.0016 \leq \phi \leq 0.0067$).

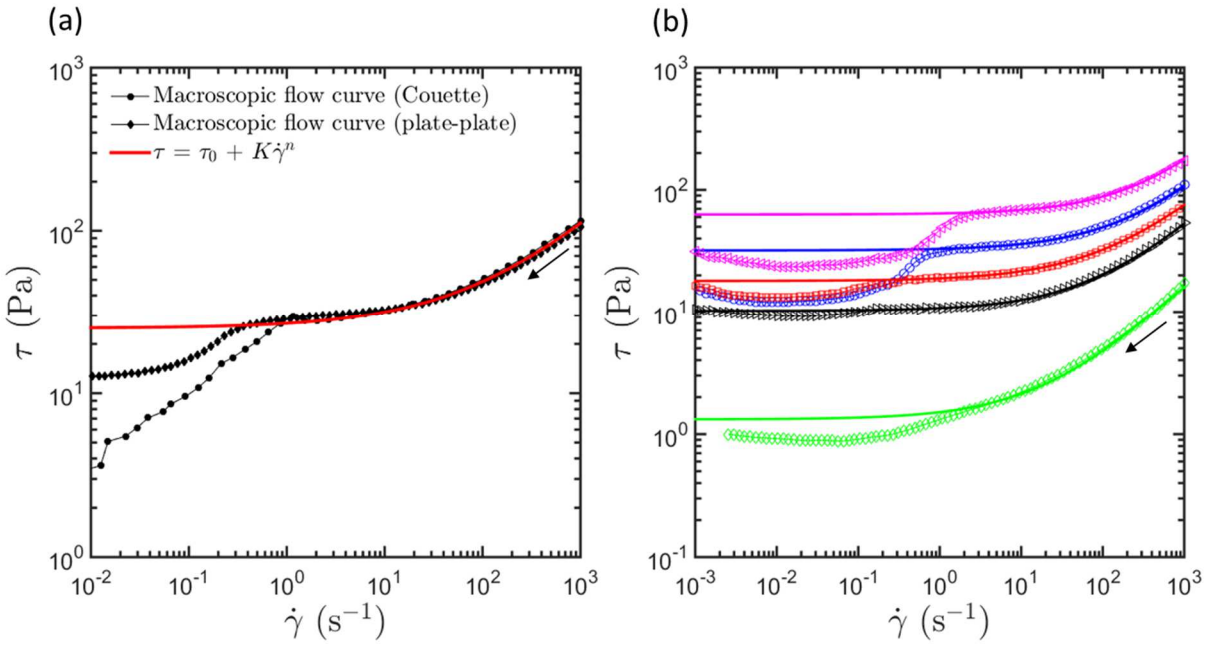

Figure 3-2. (a) Flow curves obtained for a 0.85 wt% TEMPO-oxidized NFC suspension. The curve with black circle symbols represents $\tau - \dot{\gamma}$ curves that were obtained using a Couette rheometer by sweeping down the macroscopic shear rate $\dot{\gamma}$ from 10^3 to 10^{-2} s^{-1} in 35 steps with times $\delta t = 50$ s. The curve with black diamond symbols shows $\tau - \dot{\gamma}$ curve obtained using a plate-plate rheometer by sweeping down the macroscopic shear rate $\dot{\gamma}$ from 10^3 to 10^{-2} s^{-1} in 70 steps with times $\delta t = 50$ s. (b) Macroscopic flow curves obtained for various NFC suspensions concentrated at $0.3, 0.56, 0.7, 0.85,$ and 1 wt% using a plate-plate rheometer. In graphs (a) and (b), the solid lines represent the fits of the Herschel-Bulkley model (eqn (1)).

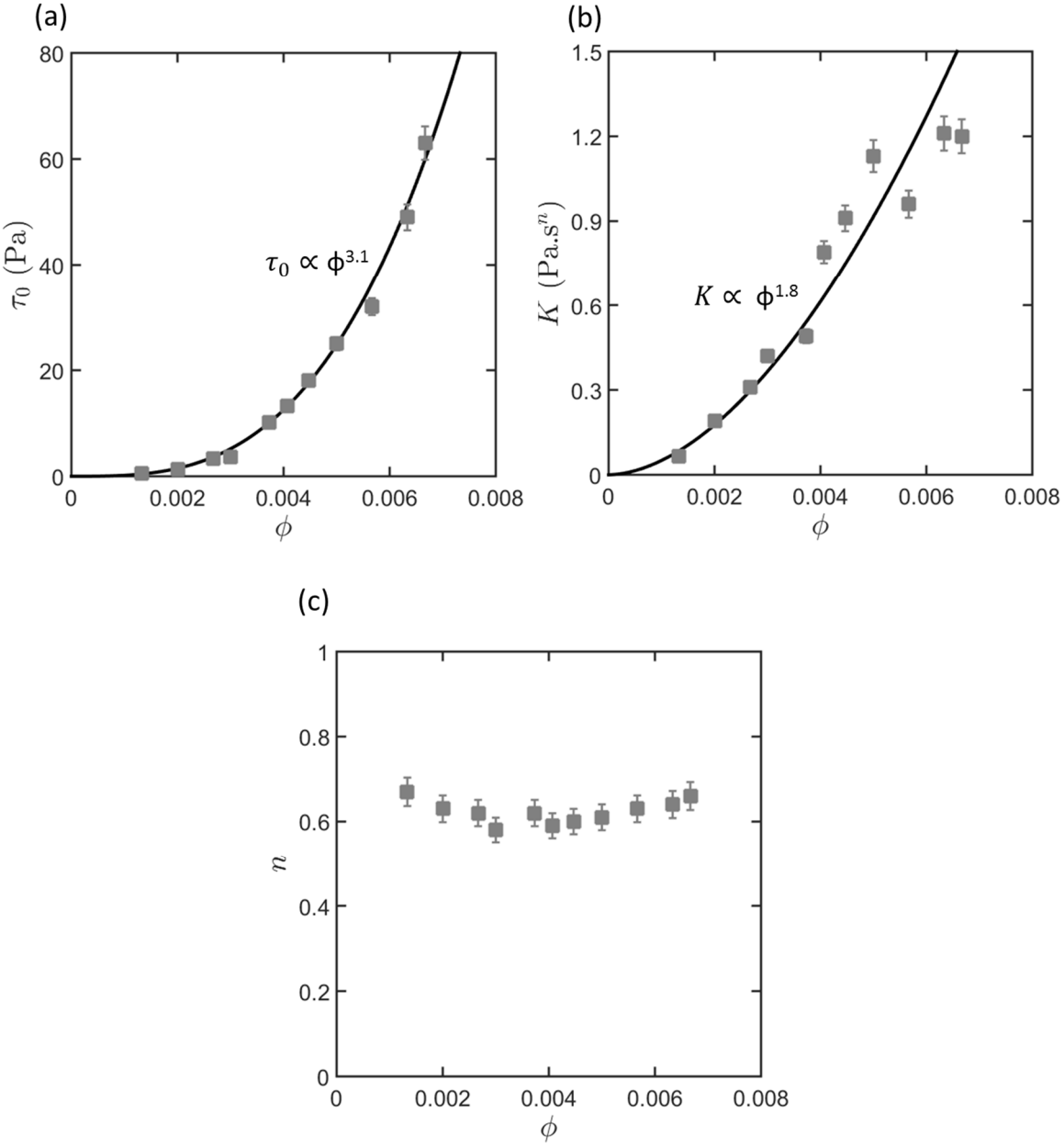

Figure 3-3. Evolution of the parameters of the Herschel-Bukley law as a function of the NFC content ϕ: steady state yield stress τ_0 (a), consistency K (b), and flow index n (c). Lines represent the power-law fits for the yield stress (a) and the consistency (b), respectively.

3.4 Micromechanical analysis

As mentioned in the introduction, several experimental studies have already reported similar scaling laws to those shown in eqn (2) for other systems such as non-colloidal and colloidal fibrous suspensions[24,25,49,26] as well as colloidal gels[27,28] or other non-bonded fibrous media[50,51,52]. Other theoretical studies tried to recover the power-law exponents of these macroscale expressions using multiscale modeling approaches. For example, in an early theoretical study, van Wik[50] proved that the isostatic compression stress of non-bonded networks of randomly

orientated, semi-flexible, slender, elastic, dry and straight fibers followed a scaling law similar to eqn (2a) with a power-law exponent $e = 3$, neglecting friction forces at fiber contacts and assuming that fiber bending was the leading fiber deformation mechanism. Later, Bennington *et al*[49] adopted a similar approach to predict the shear yield stress in concentrated pulp fiber suspensions (assuming the suspension isotropy), leading to the same power-law exponent e. By revisiting the work of van Wik[50], Toll and Månson[51] and Toll[52] emphasized the critical role of the fiber orientation on macroscale stresses. The authors showed that if $e = 3$ in the case of the compression of randomly orientated straight fibers, it could raise up to 5 for planar random fibrous networks, in accordance with experimental trends. Other network modeling approaches were also developed for polymeric concentrated fiber suspensions to predict the values of the power-law exponent g observed with these systems in the viscous/high shear rate regime[53,54,55]. By assuming that (i) contact forces between fibers were induced by the shearing of the (non)-Newtonian suspending fluid in the vicinity of fiber-fiber contact zones and (ii) the connectivity the considered fibrous networks was well predicted by the tube model[56] , most of the authors found that g was equal to 2.

The aforementioned remarks show that the macroscale rheological properties of a wide class of concentrated fibrous soft materials are largely dominated at lower scales by (i) the geometry of fibers and their architecture (position, content and orientation), and (ii) the deformation mechanisms of the fibers and their contacts. Hence, in the following subsections, accounting both for the observed multiscale fibrous structures and macroscale rheological properties of NFC suspensions, we propose a multiscale model to link the fine scale mechanics of local these suspensions with their macroscale rheology.

3.4.1 Macroscale stresses and nanoscale interaction forces

Keeping in mind the experimental results in sections 2 and 3, the considered TEMPO-oxidized NFC suspensions can be reasonably considered to be stabilized and unflocculated concentrated fiber suspensions with a Newtonian suspending fluid and semi-flexible slender elastic and curved nanofibers. The characteristic geometrical parameters of these elements, namely $d, l, r, n_{seg}, l_{seg}, \theta_{seg}$, were estimated from the micrographs of Fig. 3-1.c-d (Fig 3-4. for idealized representations of the considered NFCs). At the microscale, typically the order of the nanofibril length l, nanofibrils form a connected fibrous network without microscale spatial heterogeneities (Fig. 3-1.c-d, the rare pulp fibers were neglected for simplicity sake). During flow, nanofibrils translate, rotate and deform (see next subsection) with the suspending fluid while being subjected to four principal interaction forces. Two forces are related to their interactions with the suspending fluid far from fiber-fiber contact zones or bonds, namely forces $\mathbf{f}^B$ induced by the Brownian motion in the suspending fluid, and long range hydrodynamic viscous forces $\mathbf{f}^{hl}$ that are also induced by the fluid during the suspension flow. The two other forces, *i.e.*, $\mathbf{f}^{col}$ and $\mathbf{f}^{hs}$, occur in the bond zones and are related to colloidal and short range hydrodynamic viscous interactions, respectively. All the aforementioned nanoscale forces contribute to the

macroscale Cauchy stress tensor $\boldsymbol{\sigma}$ of the considered suspensions. Assuming rationally that the suspensions are incompressible, the stress tensor $\boldsymbol{\sigma}$ can be expressed as follows:

$$\boldsymbol{\sigma} \approx -p\boldsymbol{\delta} + \boldsymbol{\sigma}^{B} + \boldsymbol{\sigma}^{hl} + \boldsymbol{\sigma}^{hs} + \boldsymbol{\sigma}^{col}, \tag{4}$$

where p is the incompressibility pressure, $\boldsymbol{\delta}$ the identity tensor, and where $\boldsymbol{\sigma}^{B}$, $\boldsymbol{\sigma}^{hl}$, $\boldsymbol{\sigma}^{hs}$ and $\boldsymbol{\sigma}^{col}$ represent macroscale stress contributions that are associated with the nanoscale forces $\mathbf{f}^{B}$, $\mathbf{f}^{hl}$, $\mathbf{f}^{hs}$ and $\mathbf{f}^{col}$, respectively. The links between the stress contributions, their associated interaction forces and the microstructure of the suspensions can be deduced from theoretical or numerical upscaling processes.

The stress contribution $\boldsymbol{\sigma}^{B}$ is obtained from the expression reported for rod-like objects[57] with high aspect ratio r:

$$\boldsymbol{\sigma}^{B} = \tfrac{12}{\pi l^3}\phi r^2 k_B T(\mathbf{A} - \tfrac{1}{3}\boldsymbol{\delta}), \tag{5}$$

where k_B is the Boltzmann constant, T the suspension temperature and where $\mathbf{A}$ is the second order fiber orientation tensor[48] that is defined in a discrete form as follows:

$$\mathbf{A} = \tfrac{1}{N}\sum_{i=1}^{N} \mathbf{p}_i \otimes \mathbf{p}_i, \tag{6}$$

where the vectors $\mathbf{p}_i$ represent the mean unit tangent vectors of the N nanofibers i that are contained in a representative elementary volume of the suspension (Fig. 3-4).

A reasonable estimate of $\boldsymbol{\sigma}^{hl}$ induced by long range hydrodynamic forces is obtained from the micromechanical model that has been developed by Lipscomb *et al.*[59] for Newtonian fiber suspensions in the semi-dilute regime:

$$\boldsymbol{\sigma}^{hl} = 2\mu\mathbf{D} + 4\mu\phi(\mathbf{D} + \tfrac{r^2}{4\ln r}\mathbb{A} : \mathbf{D}), \tag{7}$$

where $\mathbf{D} = (\boldsymbol{\nabla}\mathbf{v} + {}^{t}\boldsymbol{\nabla}\mathbf{v})/2$ is the strain-rate tensor ($\mathbf{v}$ being the macroscale suspension velocity and $\boldsymbol{\nabla}\mathbf{v} = \mathbf{v} \otimes \boldsymbol{\nabla}$), and where $\mathbb{A}$ is the fourth order fiber orientation tensor[58], defined as follows:

$$\mathbb{A} = \tfrac{1}{N}\sum_{i=1}^{N} \mathbf{p}_i \otimes \mathbf{p}_i \otimes \mathbf{p}_i \otimes \mathbf{p}_i. \tag{8}$$

The generic expressions of the stress contributions that are induced by viscous and colloidal bond forces are deduced from the following discrete forms[44]:

$$\boldsymbol{\sigma}^{\alpha} = \tfrac{2}{\pi l^3}\phi r^2 z^{\alpha} \xi_c^{\alpha} f_c^{\alpha} \tfrac{1}{B^{\alpha}} \sum_{b=1}^{B^{\alpha}} \boldsymbol{\xi}_b^{\alpha *} \bigotimes \mathbf{f}_b^{\alpha *} \tag{9}$$

where the notation "α" stands either for "hs", *i.e.*, short range hydrodynamic interactions, or for "col", *i.e.*, colloidal interactions. Hence, B^{α} is the total number of α-bonds in the representative volume, whereas z^{α} is the mean coordination number per nanofiber (or the mean number of nanofiber-nanofiber bonds per nanofiber) related to the α-bonds. In addition, $\boldsymbol{\xi}_b^{\alpha *} = \mathbf{G}_i\mathbf{G}_j/\xi_c^{\alpha}$ is the dimensionless placement vector related to the α-bond b, where, (i) as depicted in Fig. 3-4, G_i and G_j are the centers of mass of the two nanofibers i and j interacting at the α-bond b, and (ii) ξ_c^{α} is the characteristic distance $\|\mathbf{G}_i\mathbf{G}_j\|$ between these nanofibers in the representative volume. Finally, $\mathbf{f}_b^{\alpha *} = \mathbf{f}_b^{\alpha}/f_c^{\alpha}$ is the dimensionless α-bond force between the

interacting nanofibers i and j, whereas the scalar f_c^α represents the characteristic value of the force magnitude $\|\mathbf{f}_b^\alpha\|$ of the α-bond.

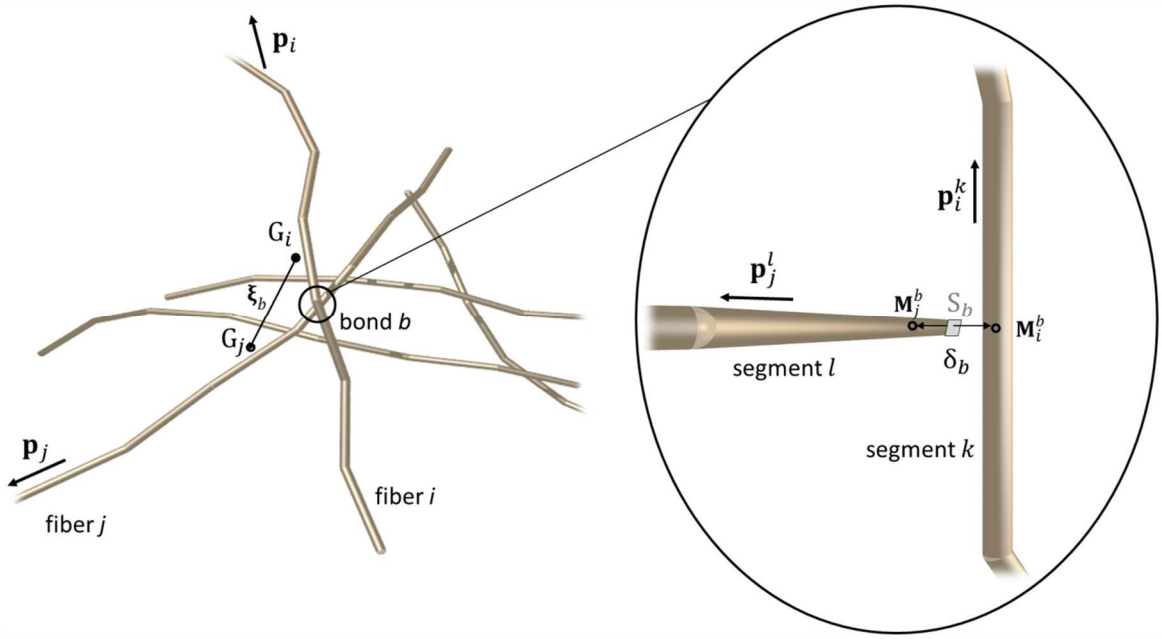

Figure 3-4. Idealized representation of interacting NFCs and zoom on an interaction bond.

The above stress contributions emphasize the major and coupled roles exerted by the NFC suspension fibrous architectures and nanomechanics on their macroscale rheology. They can be calculated from proper estimates of the kinematics of NFCs (subsection 4.2), associated to the fibrous nanostructures (subsection 4.3) and the interaction forces at bonds.

During the suspension flow, two neighboring NFCs i and j interact *via* hydrodynamic interactions. When the distance between two nanofibers is sufficiently large, typically above the nanofiber diameter d, long range hydrodynamics interactions occur. Their effects on the macroscale stress tensor $\boldsymbol{\sigma}$ have been taken into account in the Newtonian stress contribution $\boldsymbol{\sigma}^{hl}$ (eqn (7)). In other cases, *i.e.*, when the inter-fiber distance h^{hs} is below d, a hydrodynamic bond arises and short range hydrodynamic interactions occur[28,27,60]. In this small confined zone of nanoscale size, the molecules of the Newtonian suspending fluid are potentially subjected to complex flow mechanisms, leading to nanoscale lubrication forces $\mathbf{f}_b^{hs}$. Using fine scale simulations with Molecular Dynamics simulation, Barrat and Bocquet[61] showed that the nanoscale efforts required to induce the flow of water molecules remained linear functions of the nanoscale flow rates of the fluid within confined nanoscale size geometries. Hence, for the studied TEMPO-oxidized NFC suspensions, a similar relationship is expected to occur between the nanoscale short-range hydrodynamic force $\mathbf{f}_b^{hs}$ and the relative velocity $\Delta\mathbf{v}_b$ between two bonded nanofibers i and j at the hydrodynamic bond b. As the bonding zone depends on the relative orientation of the interacting nanofibers (Fig. 3-4), it was assumed that the short-range hydrodynamic force $\mathbf{f}_b^{hs}$ varies as a function of S_b, *i.e.*, the rhomb surface defined by the projection of the bonded nanofibers onto the normal plane of the bonding zone[54,62]

$$S_b = \frac{d^2}{\|\mathbf{p}_i^k \times \mathbf{p}_j^l\|}, \tag{10}$$

where the unit vectors $\mathbf{p}_i^k$ and $\mathbf{p}_j^l$ are the tangent vectors of the two fiber segments k and l, belonging to the contacting fibers i and j, respectively. Thus, the following linear form of $\mathbf{f}_b^{hs}$ is assumed:

$$\mathbf{f}_b^{hs} = \eta S_b \Delta \mathbf{v}_b, \tag{11}$$

where η can be regarded as an equivalent nanoscale bond viscosity. Hence, from the dimensionless framework in eqn (9), the above expression yields the following expression of the characteristic hydrodynamic interaction force f_c^{hs}:

$$f_c^{hs} = \eta S_{bc} \Delta v_{bc}, \tag{12}$$

where S_{bc} and Δv_{bc} are characteristic values of S_b and $\|\Delta \mathbf{v}_b\|$, respectively.

In the studied stabilized TEMPO-oxidized NFC suspensions, nanofibers also interact with their neighbors *via* repulsive colloidal long-range electrostatic forces $\mathbf{f}_b^{col}$. In an simplified view, these colloidal forces arise from the interpenetration of the ion layers that surround each NFC in colloidal bonding zones[27,28,63]. Thus, their intensity is expected to vary as a function of (i) the distance δ_b^{col} between the two nanofiber segments of nanofibers in interaction[27,28] and, (ii) the characteristic of the bond surface S_b (as for $\mathbf{f}_b^{hs}$). This leads to the following generic expression for the colloidal forces $\mathbf{f}_b^{col}$:

$$\mathbf{f}_b^{col} = \sigma^{col}(\delta_b^{col}) S_b \frac{\Delta \mathbf{v_b}}{\|\Delta \mathbf{v_b}\|} \tag{13}$$

where σ^{col} is a colloidal force per unit of bond area. Its intensity depends on the NFC-NFC distance δ_b^{col} and the NFC ionic environment. Thus, introducing characteristic values σ_c^{col} and δ_c^{col} that are associated with σ^{col} and δ^{col}, respectively, the characteristic colloidal force f_c^{col} in eqn (9) is expressed as follows:

$$f_c^{col} = \sigma_c^{col}(\delta_c^{col}) S_{bc}. \tag{14}$$

In colloidal systems where repulsive electrostatic forces dominate, the critical thickness h^{col} above which these interactions can be neglected is taken as the critical Debye screening length κ^{-1}. Several studied have shown the drastic effects of the Debye screening length κ^{-1} on the rheology of colloidal systems[27,28,63,64]. Thus, to determine the occurrence of colloidal interaction forces in the studied NFC systems, κ^{-1} was estimated using the methodology proposed by Ishii *et al.*[65] for aqueous TEMPO-oxidized NFC suspensions. Assuming that (i) the major ionic species of the aqueous NFC suspensions are Na^+ and COO^- (dissociated carboxylate groups), and (ii) neglecting the effect of counter ion condensation, κ^{-1} can be written as follows:

$$\kappa^{-1} \propto (8\pi l_B \rho N_A \Gamma_{COOH} \phi)^{-0.5}, \tag{15}$$

where l_B is the Bjerrum length (= 0.71 nm in water at 25°C), ρ is the specific mass of cellulose ($\simeq$ 1500 kg m^{-3}) and N_A the Avogadro's constant. According to the last expression, the Debye

screening length κ^{-1} ranges between 2.5 nm (for $\phi = 0.0067$) and 6 nm (for $\phi = 0.0013$). It increases with decreasing NFC content ϕ and the dilution of NFC suspensions with pure water decreases the ionic concentration and thus the electric screening induced by these ions. Above this inter-fiber distance, colloidal interactions are supposed to be negligible, whereas below, interaction forces occur following the generic eqn (13).

3.4.2 Kinematics of NFCs

Eqns. (11) and (13) show that it is necessary to get a relevant estimate of the relative velocity field $\Delta\mathbf{v}_b$ to assess the bonding forces $\mathbf{f}_b^{hs}$ and $\mathbf{f}_b^{col}$ and their associated macroscale stress contributions eqn (9). A possible method would consist in solving numerically momentum balances for all the NFCs contained in representative volumes[66,67,68]. This would provide exact values of $\Delta\mathbf{v}_b$ but would conduct to extremely long computation times. Instead, as commonly achieved to build relevant macroscale analytic estimates of the macroscale stress contributions[53,55,39], nanoscale kinematical hypotheses were stated for the motion of NFCs during the suspension flow as described hereafter. Hence, the motions of the centers of mass G_i and G_j of two NFCs linked at bond b are affine functions of the macroscale velocity field $\mathbf{v}$ of the suspension, so that their relative velocity $\Delta\mathbf{v}_{bG}$ is expressed as follows

$$\Delta\mathbf{v}_{bG} = \mathbf{v}_{G_j} - \mathbf{v}_{G_i} \approx \boldsymbol{\nabla}\mathbf{v} \cdot G_iG_j \tag{16}$$

In addition, we assumed that the deformation of NFCs during the suspension flow remains limited (this will be further discussed in the following section), so that at a first order approximation, NFCs are only subjected to translations and rotations.

Finally, the rotation of the NFCs was approached by Jeffery-based models[40,37]. As other fiber suspensions, the orientation of NFCs during flow drastically evolves[12,3], which affects the suspension rheology (eqn (17)). The Jeffery-based models capture the main features of these evolutions. Thus, the rotation $\dot{\mathbf{p}}_i$ of the mean orientation vector $\mathbf{p}_i$ of the NFC i was expressed as:

$$\dot{\mathbf{p}}_i = \mathbf{W}\cdot\mathbf{p}_i + \lambda(\mathbf{D}\cdot\mathbf{p}_i)\cdot(\boldsymbol{\delta} - \mathbf{p}_i\bigotimes\mathbf{p}_i) + D_r\tfrac{1}{\psi}\tfrac{\partial\psi(\mathbf{p})}{\partial\mathbf{p}}(\boldsymbol{\delta} - \mathbf{p}_i\bigotimes\mathbf{p}_i), \tag{17}$$

where $\mathbf{W} = (\boldsymbol{\nabla}\mathbf{v} - {}^t\boldsymbol{\nabla}\mathbf{v})/2$ is the vorticity tensor and where λ is a shape factor related to the geometry of the nanofibers (see Appendix 1 in Supplementary Materials for the used estimate). The last term of the right side of eqn (17) was initially proposed to account for Brownian rotary diffusion. It depends on the orientation distribution function $\psi(\mathbf{p})$ and its gradient and introduces a Brownian rotary diffusion coefficient D_r. In this study, this mechanism was *a priori* neglected. As pointed out later, Brownian effects are shown to play a secondary role on the rheology of the studied suspensions within the investigated testing conditions (Fig. 3-7). However, it is also well known that the rotation of a fiber in concentrated fiber suspensions is restrained by the presence of its neighbors[69,68,70,71]. To account for this phenomenon, we used Jeffery's equation purposely modified by Folgar and Tucker[37], where the constant D_r in eqn

(17) has been replaced by $C_I\sqrt{2\mathbf{D}:\mathbf{D}}$, and where the dimensionless interaction coefficient C_I[37,70] (typically ranging between 10^{-2} and 10^{-3}) gauges the importance of this effect.

Hence, the bond relative velocity $\Delta\mathbf{v}_b$ is expressed as follows, accounting for the aforementioned assumptions:

$$\Delta\mathbf{v}_b = \Delta\mathbf{v}_{bG} + \left\|\mathbf{G}_j\mathbf{M}_j^b\right\|\dot{\mathbf{p}}_j - \left\|\mathbf{G}_i\mathbf{M}_i^b\right\|\dot{\mathbf{p}}_i, \tag{18}$$

where M_i^b and M_j^b are located on the centerlines of the NFCs i and j, respectively, below and above the bond b (Fig. 3-4), and where $\Delta\mathbf{v}_{bG}$ and $\dot{\mathbf{p}}_k$ ($k = i$ and j) are estimated using eqn (16) and (17), respectively.

3.4.3 Microstructure modeling

The experimental characterization of the microstructures formed by NFCs in water suspension (at rest but also during shearing) is a challenging problem. The morphology of NFCs is usually characterized using AFM and TEM images in a dry state (Fig. 3-1)[48]. Few studies attempted to get structural information using NFC suspensions. Using small-angle X-ray scattering (SAXS) analyses, Torres-Randon *et al.*[2] and Håkansson *et al.*[3] showed that NFCs aligned along the flow direction while being sheared in Poiseuille-like flow configurations with micrometric characteristic size. However, compared with non-colloidal fibrous systems[62,71,73] due to the nanoscale size of the NFCs, it is still difficult to get direct 3D images of their architectures in the suspensions. To circumvent this difficulty, we used a numerical generation process to mimic realistic suspension architectures, gathering both data obtained in section 3 and Fig. 3-1 and those from the literature[3,12]. Thus, idealized three-dimensional NFC networks of representative elementary volume Ω of size $V = 1400 \times 1400 \times 1400$ nm^3 were generated extending the methodology proposed by Le Corre *et al.*[54] and Vassal *et al.*[74]. This procedure is detailed in Appendix 2 in Supplementary Materials.

The connectivity of the generated NFC networks was assessed using a deterministic methodology based on a soft-core approach similar to that adopted in the tube-model approaches[56,62]. Note that these approaches are known to provide relevant estimation of the connectivity of fibrous systems with slender fibers[62,73]. Hence, a cylindrical control volume Ω_α of size $V_\alpha = \pi l_{seg}(d + h^\alpha)^2$ centered on the centerline of the segment k belonging to a fiber i was defined. The parameter h^α was the inter-bond distance above which the α-bond interaction forces could be considered to be negligible. The parameter h^α was d and $2\kappa^{-1}$ for *hs* or *col* bonds, respectively. Each fiber segments l that belonged to a fiber j whose centerline intersected the control volume Ω_α was added to the connectivity set of bonds B^α. It was checked that this generation procedure yielded the prediction of the analytical tube model for straight fibers ($\theta_{seg} = 0$)[56]. In this case, the tube model prediction of the fiber coordination number z was

$$z = 4\left(\frac{d+h_\alpha}{d}\right)^2\phi\left(\frac{2}{\pi}\frac{l}{(d+h_\alpha)}\Phi_1 + \Phi_2 + 1\right), \tag{19}$$

where the discrete expressions for the orientation functions Φ_1 and Φ_2 were defined as follows:

$$\Phi_1 = \frac{1}{N^2}\sum_{i=1}^{N}\sum_{j=1}^{N}\left\|\mathbf{p}_i \otimes \mathbf{p}_j\right\| \qquad \text{and} \qquad \Phi_2 = \frac{1}{N^2}\sum_{i=1}^{N}\sum_{j=1}^{N}\left|\mathbf{p}_i \cdot \mathbf{p}_j\right|. \tag{20}$$

Fig. 3-5 and 3-6 show several microstructural descriptors that were calculated for the generated NFC networks with 3D random and for marked flow-induced orientations. To obtain these descriptors, 20 elementary volumes per investigated microstructure configuration were generated to get mean trends and error bars. The following comments can be drawn from these figures.

Fig. 3-5.e-f show the distribution of the projected bonding areas S_b, *i.e.,* the rhomb surface formed by two mutually bonded nanofibers, as defined in eqn (10). This geometric parameter only depended on the nanofiber orientation[76] and was not affected neither by the nanofiber content ϕ, nor by the thickness h^α. Thus, orientated fibrous networks induced an enlargement of the S_b-distribution towards higher values, leading to an increase in the mean characteristic value S_c.

The distribution of the distance $\|\boldsymbol{\xi}_b^\alpha\|$ between centers of mass for the mutually interacting fibers is shown in the histograms of Fig. 3-5.e-f. Regardless of the fibrous network orientation, the mean characteristic value ξ_c did not depend on h^α and was close to $l/3$, even if the shapes of the distribution functions exhibited some slight differences. Others numerical experiments (not shown here) revealed that ξ_c was mainly affected by nanofiber clustering[76], *i.e.*, the spatial repartition of the centers of mass G_i in Ω, and by the NFC waviness that was controlled by θ_{seg}.

Fig.3-6.a-b shows the evolution of the mean coordination numbers z^α as a function of the NFC content ϕ. Regardless of the type of α-bonds, namely hydrodynamic *hs*, colloidal *col* or purely geometrical 0 (corresponding to $h^0 = 0$) bonds, z^α (i) reached non negligible values even at the very low investigated NFC contents, (ii) and drastically increased with the NFC content ϕ. Considering eqn (9), this effect is expected to severely increase bond stress contributions. In accordance with eqn (20) and eqn (15), the mean coordination numbers z^α were affine or power-law type (with a power-law exponent close to 0.65) functions of ϕ for hydrodynamic or geometrical bonds, and for colloidal bonds, respectively. Note also that, regardless of the NFC orientation and content, the coordination numbers were much higher for *hs* and *col*-bonds than for the purely geometrical case.

Although an increase in S_c is observed with increasing the NFC orientation (Fig. 3-5.e,f), orientated fibrous networks exhibited in the same time much lower coordination numbers z^α (Fig. 3-6). These combined and competing effects could alter the bond stress contributions (eqn (9)). In addition, Fig. 3-6 shows that the NFC waviness has an important effect on the network connectivity. This effect is limited for 3D microstructures (Fig. 3-6.a), whereas a noteworthy increase in the mean coordination number with the NFC waviness is observed for orientated microstructures (Fig. 3-6.b).

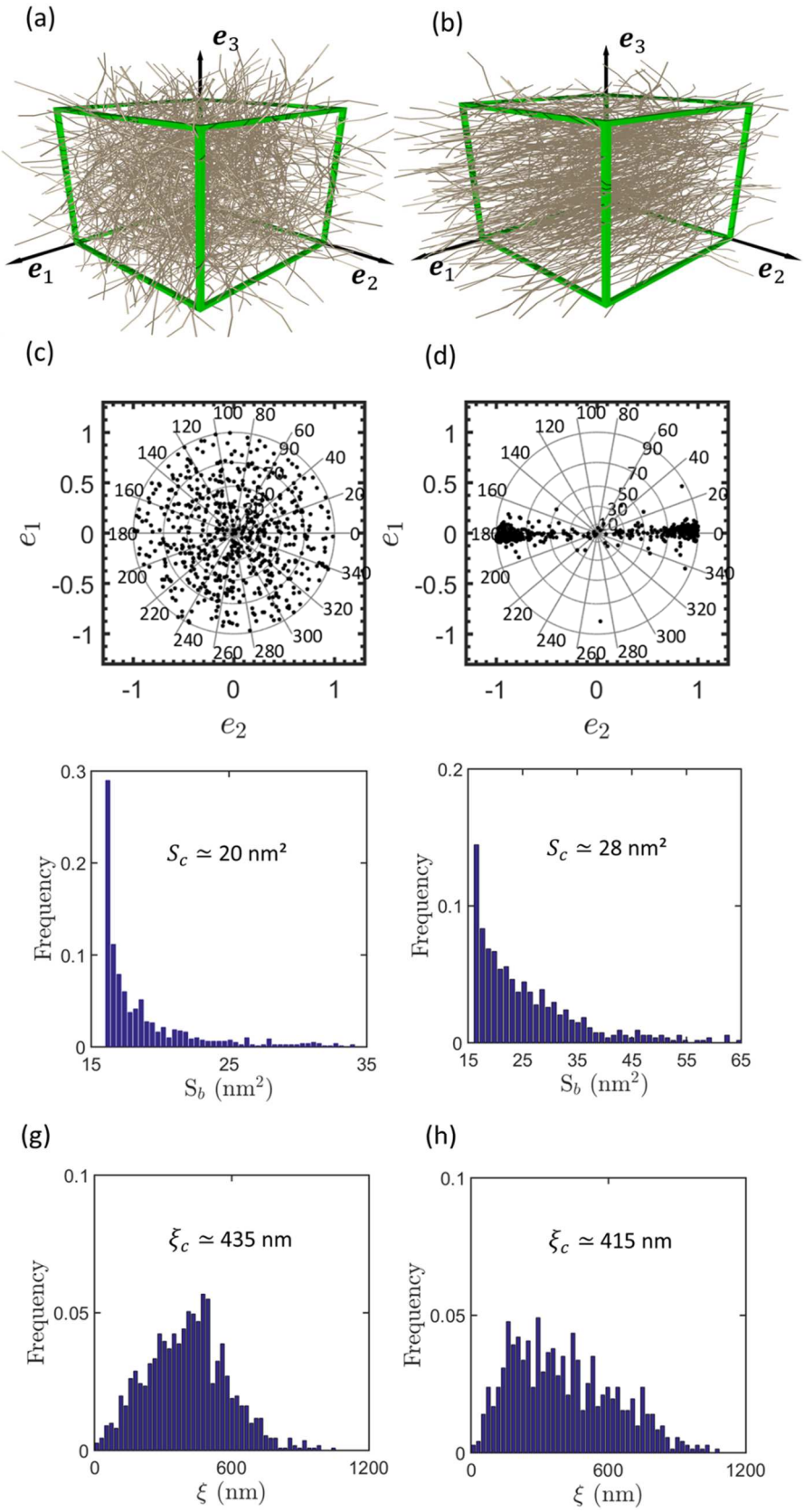

Figure 3-5. Example of two idealized NFC networks for a nanofiber content $\phi = 0.004$ with 3D random orientation (a) and flow-induced orientation (b). For both types of microstructures, the orientation vectors p_i of each tortuous NFC i were represented using a stereographic projection (pole figure of orientation) along the e_3-direction (c,d). Typical distribution histograms of the projected bonding area S_b (e,f) and of the distance $\|\xi_b^\alpha\|$ between the centers of mass of interacting NFCs (g,h).

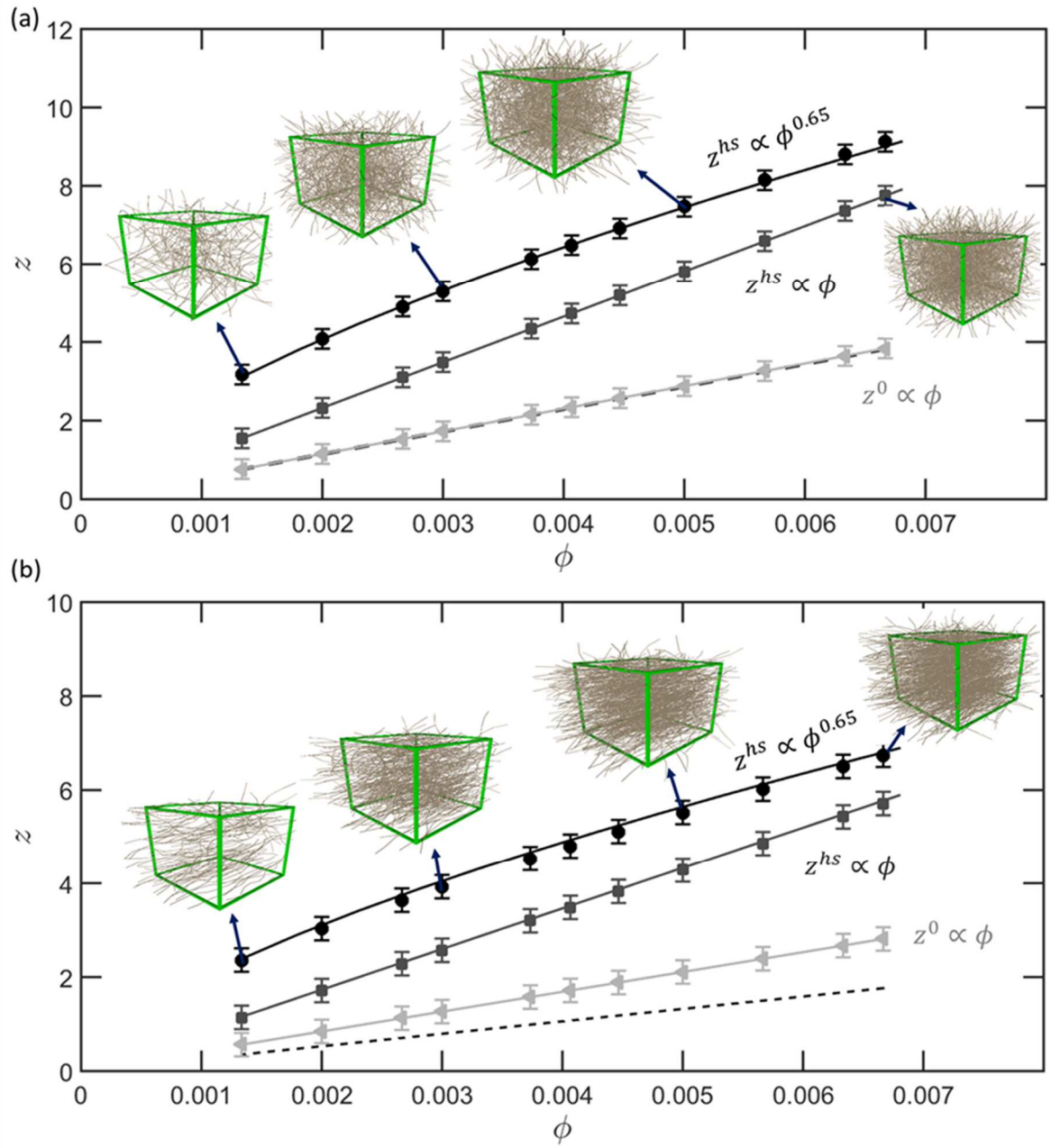

Figure 3-6. Evolution of the mean coordination numbers z^α as a function of the NFC content ϕ for NFC architectures with various interaction thicknesses h^α (namely $h^0 = 0, h^{hs} = d, h^{col} = 2\kappa^{-1}$), NFC waviness ($\theta_{seg} = \pi/8$), for 3D random orientations (a) or flow-induced orientations (b). In both graphs, the dashed lines represent the evolution of the mean coordination numbers z^0 for straight NFCs ($\theta_{seg} = 0$) and $h^0 = 0$).

3.5 Model prediction and discussion

From the experimental microstructure measurements combined with the analytical and numerical developments presented in the two previous sections, stress contributions involved in eqn (4) were assessed and compared with rheometry results (section 3). For that purpose, the steady state flow curves shown in Fig. 3-2 were fitted using eqn (5-9) and the generated flow-induced microstructures (section 4). This approach enabled the forces f_c^{col} and f_c^{hs} to be determined. The two graphs shown in Fig. 3-7.a-b illustrate the relevance of this procedure for a low and a high NFC content ϕ, respectively. The model prediction fits fairly well the experimental trends, namely the occurrence of a steady state macroscale yield stress τ_0 at low macroscale shear rates $\dot{\gamma}$, with a progressive shear thinning behavior as $\dot{\gamma}$ is increased. The increase of τ_0 with ϕ is also well reproduced by the model, as illustrated in Fig. 3-7. Fig. 3 7.a-b also shows the evolution of the different stress contributions used in eqn (4) to compute the macroscale steady state shear stress τ. Several interesting remarks listed in the following paragraphs can be drawn, independently from the considered nanofiber orientation.

Regardless of the shear rate and the NFC content, the Brownian shear stress contribution τ^B was always at least two decades lower than the experimental values recorded for τ. Accordingly, this result demonstrates that Brownian motion and its stress-induced contribution play a minor role in the rheology of the stabilized TEMPO-oxidized NFC suspensions, at least for the studied flow conditions. This result also supports the *a priori* assumption, stated in subsection 4.2, that the flow-induced evolution of the NFC orientation could be predicted using a modified Jeffery's equation without Brownian diffusion term.

As expected, long range hydrodynamic interactions and their macroscale stress contributions τ^{hl} increased linearly as a function of $\dot{\gamma}$. The shear stress τ^{hl} was very small at low shear rates, *i.e.*, in the same order of magnitude as the Brownian stresses. At the highest shear rate (10^3 s^{-1}), its magnitude represented $\approx 20\%$ to $\approx 2\%$ of the macroscale shear stress as the NFC content was increased from 0.0013 to 0.0067. Thus, at high shear rates and low fiber contents, long range hydrodynamic interactions contributed to the overall suspension stress. Otherwise, they have a second order effect. Together with the conclusions drawn in the previous point, this also suggests that both short range hydrodynamics and colloidal interactions mainly govern the rheology of the stabilized TEMPO-oxidized NFC suspensions.

Fig. 3-7.a-b shows that the short range stress contribution τ^{hs} increased linearly as a function of $\dot{\gamma}$. This property is directly connected to the Newtonian expression of the forces $\mathbf{f}_b^{hs}$ (see eqn(11)). Using a rigorous upscaling process, *i.e.*, without the *a priori* affine assumption eqn. (16)), Le Corre *et al.*[77] theoretically proved that for such Newtonian interaction forces, the macroscale stress tensor $\boldsymbol{\sigma}^{hs}$ was a linear function of the macroscale strain rate tensor $\mathbf{D}$. In addition, Fig. 3-7.a-b also shows that τ^{hs} is in the same order of magnitude as τ^{hl} for the lowest NFC content, whereas, for the highest contents, τ^{hs} was at least ten times higher, showing that τ^{hl} mainly contributed to the viscous behavior of the suspensions as the shear rate was increased.

The colloidal stress contribution τ^{col} was the major stress contribution at low shear rates (Fig. 3-7.a-b): a sufficient macroscale external stress is required to overcome repulsive colloidal forces to continuously extract NFCs from their current network configuration towards a new one with identical steady state structure descriptors.

The physical origins of the shear thinning behavior observed in colloidal systems are multiple, and still constitute an open question[29]. In the developed model, the potential origin of the shear thinning behavior of NFC suspensions could be the simultaneous occurrence of colloidal and short (in some cases long) range hydrodynamic interactions in a high shear rate regime that ranged from 10 to 10^3 s^{-1} [27,28].

The conclusions drawn from the previous points are still valid when the model was fitted for 3D random fibrous networks, *i.e.*, when the potential flow-induced orientation was not taken into account.

To further discuss the results and their relevance, Fig. 3-7.d shows the evolution of the characteristic colloidal forces f_c^{col} at low shear rates as a function of the NFC content ϕ. The estimated colloidal forces were very small (< 1 pN) and fell within the range that could be expected from (i) the idealized DLVO theory with the considered electrostatic potentials[78,79], and (ii) from the measured forces for model colloidal systems[78]. Fig. 3-7.d also shows the effect of the orientation of the NFC fibrous networks since flow-induced structures yielded colloidal forces twice higher than for 3D random networks. This effect could be related to the lower coordination number z^{col} for the orientated networks (Fig. 3-6)). In addition, Fig. 3-7.d shows the pronounced increase of f_{c0}^{col}, as a function of ϕ at low shear rates. Regardless of the fibrous orientation, the same relationship $f_{c0}^{col} \propto \phi^{1.35}$ was obtained. This trend could be related to two combined effects: the decrease in the Debye length κ^{-1} (see eqn (15)) and the variations in the electrostatic interaction potentials with increasing the NFC content ϕ.

Fig. 3-7.a-b and Fig. 3-7.e,f show that the shear stress τ^{col} and colloidal forces f_c^{col} increased with increasing the shear rate $\dot{\gamma}$. As expected, the same trend is obtained for long and short range hydrodynamic interaction forces (Fig. 3-7.e,f). These nanoscale interactions may induce the deformation of NFCs (assumed to remain limited in the developed model). This would lead to an increase in the elastic energy stored into the NFCs and to a decrease in the inter-bond distance δ^{col}, *i.e.*, to an increase in the electrostatic forces and consequently in the shear stress τ^{col}. This scenario should be confirmed using for example direct simulation at the NFC scale.

Finally, the relevance of the model was assessed in regards with the network connectivity. A macroscale shear yield stress at low shear rates results from the existence of a continuous network of connected colloidal nanofibers along the sheared thickness of the suspension. This condition is fulfilled when the mean coordination of the NFC network is above the geometrical percolation threshold, *i.e.*, above a critical coordination number z_c. Berhan and Sastry[80] studied the percolation threshold for networks of helical fibers using a generation procedure that

was similar to that of this study. For fiber networks with 3D random orientation, these authors have shown that z_c can be expressed as follows:

$$z_c = 1 + c_1(2r)^{-c_2}, \tag{21}$$

where $c_1 = 5.231$ and $c_2 = 0.569$ for straight fibers and $c_1 = 11.156$ and $c_2 = 0.664$ for curved fibers that are similar to the studied NFCs. In both cases, z_c is close to 1.15. Further, Balberg *et al.*[81] also demonstrated that the percolation threshold z_c for orientated straight fibers in the perpendicular direction to the fiber alignment was close to that for isotropic networks. This prediction was obtained using a volume excluded theory that was similar to the tube model, replacing the cylinder by a sphero-cylinder. Consequently, a critical percolation threshold is expected to occur when $z_c^0 > 1.15$ for the studied NFC suspensions. Fig. 3-6.b shows that this condition was not fulfilled for orientated networks and for $\phi < 0.003$ when the connectivity was estimated using the geometrical coordination number z^0. On the contrary, a shear yield stress should practically exist for all NFC contents, accounting for the colloidal forces. Indeed over the investigated range of NFC content, the connectivity z^{col} was above the critical coordination number z_c^{col}, that ranged between 1.43 and 1.27 as the NFC content ϕ increased from 0.0013 to 0.0067 (note that to estimate values of z_c^{col}, we took into account the NFC diameter and the Debye length in the estimate of the aspect ratio r in eqn (21), *i.e.*, $r = l/(d + h^{col})$.

A similar reasoning applies for the short range hydrodynamic forces. In this case, the percolation should be attained for $z_c^h > 1.25$. Fig. 3-6.b shows that the connectivity z^{hs} was also above this critical coordination number except for the lowest investigated NFC content.

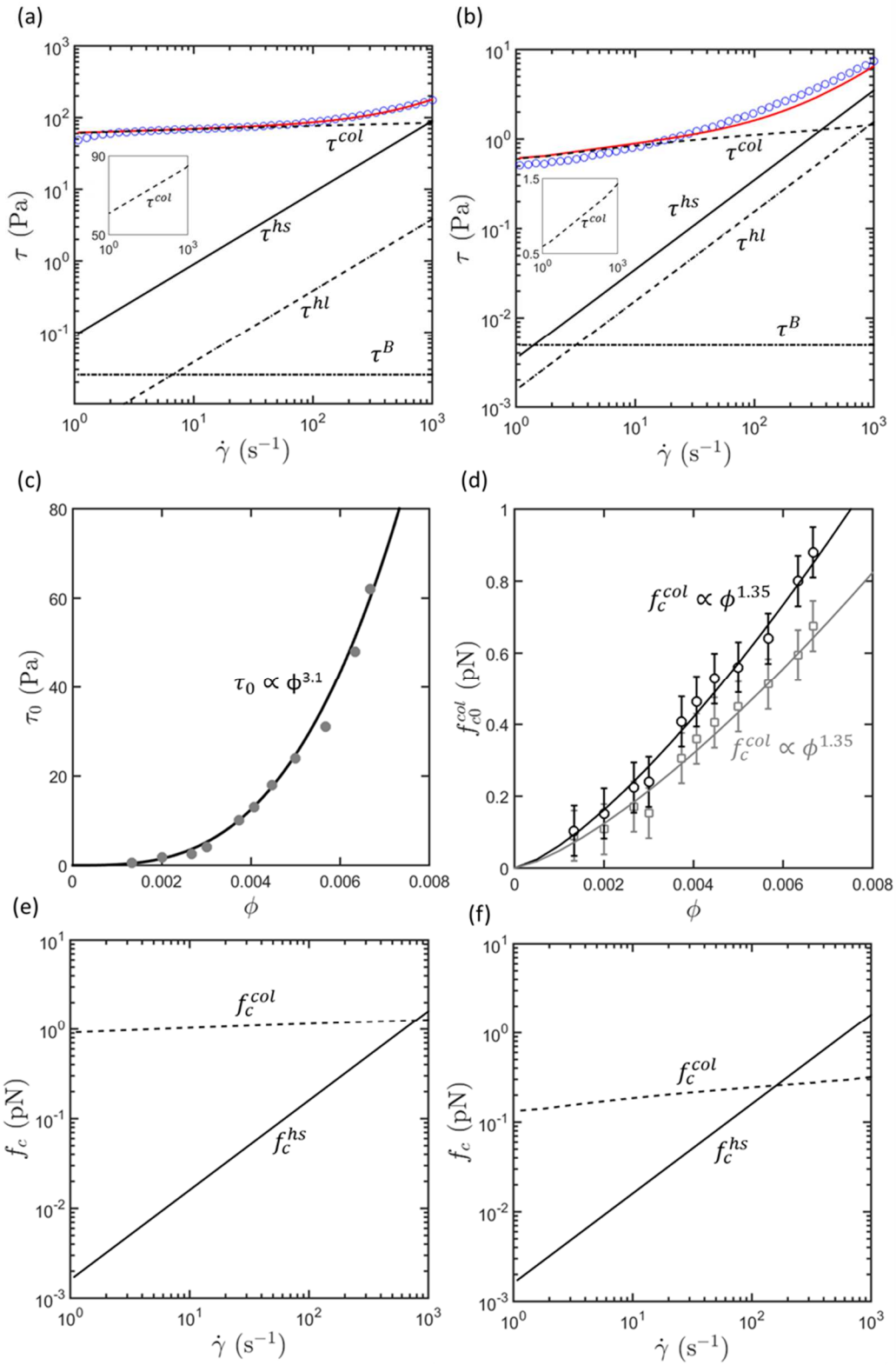

Figure 3-7. (a-b) Macroscopic steady state shear stress as a function of the shear rate (curves with blue circle symbols) obtained for two TEMPO-oxidized NFC suspensions ($\phi = 0.0067$ and $\phi = 0.0013$), and prediction of the micromechanical (continuous red lines). The other lines represent the contributions that are induced by the Brownian motion τ^B, long and short hydrodynamic interactions τ^{hl}, τ^{hs} and colloidal interactions τ^{col}. (c) Prediction of the dynamic yield stress τ_o of the micromechanical model. (d) Evolution of the characteristic colloidal force f_c^{col} as a function of the NFC content ϕ for random (grey color) and orientated fibrous microstructures (black color). (e-f) Predictions of the characteristic colloidal f_c^{col} and short hydrodynamic forces f_c^{hs} as a function of $\dot{\gamma}$ for two TEMPO-oxidized NFC suspensions ($\phi = 0.0067$ and $\phi = 0.0013$).

3.6 Conclusion

The objective of this study was to relate the macroscale rheology of NFC suspensions to their complex nanostructure and deformation nano-mechanisms. For that purpose, we characterized the shear rheology of stabilized and unflocculated NFC colloidal suspensions, namely TEMPO-oxidized NFC aqueous suspensions at high pH and low ionic strength. The geometry of NFCs was characterized from TEM images, showing that NFCs could be considered to be slender and wavy fibers with nanometric diameters. The steady state rheology of the NFC suspensions was studied using plate-plate and Couette rheometers, showing that the suspensions behaved as Herschel-Bulkley fluids with a shear-thinning behavior. The yield stress and the consistency of these suspensions were power-law functions of the NFC content.

Besides, an original multiscale model was developed for the prediction of the observed experimental trends. NFC suspensions were considered to be stabilized and unflocculated colloidal and concentrated suspensions. The suspending fluid was seen as Newtonian and NFCs were considered to be slender and wavy nanofibers subjected to translation and rotation motions. The model took into account the contributions to the macroscale rheology of NFC suspensions of the interaction forces between the fluid and the NFCs, namely Brownian and long range fluid-NFC hydrodynamic interactions, as well as nanoscale short range hydrodynamic and repulsive colloidal interactions between NFCs. The nanoscale constitutive parameters of the model were identified using the experimental database and realistic 3D networks of NFCs that were numerically generated to mimic the nanostructures of NFC suspensions under shear flow.

For the studied flow conditions, the model prediction showed that both short range hydrodynamics and colloidal interactions mainly governed the rheology of TEMPO-oxidized NFC suspensions. On the contrary, Brownian motion, and its stress-induced contribution only played a minor role in the rheology of TEMPO-oxidized NFC suspensions. Similarly, the contribution of long range hydrodynamic interactions was minor, except for high shear rates and low NFC contents. The main contributor to the viscous macroscopic stress was short range hydrodynamic interactions. At low shear rates ($\approx 1\ s^{-1}$), colloidal interactions between NFCs were the major stress contribution and could be at the origin of a steady state yield stress. At high shear rates, the contribution of colloidal interactions was in the same order of magnitude than that of short (in some cases long) range hydrodynamic interactions. The simultaneous occurrence of colloidal and short (in some cases long) range hydrodynamic interactions could be at the origin of the shear thinning behavior of NFC suspensions for shear rates that ranged from 10 to $10^3\ s^{-1}$.

The model enabled both characteristic colloidal and short range hydrodynamic forces to be estimated. The estimated colloidal forces were very small: approximately 1 pN for the highest shear rates. These forces were in the same order of magnitude as those that could be expected from the DLVO theory or from measured forces for model colloidal systems[10,78].

The suitability of the model was also assessed in regards with the NFC network connectivity. In the entire range of investigated NFC contents, the mean coordination number of the NFC network estimated by taking into account the Debye length was higher than the theoretical percolation threshold which represents the lower limit for the existence of a yield shear stress.

The proposed multiscale model could be enhanced to extend its validity domain. For example, it could be interesting to take into account the bending and the twisting of NFCs induced by colloidal and hydrodynamic forces. Taking into account these mechanisms into a semi-analytical model still constitutes a challenging task for networks of slender fibers with long inter-bond distances, such as the studied NFC networks[32]. Direct simulations at the NFC scale would probably provide useful information. Attractive colloidal forces could also be taken into account to model the rheology of flocculated systems. This is a very challenging task. Despite recent progress for the description of the motion of rigid clusters made of non-Brownian and non-colloidal fibers in dilute regime[82], this remains an open question for concentrated colloidal fiber suspensions.

3.7 Appendix 1

For a prolate ellipsoid with an aspect ratio $r' = a/b$ (where a and b are the major and minor axes of the prolate ellipsoid, respectively), the shape factor writes $\lambda = (r'^2 - 1)/(r'^2 + 1)$[40]. For more complicated particles such as the studied NFCs, the estimate of λ is not straightforward[72]. For simplicity sake, as depicted in Fig. 3-8, a first order estimation of λ was used. Hence, the coefficient λ was calculated from the prolate ellipsoid that displays the same inertia axes and moments as NFC i.

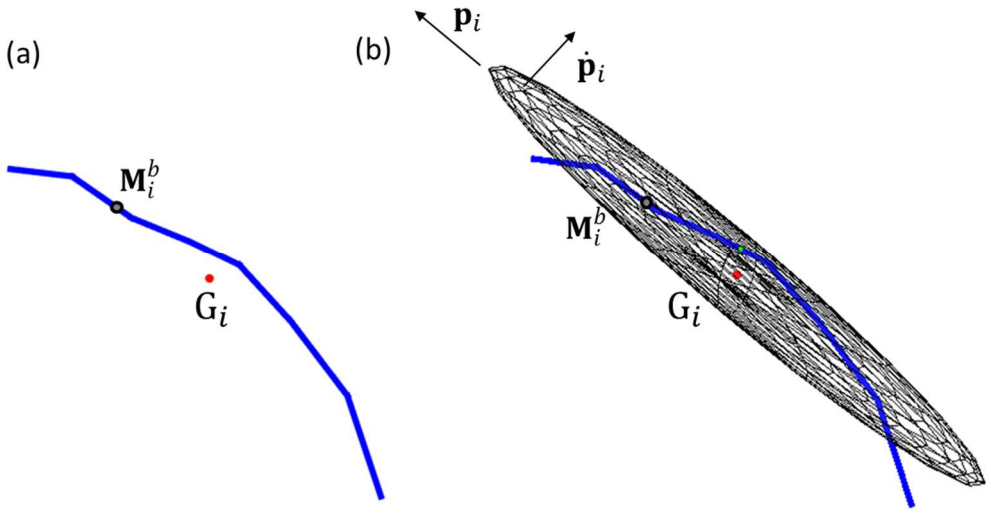

Figure 3-8. Sketch that shows (a) the NFC i and (b) its associated equivalent prolate ellipsoid with the same inertia axes and moments.

3.8 Appendix 2

Each tortuous nanofiber i of diameter d and length l contained n_{seg} straight segments of length l_{seg} that had a random relative misorientation θ_{seg}. Their center of mass G_i was randomly placed in the elementary volume Ω. Following this procedure, various fibrous networks with various nanofiber contents ϕ were generated with random orientation of nanofibers, *i.e.*, the generated microstructures exhibited isotropic fiber orientation with second order orientation tensors $\mathbf{A} = \frac{1}{3}\mathbf{e}_i \otimes \mathbf{e}_i$ (Fig. 3-5.a and Fig. 3-5.c for the corresponding pole figure of orientation). This type of microstructures was chosen because it constituted a reference state, potentially close to that of NFC suspensions at rest (where Brownian motion presumably induces particle dispersion[3,57]).

To mimic microstructures with a pronounced NFC orientation along the flow direction[3] under shear flow, *i.e.*, for $\boldsymbol{\nabla}\mathbf{v} = \dot{\gamma}\mathbf{e}_1 \otimes \mathbf{e}_2$, the evolution of the mean orientation vector $\mathbf{p}_i$ of each NFC i was computed up to the steady state overall orientation of the fibrous networks, solving the Jeffery-based model (eqn (17)) with $D_r = \mathrm{C_I}\sqrt{2\mathbf{D}:\mathbf{D}}$ and $C_I = 10^{-3}$[37,70]. For convenience, calculations were done using the expansion in spheric harmonics up to the fourth order[58] of the orientation distribution ψ . Hence, the following approximation was used[75]:

$$\frac{1}{\psi}\frac{\partial\psi(\mathbf{p})}{\partial\mathbf{p}} \approx 4\frac{-21\mathbf{A}\cdot\mathbf{p}+63\mathbf{p}\cdot\mathbb{A}:\mathbf{p}\otimes\mathbf{p}}{3-42\mathbf{A}:\mathbf{p}\otimes\mathbf{p}+63\mathbf{p}\otimes\mathbf{p}:\mathbb{A}:\mathbf{p}\otimes\mathbf{p}}, \tag{22}$$

All the simulations were run using Matlab and a suitable time step $\Delta t = \Delta\gamma/\dot{\gamma}$ such that $\Delta\gamma = 0.01$ until reaching a steady state, which was close to a shear strain $\gamma = 100$. Then, the simulation procedure led to orientated fibrous microstructures with $\mathbf{A} \approx 0.9\mathbf{e}_1 \otimes \mathbf{e}_1 + 0.05\ (\mathbf{e}_2 \otimes \mathbf{e}_2 + \mathbf{e}_3 \otimes \mathbf{e}_3)$ (Fig. 3-5.b and Fig. 3-5.d for the corresponding pole figures of orientation). In accordance with the Jeffery-based models, it is worth to note that the resulting fiber orientation only depended on initial orientation state and on the applied shear strain, but not on the shear rate $\dot{\gamma}$.

References

1 A. Dufresne, Nanocellulose: From Nature to High Performance Tailored Materials, Walter de Gruyter, 2012.

2 J. G. Torres-Rendon, F. H. Schacher, S. Ifuku and A. Walther, Biomacromolecules, 2014, 15, 2709–2717.

3 K. M. O. Håkansson, A. B. Fall, F. Lundell, S. Yu, C. Krywka, S. V. Roth, G. Santoro, M. Kvick, L. Prahl Wittberg, L. Wågberg and L. D. Söderberg, Nat. Commun., 2014, 5.

4 A. J. Benítez, J. Torres-Rendon, M. Poutanen and A. Walther, Biomacromolecules, 2013, 14, 4497–4506.

5 Y. Kobayashi, T. Saito and A. Isogai, Angew. Chem., 2014, 126, 10562–10565.

6 R. J. Moon, A. Martini, J. Nairn, J. Simonsen and J. Youngblood, Chem. Soc. Rev., 2011, 40, 3941–3994.

7 T. Saito, Y. Nishiyama, J.-L. Putaux, M. Vignon and A. Isogai, Biomacromolecules, 2006, 7, 1687–1691.

8 A. Isogai, T. Saito and H. Fukuzumi, Nanoscale, 2011, 3, 71–85.

9 K. Sim, J. Lee, H. Lee and H. J. Youn, Cellulose, 2015, 22, 3689–3700.

10 H. Fukuzumi, R. Tanaka, T. Saito and A. Isogai, Cellulose, 2014, 21, 1553–1559.

11 A. B. Fall, S. B. Lindström, O. Sundman, L. Ödberg and L. Wågberg, Langmuir, 2011, 27, 11332–11338.

12 H. Sehaqui, N. Ezekiel Mushi, S. Morimune, M. Salajkova, T. Nishino and L. A. Berglund, ACS Appl. Mater. Interfaces, 2012, 4, 1043–1049.

13 A. B. Fall, S. B. Lindström, J. Sprakel and L. Wågberg, Soft Matter, 2013, 9, 1852–1863.

14 F. Martoïa, C. Perge, P. J. J. Dumont, L. Orgéas, M. A. Fardin, S. Manneville and M. N. Belgacem, Soft Matter, 2015, 11, 4742–4755.

15 M. Mohtaschemi, K. Dimic-Misic, A. Puisto, M. Korhonen, T. Maloney, J. Paltakari a nd M. J. Alava, Cellulose, 2014, 21, 1305–1312.

16 O. Nechyporchuk, M. N. Belgacem and F. Pignon, Cellulose, 2015, 22, 2197–2210.

17 D. Bonn, J. Paredes, M. M. Denn, L. Berthier, T. Divoux and S. Manneville, A rXiv150205281 Cond-Mat, 2015.

18 A. W. K. Ma, M. R. Mackley and S. S. Rahatekar, Rheol. Acta, 2007, 46, 979–987.

19 T. Saarinen, S. Haavisto, A. Sorvari, J. Salmela and J. Seppälä, Cellulose, 2014, 21, –1275.

20 P. Coussot, Rheometry of Pastes, Suspensions, and Granular Materials: Applications Industry and Environment, John Wiley & Sons, 2005.

21 P. Coussot, J. Non-Newton. Fluid Mech., 2014, 211, 31–49.

22 P. C. F. Møller, J. Mewis and D. Bonn, Soft Matter, 2006, 2, 274–283.

23 G. Ovarlez, S. Cohen-Addad, K. Krishan, J. Goyon and P. Coussot, J. Non-Newton. Fluid Mech., 2013, 193, 68–79.

24 M. Mohtaschemi, A. Sorvari, A. Puisto, M. Nuopponen, J. Seppälä and M. J. Alava, Cellulose, 2014, 21, 3913–3925.

25 S. Varanasi, R. He and W. Batchelor, Cellulose, 2013, 20, 1885–1896.

26 Kerekes, Nord. Pulp Pap. Res. J., 2006, 21, 598–612.

27 W. B. Russel, D. A. Saville and W. R. Schowalter, Colloidal Dispersions, Cambridge University Press, 1992.

28 J. Mewis and N. J. Wagner, Colloidal Suspension Rheology, Cambridge University , 2012.

29 P. Coussot, Soft Matter, 2007, 3, 528–540.

30 M. J. Solomon and P. T. Spicer, Soft Matter, 2010, 6, 1391–1400.

31 S. R. Raghavan and J. F. Douglas, Soft Matter, 2012, 8, 8539–8546.

32 R. C. Picu, Soft Matter, 2011, 7, 6768–6785.

33 D. Rodney, B. Gadot, O. R. Martinez, S. R. du Roscoat and L. Orgéas, Nat. Mater., 2015.

34 A. P. Philipse, Langmuir, 1996, 12, 1127–1133.

35 A. S. Michaels and J. C. Bolger, Ind. Eng. Chem. Fundam., 1962, 1, 153–162.

36 R. J. Hunter and S. K. Nicol, J. Colloid Interface Sci., 1968, 28, 250–259.

37 F. Folgar and C. L. Tucker, J. Reinf. Plast. Compos., 1984, 3, 98–119.

38 D. L. Koch, Phys. Fluids, 1995, 7, 2086–2088.

39 G. Natale, M. C. Heuzey, P. J. Carreau, G. Ausias and J. Férec, AIChE J., 2014, 60, 1476–1487.

40 G. B. Jeffery, Proc. R. Soc. Lond. Math. Phys. Eng. Sci., 1922, 102, 161–179.

41 G. V. Vinogradov, G. B. Froishteter, K. K. Trilisky and E. L. Smorodinsky, Rheol. Acta, 1975, 14, 765–775.

42 S. P. Meeker, R. T. Bonnecaze and M. Cloitre, J. Rheol., 2004, 48, 1295–1320.

43 S. Marze, D. Langevin and A. Saint-Jalmes, J. Rheol., 2008, 52, 1091–1111.

44 G. Ovarlez, S. Rodts, X. Chateau and P. Coussot, Rheol. Acta, 2009, 48, 831–844.

45 T. Gallot, C. Perge, V. Grenard, M.-A. Fardin, N. Taberlet and S. Manneville, Rev. . Instrum., 2013, 84, 045107.

46 T. Divoux, V. Grenard and S. Manneville, Phys. Rev. Lett., 2013, 110.

47 C. W. Macosko, Rheology: principles, measurements, and applications, VCH, 1994.

48 I. Usov, G. Nyström, J. Adamcik, S. Handschin, C. Schütz, A. Fall, L. Bergström and R. Mezzenga, Nat. Commun., 2015, 6.

49 C. P. J. Bennington, R. J. Kerekes and J. R. Grace, Can. J. Chem. Eng., 1990, 68, 748–757.

50 C. van Wik, J Text. Inst., 1946, 37, 285–289.

51 S. Toll and J.-A. E. Månson, J. Rheol., 1994, 38, 985–997.

52 S. Toll, Polym. Eng. Sci., 1998, 38, 1337–1350.

53 C. Servais, J.-A. E. Månson and S. Toll, J. Rheol., 1999, 43, 991–1004.

54 S. L. Corre, P. Dumont, L. Orgéas and D. Favier, J. Rheol., 2005, 49, 1029–1058.

55 J. Férec, G. Ausias, M. C. Heuzey and P. J. Carreau, J. Rheol., 2009, 53, 49–72.

56 S. Toll, J. Rheol., 1993, 37, 123–125.

57 R. G. L. Larson, The Structure and Rheology of Complex Fluids, Oxford University Press, New York, 1 edition., 1998.

58 S. G. Advani and C. L. Tucker. II, J. Rheol., 1987, 31, 751–784.

59 G. G. Lipscomb II, M. M. Denn, D. U. Hur and D. V. Boger, J. Non-Newton. Fluid Mech., 1988, 26, 297–325.

60 T. G. M. V. de Ven, Colloidal Hydrodynamics, Academic Press, 1989.

61 J.-L. Barrat and L. Bocquet, Phys. Rev. Lett., 1999, 82, 4671–4674.

62 O. Guiraud, L. Orgéas, P. J. J. Dumont and S. R. du Roscoat, J. Rheol., 2012, 56, 593–623.

63 A. M. Wierenga and A. P. Philipse, Langmuir, 1997, 13, 4574–4582.

64 A. Wierenga, A. P. Philipse, H. N. W. Lekkerkerker and D. V. Boger, Langmuir, 1998, 14, 55–65.

65 D. Ishii, T. Saito and A. Isogai, Biomacromolecules, 2011, 12, 548–550.

66 R. R. Sundararajakumar and D. L. Koch, J. Non-Newton. Fluid Mech., 1997, 73, 205–.

67 G. Ausias, X. J. Fan and R. I. Tanner, J. Non-Newton. Fluid Mech., 2006, 135, 46–57.

68 P. J. J. Dumont, S. Le Corre, L. Orgéas and D. Favier, J. Non-Newton. Fluid Mech., 2009, 160, 76–92.

69 M. P. Petrich, D. L. Koch and C. Cohen, J. Non-Newton. Fluid Mech., 2000, 95, 101–133.

70 S. G. Advani, Flow and Rheology in Polymer Composites Manufacturing, Elsevier, 1994.

71 S. Wegner, T. Börzsönyi, T. Bien, G. Rose and R. Stannarius, Soft Matter, 2012, 8, 10950–10958.

72 F. P. Bretherton, J. Fluid Mech., 1962, 14, 284–304.

73 L. Orgéas, P. J. J. Dumont, J.-P. Vassal, O. Guiraud, V. Michaud and D. Favier, J. Mater. Sci., 2011, 47, 2932–2942.

74 J.-P. Vassal, L. Orgéas, D. Favier, J.-L. Auriault and S. Le Corre, Phys. Rev. E, 2008, 77, 011303.

75 M. Djalili-Moghaddam and S. Toll, J. Non-Newton. Fluid Mech., 2005, 132, 73–83.

76 W. W. Sampson, Modelling Stochastic Fibrous Materials with Mathematica®, Springer Science & Business Media, 2008.

77 S. Le Corre, D. Caillerie, L. Orgéas and D. Favier, J. Mech. Phys. Solids, 2004, 52, 395–421.

78 J.N. Israelachvili, Intermolecular and Surface Forces, Third Edition: Revised Third , Academic Press, Amsterdam, 3 Edition., 2011.

79 J. Araki, Soft Matter, 2013, 9, 4125–4141.

80 L. Berhan and A. M. Sastry, Phys. Rev. E, 2007, 75, 041121.

81 I. Balberg, C. H. Anderson, S. Alexander and N. Wagner, Phys. Rev. B, 1984, 30, [2]3933–3943.

82 E. Abisset-Chavanne, F. Chinesta, J. Férec, G. Ausias and R. Keunings, J. Non-Newton. Fluid Mech., 2015, 222, 34–44.

1 T. Saito, Y. Nishiyama, J.-L. Putaux, M. Vignon and A. Isogai, *Biomacromolecules*, 2006, 7, 1687–1691.

2 A. Isogai, T. Saito and H. Fukuzumi, *Nanoscale*, 2011, 3, 71–85.

3 R. J. Moon, A. Martini, J. Nairn, J. Simonsen and J. Youngblood, *Chem. Soc. Rev.*, 2011, 40, 3941–3994.

4 Y. Kobayashi, T. Saito and A. Isogai, *Angew. Chem.*, 2014, 126, 10562–10565.

5 A. Dufresne, *Nanocellulose: From Nature to High Performance Tailored Materials*, Walter de Gruyter, 2012.

6 H. Sehaqui, N. Ezekiel Mushi, S. Morimune, M. Salajkova, T. Nishino and L. A. Berglund, *ACS Appl. Mater. Interfaces*, 2012, 4, 1043–1049.

7 K. M. O. Håkansson, A. B. Fall, F. Lundell, S. Yu, C. Krywka, S. V. Roth, G. Santoro, M. Kvick, L. Prahl Wittberg, L. Wågberg and L. D. Söderberg, *Nat. Commun.*, 2014, 5.

8 F. Martoïa, C. Perge, P. J. J. Dumont, L. Orgéas, M. A. Fardin, S. Manneville and M. N. Belgacem, *Soft Matter*, 2015, 11, 4742–4755.

9 M. Mohtaschemi, K. Dimic-Misic, A. Puisto, M. Korhonen, T. Maloney, J. Paltakari and M. J. Alava, *Cellulose*, 2014, 21, 1305–1312.

10 O. Nechyporchuk, M. N. Belgacem and F. Pignon, *Cellulose*, 2015, 22, 2197–2210.

11 D. Bonn, J. Paredes, M. M. Denn, L. Berthier, T. Divoux and S. Manneville, *ArXiv150205281 Cond-Mat*, 2015.

12 A. W. K. Ma, M. R. Mackley and S. S. Rahatekar, *Rheol. Acta*, 2007, 46, 979–987.

13 P. Coussot, *Rheometry of Pastes, Suspensions, and Granular Materials: Applications in Industry and Environment*, John Wiley & Sons, 2005.

14 P. Coussot, *J. Non-Newton. Fluid Mech.*, 2014, 211, 31–49.

15 P. C. F. Møller, J. Mewis and D. Bonn, *Soft Matter*, 2006, 2, 274–283.

16 G. Ovarlez, S. Cohen-Addad, K. Krishan, J. Goyon and P. Coussot, *J. Non-Newton. Fluid Mech.*, 2013, 193, 68–79.

17 M. Mohtaschemi, A. Sorvari, A. Puisto, M. Nuopponen, J. Seppälä and M. J. Alava, *Cellulose*, 2014, 21, 3913–3925.

18 S. Varanasi, R. He and W. Batchelor, *Cellulose*, 2013, 20, 1885–1896.

19 Kerekes, *Nord. Pulp Pap. Res. J.*, 2006, 21, 598–612.

20 W. B. Russel, D. A. Saville and W. R. Schowalter, *Colloidal Dispersions*, Cambridge University Press, 1992.

21 J. Mewis and N. J. Wagner, *Colloidal Suspension Rheology*, Cambridge University Press, 2012.

22 P. Coussot, *Soft Matter*, 2007, 3, 528–540.

23 M. J. Solomon and P. T. Spicer, *Soft Matter*, 2010, 6, 1391–1400.

24 A. P. Philipse, *Langmuir*, 1996, 12, 1127–1133.

25 A. S. Michaels and J. C. Bolger, *Ind. Eng. Chem. Fundam.*, 1962, 1, 153–162.

26 R. J. Hunter and S. K. Nicol, *J. Colloid Interface Sci.*, 1968, 28, 250–259.

27 F. Folgar and C. L. Tucker, *J. Reinf. Plast. Compos.*, 1984, 3, 98–119.

28 D. L. Koch, *Phys. Fluids 1994-Present*, 1995, 7, 2086–2088.

29 G. Natale, M. C. Heuzey, P. J. Carreau, G. Ausias and J. Férec, *AIChE J.*, 2014, 60, 1476–1487.

30 G. B. Jeffery, *Proc. R. Soc. Lond. Math. Phys. Eng. Sci.*, 1922, 102, 161–179.

31 G. V. Vinogradov, G. B. Froishteter, K. K. Trilisky and E. L. Smorodinsky, *Rheol. Acta*, 1975, 14, 765–775.

32 S. P. Meeker, R. T. Bonnecaze and M. Cloitre, *J. Rheol.*, 2004, 48, 1295–1320.

33 S. Marze, D. Langevin and A. Saint-Jalmes, *J. Rheol.*, 2008, 52, 1091–1111.

34 G. Ovarlez, S. Rodts, X. Chateau and P. Coussot, *Rheol. Acta*, 2009, 48, 831–844.

35 T. Gallot, C. Perge, V. Grenard, M.-A. Fardin, N. Taberlet and S. Manneville, *Rev. Sci. Instrum.*, 2013, 84, 045107.

36 T. Divoux, V. Grenard and S. Manneville, *Phys. Rev. Lett.*, 2013, 110.

37 C. W. Macosko, *Rheology: principles, measurements, and applications*, VCH, 1994.

38 I. Usov, G. Nyström, J. Adamcik, S. Handschin, C. Schütz, A. Fall, L. Bergström and R. Mezzenga, *Nat. Commun.*, 2015, 6.

39 C. P. J. Bennington, R. J. Kerekes and J. R. Grace, *Can. J. Chem. Eng.*, 1990, 68, 748–757.

40 C. van Wik, *J Text. Inst.*, 1946, 37, 285–289.

41 S. Toll and J.-A. E. Månson, *J. Rheol.*, 1994, 38, 985–997.

42 S. Toll, *Polym. Eng. Sci.*, 1998, 38, 1337–1350.

43 C. Servais, J.-A. E. Månson and S. Toll, *J. Rheol.*, 1999, 43, 991–1004.

44 S. Le Corre, P. Dumont, L. Orgéas and D. Favier, *J. Rheol.*, 2005, 49, 1029–1058.

45 J. Férec, G. Ausias, M. C. Heuzey and P. J. Carreau, *J. Rheol.*, 2009, 53, 49–72.

46 S. Toll, *J. Rheol.*, 1993, 37, 123–125.

47 R. G. Larson, *The Structure and Rheology of Complex Fluids*, Oxford University Press, New York, 1 Edition., 1998.

48 S. G. Advani and C. L. Tucker. II, *J. Rheol.*, 1987, 31, 751–784.

49 G. G. Lipscomb II, M. M. Denn, D. U. Hur and D. V. Boger, *J. Non-Newton. Fluid Mech.*, 1988, 26, 297–325.

50 T. G. M. Van de Ven, *Colloidal Hydrodynamics*, Academic Press, 1989.

51 J.-L. Barrat and L. Bocquet, *Phys. Rev. Lett.*, 1999, 82, 4671–4674.

52 O. Guiraud, L. Orgéas, P. J. J. Dumont and S. R. du Roscoat, *J. Rheol.,* 2012, 56, 593–623.

53 A. M. Wierenga and A. P. Philipse, *Langmuir*, 1997, 13, 4574–4582.

54 A. Wierenga, A. P. Philipse, H. N. W. Lekkerkerker and D. V. Boger, *Langmuir*, 1998, 14, 55–65.

55 D. Ishii, T. Saito and A. Isogai, *Biomacromolecules*, 2011, 12, 548–550.

56 R. R. Sundararajakumar and D. L. Koch, *J. Non-Newton. Fluid Mech.*, 1997, 73, 205–239.

57 G. Ausias, X. J. Fan and R. I. Tanner, *J. Non-Newton. Fluid Mech.*, 2006, 135, 46–57.

58 P. J. J. Dumont, S. Le Corre, L. Orgéas and D. Favier, *J. Non-Newton. Fluid Mech.*, 2009, 160, 76–92.

59 M. P. Petrich, D. L. Koch and C. Cohen, *J. Non-Newton. Fluid Mech.*, 2000, 95, 101–133.

60 S. G. Advani, *Flow and Rheology in Polymer Composites Manufacturing*, Elsevier, 1994.

61 S. Wegner, T. Börzsönyi, T. Bien, G. Rose and R. Stannarius, *Soft Matter*, 2012, 8, 10950–10958.

62 F. P. Bretherton, *J. Fluid Mech.*, 1962, 14, 284–304.

63 L. Orgéas, P. J. J. Dumont, J.-P. Vassal, O. Guiraud, V. Michaud and D. Favier, *J. Mater. Sci.*, 2012, 47, 2932–2942.

64 J.-P. Vassal, L. Orgéas, D. Favier, J.-L. Auriault and S. Le Corre, *Phys. Rev. E*, 2008, 77, 011303.

65 M. Djalili-Moghaddam and S. Toll, *J. Non-Newton. Fluid Mech.*, 2005, 132, 73–83.

66 W. W. Sampson, *Modelling Stochastic Fibrous Materials with Mathematica®*, Springer Science & Business Media, 2008.

67 S. Le Corre, D. Caillerie, L. Orgéas and D. Favier, *J. Mech. Phys. Solids*, 2004, 52, 395–421.

68 J.N. Israelachvili, *Intermolecular and Surface Forces, Third Edition*, Academic Press, Amsterdam, 3 Edition., 2011.

69 J. Araki, *Soft Matter*, 2013, 9, 4125–4141.

70 L. Berhan and A. M. Sastry, *Phys. Rev. E*, 2007, 75, 041121.

71 I. Balberg, C. H. Anderson, S. Alexander and N. Wagner, *Phys. Rev. B*, 1984, 30, 3933–3943.

Acknowledgements

The authors gratefully acknowledge D. Dallerac (LGP2) for the technical support in the chromatography experiments and the Electron Microscopy facility of the NanoBio-ICMG Chemistry Platform for granting access to its equipment.

Chapitre 4

On the origins of the elasticity of cellulose nanofiber nanocomposites and nanopapers: a micromechanical approach

Ce chapitre est basé sur un article en préparation (*Nanoscale*), F. Martoïa, P.J.J. Dumont, L. Orgéas, M.N. Belgacem, J.-L. Putaux, 2015.

Abstract

Cellulose nanofibrils (NFC) are slender nanoparticles with outstanding mechanical properties that are used to enhance the mechanical properties of polymer nanocomposites and fabricate dense and transparent nanopapers. However, the reinforcement effect of these nanoparticles is not as efficient for the elastic properties as expected by the classical models for polymer composites or fibrous materials. In this study, nanocomposite films made of TEMPO-oxidized NFCs and polyethylene oxide (PEO) were prepared by varying the NFC content over a wide range. The structural properties of these materials were characterized using AFM, TEM, SEM-FEG and XRD. These techniques showed that NFC nanocomposite films and nanopapers formed dense networks of tortuous NFCs with planar and random orientations. DMA experiments also revealed that the cohesive bonds between NFCs contributed greatly to the overall elastic responses of these nanocomposites, even for low NFC contents. Based on these observations, we report an original multiscale network model for the elastic properties of NFC nanocomposites and nanopapers where the governing deformation mechanisms occurred at the numerous NFC-NFC bonds between NFCs and in the amorphous NFC regions, whereas the semicrystalline NFC regions were considered rigid bodies. This approach led to the formulation of an analytical expression for the stiffness tensors of NFC nanocomposites and nanopapers and revealed the effects of the network structure on their mechanical responses. The model predictions were satisfactory over the range of investigated NFC contents. In particular, this model showed the predominant role of the amorphous regions on the elastic response, whereas the contribution of the NFC-NFC bonds became significant at high NFC contents.

.

4.1 Introduction

Polymer nanocomposites[1,2,3,4,5,6] reinforced with cellulose nanofibrils (NFCs) as well as dense and transparent NFC nanopapers[7,8,9,10] have received considerable attention over the last ten years. One of the main reasons for the growing interest in utilizing NFCs as reinforcement nanoparticles in composites stems from the possibility of exploiting both their outstanding intrinsic mechanical properties and their pronounced slenderness ($100 < l/d < 500$). These emerging biobased nanomaterials, often produced in the form of films, have great potential in a wide variety of applications, such as electronics[8,11,12] and packaging[10,13,14].

NFCs are renewable semicrystalline fibrous nanoparticles that are the main reinforcing constituents of plant cell walls[15]. They are commonly isolated from cellulosic fibres using a combination of chemical and mechanical treatments[2,16]. The most commonly used pretreatment to obtain suspensions of well-individualized NFCs is TEMPO-mediated oxidation of cellulosic fibres[17,18]. This pretreatment preserves the crystalline structure of cellulose and introduced negatively charged carboxyl groups on the fibril surface, leading to homogeneous and electrostatically stabilized aqueous colloidal suspensions[17,18,19]. The resulting NFC suspensions usually contain a very large amount of slender individualized nanofibrils with a mean diameter that ranges between 3 and 5 nm and a mean length that ranges between 1 and 1.5 µm (Fig. 4-1.a-b). The crystallinity of nanofibrils commonly ranges between 60% and 80%.

When they are well-dispersed in polymer matrices, NFCs provide a considerable reinforcing effect, even at very low volume fractions[20,1,21]. In general, NFC-reinforced polymers exhibit a drastic increase in both their elastic and plastic properties, as shown in Fig. 4-1.g for nanocomposite films made of TEMPO-oxidized NFCs and polyethylene oxide (PEO). This reinforcement effect is often preserved up to 500 K, *i.e.*, the temperature at which cellulose decomposes[22,1]. The DMA curves in Fig. 4-1.h provide evidence of the progressive thermal stabilization of a PEO matrix for $T > T_m = 338$ K with increasing NFC content. This peculiar thermo-mechanical behaviour is inherent to nanocomposites that are reinforced with slender cellulosic nanofibres. This behaviour is usually attributed to the presence of a continuous and rigid network of NFCs connected through cohesive hydrogen bonds and its effect on the mechanical properties of the composites[22,23,1].

In general, the elastic properties of NFC nanocomposites and nanopapers increase linearly with the NFC volume fraction ϕ (Fig. 4-1.g)[3,24,25,26]. Surprisingly, the elastic moduli of these materials are systematically lower than the theoretical predictions of most of the classical micromechanical models that were developed for fibre-reinforced polymer composites, papers or non-woven fabrics[3,25,27,28]. For example, Josefsson *et al.*[28] reported that various analytical micromechanical models, namely, classical laminate theory[29], and the Tsai-Pagano[30], Cox[31] and Krenchel[32] models, failed to predict the macroscale elastic properties of nanopapers. Using these models to estimate the NFC elastic moduli led to values that were much lower than those commonly reported in the literature[33,34]. The same conclusion was drawn for NFC reinforced nanocomposites[3,25]. Indeed, Fig. 4-1.g shows that the Young's moduli E of various

nanocomposite films with planar random orientations could be nicely fitted using the Cox model with $E = \phi E_{NFC}/3$. However, this would lead to a very low value of the NFC Young's modulus of $E_{NFC} = 33$ GPa. Several factors could explain this discrepancy.

First, the dispersion of NFCs in polymer matrices has to be considered. Obtaining homogeneous dispersions of NFCs within polymer matrices is challenging and is the subject of intense research[2,1]. When introduced into non-polar media, NFCs exhibit a strong tendency for self-association due to the omnipresence of interacting surface hydroxyl groups[26,1,2]. This effect is not taken into account in the previously mentioned models. The dispersion of NFCs in host polymers can be improved either by surface chemical modification of NFCs[35,36] or by using a surfactant compatibilizer[37]. Despite real improvements made over the last few years, the most straightforward processing route to obtain homogeneous and well-dispersed nanocomposites with high mechanical performances consists of using aqueous polymer dispersions and solutions[22,20,21,24]. This processing route enables the individualization state of NFCs to be preserved, as shown in Fig. 4-1.c. However, even using such favourable processing conditions, the resulting nanomaterials systematically exhibit lower mechanical performances compared with the predictions of the classical micromechanical models[24] (Fig. 4-1.g).

In addition, NFC nanostructure descriptions could be improved in analytical estimates. Observing the microstructures of nanocomposites and nanopapers is difficult. They are often characterized using AFM, FE-SEM and TEM[38,39,20,40]. The overall orientation of NFCs is also usually assessed using X-ray diffraction[41]. Fig. 4-1 shows that the NFC networks in nanocomposite films or nanopapers usually form dense, layered and highly connected fibrous nanostructures[38,41] with pronounced planar NFC orientations. In addition, TEMPO-oxidized NFCs are slender wavy nanofibres that display both straight crystalline segments (here 80%) and so-called amorphous kinks (here 20%)[19]. These two features are not taken into account in the previously mentioned models. Contrary to many classical micrometric fibrous systems, such as papers or non-woven fabrics[42,43,44], it is very difficult to characterize and thus model the placements and orientations of NFCs in their networks as well as their connectivity, which is known to have an important role in the mechanical responses of these materials. For other micrometric or nanometric fibrous systems where proper 3D images of the fibrous architectures are not available, analytical or numerical structure generators were developed to estimate the previously mentioned suitable descriptors[45,46,47,27,48,49]. For NFC-based materials, Kulachenko *et al.*[27] recently used a numerical generation procedure to numerically evaluate the mechanical behaviour of NFC nanopapers. However, the authors did not provide compact analytical descriptors to describe the fibrous nanostructures. More recently, we proposed[50] a semi-analytical model dedicated to NFC suspensions in which several nanoscale constitutive parameters, such as the connectivity, bonding area and the distance between the centre of mass of interacting NFCs, were identified using realistic elementary volumes of the fibrous NFC nanostructures that were numerically generated.

Finally, the deformation mechanisms at the NFC scale are questionable. There is a lack of experimental data on (i) the mechanical behaviour of NFCs and (ii) the nature of the nanoscale forces transmitted between bonded NFCs and between NFCs and the surrounding polymer matrix (in the case of nanocomposites). However, several studies have provided useful information from direct or indirect experimental methods on the elastic modulus of several bundles of nanofibrils[33] using an AFM and nanoscale three-point bending tests. For proper testing conditions, the measured Young's moduli of NFC bundles were close to 90 GPa. In comparison with the Young's moduli reported in other studies[51,52] for crystalline cellulose, which ranged between 120 and 150 GPa, this lower value was attributed both to the bundle architecture of the sample and to the presence of amorphous regions. Using a similar experimental setup, Iwamoto *et al.*[34] reported a value of 145 GPa for the elastic modulus of single and highly crystalline TEMPO-oxidized fibrils that were extracted from tunicate. The morphology of these fibrils was close to that shown in Fig. 4-1. Few experimental studies assessed the stress transfer mechanisms. Recently, Raman spectroscopy was employed to measure the strain of NFCs at the molecular level in deformed nanocomposites and nanopapers[53,54]. For polylactic acid (PLA) nanocomposites reinforced with TEMPO-oxidized NFCs ($\phi \approx 0.1, 0.17$ and 0.2), Bulota *et al.*[53] showed that, during tensile deformation, in the elastic regime, the nanoscale deformation of NFCs weakly depended on the NFC content ϕ and was close to the deformation exhibited in nanopapers prepared with the same NFCs. This interesting experimental result suggests that, for a wide range of NFC contents, the mechanics of NFC networks in polymer matrices is weakly affected by the presence of the matrix. In addition, Kulachenko *et al.*[27] brought additional information on the elastic properties of nanopapers using fine-scale numerical simulations. In particular, this study showed the major influence of the elastic deformations of both the NFC amorphous regions and NFC bonds on the Young's modulus of the nanopaper. However, this numerical model was not associated with any multiscale analytical framework.

In this context, the objective was to develop an analytical micromechanical model for the prediction of the elastic properties of NFC-reinforced nanocomposites and nanopapers using the experimental results shown in Fig. 4-1. The model takes into account (i) the tortuosity of TEMPO-oxidized NFCs and (ii) the spatially heterogeneous mechanical properties related to the semicrystalline and amorphous cellulose regions of these particles. The model also takes into account (iii) the complexity of the networks formed by NFCs and (iv) their associated deformation micromechanisms. First, from the analysis of TEM and AFM images and XRD patterns (Fig. 4-1), an idealized fibril model that takes into account the presence of straight segments and kinks along the NFC length as well as their relative disorientation was developed. Then, these model nanofibrils were used to numerically generate realistic elementary volumes of the fibrous nanostructures of the nanocomposites and nanopapers. Several microstructural descriptors, such as the mean number of contacts per nanofibre, were determined. Combining these data with the numerical and experimental data available from the literature, relevant deformation micromechanisms were assumed. Finally, the nanoscale micromechanics

were upscaled using a rigorous theoretical framework, namely, homogenization with multiple scale asymptotic expansions for discrete structures, leading to an analytical expression for the stiffness tensors of NFC nanocomposites and nanopapers. This model provides insights into the origins of the low elastic properties of NFC nanocomposites and nanopapers.

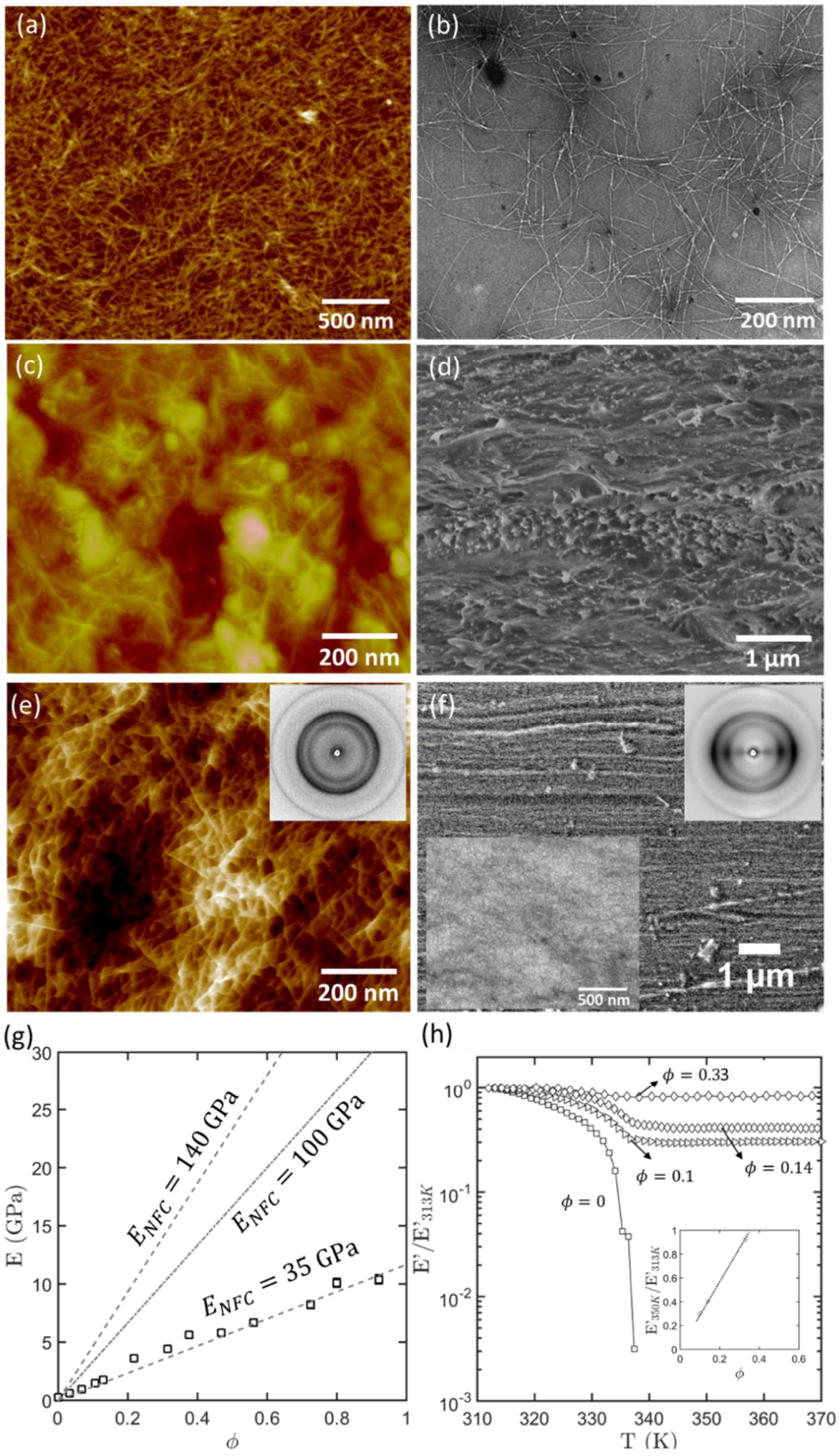

Figure 4-1. (a) AFM and TEM (b) micrographs of a TEMPO-oxidized NFC film obtained after drying a suspension at 0.01 wt% and 0.001 wt%, respectively. (c, e) AFM micrographs that show the surface of (c) a nanocomposite ($\phi = 0.14$) and (e) a TEMPO-oxidized NFC film. (d, f) SEM cross-sections that show the internal microstructure of (d) a nanocomposite ($\phi = 0.31$) and (f) a TEMPO-oxidized NFC film. The insets in Figures e and f show two X-ray diffraction patterns of a pure TEMPO-oxidized NFC film obtained in the plane and cross-sectional directions, respectively. The other inset in Figure f shows a TEM micrograph of the ultrathin transverse section of the NFC nanopaper after immerging into water to reveal the fibrous structure of the film after hygroexpansion. (g) Evolution of the elastic modulus E as a function the nanofibre content ϕ. The lines show the predictions of the Cox model. (h) Normalized dynamic tensile modulus $E'/E'_{313\ K}$ as a function of the temperature at 1 Hz for various NFC-reinforced nanocomposites.

4.2 Theory

The network model was built on several assumptions related to both the fibrous NFC architectures (section 2.1) and deformation mechanisms at the NFC scale (section 2.2). These elements were implemented in a theoretical homogenization upscaling technique (section 2.3) in which additional kinematical assumptions were stated to obtain a compact and theoretical estimate (section 2.4).

4.2.1 Microstructure idealization

As mentioned previously, the determination of the morphological properties of NFCs is the subject of intense research[55]. Here, several descriptors of the NFC geometry were estimated from TEM micrographs, as shown in Fig. 4-1.b. We measured a mean NFC diameter d of 4 nm and a mean NFC length l of 1200 nm, *i.e.,* a mean NFC aspect ratio $r = l/d \approx 300$. It is worth noting that these dimensions were on the same order of magnitude as those reported by Usov *et al.*[55] using AFM and TEM images from TEMPO-oxidized NFCs extracted from wood fibres. In addition, Fig. 4-1 shows that TEMPO-oxidized fibrils were tortuous and consisted of an assembly of approximately $n_{seg} = 7$ slender straight segments with a mean length of $l_{seg} = 171$ nm interspersed with kinks with a mean length of $l_a \approx d$. The mean misorientation angle θ_{seg} between each consecutive segment of an individual NFC was close to $\pi/8$ rad.

Then, the geometric parameters of the nanofibres (d, l, n_{seg}, l_{seg}, and θ_{seg}) were used in a numerical microstructure generation process similar to that reported by Martoïa *et al.*[50]. Each tortuous nanofibre with centre of mass G^i was first randomly positioned in a representative elementary volume Ω of size $V = 1400 \times 1400 \times 1400$ nm^3. Following this procedure, various fibrous networks with various nanofibre contents ϕ were generated with random 3D orientation of the nanofibres. Then, to mimic realistic planar NFC networks (Fig. 4-1), each generated volume with random orientation of nanofibres was numerically subjected to a simple compression test along the $\boldsymbol{e}_3$-direction. The evolution of the mean orientation vector $\mathbf{p}^i$ of each NFC i that progressively aligned in the $(\boldsymbol{e}_1, \boldsymbol{e}_2)$-plane was computed by solving the Jeffery's equation until a nearly planar NFC orientation was reached[50]. Fig. 4-2.b shows an example of a typical idealized NFC network that was generated using this procedure ($\phi = 0.01$). This figure also shows the stereographic projection (pole figure of orientation) of vectors $\mathbf{p}^i$, which reveals the near-random distribution of the nanofibres along the $(\boldsymbol{e}_1, \boldsymbol{e}_2)$-plane. It is worth noting that other fibrous architectures (random, unidirectional with or without clustering) could also be obtained using this generation procedure.

The connectivity of the generated NFC networks was then assessed using a deterministic methodology based on a soft-core approach similar to that adopted in the statistical tube-model approaches[56]. A cylindrical control volume Ω of size $V = \pi l_{seg} d^2$ centered on the centerline of the segment k belonging to a fibre i was defined. Each fibre segments l that belonged

to a fibre j, the centreline of which intersected the control volume Ω, was added to the connectivity set of "hydrogen" bonds $\mathcal{B}^h$ contained in the representative volume Ω. This generation procedure yielded the prediction of the analytical tube model for straight fibres ($\theta_{seg} = 0$). In this case, the tube model prediction of the fibre coordination number Z^h, *i.e.*, the number of NFC bonds h per NFC, was

$$Z^h = 4\phi(\tfrac{2}{\pi} r\Phi_1 + \Phi_2 + 1), \tag{1}$$

where the discrete expressions for the orientation functions Φ_1 and Φ_2 were defined as follows:

$$\Phi_1 = \tfrac{1}{N^2}\sum_{i=1}^{N}\sum_{j=1}^{N}\|\mathbf{p}^i \otimes \mathbf{p}^j\| \qquad \text{and} \qquad \Phi_2 = \tfrac{1}{N^2}\sum_{i=1}^{N}\sum_{j=1}^{N}|\mathbf{p}^i \cdot \mathbf{p}^j|, \tag{2}$$

where N is the number of NFCs in the representative volume.

Our numerical results revealed that the mean coordination number of the tortuous NFC Z^h could be well predicted analytically using eqn(1) with the orientation functions Φ_1 and Φ_2 calculated from the unit tangent vectors of the NFC segments (Fig. 4-2.a). Regardless of the nanofibre content, Fig. 4-2.c shows that the mean coordination number of the tortuous NFCs Z^h (continuous line) was slightly higher ($\approx 8\%$) than that expected for straight fibres (dashed line).

Several numerical studies[57] showed that a critical number of contacts $Z^h \approx 5$ is required to form fully connected planar networks without disjointed substructures. It is interesting to note that due to the pronounced slenderness of NFCs, *i.e.,* $r = 300$, Z^h was significantly higher than 5 for the investigated range of NFC contents: Z^h increased drastically from 16 for $\phi \approx 0.03$ up to $Z^h \approx 490$ in pure NFC nanopapers. This increase was in accordance with the evolution of the DMA curves (Fig. 4-1.h), which showed the potential network-induced thermal stabilization of the polymer matrix. Thus, NFC-based nanocomposites and nanopapers are highly connected fibrous materials in which contact micromechanics is a crucial parameter in the theoretical modelling.

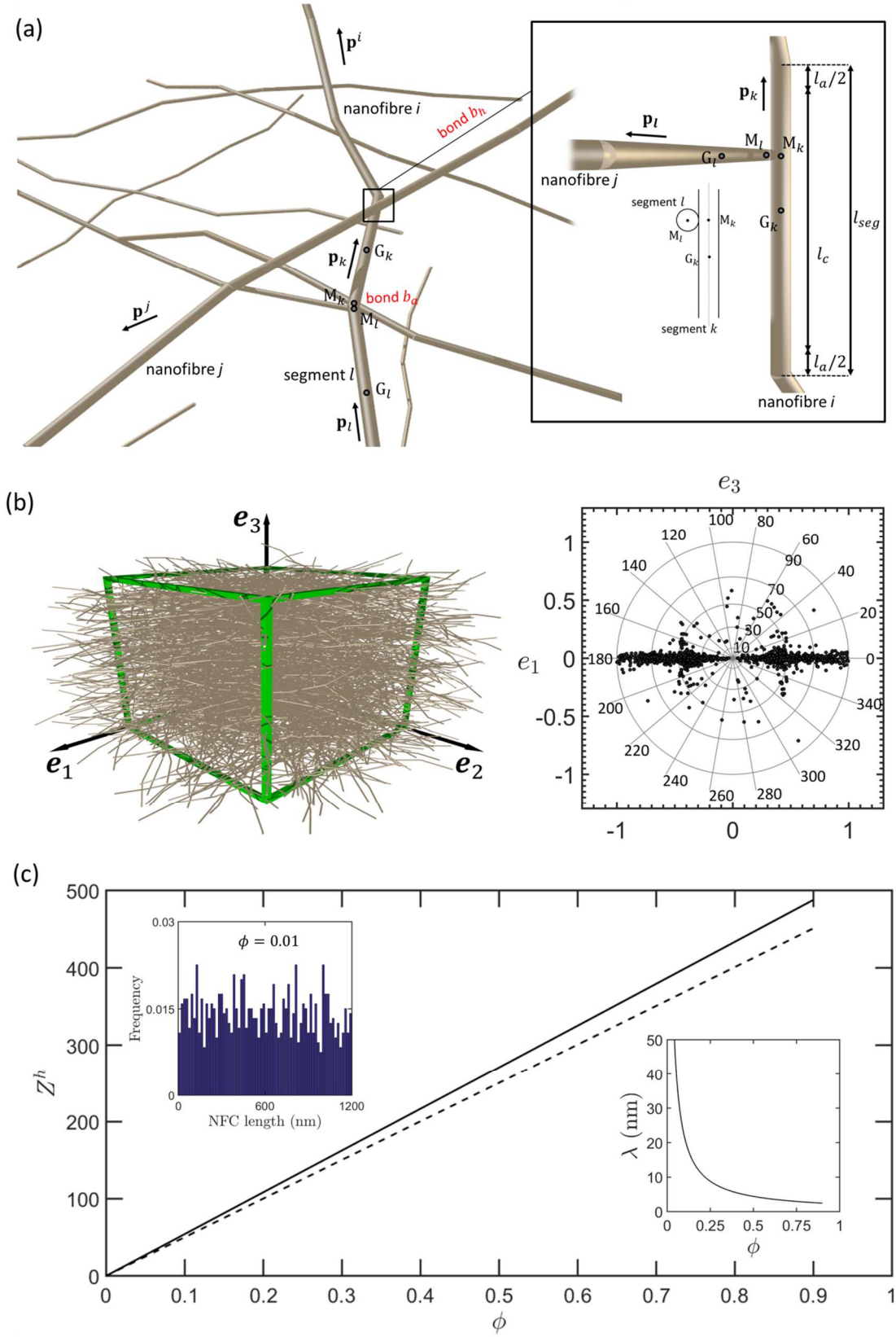

Figure 4-2. (a) Idealized representation of interacting NFCs and zoom on an interaction bond. (b) Example of an idealized NFC network with a low nanofibre content $\phi = 0.01$ and with random planar orientation. The mean orientation vectors $\mathbf{p}^i$ of each tortuous NFC i were represented using a stereographic projection along the $\mathbf{e}_2$ direction. (c) Evolution of the mean coordination numbers Z^h as a function of the NFC volume fraction ϕ for fibrous networks of tortuous NFCs (continuous line). The dashed line is the prediction for straight nanofibres. The inset (on the right side) shows the evolution of the intercontact distance $\lambda = l/(1 + Z^h)$ as a function of the NFC volume fraction ϕ. The histogram in inset shows that the NFC-NFC bonds were uniformly distributed along the NFC length.

4.2.2 Microstructure assumptions

From the previous experimental and numerical data, the elasticities of the nanocomposites were interpreted in light of the NFC network mechanics, assuming that their properties were mainly governed by the fibrous architectures. This assumption was supported by the following observations:

- In the elastic domain, the mechanics of the NFC networks were weakly affected by the presence of the polymer matrix (see the previous comments related to the study of Bulota *et al.*[53]).
- The elastic properties of the nanocomposites were, for a wide range of NFC contents (at least for $\phi > 0.3$), weakly affected by the temperature (even well beyond the melting temperature of the polymer matrix, Fig. 4-1.g).

Therefore, to study the mechanics of the NFC networks and, consequently, the mechanics of the nanocomposites with equivalent nanofibre contents, it was assumed that NFCs were slender beams consisting of an average of $n_{seg} = 7$ crystalline rods linked by amorphous kinks. To date, the structural arrangements of NFCs have not been fully elucidated. However, this idealization of the NFC geometry was supported by the study of Nishiyama *et al.*[58], who reported, using small angle neutron diffraction, that ramie fibrils exhibited quasi-periodic ordered-disordered regions along their length. The authors also revealed that the length of the ordered zones l_c was close to 150 nm ($l_c \approx 167$ nm in the fibril model in Fig. 4-2.a). Accounting for the previously mentioned remarks, the kinks (as noted below b_a) with lengths $l_a \approx d$ were assumed to be amorphous or disordered cellulose regions. Hence, these zones (Fig. 4-2.a) were assigned a mean elastic modulus of $E_a \approx 5$ GPa[59,60] and, assuming a Poisson ratio of $\nu = 0.33$, a mean shear modulus of $G_a \approx 1.9$ GPa. In contrast, the rods with lengths $l_c \approx 167$ nm (see Fig. 4-2.a) were assumed to be ordered regions with a crystallinity of 80% (based on XRD measurements). Thus, accounting for the theoretical evaluations and experimental measurements dedicated to pure cellulose crystals[61,62] that gave a longitudinal modulus of 150 GPa and a transverse modulus of 50 GPa, the semi-crystalline rods of length $l_c \approx 167$ nm (Fig. 4-2.a) were assigned, using the rule of mixture, a mean longitudinal elastic modulus of $E_c^l \approx 120$ GPa, a mean transverse modulus of $E_c^t \approx 40$ GPa and, assuming a transverse Poisson ratio of $\nu = 0.33$, a mean transverse shear modulus of $G_c^t \approx 19$ GPa.
It has already been reported in many theoretical and numerical studies dealing with the mechanics of papers[63] and NFC nanopapers[27] that the elastic deformations of the fibre-to-fibre bond regions also play significant roles in their elasticities. In accordance with these studies, it was assumed that NFCs were connected through rod-rod elastic bonds b_h (Fig. 4-2.a).

While subjecting such idealized NFC networks (Fig. 4-2.b) to macroscopic mechanical loadings, each inter-contact NFC segment could be stretched, sheared, bent and twisted[64]. At $\phi = 0.5$, the semicrystalline rod segments of length λ and with characteristic kink sizes of l_a were practically equal (Fig. 4-2.c). As the elastic properties of the semicrystalline rod segments

were ten times higher than those of amorphous regions, it was reasonable to assume that their deformations were negligible compared with those of amorphous kinks. At higher NFC contents, this assumption was even more valid because the lengths of the semicrystalline rod segments decreased (Fig. 4-2.c), and consequently, their stiffnesses increased. Thus, for $\phi \geq 0.5$, the micromechanics was reduced to the problem of quasi-rigid beams, namely, the semicrystalline rod segments linked by amorphous kinks or bonds b_a and hydrogen bonds b_h in each NFC-NFC contact zone. This scenario will be adopted in the following section. However, below $\phi = 0.5$, its validity becomes more and more questionable.

Under such circumstances, when the considered fibrous networks were subjected to a macroscopic displacement gradient $\nabla\mathbf{U}$, the infinitesimal displacement $\mathbf{u}_k^{\mathrm{M}_k}$ of a point M_k of a rod k (belonging to a nanofibre i) located at a curvilinear abscissa s_k from its centre of mass G_k along the rod centreline of tangent unit vector $\mathbf{p}_k$ ($\mathbf{G}_k\mathbf{M}_k = \mathrm{s}_k\mathbf{p}_k$) was written as follows:

$$\mathbf{u}_k^{\mathrm{M}_k} = \mathbf{u}_k + \mathrm{s}_k\mathbf{w}_k \times \mathbf{p}_k, \tag{3}$$

where $\mathbf{u}_k$ is the infinitesimal displacement of G_k and $\mathbf{w}_k$ the rotation of the rod k.

The displacements and rotation of the rods induced the deformation of both the kinks b_a and the rod-rod bonds b_h. Hence, it is assumed that the deformations of bonds b_a and b_h mainly induced shear reaction forces $\mathbf{f}_a$ and $\mathbf{f}_h$ and reaction moments $\mathbf{m}_a$ and $\mathbf{m}_h$, respectively. In practice, the bonds and their vicinity exhibited complex shapes and mechanical behaviours. Phenomenological generic linear expressions for $\mathbf{f}_\alpha$ and $\mathbf{m}_\alpha$ (where the subscript "α" stands either for kink bonds "a" or rod-rod contact bonds "h") were proposed as follows:

$$\mathbf{f}_\alpha = K_\alpha \Delta\mathbf{u}_\alpha, \tag{4}$$

and

$$\mathbf{m}_\alpha = K'_\alpha \Delta\mathbf{w}_\alpha \ , \tag{5}$$

with $\Delta\mathbf{u}_\alpha$ and $\Delta\mathbf{w}_\alpha$ the infinitesimal relative displacement and rotation of the connected rods k and l:

$$\Delta\mathbf{u}_\alpha = \mathbf{u}_k - \mathbf{u}_l + \Delta\mathbf{w}_\alpha \times (\mathrm{s}_k\mathbf{p}_k - \mathrm{s}_l\mathbf{p}_l), \tag{6}$$

$$\Delta\mathbf{w}_\alpha = \mathbf{w}_k - \mathbf{w}_l. \tag{7}$$

The translational K_α and rotational K'_α bond stiffnesses were assumed to be linear and quadratic functions of the representative descriptors of the bond cross sections S_α ($K_\alpha = k_\alpha \mathrm{S}_\alpha$ and $K_\alpha = k'_\alpha {\mathrm{S}_\alpha}^2$), respectively. A suitable descriptor of S_a is typically $\pi d^2/4$, *i.e.*, the cross sectional circular area of the amorphous kinks, whereas S_b is often considered to be proportional to the rhomb surface[65,50] defined by the projection of the connected rods (k and l) onto the normal plane of the bonding zone $d^2/\|\mathbf{p}_k \times \mathbf{p}_l\|$.

Hence, by introducing $\mathcal{B}_k^\alpha$, i.e., the set of bonds b_α of rod k, the momentum balance that governs the quasi-static motion of a given rod k was expressed as follows[66,67]:

$$\begin{cases} \sum_{\mathcal{B}_k^a} \mathbf{f}_a + \sum_{\mathcal{B}_k^h} \mathbf{f}_h = \mathbf{0} \\ \sum_{\mathcal{B}_k^a} \mathbf{m}_a + \sum_{\mathcal{B}_k^h} \mathbf{m}_h = \sum_{\mathcal{B}_k^a} s_k^a \mathbf{f}_a \times \mathbf{p}_k + \sum_{\mathcal{B}_k^h} s_k^h \mathbf{f}_h \times \mathbf{p}_k \end{cases} . \tag{8}$$

4.2.3 Theoretical upscaling

There is a close analogy between the micromechanical problem presented in the above section and that developed by Le Corre *et al.*[66,67] to model the rheology of highly concentrated fibre bundle suspensions with planar bundle orientation and Newtonian bundle-bundle interactions. To be convinced of this, the present elastic interactions b_α and the infinitesimal displacement and rotation fields of the rods could be replaced by the viscous interactions and the translational and rotational velocity fields of the bundles in the suspensions that were studied by Le Corre *et al.*[66,67]. To study the nature and the properties of the equivalent continuous medium related to this type of micromechanics, the authors used the homogenization method for discrete structures with multiscale asymptotic expansion[68]. They showed[68,66] that, under good scale separation conditions, when the macroscale size of the studied fibrous materials was much larger than the fibre length (this condition is largely fulfilled with the investigated nanocomposites), the local reaction forces $\mathbf{f}_\alpha$ typically kept their generic form (eqn(4)). In addition, the relative infinitesimal displacement $\Delta\mathbf{u}_\alpha$ in eqn(6) could be approximated at the first order by

$$\Delta\mathbf{u}_\alpha \approx \delta\mathbf{u}_k - \delta\mathbf{u}_l + \nabla\mathbf{U}.\boldsymbol{\xi}_\alpha + \mathbf{w}_l \times \mathrm{s}_l\mathbf{p}_l - \mathbf{w}_k \times \mathrm{s}_k\mathbf{p}_k), \tag{9}$$

where $\delta\mathbf{u}_k$ and $\delta\mathbf{u}_l$ are the first order displacement fluctuations around the macroscopic displacement field $\mathbf{U}$ and where $\boldsymbol{\xi}_\alpha = \mathbf{G}_k\mathbf{G}_l = \mathrm{s}_k\mathbf{p}_k - \mathrm{s}_l\mathbf{p}_l$.

The homogenization method[68,66] also showed that, under these conditions, the equivalent macroscale continuum is a standard Cauchy medium with a macroscale symmetric stress tensor $\boldsymbol{\sigma}$ that takes the following generic discrete form:

$$\boldsymbol{\sigma} = \frac{1}{V}\sum_{\mathcal{B}_k^a} \boldsymbol{\xi}_a \otimes \mathbf{f}_a + \frac{1}{V}\sum_{\mathcal{B}_k^h} \boldsymbol{\xi}_h \otimes \mathbf{f}_h \ , \tag{10}$$

where V is the volume of the representative elementary volume. By introducing $B^\alpha/V = n_{seg} n z^\alpha/2$, the number of α-bonds per unit volume and n the number of nanofibres per unit volume N/V ($z^\alpha$is the number of bonds b_α per segment), $\boldsymbol{\sigma}$ could be finally expressed as follows:

$$\boldsymbol{\sigma} = k_a z^a \frac{\pi d^2 n_{seg} n}{8} \frac{1}{B^a} \sum_{\mathcal{B}_k^a} \boldsymbol{\xi}_a \otimes \Delta\mathbf{u}_a + k_h z^h \frac{d^2 n_{seg} n}{2} \frac{1}{B^h} \sum_{\mathcal{B}_k^h} \frac{1}{\|\mathbf{p}_k \times \mathbf{p}_l\|} \boldsymbol{\xi}_h \otimes \Delta\mathbf{u}_h \tag{11}$$

Still using the homogenization method[68,66], it was shown that the first order fluctuations $\delta\mathbf{u}_k$ and $\mathbf{w}_k$ are linear functions of the macroscale displacement gradient $\nabla\mathbf{U}$ and that $\boldsymbol{\sigma}$ is a linear function of the macroscale strain tensor $\boldsymbol{\varepsilon} = (\nabla\mathbf{U} + \nabla\mathbf{U}^t)/2$:

$$\boldsymbol{\sigma} = (\mathbb{C}^{\boldsymbol{a}} + \mathbb{C}^{\boldsymbol{h}}) : \boldsymbol{\varepsilon}, \tag{12}$$

where $\mathbb{C}^a$ and $\mathbb{C}^h$ are the symmetric macroscopic elastic stiffness tensors related to kink bonds and segment-segment bonds, respectively.

4.2.4 Analytical estimates

Two strategies could be used to estimate the value of the components of the stiffness tensors, $\mathbb{C}^a$ and $\mathbb{C}^h$**.** The first strategy would consist in solving, *e.g.,* using discrete element simulation[67,69], the mechanical equilibrium of the representative elementary volumes, such as that shown in Fig. 4-2.b, when subjected to macroscopic displacement gradients $\nabla\mathbf{U}$. The second strategy, which was used in this study, led to analytical estimates of $\mathbb{C}^a$ and $\mathbb{C}^h$ from additional assumptions both on the NFC nanostructures and kinematics. These assumptions are described below:

- It was assumed that eqn(1) gave a proper prediction of the mean coordination number Z^h. It was also assumed that the segment-segment bonds were uniformly distributed along the NFC length, so that $z^h = Z^h/n_{seg}$ (see the inset in Fig. 4-2.c). In addition, z^a was easily deduced from n_{seg}: $z^a = 2(n_{seg}-1)/n_{seg}$.

- The two terms inside the summation of eqn(11) were assumed to be weakly correlated, so that $1/\|\mathbf{p}_k \times \mathbf{p}_l\|$ was extracted from the summation and approximated by its mean value. This is equivalent to stating that the bond area S_h could be approximated by its mean value $\bar{S}_h$:

$$\bar{S}_h = \frac{d^2}{\|\mathbf{p}_k \times \mathbf{p}_l\|} \approx \frac{d^2}{\varphi_1}, \tag{13}$$

  where $\varphi_1 = \frac{1}{{N_{seg}}^2}\sum_{k=1}^{N_{seg}}\sum_{l=1}^{N_{seg}}\|\mathbf{p}_k \otimes \mathbf{p}_l\|$ with $N_{seg} = n_{seg}N$.

- The infinitesimal displacement field $\mathbf{u}_k$ of rod k was assumed to be an affine function of the macroscopic displacement gradient $\nabla\mathbf{U}$. This assumption led to neglecting the first right-hand term in the expression of $\Delta\mathbf{u}_\alpha$, *i.e.*, $\delta\mathbf{u}_k - \delta\mathbf{u}_l \approx \mathbf{0}$. By performing discrete element simulations to compute the effective elastic properties of papers, Marulier[69] showed that this approximation practically led to the same results.

- The rotation of the rod k noted $\mathbf{w}_k \times \mathbf{p}_k$ was assumed to follow that subjected by the macroscale transformation. This can be expressed as follows:

$$\mathbf{w}_k \times \mathbf{p}_k = \nabla\mathbf{U}.\,\mathbf{p}_k - \mathbf{p}_k \otimes \mathbf{p}_k \otimes \mathbf{p}_k : \boldsymbol{\varepsilon}. \tag{14}$$

  Thus, accounting for the two previous assumptions, $\Delta\mathbf{u}_\alpha$ was rewritten:

$$\Delta\mathbf{u}_\alpha = \left(\mathrm{s}_k\ \mathbf{p}_k \otimes \mathbf{p}_k \otimes \mathbf{p}_k - \mathrm{s}_l\ \mathbf{p}_l \otimes \mathbf{p}_l \otimes \mathbf{p}_l\right) : \boldsymbol{\varepsilon}. \tag{15}$$

Finally, after some analytical developments, detailed in Appendix 2, a simple and compact analytical estimate of the stiffness tensor $\mathbb{C} = \mathbb{C}^{\boldsymbol{a}} + \mathbb{C}^{\boldsymbol{h}}$ was obtained:

$$\mathbb{C} = \left(k_a \frac{\pi}{8}(n_{seg}-1) + k_h Z^h \frac{1}{12\varphi_1}\left(1 - \frac{n_{seg}}{Z^h}\right)\right) n d^2 l_{seg}^2 \mathbb{A}, \tag{16}$$

where $\mathbb{A}$ is the fourth-order rod orientation tensor defined as[68]:

$$\mathbb{A} = \frac{1}{N_{seg}} \sum_{k=1}^{N_{seg}} \mathbf{p}_k \otimes \mathbf{p}_k \otimes \mathbf{p}_k \otimes \mathbf{p}_k. \tag{17}$$

In particular, when nanopapers and nanocomposites are subjected to a tensile loading, eqn(16) led to the following expression of the Young's modulus E:

$$E = \Big(k_a \frac{\pi}{8} (n_{seg} - 1) + k_h Z^h \frac{1}{12\varphi_1} (1 - \frac{n_{seg}}{Z^h}) \Big) n d^2 l_{seg}^2 \Big(\mathrm{A}_{1111} - \frac{\mathrm{A}_{2211}}{\mathrm{A}_{2222}} \mathrm{A}_{1122} \Big), \tag{18}$$

where $\mathrm{A}_{1111}, \mathrm{A}_{2211}, \mathrm{A}_{2222}$ and A_{1122} are the components of the fourth-order orientation tensor that can be estimated from the numerical microstructure generation process in subsection 2.1.

Eqn(18) shows the role played by the NFC geometry (l_{seg}, d, n_{seg}), content ($n = 4\phi/(d^2 l)$), and orientation ($\mathbb{A}$, φ_1) as well as the key role played by the bond stiffnesses (k_a, k_h) on the macroscale elastic modulus of NFC-based nanocomposites and nanopapers. It also shows the importance of having a relevant representation of the NFC nanostructures to properly estimate the connectivity Z^h (section 2.1).

4.3 Model prediction and discussion

To complete the description of the NFC geometry and architecture, the bond stiffnesses k_a and k_h were the only remaining parameters of the model to be determined. A first order estimate of the shear stiffness of the kinks k_a is G_a/l_a. By introducing this estimate into eqn(19), the amorphous contribution E_a to the overall Young's modulus E was estimated. This contribution is shown in Fig. 4-3. Similarly, with the knowledge of E_a, the bond stiffness k_h was estimated from the best fit of the overall Young's modulus E to the experimental data. We found that $k_h = 7.44 \times 10^{15}$ N m^{-3}. This led to the E_h contribution plotted in Fig. 4-3 from which several important remarks can be drawn.

- A very nice fit of the experimental data was obtained using the analytical estimate of the elastic modulus E (eqn(18)). Surprisingly, the model prediction was still satisfactory below the model validity domain, *i.e.*, below $\phi = 0.5$.
- The model prediction shows that the amorphous bonds played an important role in the elasticity of the studied NFC nanocomposites and nanopapers. In the validity domain of the model, *i.e.*, above $\phi = 0.5$, E_a represents 98% to 73% of E as the NFC content varied from 0.5 to 0.9. In addition, E_a increased linearly with ϕ. This trend can be explained from eqn(16) because E_a is a linear function of $n = 4\phi/(d^2 l)$.
- The contribution of NFC-NFC bonds to the elastic properties was lower but could not be neglected. The contribution E_h to the elastic modulus E was a power-law function of ϕ with an exponent of 2. As shown in eqn(16), E_h is a function of nZ^h, where n and Z^h are linear functions of the nanofibre content ϕ.

- The value of k_h led to an overall bond stiffness $K_h = 0.09$ N m^{-1}. This estimate was compared with the stiffness K_h^* that would correspond to a full and perfect bonding region with typical size $\bar{S}_h$. A reasonable estimate of K_h^* is $G_c^t d = 62$ N m^{-1} was obtained by considering the simple shear of such perfect bonding region between the centrelines of two contacting NFCs. The origin of the important difference between K_h and K_h^* could be related to the irregular geometry[55] of bonds, as NFCs do not exhibit rectangular and coincident cross sections. As already been observed in other cellulose fibrous materials[71,43], the effective bonding area can be much smaller than $\bar{S}_h$. For example, by closely analysing the 3D microstructures of unbeaten bleached softwood papers, Marulier *et al.*[71,43] showed that the effective bond surface area was approximately 10% of the full contact area $\bar{S}_h$. Another origin of this discrepancy could result from inefficient physicochemical bonding mechanisms at the interfaces between contacting NFCs[38,72,] . These two scenarios could be coupled. Additional fine scale observations and characterizations as well as molecular dynamics simulations would contribute to a better understanding of the potential mechanisms at the origin of this discrepancy.
- Further, the significance the NFC-NFC bond stiffness k_h was investigated in regards of the stored energy per unit surface area E_h in the bonds. This energy was roughly estimated as $E_h \approx \frac{1}{2} k_h \Delta\overline{u}^2$, where $\Delta\overline{u}$ is the average relative displacement in the bond region between two interacting NFCs. It was estimated from eqn(15) as follows $\Delta\overline{u} \approx \left(\frac{l_{seg}}{4}\right)^2 \varepsilon^2$ with ε the tensile macroscopic tensile strain. Hence, by considering a tensile strain at breakage of $\varepsilon_r \approx 4\%$ for the nanopaper, E_h was approximately 0.2×10^{-22} kJ/nm^2. As reported in the literature, the energy at breakage of paper bonds between cellulose fibres[72,73] or between model cellulose films[74] ranges between 0.5×10^{-22} kJ/nm^2 and 1×10^{-22} kJ/nm^2. These bonds are brittle and thus these energies at breakage can be considered to roughly correspond to elastic energies, showing that our estimate for the stiffness of NFC-NFC bond properties is reasonable.
- The stiffness of the amorphous zone k_a was estimated by assuming that shear was the main deformation mechanism that occurred in these zones and that their effective cross section was close to S_a. These assumptions have to be regarded carefully because the deformation mechanisms and kink nanostructures could be extremely complex[55,75]. Once again, fine scale experimental characterizations[75] and molecular dynamics simulations[76,77] would enable a proper understanding of the geometry and mechanics of kinks.

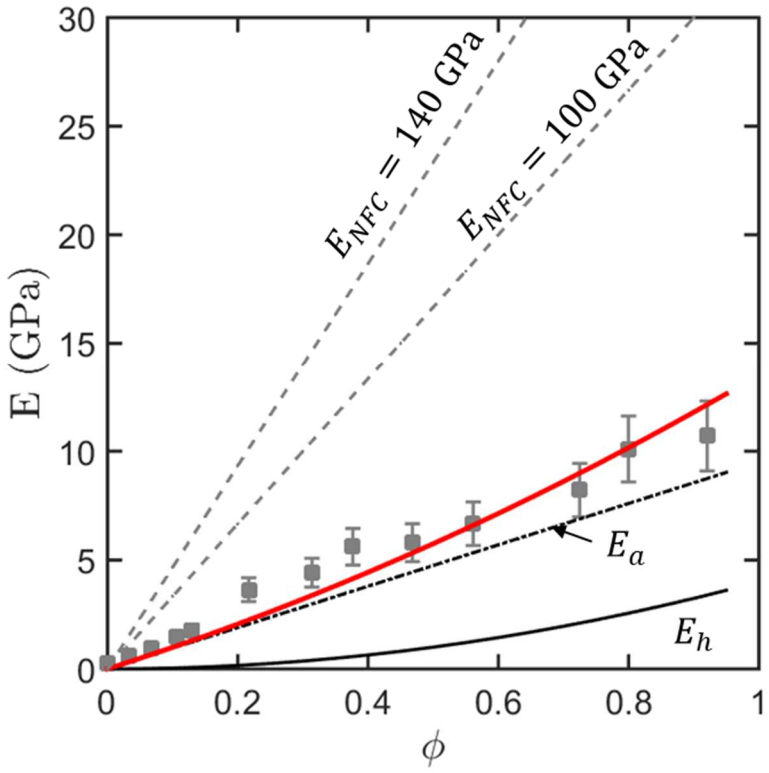

Figure 4-3. Young's modulus E of the fabricated films as a function of the NFC content ϕ. The continuous red line shows the prediction of the micromechanical model stated in eqn(18). The other black lines represent the contributions that are induced by the kink bonds E_a (dash-dotted line) and NFC-NFC bonds E_h (continuous line). The fits were obtained using an equivalent bond stiffness of 7.44×10^{15} N m^{-3}. The mean experimental values were assigned a relative deviation of 15%. The grey dashed lines are the prediction of the Cox model.

4.4 Conclusion

The objective of this study was to relate the macroscale elasticity of NFC nanocomposites and nanopapers to their complex nanostructures and deformation nanomechanisms. To accomplish this goal, nanocomposites films made of TEMPO-oxidized NFCs and a water soluble polymer matrix of polyethylene oxide (PEO) were fabricated using film casting with various NFC contents that ranged from 0 to 100 wt%. The nanostructure properties of the nanocomposites were studied using AFM, TEM, SEM-FEG and XRD, showing that NFCs formed intricate planar fibrous nanostructures in accordance with the literature results. Tensile tests showed that their elastic moduli increased linearly as functions of the nanofibre content ϕ. In addition, DMA tests showed progressive thermal stabilization of the polymer matrix with increasing NFC content. This particular thermo-mechanical behaviour is usually attributed to the presence of a continuous and rigid network of NFC connected through cohesive hydrogen bonds.

Therefore, to better understand the nanostructures of NFC nanocomposites and nanopapers, we first proposed an idealized nanofibril model built from several geometrical parameters that were estimated using TEM images. In particular, NFCs were considered to be tortuous and

slender nanofibres with successive ordered semicrystalline segments interspersed with amorphous kinks. A numerical generator of NFC networks was used to obtain realistic elementary volumes of planar nanostructures with randomly oriented NFCs. This procedure enabled several suitable descriptors to be determined for NFC-based materials. For example, in the experimental range of NFC contents, *i.e.*, $0.03 \leq \phi \leq 0.92$, the mean coordination number of the tortuous NFCs Z^h was shown to range between 16 and 490. Thus, all of the studied NFC-based materials were fully connected without disjointed substructures. These results also suggest that the micromechanics of NFC-NFC bonds have to be considered for proper modelling of the mechanical properties of these materials.

In this context, an original multiscale model was developed for the prediction of the elastic properties of NFC nanocomposites and nanopapers, in which the shear of NFC-NFC bonds and kink bonds in NFC-based materials was considered the governing deformation mode. In this approach, the deformation was assumed to be localized at the numerous NFC-NFC interfaces between NFCs and in the amorphous NFC regions, whereas the semicrystalline NFC regions were considered to be rigid bodies because of their high intrinsic stiffnesses compared with the amorphous regions. Furthermore, in the elastic regime, the role of the polymer matrix was reasonably neglected. The upscaling approach was based on the theoretical framework of the homogenization with multiscale asymptotic expansions for discrete structures. A compact and simple analytical expression for the stiffness tensor of NFC nanocomposites and nanopapers was established. The local stiffnesses of the kink bond regions and the NFC-NFC bonds were determined using the experimental database and the numerically generated NFC nanostructures. The results showed the predominant role played by the amorphous kinks on the elastic properties. The contribution of the NFC-NFC bonds was significant for the highest NFC contents. The NFC-NFC bond stiffness was very low compared with the theoretical estimate of this property, assuming simple shear of a perfect bonding region between contacting NFCs. Irregular and partial bonding surface areas as well as poor physicochemical interfacial bonding mechanisms could explain these low values. For both types of bonds, further experimental investigation and simulations are required to enhance the descriptions of their geometries and mechanics.

4.5 Appendix 1

1 – Extraction of NFCs

TEMPO-oxidized NFC suspensions with 1 wt% of NFCs were extracted from a commercial eucalyptus bleached kraft pulp (Celbi, Portugal) using a similar processing route to that reported by Martoïa *et al.*[78].

2 – Nanocomposite processing

Polyethylene oxide (PEO) with a viscosity average molecular weight M_v of 1 000 000 (Sigma Aldrich., France) was first dissolved in deionized water to obtain a 1 wt% solution. Then, various amounts of NFC suspensions were added to the PEO solutions to prepare PEO/NFC mixtures containing 0, 5, 10, 15, 20, 30, 40, 50, 60, 70, 80, 90, and 100 wt% of NFCs. The mixtures were homogenized (IKA T5, digital Ultra-Turrax) at 5 000 rpm for 30 s and then placed in ultrasonic baths for 5 min to remove all of the air bubbles trapped in the mixtures. Nanocomposite films (Fig. 4-4) were obtained by casting the mixtures in circular Teflon moulds with 150-mm diameters and drying under a fume hood at room temperature ($T \approx$ 20°C).

The mean thickness of the films e ($e \approx 15 - 20$ µm) was measured using a digital paper micrometer, and the basic weight W was estimated by measuring the weight of rectangular specimens of films (70 mm × 60 mm). The volume fractions of NFC ϕ and PEO ϕ_{PEO}were assessed using the film density $\rho = W/e$ and the mass fraction of each constituent x_i as follows:

$$\phi_i = x_i \frac{\rho}{\rho_i}. \tag{20}$$

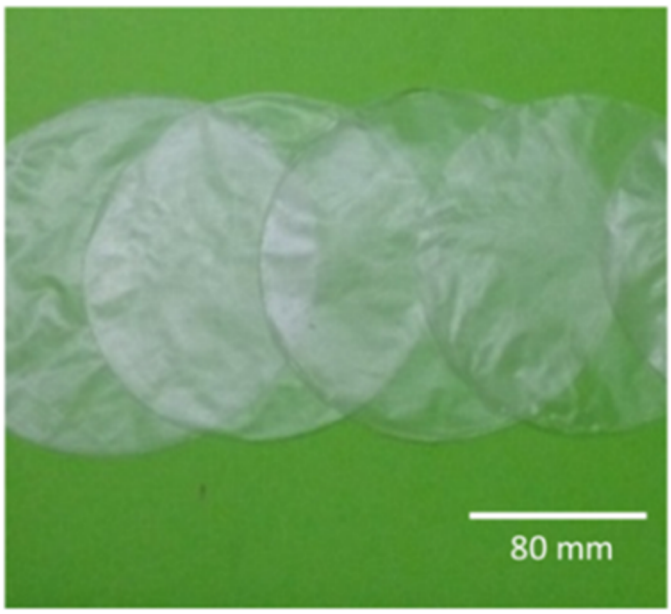

Figure 4-4. Photographs of the processed nanocomposite films.

3 – Microstructure characterization

The surface of the nanocomposite films was observed using a Nanoscope III AFM (Veeco, Canada) operating in tapping mode with an OTESPA silicon cantilever (Bruker, USA) at different locations over scanning regions of 3 µm × 3 µm and 1.1 µm × 1.1 µm.
The microstructure of the nanocomposite films was observed by scanning electron microscopy. Some films were fractured after freezing in liquid nitrogen and surface-coated with a thin (2-3 nm) layer of Au/Pd. Secondary electron images of the film cross section were recorded in high vacuum using a Zeiss Ultra 55 microscope equipped with a field emission gun (FEG) and operating at 2 kV. Other films were embedded in Epon resin and the resulting blocks were surfaced with a diamond knife in a Leica Ultracut UC6 ultramicrotome in order to visualize the cross section of the films. The blocks were observed in a low pressure of air (40 Pa) with a FEI Quanta-FEG 250 microscope operating at 3 kV.

Transmission electron microscopy (TEM) was used to characterize the NFC morphology. Droplets of a dilute (0.001 wt%) NFC suspension were deposited onto glow-discharged carbon-coated copper grids and the specimens were negatively stained with 2% uranyl acetate. Ultrathin (50-70 nm) cross-sections of Epon-embedded strips of NFC films were cut at room temperature using a Leica Ultracut UC6 ultramicrotome and collected on carbon-coated TEM grids. All specimens were observed in a Philips CM200 microscope operating at 80 kV and the images were recorded on Kodak SO163 films.

The nanofibril orientation in the films was characterized by X-ray diffraction. Strips of cellulose films were fixed on a 0.2-mm collimator in such a way that they were oriented parallel or perpendicular to the X-ray beam. The specimens were X-rayed in transmission mode in a vacuum chamber with a Ni-filtered CuK radiation ($\lambda = 0.1542$ nm), using a Philips PW3830 generator operating at 30 kV and 20 mA. Two-dimensional diffraction patterns were recorded on Fujifilm imaging plates, read with a Fujifilm BAS-1800II bioimaging analyser.

4 – Mechanical characterization

Uniaxial tensile tests were performed on rectangular specimens (mean width $\approx$ 4 mm and mean initial length $l_0 \approx 40$ mm) at a constant strain-rate $\dot{\varepsilon} = 0.01$ s^{-1} $= 0.01$ s^{-1} using an Instron testing machine equipped with a force sensor of 50 N. Before testing, nanocomposite films were stored for at least 1 day under controlled conditions ($T = 25$°C and $HR = 56\%$).
Thermomechanical measurements were conducted using a DMA RSA3 (TA Intruments, USA) in tensile mode. The tests were performed at a constant frequency of 1 Hz and with a strain amplitude of 0.05% on rectangular specimens (mean width $\approx$ 4 mm and mean initial length $l'_o \approx 10$ mm). The samples were heated from 300 K to 450 K at 5 K min^{-1}.

4.6 Appendix 2

Accounting for all the assumptions stated in section 2.4, the macroscale stress tensor $\boldsymbol{\sigma}$ eqn(11) could easily be expressed as follows:

$$\boldsymbol{\sigma} = \left(k_a z^a \frac{\pi d^2 n_{seg} n}{8} (\mathbb{B}_1^a + \mathbb{B}_2^a) + k_h z^h \frac{d^2 n_{seg} n}{2\varphi_1} (\mathbb{B}_1^h + \mathbb{B}_2^h) \right) : \boldsymbol{\varepsilon}, \tag{21}$$

where

$$\begin{cases} \mathbb{B}_1^\alpha = \frac{1}{B^\alpha} \sum_{N_{seg}} \sum_{\mathcal{B}_k^\alpha} \mathrm{s}_k^2 \mathbf{p}_k \otimes \mathbf{p}_k \otimes \mathbf{p}_k \otimes \mathbf{p}_k \\ \mathbb{B}_2^\alpha = \frac{1}{B^\alpha} \sum_{N_{seg}} \sum_{\mathcal{B}_k^\alpha} \mathrm{s}_k \mathrm{s}_l \mathbf{p}_l \otimes \mathbf{p}_k \otimes \mathbf{p}_k \otimes \mathbf{p}_k \end{cases}. \tag{22}$$

The case of the rod-rod bonds b_h was considered separately from the case of amorphous kink bonds b_a, to simplify the expression of the tensors $\mathbb{B}_i^\alpha$.

Case of rod-rod bonds $\mathrm{b_h}$

By assuming that rod-rod bonds were uniformly distributed along the rod length, the following discrete sums can be written[79]:

$$\begin{cases} \sum_{\mathcal{B}_k^h} \mathrm{s}_k^2 \approx z^h \frac{l_{seg}^2}{12} (1 - \frac{1}{z^h}) \\ \sum_{\mathcal{B}_k^h} \mathrm{s}_k \approx 0 \end{cases}. \tag{23}$$

Then, by assuming that s_k and s_l are uncorrelated, the expressions of $\mathbb{B}_1^h$ and $\mathbb{B}_2^h$ are

$$\begin{cases} \mathbb{B}_1^h \approx \frac{l_{seg}^2}{6} (1 - \frac{1}{z^h}) \mathbb{A} \\ \mathbb{B}_2^h \approx 0 \end{cases}, \tag{24}$$

where $\mathbb{A}$ is the fourth-order rod orientation tensor defined in eqn(17). These two relations were validated using the microstructure generator.

Case of amorphous kink bonds $\mathrm{b_a}$

In this particular case, bonds are systematically located at the extremities of the rods, so that

$$\forall\ k, \mathrm{s}_k{}^2 = l_{seg}^2/4, \tag{25}$$

and

$$\sum_{\mathcal{B}_k^a} \mathrm{s}_k^2 \approx z^a \frac{l_{seg}^2}{4} \text{ and } \mathbb{B}_1^a \approx \frac{l_{seg}^2}{2} \mathbb{A}, \tag{26}$$

and we also checked that $\mathbb{B}_2^a \approx \mathbf{0}$ using the microstructure generator.

Références

1 A. Dufresne, Nanocellulose: From Nature to High Performance Tailored Materials, Walter de Gruyter, 2013.

2 I. Siró and D. Plackett, Cellulose, 2010, 17, 459–494.

3 K.-Y. Lee, Y. Aitomäki, L. A. Berglund, K. Oksman and A. Bismarck, Compos. Sci. Technol., 2014, 105, 15–27.

4 S. J. Eichhorn, A. Dufresne, M. Aranguren, N. E. Marcovich, J. R. Capadona, S. J. Rowan, C. Weder, W. Thielemans, M. Roman, S. Renneckar, W. Gindl, S. Veigel, J. Keckes, H. Yano, K. Abe, M. Nogi, A. N. Nakagaito, A. Mangalam, J. Simonsen, A. S. Benight, A. Bismarck, L. A. Berglund and T. Peijs, J. Mater. Sci., 2009, 45, 1–33.

5 R. J. Moon, A. Martini, J. Nairn, J. Simonsen and J. Youngblood, Chem. Soc. Rev., 2011, 40, 3941–3994.

6 C.-N. Wu, Q. Yang, M. Takeuchi, T. Saito and A. Isogai, Nanoscale, 2013, 6, 392–399.

7 H. Zhu, S. Parvinian, C. Preston, O. Vaaland, Z. Ruan and L. Hu, Nanoscale, 2013, 5, 3787–3792.

8 J. Huang, H. Zhu, Y. Chen, C. Preston, K. Rohrbach, J. Cumings and L. Hu, ACS Nano, 2013, 7, 2106–2113.

9 M. Miao, J. Zhao, X. Feng, Y. Cao, S. Cao, Y. Zhao, X. Ge, L. Sun, L. Shi and J. Fang, J. Mater. Chem. C, 2015, 3, 2511–2517.

10 C. Aulin, G. Salazar-Alvarez and T. Lindström, Nanoscale, 2012, 4, 6622–6628.

11 M.-C. Hsieh, C. Kim, M. Nogi and K. Suganuma, Nanoscale, 2013, 5, 9289–9295.

12 Z. Shi, G. O. Phillips and G. Yang, Nanoscale, 2013, 5, 3194–3201.

13 R. Bardet, M. N. Belgacem and J. Bras, Cellulose, 2013, 20, 3025–3037.

14 S. Saini, N. Belgacem, J. Mendes, G. Elegir and J. Bras, ACS Appl. Mater. Interfaces, 2015, 7, 18076–18085.

15 J.-L. Wertz, J.-P. Mercier and O. Bédué, Cellulose Science and Technology, CRC Press, 2010.

16 H. P. S. Abdul Khalil, Y. Davoudpour, M. N. Islam, A. Mustapha, K. Sudesh, R. Dungani and M. Jawaid, Carbohydr. Polym., 2014, 99, 649–665.

17 T. Saito, S. Kimura, Y. Nishiyama and A. Isogai, Biomacromolecules, 2007, 8, 2485–2491.

18 A. Isogai, T. Saito and H. Fukuzumi, Nanoscale, 2011, 3, 71–85.

19 A. Isogai, J. Wood Sci., 2013, 59, 449–459.

20 F. Dalmas, J.-Y. Cavaillé, C. Gauthier, L. Chazeau and R. Dendievel, Compos. Sci. Technol., 2007, 67, 829–839.

21 X. Xu, F. Liu, L. Jiang, J. Y. Zhu, D. Haagenson and D. P. Wiesenborn, ACS Appl. Mater. Interfaces, 2013, 5, 2999–3009.

22 V. Favier, H. Chanzy and J.-Y. Cavaillé, Macromolecules, 1995, 28, 6365–6367.

23 V. Favier, J.-Y. Cavaillé, G. R. Canova and S. C. Shrivastava, Polym. Eng. Sci., 1997, 37, 1732–1739.

24 H. Sehaqui, Q. Zhou and L. A. Berglund, Soft Matter, 2011, 7, 7342–7350.

25 C. J. G. Plummer, S. Galland, F. Ansari, Y. Leterrier, P.-E. Bourban, L. A. Berglund and J. E. Månson, Plast. Rubber Compos., 2015, 44, 81–86.

26 C. J. G. Plummer, C. K. C. Choo, C. I. R. Boissard, P.-E. Bourban and J.-A. E. Månson, Colloid Polym. Sci., 2013, 291, 2203–2211.

27 A. Kulachenko, T. Denoyelle, S. Galland and S. B. Lindström, Cellulose, 2012, 19, 793–807.

28 G. Josefsson, G. Chinga-Carrasco and E. K. Gamstedt, RSC Adv., 2015, 5, 58091–58099.

29 S. W. Tsai, Theory of composites design, Think composites Dayton, 1992.

30 S. W. Tsai and N. J. Pagano, Invariant properties of composites materials, 1968.

31 H. L. Cox, Br. J. Appl. Phys., 1952, 3, 72–79.

32 H. Krenchel, Fibre reinforcement, Alademisk forlag, 1964.

33 Q. Cheng, S. Wang and D. P. Harper, Compos. Part Appl. Sci. Manuf., 2009, 40, 583–588.

34 S. Iwamoto, W. Kai, A. Isogai and T. Iwata, Biomacromolecules, 2009, 10, 2571–2576.

35 A. Gandini and M. N. Belgacem, Springer Berlin Heidelberg, 2015, pp. 1–38.

36 K. Missoum, M. N. Belgacem and J. Bras, Materials, 2013, 6, 1745–1766.

37 L. Heux, G. Chauve and C. Bonini, Langmuir, 2000, 16, 8210–8212.

38 A. J. Benítez, J. Torres-Rendon, M. Poutanen and A. Walther, Biomacromolecules, 2013, 14, 4497–4506.

39 T. Saito, T. Uematsu, S. Kimura, T. Enomae and A. Isogai, Soft Matter, 2011, 7, 8804–8809.

40 S. Fujisawa, T. Ikeuchi, M. Takeuchi, T. Saito and A. Isogai, Biomacromolecules, 2012, 13, 2188–2194.

41 H. Sehaqui, N. Ezekiel Mushi, S. Morimune, M. Salajkova, T. Nishino and L. A. Berglund, ACS Appl. Mater. Interfaces, 2012, 4, 1043–1049.

42 J. Viguié, P. Latil, L. Orgéas, P. J. J. Dumont, S. Rolland du Roscoat, J.-F. Bloch, C. Marulier and O. Guiraud, Compos. Sci. Technol., 2013, 89, 202–210.

43 C. Marulier, P. J. J. Dumont, L. Orgéas, S. R. du Roscoat and D. Caillerie, Cellulose, 2015, 22, 1517–1539.

44 L. Orgéas, P. J. J. Dumont, J.-P. Vassal, O. Guiraud, V. Michaud and D. Favier, J. Mater. Sci., 2011, 47, 2932–2942.

45 V. Favier, R. Dendievel, G. Canova, J.-Y. Cavaillé and P. Gilormini, Acta Mater., 1997, 45, 1557–1565.

46 F. Dalmas, R. Dendievel, L. Chazeau, J.-Y. Cavaillé and C. Gauthier, Acta Mater., 2006, 54, 2923–2931.

47 L. Berhan and A. M. Sastry, Phys. Rev. E, 2007, 75, 041121.

48 S. Lavrykov, S. B. Lindström, K. M. Singh and B. V. Ramarao, Nord. Pulp Pap. Res. J., 2012, 27, 256.
49 Salminen, Nord. Pulp Pap. Res. J., 2002, 17, 105–110.
50 F. Martoïa, P. J. J. Dumont, L. Orgéas, M. N. Belgacem and J.-L. Putaux, Soft Matter, 2015 (submitted).
51 I. Sakurada, Y. Nukushina and T. Ito, J. Polym. Sci., 1962, 57, 651–660.
52 T. Nishino, K. Takano and K. Nakamae, J. Polym. Sci. Part B Polym. Phys., 1995, 33, 1647–1651.
53 M. Bulota, S. Tanpichai, M. Hughes and S. J. Eichhorn, ACS Appl. Mater. Interfaces, 2012, 4, 331–337.
54 S. Tanpichai, W. W. Sampson and S. J. Eichhorn, Compos. Part Appl. Sci. Manuf., 2014, 65, 186–191.
55 I. Usov, G. Nyström, J. Adamcik, S. Handschin, C. Schütz, A. Fall, L. Bergström and R. Mezzenga, Nat. Commun., 2015, 6, 7564.
56 S. Toll, J. Rheol., 1993, 37, 123–125.
57 G. E. Pike and C. H. Seager, Phys. Rev. B, 1974, 10, 1421–1434.
58 Y. Nishiyama, U.-J. Kim, D.-Y. Kim, K. S. Katsumata, R. P. May and P. Langan, Biomacromolecules, 2003, 4, 1013–1017.
59 R. J. Hill, Biomacromolecules, 2008, 9, 2963–2966.
60 S. J. Eichhorn and R. J. Young, Cellulose, 2001, 8, 197–207.
61 M. Bergenstråhle, L. A. Berglund and K. Mazeau, J. Phys. Chem. B, 2007, 111, 9138–9145.
62 K. Tashiro and M. Kobayashi, Polym. Bull., 1985, 14, 213–218.
63 K. Niskanen, Mechanics of Paper Products, Walter de Gruyter, 2012.
64 J. A. Åström, J. P. Mäkinen, M. J. Alava and J. Timonen, Phys. Rev. E, 2000, 61, 5550–5556.
65 P. Latil, L. Orgéas, C. Geindreau, P. J. J. Dumont and S. R. Du Roscoat, Compos. Sci. Technol., 2011, 71, 480–488.
66 S. Le Corre, D. Caillerie, L. Orgéas and D. Favier, J. Mech. Phys. Solids, 2004, 52, 395–421.
67 S. L. Corre, P. J. J. Dumont, L. Orgéas and D. Favier, J. Rheol., 2005, 49, 1029–1058.
68 J.-L. Auriault, Int. J. Eng. Sci., 1991, 29, 785–795.
69 C. Marulier, Etude multi-échelles des couplages entre propriétés hygroélastiques des papiers et leur microstructure, PhD thesis, University of Grenoble Alpes, 2013.
70 S. G. Advani and C. L. Tucker II, J. Rheol., 1987, 31, 751–784.
71 C. Marulier, P. J. J. Dumont, L. Orgéas, D. Caillerie and S. R. du Roscoat, Nord. Pulp Pap. Res. J., 2012, 27, 245.
72 U. Hirn and R. Schennach, Sci. Rep., 2015, 5.
73 F. J. Schmied, C. Teichert, L. Kappel, U. Hirn, W. Bauer and R. Schennach, Sci. Rep., 2013, 3.

74 S. Rohm, U. Hirn, C. Ganser, C. Teichert and R. Schennach, Cellulose, 2014, 21, 237–249.

75 P. N. Ciesielski, J. F. Matthews, M. P. Tucker, G. T. Beckham, M. F. Crowley, M. E. Himmel and B. S. Donohoe, ACS Nano, 2013, 7, 8011–8019.

76 C. H. Haigler, M. J. Grimson, J. Gervais, N. Le Moigne, H. Höfte, B. Monasse and P. Navard, PLoS ONE, 2014, 9, e93981.

77 S. Paavilainen, T. Róg and I. Vattulainen, J. Phys. Chem. B, 2011, 115, 3747–3755.

78 F. Martoïa, C. Perge, P. J. J. Dumont, L. Orgéas, M. A. Fardin, S. Manneville and M. N. Belgacem, Soft Matter, 2015, 11, 4742–4755.

79 J.-P. Vassal, L. Orgéas, D. Favier, J.-L. Auriault and S. Le Corre, Phys. Rev. E, 2008, 77, 011303.

Chapitre 5

Optimization of ice templating NFC foams: microstructure and mechanical behavior

Ce chapitre est basé sur un article actuellement soumis dans le journal *ACS Applied Materials and Interfaces*, F. Martoïa, T. Cochereau, P.J.J. Dumont, L. Orgéas, M.N. Belgacem.

Abstract

We investigated how ice templating conditions affected the microstructure, shrinkage and mechanical properties of enzymatic and TEMPO-oxidized cellulose nanofibril (NFC) foams obtained using freeze drying. Two solidification techniques were explored. The first technique involved the quenching of NFC water suspensions in temperature-controlled baths, thus enabling the production of monomodal foam cell size. The second technique consisted of a mechanically stirring the solidifying suspensions followed by quenching at a lower temperature. This original technique led to interesting bimodal foam cell structures. Below a critical NFC concentration which depended on the NFC morphology and colloidal stability, the obtained foams exhibited severe shrinkage. Low quenching temperature and NFC polydispersity also negatively affected NFC foam structures. From this experimental database, processing optimization maps for NFC foams were obtained. In the best processing window, homogeneous NFC foams consisted of irregular and complex cells and exhibited open porosity, but also entrapped remaining fibers or dangling mass (branches, for enzymatic NFCs only), as revealed by FE-SEM and high-resolution synchrotron X-ray microtomography images. The compressive behavior of these foams was characterized by successive elastic, strain-hardening and densification regimes, strain localization as well as auxetic properties and was dependent on quenching temperatures. For the first time, the corresponding deformation mechanisms at the cell scale were finely analysed with 3D micrographs of a compression experiment performed inside X-ray synchrotron microtomograph. In addition, bimodal cell sizes also drastically enhanced the mechanical properties of NFC foams. Finally, both the Young's modulus and the yield stress of NFC foams exhibited power-law functions of their relative density. The power-law exponents are in accordance with other polymeric or metallic foams for TEMPO-oxidized NFCs, whereas they reach unusual high values for enzymatic NFCs, which could be related to the presence of dangling mass in the cell walls.

5.1 Introduction

Cellulose nanofibrils (NFCs) are the elementary reinforcing constituents of plant cell walls[1,2,3]. They are usually extracted from cellulose fibers by a combination of chemical pre-treatments such as, for instance, enzymatic hydrolysis[4,5] or TEMPO-mediated oxidations[6,7], and mechanical shearing[8]. NFCs are typically obtained in the form of aqueous colloidal suspensions. These suspensions can be used to manufacture a variety of promising renewable materials[9] such as foams[10,11,12] and aerogels[13,14], films and nanopapers[15].

NFC foams constitute low density (density ranging from 10 kg m^{-3} to 100 kg m^{-3}) renewable materials that exhibit interesting mechanical and insulation properties (elastic modulus: $10^{-2} \leq E \leq 5$ MPa and thermal conductivity: 18 mW $K^{-1}m^{-1} \leq \lambda \leq$ 80 mW $K^{-1}m^{-1}$). These cellular materials have a great potential in several engineering fields. For instance, they can be used in automotive industry as heat and/or sound insulation boards or for biomedical applications as filtering and purifying membranes or even as scaffolds for tissues. However, the selection and the use of a specific foam for a particular engineering application require a proper understanding and control of its microstructure and its mechanical behavior, particularly, in terms of deformation and failure mechanisms[16,17].

NFC foams are usually obtained from NFC water suspensions by ice templating, *i.e.*, after freezing the suspensions and sublimating the formed ice crystals (freeze-drying)[10,11,12]. Ice templating process research and development has received considerable attention in recent years[18,19,20] owing to its simplicity and to the wide variety of porous materials that this technique can give. However, controlling the arrangement and organisation of particles during processing is complex and still not well understood[18,19,20]. Several studies have shown that the phenomena of particle segregation and separation that occur during ice growth in aqueous colloidal suspensions depend on a large number of factors that are related to both the processing conditions (temperature field) and the nature of colloids (particle size, geometry, density, conductivity, surface charge and impurities)[18,19,20,21]. Most of the studies have so far been confined to ceramics and polymers[19,22]. Surprisingly, NFC foams are often produced under weakly controlled solidification conditions using temperatures and cooling rates that vary over narrow ranges[23,24,25,26,27]. In these studies, the solidification or freezing of NFC water suspensions is usually achieved by dipping them into liquid nitrogen or by placing them inside a freezer. Thus, to date, the links between the processing conditions, the microstructure and the mechanical performances of NFC foams have not yet been clearly established. In addition, to the best of our knowledge, no study has finely investigated the role of suspension concentration and stability on the structural and mechanical properties of NFC foams.

Thus, in this study, our objectives were to investigate not only the effects of solidification conditions (cooling rate), but also those of the desired geometry, the surface charge and the NFCs concentration on the macro-, meso- and micro-structures as well as on the mechanical behavior of the processed NFC foams. For this purpose, two types of NFC suspensions with different microstructures and colloidal stability, namely enzymatic and TEMPO-oxidized

NFC suspensions were used. The NFC suspensions were quenched at different freezing temperatures (-196°C ≤ T ≤ -10°C) that enabled the freezing rate to be varied. An original 'sorbet-like' solidification technique was also used to investigate the effect of mechanical stirring on the structure and the mechanics of NFC foams. The microstructural properties of the obtained NFC foams were investigated using both electron microscopy (FE-SEM) and synchrotron X-ray microtomography. Their mechanical properties were also investigated using both classical compression techniques and *in situ* compression tests during X-ray imaging experiments. To the best of our knowledge these experiments are original and have never been applied to NFC foams. They enabled a better understanding of the morphology of the NFC foam cells as well as a better description of their deformation and damage mechanisms during compression. Such an experimental database could then be used to develop relevant numerical and theoretical micromechanical models[28].

5.2 Materials and experimental procedures

5.2.1 Extraction and charcaterization of NFC suspensions

TEMPO-oxidized NFC suspensions at a concentration of 1 %wt were extracted from a commercial eucalyptus bleached kraft pulp (Celbi, Portugal) using a methodology similar to that already reported by Martoïa *et al.*[29]. Enzymatic NFC suspensions (at a concentration of 2 *wt*%) were provided by the Centre Technique du Papier (CTP, France). These suspensions were isolated from an enzymatically treated birch bleached kraft pulp by mechanical disintegration using a homogenizer (Model M-110 EH-30, GE Niro Soavi, USA). To prepare NFC foams with various relative densities ρ/ρ_s, where ρ_s is the density of the solid constituting the foam ($\rho_s = 1500$ kg m^{-3} for cellulose[30]), both types of suspensions were either diluted by adding deionized water, or concentrated by high speed centrifugation (10 000 rpm for 20 min).

The semi-quantitative analysis of the microstructural properties of the extracted NFC suspensions revealed that enzymatic NFC suspensions were polydisperse suspensions that contained sporadically partially fibrillated fibers (diameter ≈ 20 µm and length $\approx 150 - 300$ µm), bundles of fibrils having a diameter that ranged between 100 and 200 nm, and nanoscale elements in the form of individualized fibrils with a diameter that ranged between 20 and 50 nm (Fig. 5-1.a,c). The particle size polydispersity of TEMPO-oxidized NFC suspensions was much sharper. These suspensions contained few fibers close to their original dimensions (diameter ≈ 20 µm and length $\approx 600 - 700$ µm) and much more very slender individualized fibrils with a diameter and length that ranged between 3 and 6 nm and between 1 and 1.4 µm, respectively (Fig. 5-1.b,c). It is also worth to note that these fibrils exhibited kinks.

The content of carboxyl groups (-COOH) determined by conductimetric titration was 1.45 mmol g^{-1} for NFC obtained after TEMPO-mediated oxidation[29], whereas it was 0.075 mmol g^{-1} for enzymatic NFCs. Thus, as expected, TEMPO-oxidized NFCs were much more electrically charged and kinetically stable in water suspension.

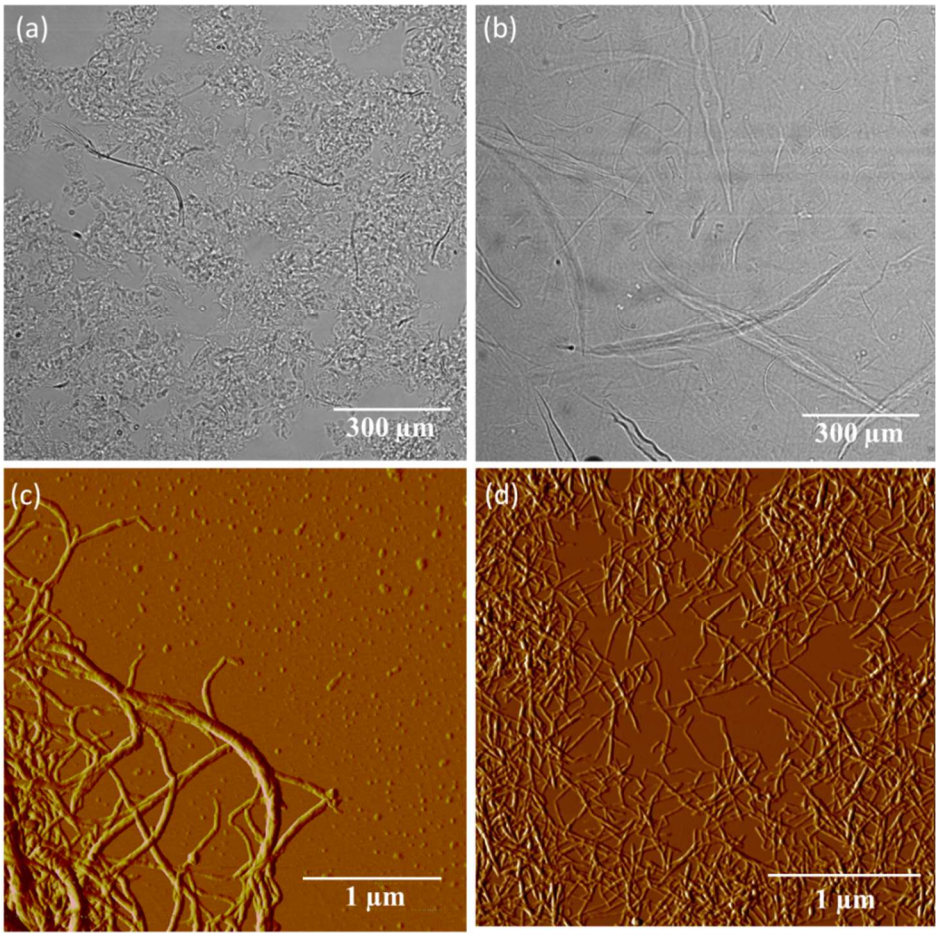

Figure 5-1. Optical micrographs of a 0.1 $wt\%$ enzymatic NFC suspension (a), and a 0.1 $wt\%$ TEMPO-oxidized NFC suspension (b). AFM micrographs of an enzymatic NFC film (c) and a TEMPO-oxidized NFC film (d) obtained after drying a suspension at 0.001 $wt\%$.

5.2.2 2D microstructural characterization by SEM-FEG

The microstructural properties of NFC foams were investigated at different scales using a scanning electron microscope equipped with a field emission gun (FEG) system (Zeiss Ultra 55 gemini column) in low vacuum conditions and with a voltage set at 2 kV. Sample preparation is crucial to obtain representative images of the cellular structure of foams. Thus, NFC foams were carefully cut using razor blades. Before taking the images, a layer of gold and palladium with a thickness of $2-3$ nm was applied to the surface of NFC foams to be imaged.

5.2.3 3D microstructural characterization by X-ray synchrotron microtomography

The microstructures of NFC foams were studied in 3D using the high-resolution X-ray synchrotron microtomograph of the ID 19 beamline at the European Synchrotron Radiation Facilities (Grenoble, France). This beamline was chosen because it delivers a very intense monochromatic beam and enables images with a high signal-to-noise ratio to be acquired.

The foams were fixed on a rotation stage between the X-ray source and the detection unit that recorded the transmitted X-rays. Then, they were rotated under the beam incrementally up to 180° to provide a set of 3000 radiographs (duration of the scan ≈ 60 s). The beam energy was set to 19 keV and a resolution of 0.32 µm was chosen to obtain accurate representations of the foam cell structures. Then, 3D images were reconstructed using a procedure based on the exploitation of the phase contrast in the images[31,32].

5.2.4 Mechanical characterization

Uniaxial compression tests were performed on cylindrical specimens (mean diameter $D \approx$ 16 mm and mean initial height $h_0 \approx 15$ mm). Before testing, NFC foams were stored for at least 1 day in controlled conditions ($T = 25$°C and $HR = 56\%$). Cyclic tests were conducted at a constant compression strain-rate of $|\dot{\varepsilon}| \simeq 0.02\ \mathrm{s}^{-1}$, using an Instron testing machine equipped with a force sensor of 50 N or 500 kN. During the tests, both the nominal compression stress $\sigma = F/S_0$ (where F was the normal force and S_0 the initial section of the foam) and the logarithmic strain $\varepsilon = \ln\left(\frac{h_z}{h_{z0}}\right)$(where h_{z0} and h_z are the initial and current height of the foam, respectively) were acquired. The Young's modulus E of the foams was estimated from the initial linear part of the $\sigma - \varepsilon$ curves and the yield stress σ_y was calculated from the intersection of the two lines delimiting, respectively, the elastic domain and the strain hardening plasticity regime above the yield stress (Fig. 5-7).

5.2.5 In situ compression test with X-ray synchrotron microtomography

The microstructure of a selected TEMPO NFC foam (obtained using a quenching temperature of −13°C) and its evolution under compression loading was studied using X-ray synchrotron microtomography.

The foam was cut in a small cube (≈ 4 mm × 4 mm × 4 mm) using a razor blade and then subjected to low strain-rate compression tests ($|\dot{\varepsilon}| = 0.005\ \mathrm{s}^{-1}$), using a specially designed micro-press equipped with a force sensor of 5 N (inset in Fig. 5-8). This setup is similar to that used in Latil *et al.*[33]. The compression test was interrupted at 3 compression strains of $\varepsilon = 0.11,\ 0.8$ and 2.2. At each compression stop, a fast scan (duration ≈ 60 s) of the deformed NFC foam was first performed at a resolution of 1.6 µm to visualize the entire sample. In addition, to obtain an accurate representation of the bulk deformation and failure micro-mechanisms that occurred at the cell scale, the deformed foam (Fig. 5-8) was also imaged using a resolution of 0.32 µm (Fig. 5-9), by performing and concatenating four additional high resolution scans along the whole height of the sample with orthogonal cross sections of ≈ 818 × 818 µm² (Fig. 5-9).

5.3 Processing of NFC foams

5.3.1 Direct quenching

In a first approach, NFC foams were prepared using a quenching technique (Fig. 5-2.a). In this context, NFC suspensions at various concentrations were poured into glass tubes (≈ 5 ml) before being quenched in various baths having a volume V of ≈ 300 ml, *i.e.*, baths with various liquids at their solid-liquid transition temperature (Fig. 5-2.a). The different used liquids enabled us to monitor the temperature of the baths and the averaged cooling rate of the NFC suspensions, as shown in Table 5-1. The photographs of the upper surface of the NFC suspensions during freezing (Fig. 5-2.b,c) revealed that away from the bottom of the tubes, the ice front was moving homogenously in the radial $\boldsymbol{e}_r$-direction. Furthermore, ice formation induced a positive volume variation and caused the suspension to flow in the vertical $\boldsymbol{e}_z$-direction of the tube. This vertical displacement was at the origin of the 'conical parts' that were visible on the top of the NFC foams (Fig. 5-3). At the end of the solidification process, frozen suspensions were dried in a freeze-dryer to induce water sublimation (Christ alpha 2-4LD plus, Christ, UK) for 48 h (Fig. 5-2). The temperature of the inner chamber of the freeze-dryer was set to −60°C and the pressure to 20 mbar.

Table 5-1. Summary of the different liquids used to freeze NFC suspensions.

Cooler	Temperature of the solid-liquid bath (°C)	Total solidification duration (min)
Benzonitrile	-13	≈ 20
Acetonitrile	-40	≈ 8
Butyl acetate	-68	≈ 6
Acetone	-80	≈ 5
Propanol	-100	≈ 4
Ethanol	-114	≈ 3
Liquid nitrogen	-196	≈ 2

5.3.2 Mechanical stirring and quenching

The previous preparation of NFC foams by quenching and then freeze-drying is interesting and easy to operate but yields anisotropic structures because of the radial and columnar growth of ice crystals during freezing (Fig. 5-2.b and Fig. 5-4.b,h). Besides, this technique does not enable materials with multiple scales of porosity to be obtained since the final architecture is induced by a unique physical mechanism that involves the segregation and redistribution of NFCs by the moving ice front[19,20]. To obtain foams with multimodal structures that are interesting for example from the mechanical properties point of view, several nucleation processes or mechanisms are required during forming[34]. For instance, multimodal polymer

foams are often obtained using sequential foaming steps or by adding different blowing agents to induce several nucleating mechanisms[34,17].

Here, we developed an alternate freezing procedure inspired from food industry or that used to process metals for thixocasting[35,36]. The adopted technique consisted in restraining, with a mechanical stirring, the dendritic and columnar ice crystal growth during solidification to obtain a first class of ice grains with rounded shape. Hence, NFC suspensions were poured into a sorbet machine and then continuously mixed at a temperature of -18°C until the suspensions exhibited an ice-cream texture (≈ 1 h). Then, glass tubes were filled with the ensuing suspensions before being quenched in a butyl-acetate bath at a temperature of -68°C to completely solidify the suspensions, with the growth of the first class of ice grains and the nucleation and growth of a second class of ice crystals. Hence, this sequential forming process used two different nucleating and solidification mechanisms to induce variations in the ice growth kinetics. It is worth to note that this forming technique could be easily implemented at the industrial scale, for instance, using a refrigerated paper blend chest.

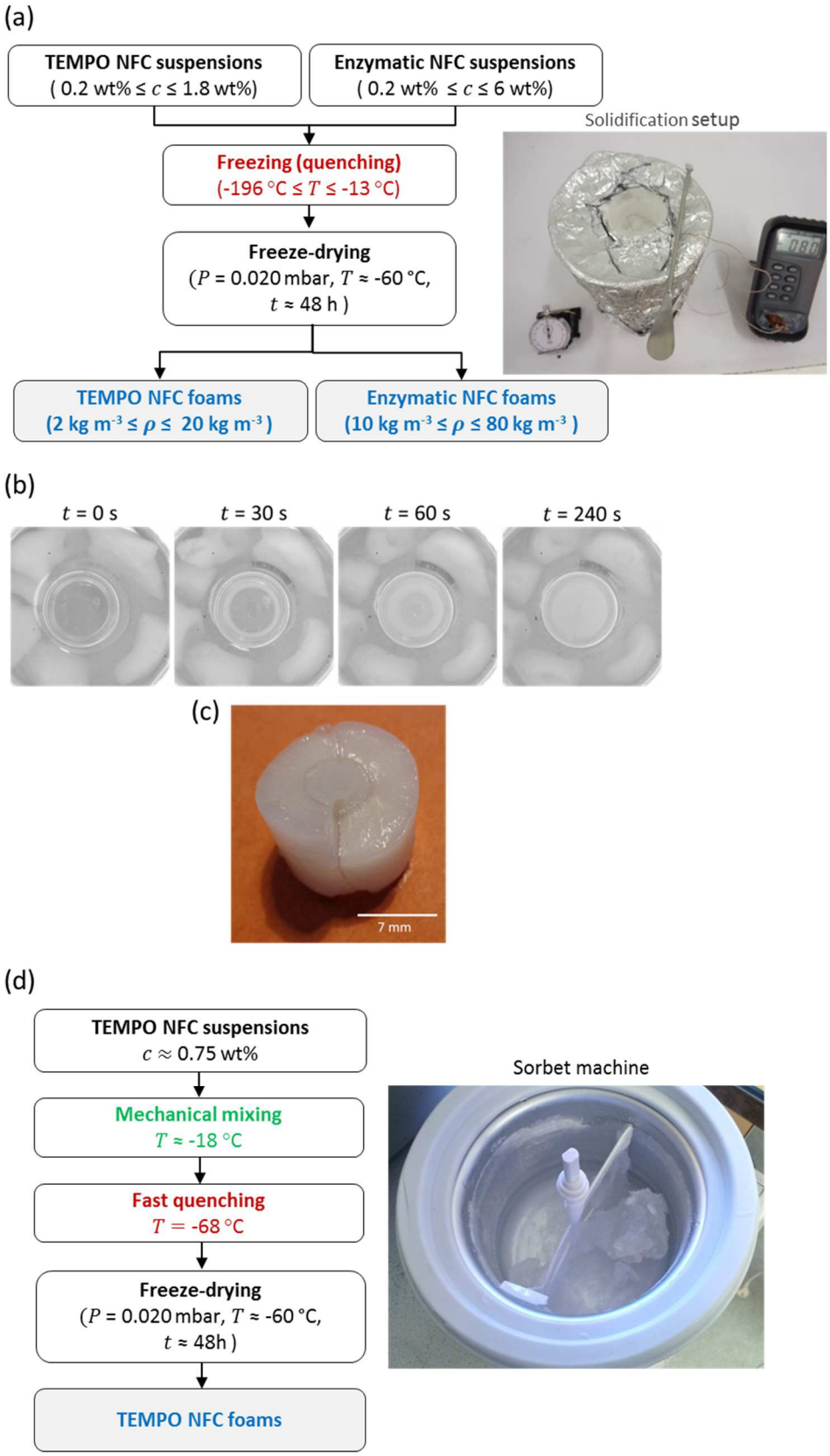

Figure 5-2. (a) Schematic representation of the quenching procedure used to obtain enzymatic and TEMPO-oxidized NFC foams. (b) Surface observations at different times *t* of a glass tube containing a TEMPO-oxidized NFC suspension that was quenched in an acetone bath. (c) Photograph of the fracture surface of an enzymatic NFC suspension after quenching in an acetone bath during 40 s. (d) Sketch of the 'sorbet-like' NFC foam processing route.

5.4 Structural characterization

A qualitative study of the macro- and meso-structures of different foams obtained by varying both the NFC concentration and the quenching temperature (freezing rate) was conducted and allowed material processing maps to be obtained within which optimal working conditions were identified (zone 1 in Fig. 5-3.a,b). Within these optimal domains, NFC foams exhibited homogeneous structures as well as a low and homogeneous macroscopic shrinkage, as shown by the photographs in Figure 5-3. Elsewhere, different apparent defects were detected.
For instance, NFC foams prepared at extremely low freezing temperature, *i.e.*, $T \simeq -196$°C, systematically displayed macro- and mesoscale defects in the form of cracks (zone 3 in Fig. 5-3.a,b). These cracks occurred during the fast solidification of the suspensions and were induced by the sudden volume change that was inherent to the liquid-to-solid phase transformation[37]. Contrary to the observations of Sehaqui *et al.*[10], the pre-cooling of the suspensions at 4°C did not prevent any crack propagation for these processing conditions.

Besides, for both types of suspensions, increasing the freezing temperatures (and thus lowering the cooling rates) yielded an increase of the foam shrinkage. Similarly, the foam shrinkage increased as the NFC concentration decreased (Fig. 5-3.c,d). The macroscopic shrinkage of the NFC foams could be potentially attributed to several combined microscale mechanisms:

- During the solidification, a particle depletion or migration could take place. This type of phenomenon is known to occur preferentially in weakly stabilized colloidal systems such as flocculated and dilute colloidal suspensions, and for low freezing rates[19,20].
- During the drying, *i.e.*, during the sublimation of ice-crystals, folding of the cells could result from the release of internal stresses that were induced in the cell walls during the nucleation and growth of ice crystals.
- During the drying, folding and shrinkage of the cell walls could also be induced by the hyroexpansion-related shrinkage of NFCs.

It is also worth to note that for both types of NFC suspensions (zone 2 in Fig. 5-3.a,b), theshrinkage diameter (Fig. 5-3c,d) was characterized by a sudden increase at a critical NFC concentration $c^* \approx 0.25$ $wt\%$ for TEMPO-oxidized NFC suspensions and $c^* \approx 0.8$ $wt\%$ for enzymatic NFC suspensions (here noticed at a freezing temperature of -68°C). This critical concentration presumably corresponded to a NFC concentration below which the entangled NFC networks lose their mechanical integrity, *i.e.*, to a critical number of bonds or interactions per nanofiber[38]. This number could also depend on the particle geometry[39,40] (aspect ratio, waviness, spatial placement and orientation) and on the particle electrostatic charge[41,42], as shown by the difference between TEMPO-oxidized NFC and enzymatic NFC suspensions. Finally, the upper limits of the processing map (zone 4 in Fig. 5-3.a,b) was roughly associated with the maximum NFC concentrations that could be obtained after centrifugation (10 000 rpm for 20 min). For these NFC concentrations, air bubbles that were introduced during the filling of the glass tube remained difficult to remove (even under low vacuum), leading to structural defects after ice sublimation.

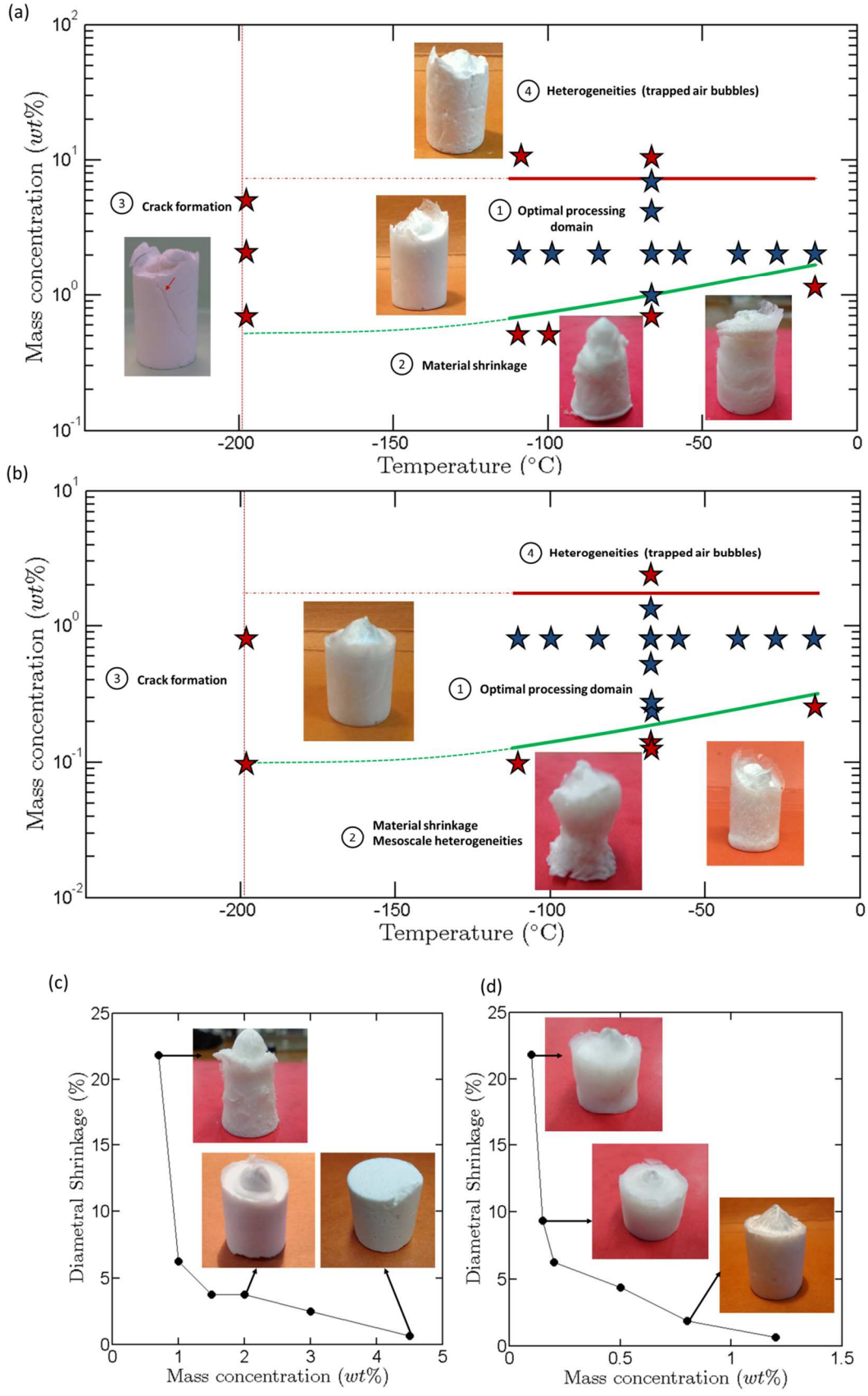

Figure 5-3. Processing maps of enzymatic NFC foams (a) and TEMPO-oxidized NFC foams (b). The graphs (c,d) show the evolution of the shrinkage diameter reduction $(D_t - D)/D_t$ (where D_t is the diameter of the tube and D the average diameter along the height of the foam), as a function of the NFC concentration: for (c) enzymatic NFC suspensions and (d) TEMPO-oxidized NFC suspensions. In graphs (c,d), the foams were obtained using a freezing temperature $T \simeq$ -68°C.

The microstructure of the homogenous NFC foams, *i.e.*, those obtained in the optimal processing domain (zone 1, Fig. 5-3a,b) were extensively studied. The SEM micrographs and 3D tomographic images that are gathered in Figure 5-4 and Figure 5-5, for TEMPO-oxidized NFCs and enzymatic NFCs, respectively, show that both types of foams exhibited complex cellular architectures and open porosity. The morphology of the cells was different from that usually observed in most of the synthetic polymer foams[16]. NFC foams consisted of an irregular arrangement of thin plates (in the form of NFC films) that occasionally intersected with remaining partially fibrillated fibers or dangling mass, *i.e.*, branches (see the comments related to Figure 5-1.a,b and SEM micrographs in Fig. 5-4.a). Besides, the 3D-rendered perspective views in Figure 5-4.e,f show that the plates were slightly curved. Their dimensions also varied and they had non-uniform thicknesses: over the plate surface (Fig. 5-4.e,f) but also from one plate to another (Fig. 5-4.g,h and Fig. 5.f,h).

In addition, TEMPO-oxidized and enzymatic NFC foams exhibited remarkable microstructural differences. The geometry of TEMPO-oxidized cell foams (Fig. 5-4) was more regular compared with that observed in enzymatic foams (Fig. 5-5). The 2D X-ray and the SEM images in Fig. 5-4 reveal the anisotropic and columnar geometry of the pores in TEMPO-oxidized foams. These structures were rather similar to many polymers foams: three plates or faces meet at each edge with interface angles that varied over a wide range of values (Fig. 5-4e,f). On the contrary, enzymatic foams exhibited more erratic and intricate structures, which made difficult the direct observations of the foam cell geometry (Fig. 5-5). These noticeable structural differences emphasize the undeniable role of the NFC nanostructures and their physico-chemical properties on the phenomena of particle segregation, entrapment and redistribution that occur during ice growth[20]. Because of their smallest dimensions and strongest colloidal stability (see the comments in section 2.1), TEMPO-oxidized NFCs were presumably more homogenously redistributed by the moving ice front, leading to more regular structures. The situation was probably more complex and chaotic with enzymatic suspensions since they were more polydisperse and exhibited meso-scale heterogeneities in the form of NFC flocs or floc chains (Fig. 5-1.a, floc size $\simeq 10-300$ µm)[29]. Larger particles or aggregates generally display less mobility. Hence, they are more easily encapsulated (instead of being redistributed) by the moving ice front[19,20]. These complex mechanisms could be at the origin of the severe structural defects and heterogeneities within the processed enzymatic foams.

The numerous multiscale observations gathered in Figure 5-4 and Figure 5-5 also show that the morphology of the pores/cells could vary drastically, as a function of the applied freezing temperature. Between −13°C and −80°C, the mean pore size sharply decreased from few hundred microns ($300-50$ µm) to a few tenths of microns ($20-10$ µm) for TEMPO-oxidized and enzymatic foams. Note also that NFC foams obtained at high freezing temperature, *i.e.*, $T = -13°C$ (Fig. 5-4.a,e,f,g,h), consisted of cells that were more polydisperse compared with those observed in NFC foams that were obtained by lowering the freezing temperature (Fig.5-4.b). However, between −80°C and −120 °C no significant variations in the pore morphology and size were clearly evidenced from the SEM micrographs. Similar noteworthy variations in the

pore morphology have also been reported by Jiang *et al.*[37] who fabricated TEMPO-oxidized foams using freezing temperatures that ranged between −20°C and −196°C. These results show that the pore size is governed by the size of ice crystals, and that the control of crystal nucleation and their growth prior to freeze-drying play a primary role in building the microstructure of NFC foams[37,27]. Thus, the following scenario could explain the final structure of NFC foam structures:

- At low freezing temperature and thus high average cooling rate, nucleation rate is higher than crystal growth rate[20]. A large number of small ice crystals are formed during freezing and the porous microstructure of NFC foams consists of uniform small pores (see for instance Fig. 5-4c). Note also that, at low freezing temperatures, there is more time for particles rearrangement, thus leading to more regular structures[20].
- At higher freezing temperature and consequently lower average cooling rate, ice crystals growth is more kinetically favored than ice nucleation[20]. Thus, a small number of large ice crystals are formed during freezing. This phenomenon was at the origin of the formation of large pores after ice sublimation.

The SEM and X-ray micrographs in Figure 5-5.c,d,e,f show the influence of NFC concentration on the structural properties of enzymatic NFC foams. As previously reported by Sehaqui *et al.*[10], denser NFC foams exhibit finer cellular architectures. A higher content of particles in the suspension generally provides more nucleation sites which results in the formation of numerous small pores[20]. For the investigated enzymatic NFC systems, and particularly for the highest NFC concentrations, the high number of NFCs in the suspensions could thus strongly affect the number of nucleation sites. In addition, for these systems, ice crystals could be constrained by the NFCs formed network, thus limiting their growth. Lastly, note that the 2D X-ray cross section views in Figure 5-5.f,h indicate that denser foams (Fig. 5-6.e) displayed a larger number of walls/plates with thick cross sections.

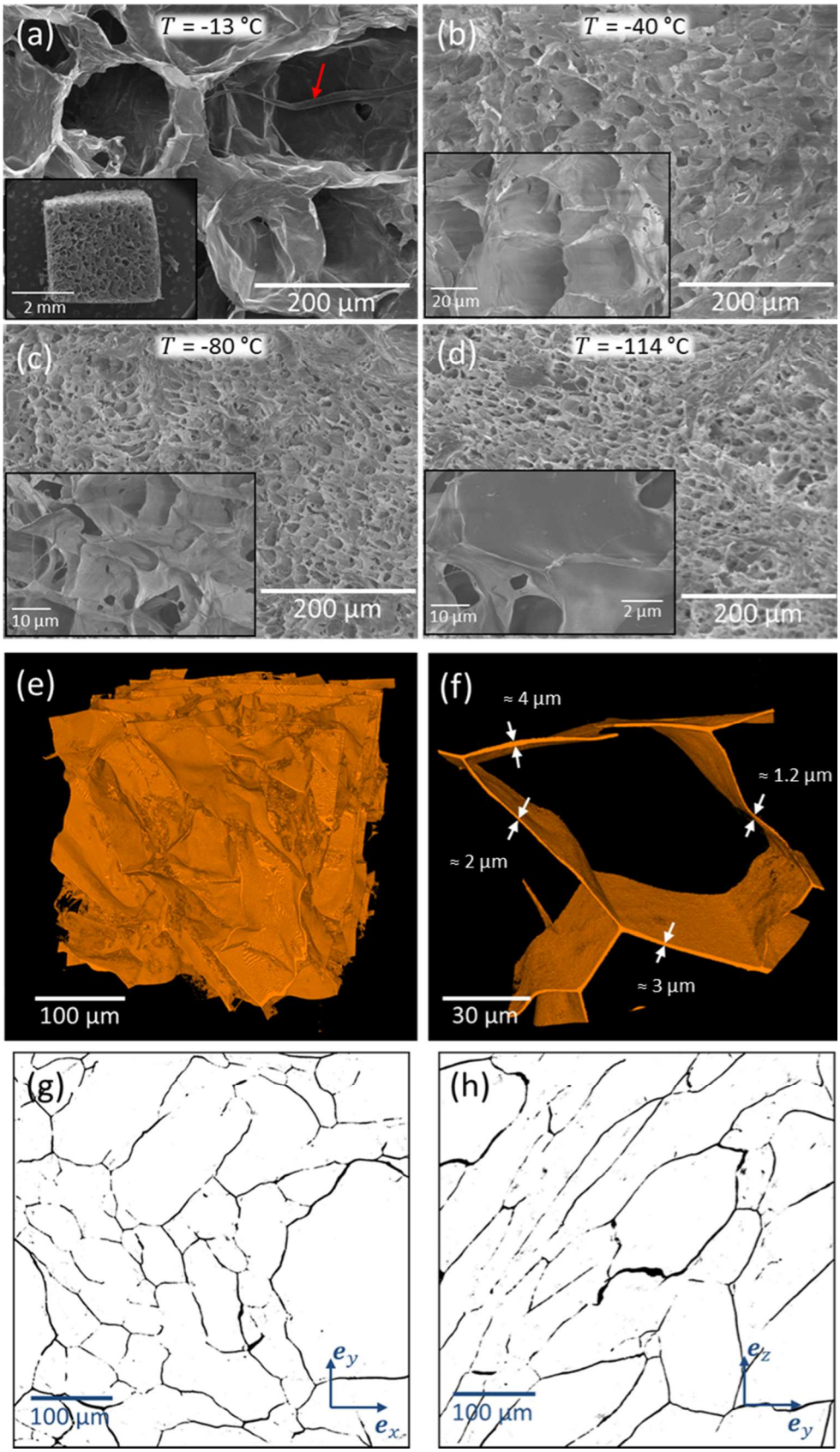

Figure 5-4. (a-d) SEM-FEG micrographs of TEMPO-oxidized NFC foams ($\rho \approx 10$ kg m^{-3}) obtained after freezing at various temperatures and then freeze-dryed. The red arrow in Fig. 5-4.a indicates a remaining partially disintegrated fiber. (e-f) 3D-rendered perspective views (voxel size: 0.32^3µm^3). (g-h) Cross section of a micrograph of a TEMPO-oxidized NFC foam (freezing temperature $T = -13$°C) obtained using X-ray synchrotron microtomography.

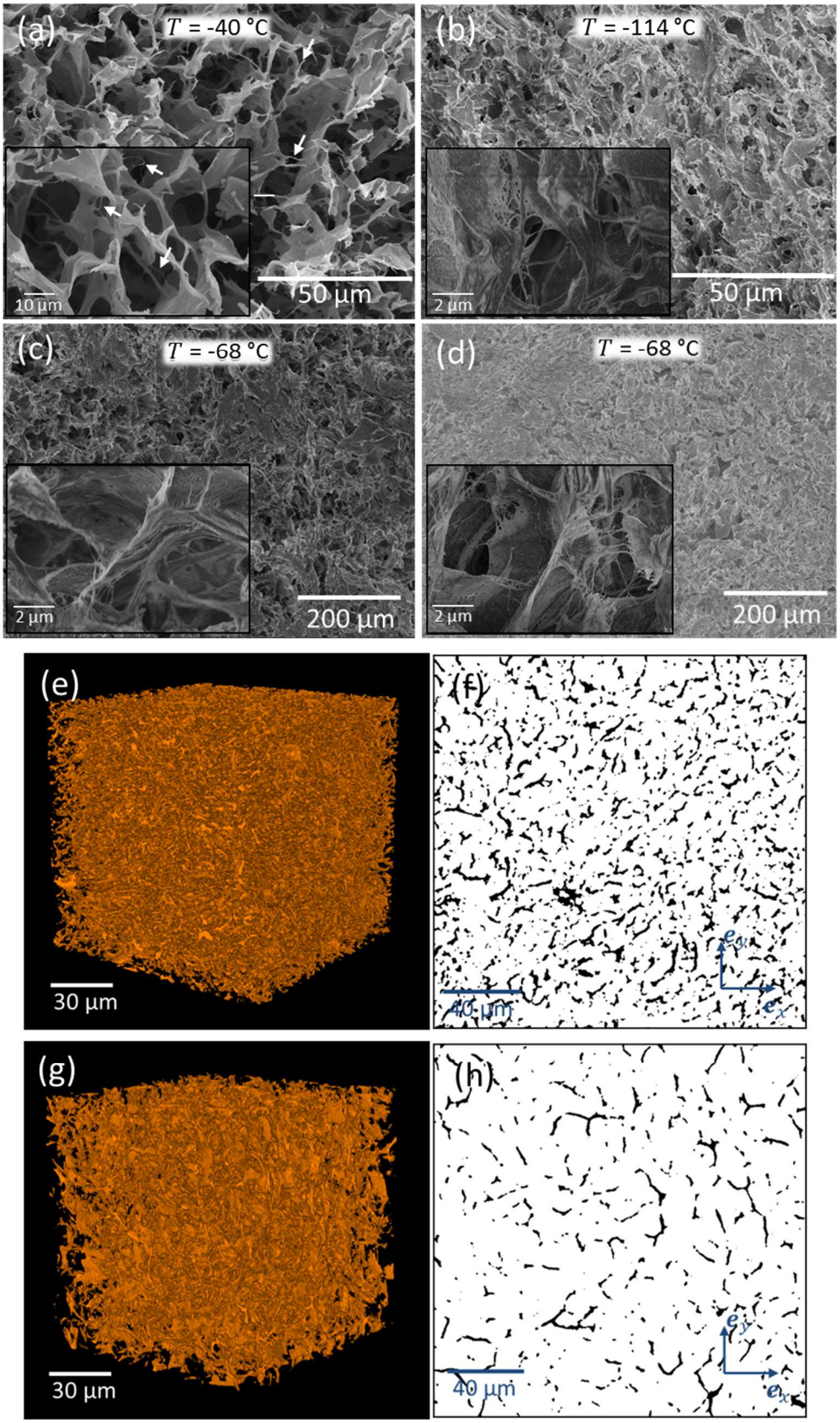

Figure 5-5. (a-b) SEM-FEG micrographs of enzymatic NFC foams ($\rho \approx 20$ kg m^{-3})) obtained after freezing at various temperatures and then freeze-dryed. The white arrows in Fig. 5-5.a show some dangling branches. Enzymatic NFC foams with $\rho \approx 20$ kg m^{-3} (c), and $\rho \approx 45$ kg m^{-3}(d) obtained after freezing at T= -68 °C and then freeze-dryed. (e, g) 3D-rendered perspective views (voxel size: 0.32^3 µm^3) and (f, h) cross section of segmented micrographs of enzymatic NFC foams (freezing temperature $T = -68$°C) obtained using X-ray synchrotron microtomography.

Finally, Figure 5-6 shows a collection of micrographs obtained for TEMPO-oxidized NFC foams ($\rho \simeq 17$ kg m^{-3}) prepared using mechanical stirring followed by quenching. The resulting foams exhibited interesting bimodal structures that consisted of some near-spherical mesoscale pores/cells with a diameter ranging from 100 µm to 600 µm that were flanked by more finer and anisotropic pores/cells in the form of 'buttresses' with dimensions that ranged between 20 and 50 µm. Note also that the fine pores shown in Fig. 5-6.c exhibited slightly smaller dimensions compared with those observed in the foams processed directly by quenching (Fig. 5-6.d). This observation is consistent with the previous remarks concerning enzymatic NFCs in Fig. 5-5.c,d,e,f. Thus, high NFC concentrations yielded foams with finer porous microstructures.

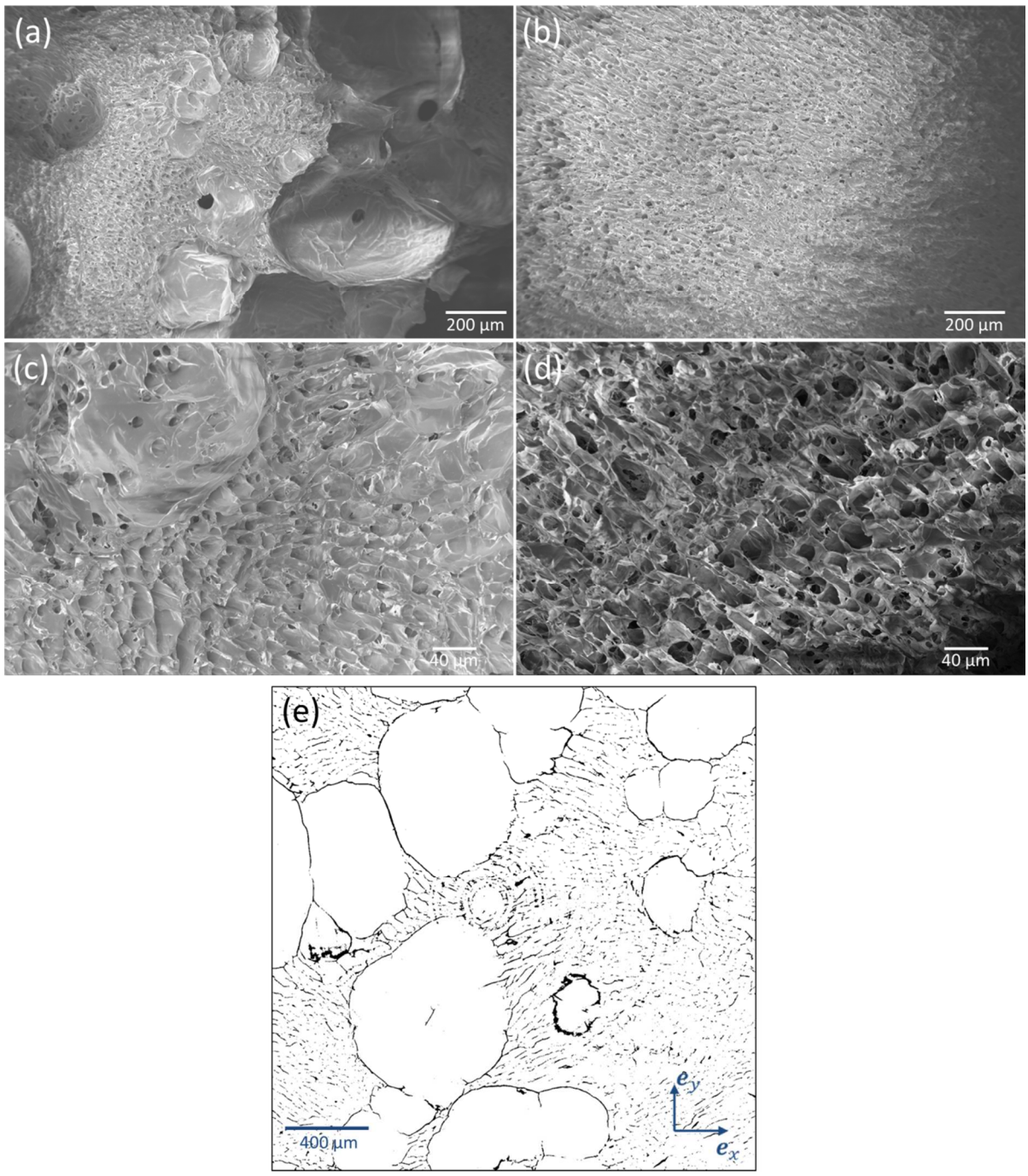

Figure 5-6.SEM micrographs showing the microstructures of various TEMPO-oxidized NFC foams obtained using the sorbet (a,c) and quenching (b,d) processes. (e) Cross-section in the horizontal plane of TEMPO-oxidized NFC foam (sorbet-like process) obtained using X-ray microtomography.

5.5 Mechanical properties

5.5.1 Macroscale and mesoscale rheological behaviour - Main aspects

The compression stress-strain curves obtained for TEMPO-oxidized and enzymatic foams were typical of many elasto-viscoplastic cellular materials[16]. Figure 5-7 shows that these curves were characterized by three distinct regimes:

- First, the NFC foams exhibited an initial linear behavior characterized by a modulus E up to an initial yield stress σ_y above which plastic deformation was marked, *i.e.*, with pronounced residual strain upon unloading ($0 \leq \varepsilon \leq 0.07$). The elastic to plastic transition was clearly marked, as for many elasto-viscoplastic foams[16].

- Above σ_y, where the consolidation of foams usually occurs[16], the stress was an increasing function of the compression strain. This strain hardening behavior was different from that usually observed for elasto-viscoplastic foams for which the strain hardening is much weaker. This strain hardening, which can be very interesting for practical structure applications, was rather close to that observed for crumpled sheets, self-locked materials and entangled fibrous media[43,44]. Note also the structural similarities between the TEMPO-oxidized NFC foam in Figure 5-4.e and the crumpled aluminium or paper thin foils studied in the litterature[43,45,46,47,48,49].
  Lastly, the loading-unloading curves showed hysteresis loops. It is worth to note that the unloading curves exhibited marked non-linear portions showing that the elastic energy stored within the cell walls upon loading would be sufficiently enough to unfold them partially.

- At higher compressive strains ($\varepsilon \geq 0.8$), all the obtained curves exhibited a densification regime characterized by a sharp increase in the compressive stress σ with the logarithmic strain ε.

The image insets in Figure 5-7 are extremely instructive and show that the uniaxial compressive tests were heterogeneous and accompanied at the meso-scale by localized buckling phenomena. These images also show the auxetic behavior, *i.e.*, the negative contractile lateral strain (negative Poisson ratio), that NFC foams systematically exhibited during compression. This behavior has already been observed in polymer foams[50] and also with crumpled foils[43]. In both cases, it is often attributed to re-entrant microstructures (see the comments in section 5.2).

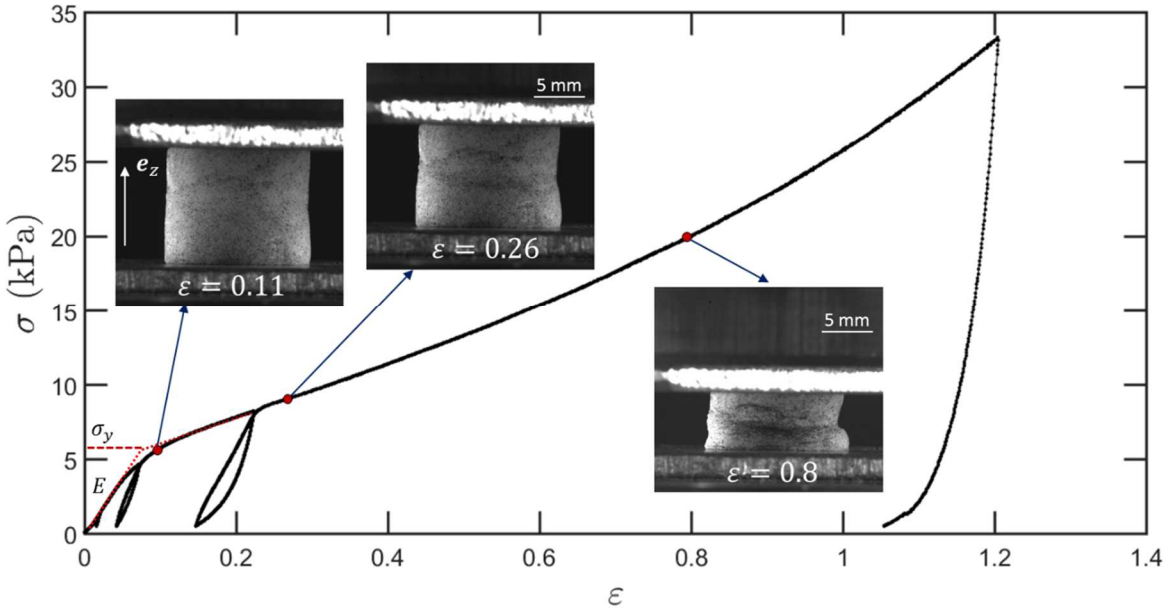

Figure 5-7. Typical stress-strain curves of a TEMPO-oxidized NFC foam ($\rho \approx 10$ kg m^{-3}) obtained after freezing at $T = -13$°C and then freeze-drying. The image insets show the evolution of the geometry of the TEMPO-oxidized foam during simple compression.

5.5.2 Deformation mechanisms at the microscale:

One *in situ* compression test was performed during X-ray experiments to unveil the stress-induced deformation and failure micro-mechanisms at the foam cell scale. Figure 5-8 shows the resulting stress-strain curve. At the beginning of the test ($0 \leq \varepsilon \leq 0.15$), the mechanical response was similar to that obtained using larger cylindrical foam samples outside the microtomograph (Fig. 5-7). Indeed, the elastic modulus $E \simeq 65$ kPa and the yield stress $\sigma_y \simeq 6$ kPa were consistent with those obtained using larger samples (Fig. 5-10). However, some differences were observed at higher strains: the stress-strain curve exhibited a weak strain-hardening regime (instead of a pronounced increase, as shown in Figure 5-7). Several potential origins may explain this discrepancy, *e.g.*, the potential degradation of the NFC structure due to the exposure to X-ray radiations and the viscoelastic effects associated with the deformation of the foam: first, the strain-rate is much lower in Figure 5-8 than that in Figure 5-7. Moreover, the compression test was interrupted to perform the scans, inducing noticeable stress relaxations, as depicted in Figure 5-8. In addition, the 2D segmented micrographs in Figure 5-7 revealed that the foam exhibited spatially heterogeneous deformation during compression (see for instance the deformation band localized in the upper part of the sample). Note that the tested sample also displayed a slight lateral contraction during compression, revealing the aforementioned auxetic effect.

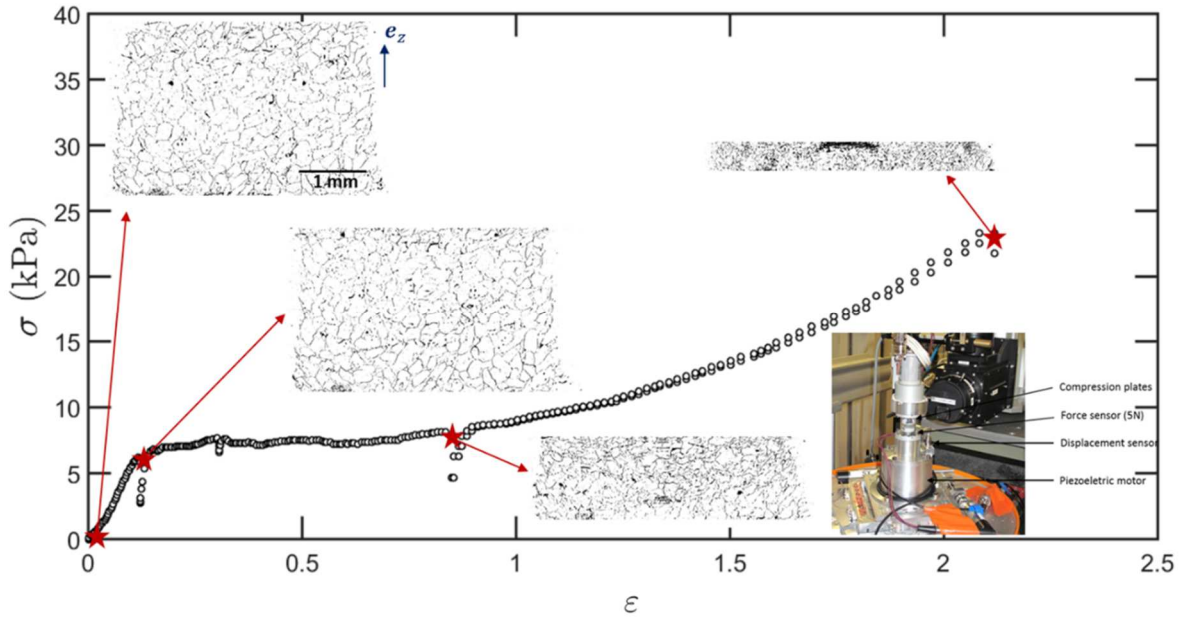

Figure 5-8. In situ compression stress-strain curve of a TEMPO-oxidized NFC foam ($\rho \approx 10$ kg m^{-3}, quenching temperature $T = -13$°C) obtained using X-ray microtomography. The insets show several cross sections along the vertical direction of a 3D segmented image (pixel size: 1.6 µm^3) that show the evolution of the geometry of the entire foam during compression.

Figure 5-9 shows an example of 3D views of the internal microstructure of the compressed NFC foam and its evolution during compression.

First compression stop - At $\varepsilon = 0.11$, *i.e.*, just at the onset of the yield stress, most of the cells in the sample were slightly deformed (and rotated), except in the vicinity of the upper compression plate (*i.e.*, above zone 1). In this localized band, the cell walls were primarily deformed by bending/buckling, in particular those oriented in a direction parallel to the compression direction. Besides, in this zone, some of the cell walls were irreversibly damaged and fractured.

Second compression stop - At $\varepsilon = 0.8$, the foam exhibited a spatially heterogeneous collapse of its cellular structure. Some of the foam cells were severely distorted. This phenomenon was associated with cell wall cracking/tearing (Fig. 5-9.b) and the formation of plastic hinges, whereas other parts of the structure were less affected by the increase in overall strain. This progressive and spatially heterogeneous load-induced collapse/crushing mechanism (local densification) could be at the origin of the gradual increase in the stiffness (strain-hardening behavior) of many NFC foams. Besides, the crushing is often induced by the high bending/buckling of the cell walls, leading to re-entrant deformation micro-mechanisms that could presumably occur at the origin of the auxetic behavior observed at the meso-scale (Fig. 5-7).

Third compression stop - At $\varepsilon = 2.2$, the structure was densely packed (all foam cells were collapsed). The foam cell walls began to impinge on each other, leading to a pronounced rise in the stress level (densification regime).

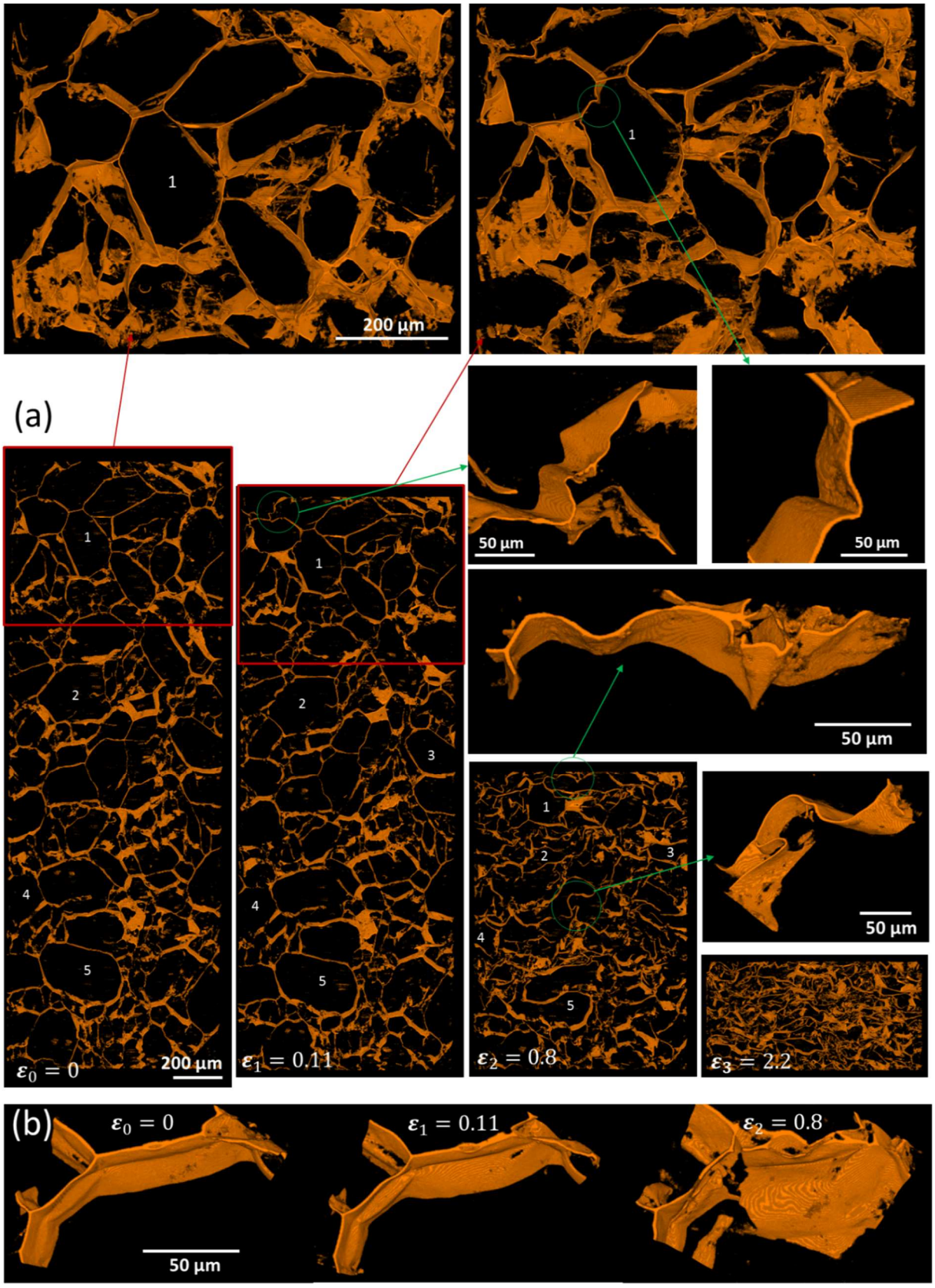

Figure 5-9. (a) 3D images (volume size $\approx 818 \times 818 \times 12$ μm^3) of the internal microstructure of a TEMPO-oxidized NFC foam ($\rho \approx 10$ kg m^{-3}, quenching temperature $T = -13$°C) and its evolution during compression. The insets show zooms on several regions of the foam. (b) 3D images of a junction between several foam cells and its deformation and fracture during compression.

5.5.3 Effect of the quenching temperature

The mechanical properties, *i.e.*, the elastic modulus E and the yield stress σ_y, of various NFC foams are plotted in Figure 5-10, as a function of their freezing temperature. These graphs revealed non-linear evolutions of the elastic modulus E and yield stress σ_y, as a function of the freezing temperature. Regardless of the type of foam, the mechanical properties were practically independent of the freezing temperature for $-120°C \leq T \leq -80°C$: as evidenced in Figure 5-4 and Figure 5-5, in this temperature range, no pronounced changes in the cellular structure of the foams were detected. In contrast, between $-80°C$ and $-13°C$, the mechanical properties of the foams increased with increasing the freezing temperature. In this range of temperatures, the mechanical response of NFC foams tripled by slightly varying the quenching temperature. In the same time, pronounced microstructure variations were recorded in Figure 5-4 and Figure 5-5 for this temperature range, regardless of the type of NFCs.

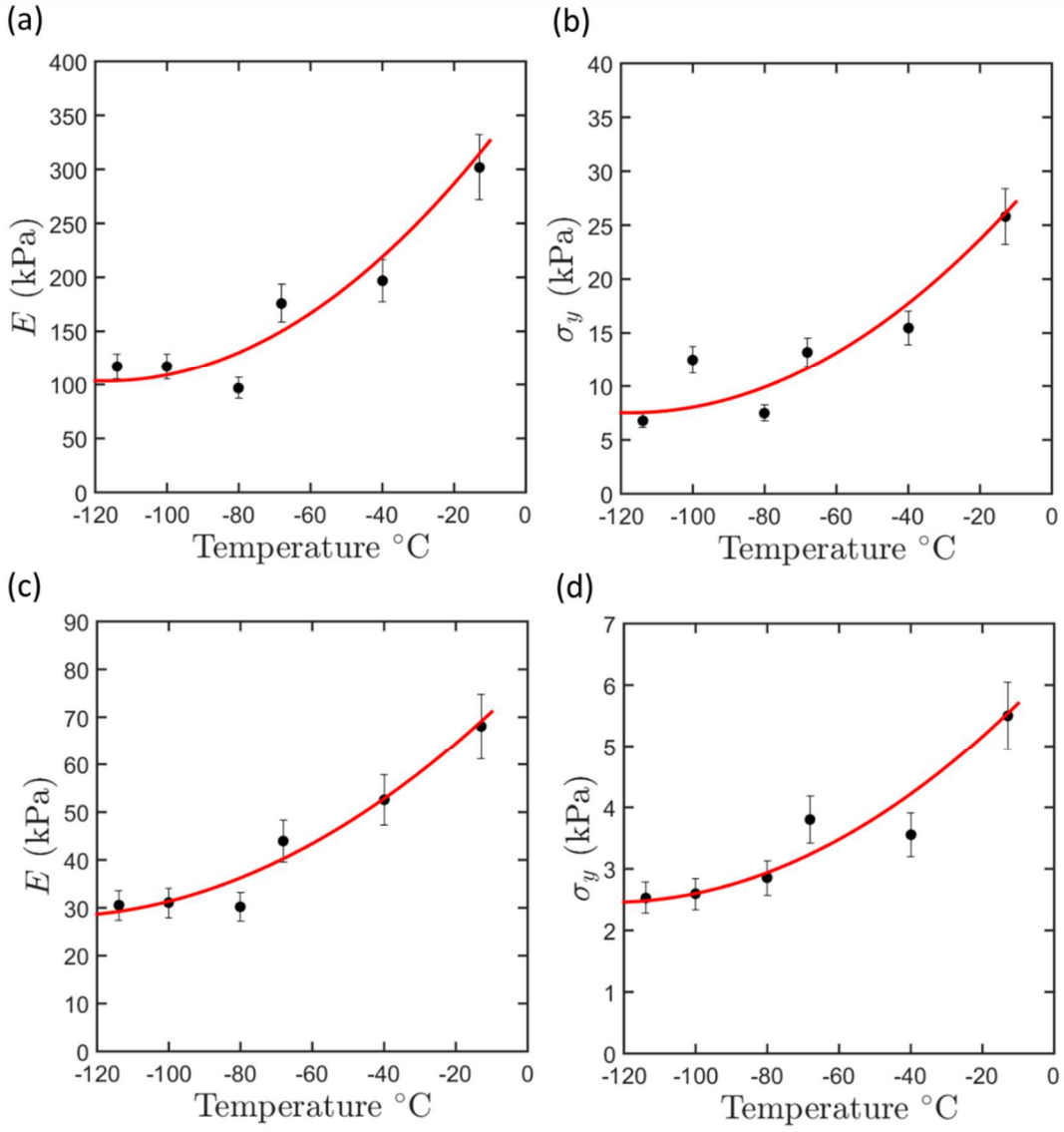

Figure 5-10. Evolution of the elastic modulus E and yield stress σ_y as a function of the freezing temperature for (a,b) enzymatic NFC foams ($\rho \approx 20$ kg m^{-3}) and (c,d) TEMPO-oxidized NFC foams ($\rho \approx 10$ kg m^{-3}).

5.5.4 Effect of mechanical stirring during freezing

The stress-strain curves plotted in Figure 5-11 show the undeniable role of the cellular architecture of NFC foams on their mechanical response[16]. The sorbet-like foam with a bimodal cellular structure exhibited higher mechanical performances with, for instance, an elastic modulus E that was three to four times greater than that of the foam prepared by quenching. Similarly, generating bimodal cellular structure doubled the yield stress of NFC foams. Note that similar enhancement of the mechanical properties was also reported for polymer foams with bimodal structures[34].

Besides, it is also interesting to mention that the specific elastic modulus of the bimodal NFC foams $E/\rho \simeq 62$ kJ kg^{-1} was close to that commonly obtained for expanded polystyrene (EPS) foams that are often used in sandwich panels[12]. Hence, these 'hybrid' biosourced materials could be potentially used for structural applications because they offer distinctive advantages such as good mechanical properties, low density and easy processing.

Several potential origins could explain the remarkable mechanical properties of the bimodal foam:

- First, the micrographs in Fig. 5-6.c show that fine pores were better formed and probably had thicker walls than those of the monomodal foams (Fig. 5-6.d).
- In addition, the thick walls surrounding the near-spherical mesoscale pores (Fig. 5-6.e) could act as 'buttresses', leading to a better consolidation of the foam structure.

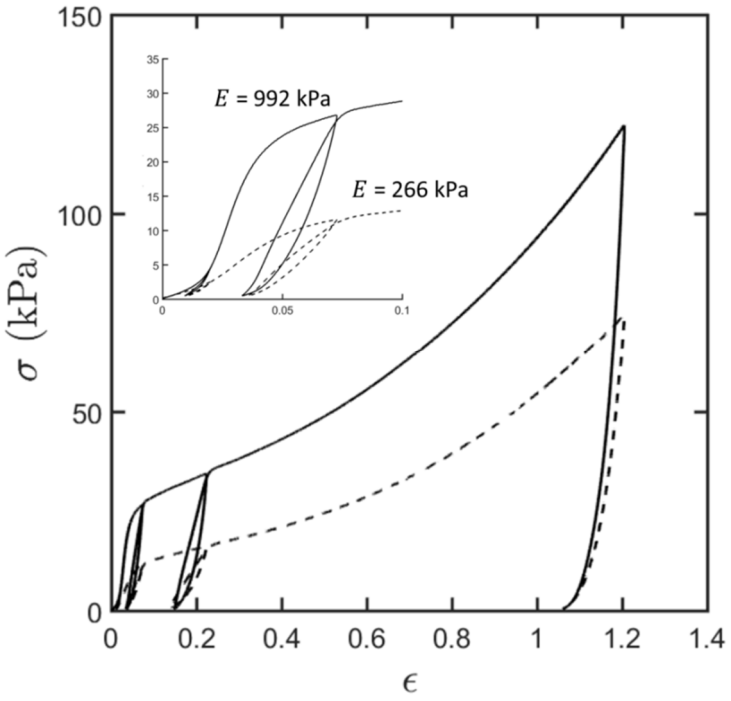

Figure 5-11. Typical stress-strain curves of TEMPO-oxidized NFC foams ($\rho \approx 16$ kg m^{-3}) processed using both the quenching (dashed line), and sorbet (solid line) processes. The inset show a zoom on the early stage of the curves.

5.5.5 Effect of relative density – Scaling laws

The evolutions of the Young's modulus E and the yield stress σ_y of both types of NFC foams, as a function of the foam relative density ρ/ρ_s are plotted in Figure 5-12, for foams prepared using a quenching temperature of −68°C. From this figure, several remarks can be drawn:
The elastic modulus E and yield stress σ_y were both power-law functions of the foam relative density ρ/ρ_s:

$$E \propto (\frac{\rho}{\rho_s})^n, \quad (1)$$

and,

$$\sigma_y \propto (\frac{\rho}{\rho_s})^m, \quad (2)$$

with power-law exponents $n = 2.29$ and 3.11, and $m = 2.22$ and 3.04 for TEMPO-oxidized and enzymatic NFC foams, respectively.

The scaling exponents ($n = 2.29$ and $m = 2.22$) of TEMPO-oxidized foams were close to those expected for classical cellular materials[16,17,43] with well-defined microstructures and deformation mechanisms, such as open ($n = 2$ and $m = 1.5$) or closed foams without thickening of edges ($n = 3$ and $m = 2$). These exponents are consistent with deformation micro-mechanisms ruled both by plate and strut bending. This assumption is in accordance with the microtomographic images (Fig. 5-9) showing bending of both ridges and thin walls of cells. However, note that the slightly higher values could be attributed to the role played by the remaining partially fibrillated fibers (Fig. 5-1).

In contrast, the scaling exponents ($n = 3.11$ and $m = 3.04$) of the enzymatic NFC foams were close to those usually obtained for aerogels, *i.e.*, $3 < n < 4$ and $2.5 < m < 3.5$[51,52,53,54]. This behavior could be directly linked to their disordered cellular structure and more precisely to the existence of dangling mass or branches that hung off the cell walls (Fig. 5-5)[55]. These portions of cells could act as "dead zones" that did not bear the applied load. Their volume fraction was difficult to determine from the 2D and 3D micrographs shown in Figure 5-5. However, it is expected to decrease as the NFC content increases and this parameter should be taken into account to properly assess the relevance of the above scaling laws[55].

Lastly, Figure 5-12 also shows the importance of controlling the internal microstructures of NFC foams: TEMPO-oxidized NFC foams have a less erratic cellular architecture than that associated with enzymatic NFC homologues, resulting in higher specific mechanical properties and lower scaling exponents.

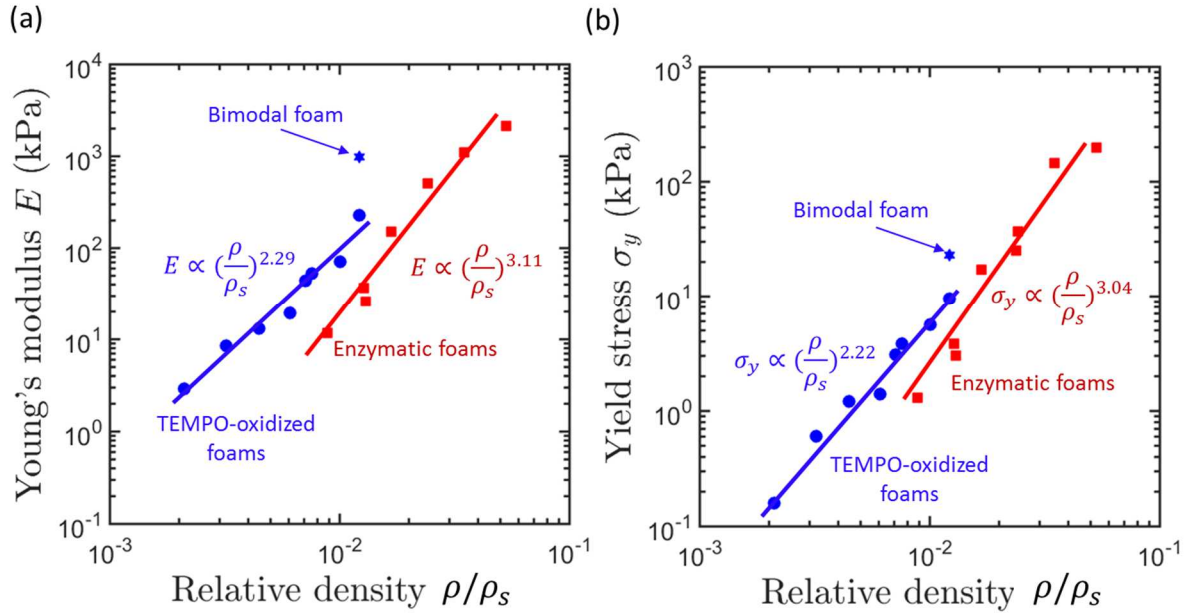

Figure 5-12. Evolution of the elastic modulus E (a) and the yield stress σ_y (b) as a function of the relative density (estimated using $\rho_s = 1500$ kg m^{-3}). Both types of foams were prepared using a quenching temperature of −68°C.

5.6 Conclusion

In this study, we investigated the effect of several factors such as NFC concentration, colloidal stability, homogeneity and polydispersity of NFC suspensions as well as the quenching temperature on the shrinkage, the microstructure and the mechanical properties of NFC foams, fabricated using two original freeze drying processing routes. Thus, NFC foams were obtained from enzymatic and TEMPO-oxidized NFC aqueous suspensions. For the first freeze-drying technique, temperature-controlled baths ($-196°C \leq T \leq -10°C$) enabled monitoring the freezing rate. The second technique was a 'sorbet-like' technique that enabled the NFC suspensions to be mechanically stirred during solidification. The shrinkage and the microstructure of NFC foams were qualitatively studied at the macro- and meso-scale using FE-SEM and 3D X-ray synchrotron microtomography images. From these experimental results, processing maps (mass concentration *vs.* temperature) were established. These maps allowed the optimal conditions for reducing foam shrinkage and obtaining homogeneous foams. We identified a critical concentration below which the homogeneity of the foam structure was impaired and shrinkage exhibited a dramatic increase. These concentrations depended on the suspension stability and were a function of the colloidal stability and morphology of NFCs.

NFC foams processed using optimal conditions exhibited homogeneous microstructure with complex cell shapes and open porosity, as well as specific features such as dangling mass (for enzymatic NFCs) or entrapped fibers that remained after the extraction process (for TEMPO-oxidized NFCs). Quenching temperature and NFC concentration were shown to govern the competition between ice nucleation and ice crystal growth, *i.e.*, the mechanisms leading to

the foam cell formation. Besides, the polydispersity of NFCs negatively affected the homogeneity of foam cell size and shape because it induced a perturbation in the motion of ice solidification front. In addition, mechanical stirring enabled the preparation of foams having bimodal cell sizes and shapes.

The mechanical properties of NFC foams were investigated using both classical compression tests. Macroscopic stress-strain compression curves exhibited three successive deformation regimes (elasticity, then plasticity with strain-hardening followed by a densification regime) that were typical of elasto-viscoplastic polymer foams. Specific strain localization and auxetic phenomena were also observed during compression. An original *in situ* compression test also revealed the deformation mechanisms of TEMPO-oxidized NFC foam during microtomography experiments. This technique revealed localized deformation bands. Severe bending and buckling of cell walls were also observed and conducted to re-entrant mechanisms that were probably responsible for the auxetic behavior of the foams. They were accompanied by cell wall tearing, both leading to the densification of the foam cells. At very high density, cell walls finally impinged on each other.

Our results also emphasized the role of processing conditions such as quenching temperature. An increase in quenching temperature progressively enhanced the NFC foam mechanical properties. Bimodal foams also exhibited enhanced mechanical properties compared with monomodal foams. In addition, the Young's modulus and the yield stress of NFC foams were power-law functions of the foam relative density. In the case of TEMPO-oxidized NFC foams, the power-law exponents were close, but slightly higher than those commonly found for polymeric or metallic foams within which the bending of the cell walls and edges is the leading deformation mechanisms. The slightly higher values could be attributed to the role played by the fibers remaining in the foams due to the extraction process. For enzymatic NFC foams, the power-law exponents are much higher and unusual. These foams exhibited a specific compression behavior that could be attributed to the role played by the process-induced dangling mass that could act as dead zones during the foam deformation. These results showed the beneficial effect on both the microstructures and the mechanical properties of NFC foams of an enhanced control of the foam processing conditions.

References

1 L. J. Gibson, *J. R. Soc. Interface*, 2012, **9**, 2749–2766.

2 D. Klemm, B. Heublein, H.-P. Fink and A. Bohn, *Angew. Chem. Int. Ed.*, 2005, **44**, 3358–3393.

3 J.-L. Wertz, J. P. Mercier and O. Bédué, *Cellulose Science and Technology*, CRC Press, 2010.

4 M. Henriksson, G. Henriksson, L. A. Berglund and T. Lindström, *Eur. Polym. J.*, 2007, **43**, 3434–3441.

5 M. Pääkkö, M. Ankerfors, H. Kosonen, A. Nykänen, S. Ahola, M. Österberg, J. Ruokolainen, J. Laine, P. T. Larsson, O. Ikkala and T. Lindström, *Biomacromolecules*, 2007, **8**, 1934–1941.

6 T. Saito, S. Kimura, Y. Nishiyama and A. Isogai, *Biomacromolecules*, 2007, **8**, 2485–2491.

7 A. Isogai, T. Saito and H. Fukuzumi, *Nanoscale*, 2011, **3**, 71–85.

8 K. Abe, S. Iwamoto and H. Yano, *Biomacromolecules*, 2007, **8**, 3276–3278.

9 T. Saito, T. Uematsu, S. Kimura, T. Enomae and A. Isogai, *Soft Matter*, 2011, **7**, 8804–8809.

10 H. Sehaqui, M. Salajková, Q. Zhou and L. A. Berglund, *Soft Matter*, 2010, **6**, 1824–1 832.

11 Z. M. Ali and L. J. Gibson, *Soft Matter*, 2013, **9**, 1580–1588.

12 A. E. Donius, A. Liu, L. A. Berglund and U. G. K. Wegst, *J. Mech. Behav. Biomed. Mater.*, 2014, **37**, 88–99.

13 H. Sehaqui, Q. Zhou and L. A. Berglund, *Compos. Sci. Technol.*, 2011, **71**, 1593–1599.

14 Y. Kobayashi, T. Saito and A. Isogai, *Angew. Chem.*, 2014, **126**, 10562–10565.

15 A. J. Benítez, J. Torres-Rendon, M. Poutanen and A. Walther, *Biomacromolecules*, 2013, **14**, 4497–4506.

16 L. J. Gibson and M. F. Ashby, *Cellular Solids: Structure and Properties*, Cambridge University Press, 1997.

17 N. Mills, *Polymer Foams Handbook: Engineering and Biomechanics Applications and Design Guide*, Butterworth-Heinemann, 2007.

18 S. Deville, *Materials*, 2010, **3**, 1913–1927.

19 S. Deville, *J. Mater. Res.*, 2013, **28**, 2202–2219.

20 W. L. Li, K. Lu and J. Y. Walz, *Int. Mater. Rev.*, 2012, **57**, 37–60.

21 S. Deville, E. Maire, G. Bernard-Granger, A. Lasalle, A. Bogner, C. Gauthier, J. Leloup and C. Guizard, *Nat. Mater.*, 2009, **8**, 966–972.

22 L. Qian and H. Zhang, *J. Chem. Technol. Biotechnol.*, 2011, **86**, 172–184.

23 T. C. F. Silva, Y. Habibi, J. L. Colodette, T. Elder and L. A. Lucia, *Cellulose*, 2012, **19**, 1945–1956.

24 J. Lin, L. Yu, F. Tian, N. Zhao, X. Li, F. Bian and J. Wang, *Carbohydr. Polym.*, 2014, **109**, 35–43.

25 W. Chen, H. Yu, Q. Li, Y. Liu and J. Li, *Soft Matter*, 2011, **7**, 10360–10368.

26 L. Melone, L. Altomare, I. Alfieri, A. Lorenzi, L. De Nardo and C. Punta, *J. Photochem. Photobiol. Chem.*, 2013, **261**, 53–60.

27 F. J. O'Brien, B. A. Harley, I. V. Yannas and L. Gibson, *Biomaterials*, 2004, **25**, 1077–1086.

28 P. Srinivasa and A. Kulachenko, *Mech. Mater.*, 2015, **80, Part A**, 13–26.

29 F. Martoïa, C. Perge, P. J. J. Dumont, L. Orgéas, M. A. Fardin, S. Manneville and M. N. Belgacem, *Soft Matter*, 2015, **11**, 4742–4755.

30 L. Salmén and C. Fellers, *J. Pulp Pap. Sci.*, 1989, **15**, J63–J65.

31 M. A. Beltran, D. M. Paganin, K. Uesugi and M. J. Kitchen, *Opt. Express*, 2010, **18**, 6423.

32 D. Paganin, S. C. Mayo, T. E. Gureyev, P. R. Miller and S. W. Wilkins, *J. Microsc.*, 2002, **206**, 33–40.

33 P. Latil, L. Orgéas, C. Geindreau, P. J. J. Dumont and S. R. Du Roscoat, *Compos. Sci. Technol.*, 2011, **71**, 480–488.

34 C. Zhang, B. Zhu, D. Li and L. J. Lee, *Polymer*, 2012, **53**, 2435–2442.

35 D. Brabazon, D. J. Browne and A. J. Carr, *Mater. Sci. Eng. A*, 2002, **326**, 370–381.

36 D. H. Kirkwood, *Int. Mater. Rev.*, 1994, **39**, 173–189.

37 F. Jiang and Y.-L. Hsieh, *J. Mater. Chem. A*, 2013, **2**, 350–359.

38 S. Varanasi, R. He and W. Batchelor, *Cellulose*, 2013, **20**, 1885–1896.

39 S. Toll, *J. Rheol. 1978-Present*, 1993, **37**, 123–125.

40 L. Berhan and A. M. Sastry, *Phys. Rev. E*, 2007, **75**, 041121.

41 A. P. Philipse, *Langmuir*, 1996, **12**, 1127–1133.

42 R. J. Hill, *Biomacromolecules*, 2008, **9**, 2963–2966.

43 O. Bouaziz, J. P. Masse, S. Allain, L. Orgéas and P. Latil, *Mater. Sci. Eng. A*, 2013, **570**, 1–7.

44 R. C. Picu, *Soft Matter*, 2011, **7**, 6768–6785.

45 Y.-C. Lin, J.-M. Sun, H. W. Yang, Y. Hwu, C. L. Wang and T.-M. Hong, *Phys. Rev. E*, 2009, **80**, 066114.

46 A. D. Cambou and N. Menon, *Proc. Natl. Acad. Sci.*, 2011, **108**, 14741–14745.

47 S. Cottrino, P. Viviès, D. Fabrègue and E. Maire, *Acta Mater.*, 2014, **81**, 98–110.

48 E. Sultan and A. Boudaoud, *Phys. Rev. Lett.*, 2006, **96**, 136103.

49 A. S. Balankin and O. S. Huerta, *Phys. Rev. E*, 2008, **77**, 051124.

50 R. Lakes, *Science*, 1987, **235**, 1038–1040.

51 R. Sescousse, R. Gavillon and T. Budtova, *Carbohydr. Polym.*, 2011, **83**, 1766–1774.

52 T. Woignier, J. Phalippou and R. Vacher, *J. Mater. Res.*, 1989, **4**, 688–692.

53 T. Woignier, J. Reynes, A. Hafidi Alaoui, I. Beurroies and J. Phalippou, *J. Non-Cryst. Solids*, 1998, **241**, 45–52.

54 H.-S. Ma, A. P. Roberts, J.-H. Prévost, R. Jullien and G. W. Scherer, *J. Non-Cryst. Solids*, 2000, **277**, 127–141.

55 N. Hüsing and U. Schubert, *Angew. Chem. Int. Ed.*, 1998, **37**, 22–45.

Conclusion générale et perspectives

L'objectif général de ce travail était d'étudier l'incorporation de nanorenforts biosourcés aux propriétés mécaniques intéressantes, à savoir des nanofibrilles de cellulose (NFC), dans des matériaux composites à matrice polymère et dans des mousses. Nous avons vu que ces nouveaux matériaux biosourcés pouvaient être utilisés par exemple pour la conception de structures sandwich. Dans cette étude à caractère expérimental, théorique et numérique, nous avons cherché à proposer des pistes pour optimiser les procédés d'élaboration et les propriétés en service de ces matériaux.

Nous avons d'abord élaboré des suspensions aqueuses de NFC obtenues à partir de fibres de pâte à papier en utilisant deux voies d'extraction chimio-mécanique différentes : une voie enzymatique et une voie d'oxydation TEMPO. Les suspensions enzymatiques comportent trois classes de particules : quelques rares fibres partiellement fibrillées ayant un diamètre de 10 à 20 µm et une longueur de 100 à 300 µm, une fraction d'éléments fibreux de taille intermédiaire ayant un diamètre supérieur à 80 nm et une longueur comprise entre 5 et 10 µm ainsi qu'une fraction d'éléments plus petits ayant un diamètre de l'ordre de 20 à 40 nm et une longueur comprise entre 2 et 5 µm. Ces suspensions sont donc très polydispersées. Par ailleurs, leur faible charge de surface leur confère une faible stabilité au repos (suspensions floculées). En revanche, les suspensions TEMPO sont quant à elles stables et homogènes au repos en raison de leur forte charge de surface. En outre, elles comportent seulement deux classes de taille de particules : quelques rares fibres ayant un diamètre de 10 à 20 µm et une longueur de 400 à 600 µm et une fraction importante de fibrilles individualisées et très élancées ayant un diamètre de l'ordre de 3 à 5 nm et une longueur de 1000 à 1500 nm.

De là, nous avons plus particulièrement développé trois axes de recherche.

En premier lieu, nous avons étudié la rhéologie des suspensions concentrées de NFC. Comprendre et modéliser la rhéologie complexe de ces fluides à seuil thixotropes est primordial dans la mesure où beaucoup de procédés d'élaboration de composites ou de mousses impliquent que ces matériaux s'écoulent. Dans cet optique, des essais de rhéométrie en géométrie de Taylor-Couette ont été couplés à des observations de la structure des suspensions par des

techniques de visualisation optique et à des mesures de champs cinématiques par vélocimétrie ultrasonore (rhéo-USV). En accord avec les travaux de la littérature, nous avons vu que les suspensions de NFC enzymatiques ont tendance à floculer pour certaines vitesses de cisaillement et à se désagréger à plus fortes vitesses de sollicitation. Nous avons également montré l'influence du chemin de sollicitation (montée ou descente en taux de cisaillement) sur les phénomènes d'agrégation et de désagrégation de flocs. Au contraire, les suspensions de NFC TEMPO présentent une mésostructure stable pour toutes les conditions d'essais. Pour ces dernières suspensions, les mesures de champs cinématiques par rhéo-USV ont permis de montrer que les écoulements sont fortement hétérogènes et présentent des phénomènes de glissement aux parois, des multiples bandes de cisaillement couplées à des zones d'écoulement de type « bouchon ». Ces écoulements complexes sont caractéristiques d'une transition solide-fluide du comportement de la suspension depuis celui d'un gel solide visco-élastoplastique à faible taux de cisaillement vers celui d'un fluide visqueux à plus fortes vitesses de sollicitation. Ils peuvent être attribués à la présence de deux mécanismes antagonistes aux échelles fines : (i) la structuration ou restructuration de la suspension induite par la présence d'un réseau d'interactions colloïdales entre les NFC et (ii) la déstructuration et la réorientation de ce réseau sous l'effet de forces hydrodynamiques visqueuses. Sur la base de cette étude, un modèle rhéologique multi-échelles semi-analytique a été développé. Il s'inspire de travaux dédiés aux suspensions de fibres non-colloïdales, de nanofibres (nanotubes de carbone) et aux colloïdes. Il s'appuie sur un générateur numérique de microstructures réalistes qui prend en compte la géométrie (corps élancés tortueux) et la concentration en nanofibres mais également l'évolution de leur orientation au cours de l'écoulement. En outre, il intègre les interactions physico-chimiques et mécaniques s'exerçant à l'échelle des nanofibres : forces d'interaction colloïdales, browniennes et hydrodynamiques à courtes et longues distances. Simple à mettre en œuvre, ce modèle permet de montrer que les interactions colloïdales et hydrodynamiques, ainsi que la tortuosité et l'orientation des NFC jouent un rôle majeur sur la contrainte seuil et sur le comportement rhéofluidifiant de ces suspensions.

Plusieurs pistes de recherche pourraient être explorées à la suite de cette étude. Sur le plan expérimental, le travail que nous avons mené en cellule de Taylor-Couette avec le dispositif de vélocimétrie ultra-sonore pourrait être complété et enrichi par des mesures plus fines des champs cinématiques. Par exemple, l'ajout d'une seconde barrette de transducteurs permettrait de mesurer d'autres composantes des champs de vitesse et de détecter de possibles phénomènes 3D d'écoulements. Une analyse plus approfondie des données de « speckle » pourrait aussi être conduite afin d'estimer des profils de concentration dynamiques dans l'entrefer du rhéomètre et de quantifier les phénomènes de migration et de déplétion. Toujours avec cette même technique, il pourrait être intéressant d'étudier la rhéologie des suspensions de NFC sous écoulements élongationnels. Nous avons également vu que dans d'autres études de la littérature, l'évolution spatiale et temporelle de l'orientation des NFC sous écoulement avait pu être quantifiée par le biais de techniques de diffusion de la lumière à raons X aux petits angles. Le couplage de ces deux techniques apporterait indubitablement

des données expérimentales d'une grande richesse, notamment pour construire des modèles rhéologiques enrichis et affinés pertinents. Sur le plan théorique et numérique, le modèle rhéologique que nous avons proposé est un premier pas vers la modélisation des nombreux phénomènes complexes impliqués dans l'écoulement des suspensions de NFC. De nombreuses améliorations pourraient être apportées à ce modèle. Parmi celles-ci, on peut citer la prise en compte de mécanismes de déformation des NFC (flexion, torsion) sous écoulement afin de mieux appréhender la visco-élastoplasticité de ces suspensions notamment en régimes transitoires, (ii) de forces de van der Waals (attractives) conduisant, dans le cas des suspensions enzymatiques, à des pertes de stabilité et la présence de flocs se déstructurant plus ou moins rapidement sous écoulement.

En deuxième lieu, nous avons étudié le comportement mécanique de nanocomposites à matrice polymère renforcée par des NFC TEMPO, avec pour objectif de comprendre les effets induits par le nanorenfort sur les propriétés mécaniques macroscopiques des nanocomposites : les modèles micromécaniques classiquement utilisés dans la littérature pour prédire les propriétés élastiques des nanocomposites renforcés par des NFC sont inopérants. Pour cela, nous avons élaboré des nanocomposites à matrice hydrosoluble (PEO) sous forme de films, en faisant varier sur une très grande plage la fraction volumique de NFC. Bien qu'une description fine des nanostructures formées par les NFC soit encore difficile à réaliser, les observations recueillies par AFM, MEB-FEG et DRX tendent à montrer que les NFC s'enchevêtrent pour former des nanoréseaux de nanofibres à orientation plane et aléatoire. Jusqu'à de faibles fractions volumiques de NFC, les mesures par analyse mécanique dynamique réalisées sur ces nanocomposites montrent que ces réseaux sont formés de liaisons hydrogènes cohésives qui contribuent en très grande partie au comportement mécanique de ces matériaux. En outre, les essais de traction simple montrent que les propriétés élastiques des nanocomposites sont bien en deçà des prévisions données par les modèles micromécaniques de la littérature. De là, en s'appuyant une nouvelle fois sur des générations numériques réalistes des réseaux de NFC, nous avons proposé un modèle multi-échelles alternatif (semi-analytique) où les principaux nano-mécanismes de déformation envisagés sont ceux se produisant au niveau des très nombreuses interfaces entre NFC et dans les parties amorphes des NFC, les parties semi-cristallines des NFC étant considérées comme des corps rigides.

Ce modèle tensoriel a été validé par des essais de traction simple sur un type de nanocomposites et de nanopapiers. Cette validation pourrait être renforcée en couplant ces essais à des mesures de champs cinématiques par corrélation d'images numériques, ce qui permettrait d'estimer des coefficients de Poisson. D'autres sollicitations mécaniques macroscopiques pourraient également être réalisées : traction plane, traction bi-axiale ou cisaillement simple, etc. La validation de ce modèle pourrait aussi être consolidée en confrontant ses prévisions aux résultats expérimentaux acquis pour d'autres systèmes, en changeant par exemple la géométrie, l'orientation, le type de NFC ou bien encore le type de matrice. En outre, le modèle est basé sur les nano-mécanismes de déformation des zones amorphes et des liaisons

entre NFC. Nous avons proposé a priori des formes phénoménologiques simples pour traduire ces mécanismes, car leur caractérisation et leur modélisation restent encore un problème ouvert qui est très difficile. Des expériences visant à déformer sous AFM des portions amorphes de NFC ou sur des liaisons entre NFC isolées, déformées sous AFM pourraient sans doute permettre de mieux spécifier et quantifier ces expressions. Plusieurs pistes pourraient également être envisagées pour étendre le domaine de validité de la modélisation : prise en compte des interactions fibres matrice pour de plus faibles quantités de NFC (régimes semi-dilué et dilué), des couplages thermo-hygromécaniques, des mécanismes de rupture des liaisons, de décohésion fibre-matrice, voire de rupture de NFC pour décrire l'élasto-plasticité et l'endommagement des nanocomposites et nanopapiers. Enfin, on peut noter que le modèle proposé se place dans le cadre de la mécanique des milieux continus standards : il est valable pour une bonne séparation d'échelles entre la taille de NFC et celle de la sollicitation macroscopique. Le cadre théorique dans lequel il a été construit permet de montrer que dans le cas contraire, par exemple au voisinage d'une fissure se propageant dans le nanocomposite ou le nano-papier, le modèle se généralise en un milieu de Cosserat : une démarche similaire à celle décrite dans ce document pourrait être alors adoptée pour en construire une estimation analytique.

En troisième lieu, nous avons cherché à améliorer le contrôle et la maîtrise de la microstructure de mousses de NFC élaborées par cryodessiccation à partir des suspensions aqueuses de NFC. Nous avons préparé différentes mousses de NFC en faisant varier la température de solidification, la nature de la suspension (enzymatique et TEMPO) ainsi que sa concentration. Des conditions optimales d'élaboration conduisant à des mousses à microstructure homogène présentant un faible retrait lors de la dessiccation ont pu être dégagées pour chaque type de suspension de NFC. La structure des mousses homogènes aux échelles macro et mésoscopiques a ensuite été caractérisée par MEB et par microtomographie synchrotron à rayons X, soulignant le rôle majeur de la température de solidification et de la concentration en NFC sur la morphologie des cellules des mousses. Ces différences de morphologie induisent des propriétés mécaniques et des lois d'échelles très différentes. En outre, par rapport aux suspensions de NFC enzymatiques, les suspensions de NFC TEMPO ont tendance à former des mousses à architectures cellulaires plus régulières et aux propriétés mécaniques supérieures. Pour ces dernières, nous avons pu analyser les micromécanismes de déformation à partir d'images 3D obtenues au cours d'essais de compression in situ en microtomographie synchrotron à rayons X.

Ce travail pourrait se poursuivre selon pusieurs directions. Par exemple, nous avons montré qu'un brassage mécanique en cours de solidification permettait de fabriquer des structures cellulaires bimodales dont les propriétés mécaniques sont particulièrement intéressantes. Cette procédure d'élaboration, inspirée des techniques de solidification de la métallurgie ou de l'agro-alimentaire, n'a été explorée que succinctement dans ce mémoire et devrait être analysée plus en profondeur pour optimiser l'architecture des mousses qui en sont issues.

D'une manière plus générale, les micro-mécanismes de solidification et de dessiccation qui sont impliquées lors de l'élaboration des mousses de NFC restent encore mal compris. Leur détermination nécessiterait des études de fond. Dans cet optique, la microtomographie à rayons X à haute résolution et à faible temps d'acquisition (les temps d'imagerie sur les grands instruments sont aujourd'hui inférieurs à la seconde) permettrait des observations 3D et in situ inédites de ces mécanismes mis en jeu, constituant ainsi une base de données solide et conséquente.